TRIBHUVAN UNIVERSITY

INSTITUTE OF ENGINEERING

PULCHOWK CAMPUS

THESIS NO.: T1/079

3D Stress-Strain Analyses of Geogrid-Reinforced Pavements under Vehicle Load Configurations and Dynamics

by

Aanchal Tiwari

A THESIS

SUBMITTED TO THE DEPARTMENT OF CIVIL ENGINEERING

IN PARTIAL FULFILLMENT OF THE REQUIREMENTS FOR THE

DEGREE OF MASTER OF SCIENCE IN TRANSPORTATION ENGINEERING

DEPARTMENT OF CIVIL ENGINEERING

LALITPUR, NEPAL

APRIL, 2025

COPYRIGHT

TRIBHUVAN UNIVERSITY

INSTITUTE OF ENGINEERING

PULCHOWK CAMPUS

DEPARTMENT OF CIVIL ENGINEERING

The undersigned certify that they have read and recommended to Institute of Engineering for acceptance, a thesis entitled **"3D Stress-Strain Analyses of Geogrid-Reinforced Pavements under Vehicle Load Configurations and Dynamics"** submitted by Aanchal Tiwari (PUL079MSTrE001) in partial fulfillment of the requirement for degree of Master of Science in Transportation Engineering.

.....

Supervisor: Prof. Dr. Padma Bahadur Shahi
Visiting Faculty, Department of Civil Engineering
Institute of Engineering

.....

Supervisor: Associate ~~Prof. Dr.~~ Rajan Suwal
Faculty, Department of Civil Engineering
Institute of Engineering

.....

External Examiner: Er. Prabhat Kumar Jha
Department of Road
Ministry of Physical Infrastructure and Transport

.....

Mr. Anil Marsani
Coordinator, MSc in Transportation Engineering
Department of Civil Engineering

Date: 21 April, 2025

ABSTRACT

This thesis investigates the 3D stress-strain behavior of geogrid-reinforced pavements under dynamic vehicle load configurations. Field data was collected from the Arughat-Okhale Road section of the Mid-Hill Highway project in Gorkha, Nepal, where geogrid reinforcement has been applied. Data was logged at two sites, one with geogrid and one without, located 100 meters apart at the 1+700 CH point, measured from the Budhi Gandaki Bridge. These sites provide a direct comparison of the effects of geogrid reinforcement.

The study examines various vehicle load configurations, including the TATA Truck Tipper 1613c and the Ford Ranger 3.2 XLT Pickup, with speeds ranging from 5 to 50 km/h, including intermediate values, as well as accelerated motion with acceleration values between 0.25 and 1.0 m/s². Point/line and area load configurations were analyzed to determine which, in combination with drainage conditions (undrained or drained), best align with field observations. This work is essential for validating numerical models against field measurements taken at constant speeds, in both unreinforced and geogrid-reinforced pavement sections.

Numerical models were developed using the Tensar 40/40Q biaxial geogrid, a polypropylene material with a biaxial tensile strength of 16 kN/m at 2% strain. This research also investigates rutting and fatigue life, and their influence on the service life ratio when geogrid reinforcement is incorporated into road pavements. Additionally, it evaluates the most suitable material models for the analysis. Discrepancies identified with linear elastic models prompted the use of more advanced constitutive models, such as Mohr-Coulomb, Hardening Soil, Soft Soil, and Cam-Clay, to better capture material behavior. The study further examines the effects of vehicle acceleration and deceleration on pavement performance. Stress-strain improvements in the subgrade and base layers due to geogrid placement are analyzed to assess their roles in mitigating structural deficiencies and surface distresses.

Keywords: Geogrid Reinforcement, Stress-Strain Behavior, Vehicle Load Configuration, Vehicle Load Dynamics, Pavement Performance

ACKNWOLEDGEMENT

I would like to express my deepest gratitude to my esteemed research supervisors, Prof. Dr. Padma Bahadur Shahi, and Associate Prof. Dr. Rajan Suwal for their continuous guidance, support, and invaluable feedback throughout the course of my research. Their expertise, encouragement, and constructive suggestions have been instrumental in shaping this thesis.

I would also like to extend my sincere thanks to the Program Coordinator Assistant Prof. Anil Marsani of M.Sc. in Transportation Engineering for providing the necessary academic support and resources during my studies.

My sincere thanks go to Assistant Prof. Dr. Pradip Kumar Shrestha, Chief of the Research and Training Unit (RTU), Pulchowk Campus, and to Er. Prabhat Kumar Jha from the Ministry of Physical Infrastructure and Transport (MoPIT), for providing access to field instrumentation, monitoring opportunities, and the necessary research facilities that were crucial to this study.

I would like to give special thanks to Assistant Prof. Dr. Rojee Pradhananga and Assistant Prof. Dr. Ram Chandra Tiwari for their invaluable suggestions, guidance, and encouragement, which have significantly shaped the direction and quality of this work.

I also extend my thanks to CMTL and the Heavy Lab staffs for their assistance with laboratory tests, including Hydrometer, Permeability, Triaxial, and Consolidation tests, useful for higher material models. I would like to remember Assistant Prof. Kalyan Poudel for his invaluable support throughout the lab tests.

Finally, I would like to express my gratitude to my family, friends, and all those who have directly or indirectly contributed to the completion of this research.

Name: Aanchal Tiwari
Roll No. : 079/MSTrE/001

TABLE OF CONTENTS

LIST OF TABLES

LIST OF FIGURES

LIST OF SYMBOLS

γ_{unsat}	Unsaturated Unit Weight (kN/m^3)
γ_{sat}	Saturated Unit Weight (kN/m3)
E	Resilient Modulus (MPa)
$MR_{support}$	Effective Resilient Modulus of the Supporting Layer (MPa)
h	Thickness of Granular Layer (mm)
EA1	Longitudinal Stiffness at 2% Strain Longitudinal (kN/m)
EA2	Transverse Stiffness at 2% Strain Transverse (kN/m)
GA	Shear Stiffness (kN/m)
K	Geotextile Stiffness (kN/m)
k Eq.	Equivalent Geogrid Stiffness (kN/m)
Tcycle	Time Period per Cycle (Seconds)
f	Frequency of Motion (Hz)
Ω	Angular Velocity (rad/sec.)
Φ	Phase Angle (Degrees)
Δt	Dynamic Time Step (Seconds)
V	Velocity of Motion (km/h or, m/sec)
a	Acceleration of Motion (m/sec2)
P	Perimeter of Wheel (m)
l_e	Target Element Dimension (m)
r_e	Relative Element Size Factor
$x_{max}, y_{max,}\ z_{max}$	Maximum Coordinate of the Model in x, y, and z Directions
$x_{min}, y_{min,}\ z_{min}$	Minimum Dimension of the Model in x, y, and z Directions
BC @ X_{min}	Boundary Condition along X-minimum
BC @ Y_{min}	Boundary Condition along Y-minimum
BC @ Z_{min}	Boundary Condition along Z-minimum
BC @ X_{max}	Boundary Condition along X-maximum
BC @ Y_{max}	Boundary Condition along Y-maximum
BC @ Z_{max}	Boundary Condition along Z-maximum
σ_1	Major Principal Stress, Sigma 1 (kN/m2)

σ_2	Intermediate Principal Stress, Sigma 2 (kN/m2)
σ_3	Minor Principal Stress, Sigma 3 (kN/m2)
e_1	Major Principal Strain (m)
e_2	Intermediate Principal Strain (m)
e_3	Minor Principal Strain (m)
u	Total Displacement (m)

LIST OF ABBREVIATIONS

3D	Three-dimensional
AOS	Apparent Opening Size
CBR	California Bearing Ratio
CH	Chainage
DBST	Double Bituminous Surface Treatment
DCP	Dynamic Cone Penetrometer
DCPT	Dynamic Cone Penetration Test
EPC	Earth Pressure Cell
FEM	Finite Element Method
MARV	Minimum Average Roll Values
MQC	Manufacturing Quality Control
PP	Polypropylene Type
SLR	Service Life Ratio
MSA	Million Standard Axle

CHAPTER 1: INTRODUCTION

1.1 Background

The performance of geogrid-reinforced pavements is influenced by a complex interplay of factors, including vehicle load configurations, load dynamics, material behavior, and drainage conditions. Geogrids are synthetic materials used to reinforce pavements by enhancing load distribution, reducing deformation, and improving the structural stability of pavements, particularly in the subgrade and base layers. While geogrid-reinforced pavements have demonstrated improved durability and performance in many cases, the understanding of their three-dimensional (3D) stress-strain behavior, particularly under real-world dynamic loading conditions, remains limited.

One of the primary challenges in pavement analysis is the complexity of traffic load configurations and dynamics. Most previous studies have largely focused on static or simplified loading scenarios, which often fail to account for the effects of varying vehicle speeds, accelerations, and the distinction between point/line and area load distributions. Under dynamic traffic conditions, the stress distribution within the pavement structure changes significantly, which can have a substantial impact on the pavement's performance and longevity. For example, Chatti and Yun (1995) demonstrated that vehicle speed plays a critical role in the dynamic response of multi-layered pavements, with faster vehicles causing different stress patterns compared to slower ones. This variability is crucial when designing pavements that need to withstand real-world traffic conditions, where vehicle loads and speeds fluctuate.

Studies such as those by Wu et al. (2020) have highlighted the importance of load patterns and vehicle speeds, noting that point loads tend to generate higher surface deflections and strains compared to area-based loads. Moreover, the dynamic responses of pavements tend to decrease with increasing vehicle speed due to the viscoelastic nature of the asphalt, which suggests that loading patterns and speed should be taken into consideration when analyzing pavement performance under real-world conditions. The significant effect of dynamic

loading on pavement response calls for more accurate predictive models that reflect these factors, especially when incorporating geogrid reinforcement.

Another factor that remains inadequately explored is the interaction between geogrid reinforcement and drainage conditions, such as undrained versus drained states. The moisture content of the soil and the drainage capability of the pavement layers play a significant role in the stress-strain behavior of geogrid-reinforced pavements. Geogrid reinforcement in undrained conditions may behave differently than in drained conditions, potentially influencing the long-term stability of the pavement structure. Leng and Gabr (2002) noted that geogrid reinforcement can significantly improve the structural integrity of pavement systems, particularly when combined with adequate drainage. Their study emphasized how the interaction between reinforcement and drainage could enhance stress distribution and reduce deformations in base courses, thereby extending the life of flexible pavements. However, the effects of different drainage conditions on the 3D stress distribution in geogrid-reinforced pavements remain underexplored.

Furthermore, the optimal placement of geogrids within the pavement structure is still a subject of active research. Traditionally, geogrids are placed within the base or subgrade layers to improve load distribution and prevent excessive settlement. However, the exact placement depth that maximizes their effectiveness in reducing stress concentrations and mitigating structural deficiencies remains unclear. In this context, research by Saad et al. (2006) indicated that placing geosynthetics at the base-asphalt concrete interface significantly reduced fatigue and rutting strains, particularly in thinner bases. This finding underscores the importance of geogrid placement depth in enhancing pavement performance, especially under dynamic loading conditions.

The stiffness of geogrid materials, which varies based on specifications such as 16 kN/m, 22 kN/m, and 25 kN/m, also plays a crucial role in determining its effectiveness. Studies, such as those by Ling and Liu (2001), have shown that higher stiffness geogrids provide better load distribution and reduce vertical deformation in the subgrade, which can help prevent pavement distress, particularly in high-traffic areas. However, there is a need to further investigate how different geogrid stiffness levels interact with varying traffic loads and pavement materials to improve overall pavement resilience.

The composite use of both geogrids and geotextiles in pavement reinforcement, particularly under dynamic loading conditions, remains an underexplored area. Geotextiles are commonly used as separators or filters, while geogrids primarily serve as reinforcement materials. When combined, these materials could potentially enhance pavement performance by improving soil stabilization and drainage properties. However, their combined effect under dynamic loading, varying traffic conditions, and moisture levels remains insufficiently studied. Research by Qian et al. (2011, 2013) has shown that geogrids, particularly those with triangular apertures, provide a nearly uniform tensile resistance, which improves the performance of reinforced base courses compared to traditional biaxial geogrids. However, further studies are required to evaluate the synergistic effects of geogrid-geotextile combinations, especially under different loading scenarios.

The goal of this research is to address these gaps by conducting a detailed investigation into the 3D stress-strain behavior of geogrid-reinforced pavements under moving vehicle load conditions. The study will explore vehicle load configurations and dynamics, focusing on different traffic load patterns (point/line versus area loads), vehicle speeds (ranging from 5 to 50 km/h), and accelerations. Additionally, the influence of drainage conditions and geogrid stiffness on pavement performance will be evaluated. By investigating these factors in more detail, the research aims to provide better insights into the factors influencing the performance of geogrid-reinforced pavements, ultimately contributing to the development of more effective design and placement strategies to optimize their structural integrity and longevity.

1.2 Problem Statement

The performance of geogrid-reinforced pavements is influenced by complex interactions between vehicle load configurations, load dynamics, material behavior, and drainage conditions. However, there is a significant gap in understanding the 3D stress-strain behavior of pavements under real-world loading conditions, particularly with respect to vehicle load configurations (point/line and area) and load dynamics.

Additionally, there is a lack of validated numerical models to simulate these interactions, complicating pavement design. Linear elastic material models may not fully capture the

behavior of geogrid-reinforced pavements under dynamic loading, highlighting the need for advanced models. The effects of drainage conditions on pavement performance remain unclear.

Furthermore, the optimal placement of geogrid alone, as well as its use in combination with composite materials like geotextiles, to mitigate structural deficiencies (compressive stress-strain) and surface distresses (tensile stress-strain) under varying dynamic and drainage conditions, has not been adequately explored.

1.3 Objective of Study

The main objective of this study is to evaluate the 3D stress-strain behavior of geogrid-reinforced pavements, considering vehicle load configurations and load dynamics, in order to assess pavement performance. The specific objectives are outlined as follows:

1) To log field data, primarily stress-strain measurements and compute numerically, considering vehicle load configurations and dynamic loading conditions.
2) To develop and validate numerical models, and to identify the model that best aligns with the observed field data and numerical evaluations.
3) To investigate the enhancement in pavement performance by evaluating the percentage change in stress-strain, Service Life Ratio (SRF), with geogrid reinforcement, to effectively mitigate structural deficiencies and surface distress.

1.4 Scope of Study

This study investigates the dynamic response of geogrid-reinforced pavements under moving vehicle loads in the forward direction. The scope of the study includes:

1) Vehicle speed and acceleration: The vehicles are assumed to move at constant speeds within a range of 5 to 50 km/h, and accelerations are considered within the range of 0.25 to 1.0 m/s². These conditions aim to represent realistic traffic behavior while ensuring the feasibility of computational analysis.
2) Geogrid stiffness: The study focuses on evaluating the performance of biaxial geogrids with stiffness categories of 16kN/m, 22kN/m, and 25kN/m, commonly used in pavement reinforcement applications. The impact of these geogrid materials on stress distribution and pavement deformation is assessed under dynamic loading.

3) Vehicle configurations: The study examines the behavior of two specific vehicle types: the TATA Truck Tipper 1613c (a heavy-duty vehicle) and the Ford Ranger (a light-duty vehicle). These configurations represent a variety of load distributions and allow for an analysis of the pavement response under different dynamic loading conditions.
4) Load distribution: The vehicle loads are applied either as point/line loads or as area loads, moving along a fixed wheel path of 10 meters. This simplification is intended to facilitate computational modeling and provide insight into the behavior of pavements under different loading patterns.
5) Pavement material testing: Material properties are derived from a series of tests, including hydrometer, unconfined, permeability, direct shear, triaxial, consolidation tests, to establish the mechanical behavior of pavement materials and geogrid reinforcements.
6) Dynamic load analysis: The study focuses on the dynamic responses of pavements to traffic loads, considering the effects of vehicle speed, acceleration, and load distribution. The goal is to enhance predictive models for pavement performance under varying dynamic conditions.

1.5 Limitation of Study

Several limitations exist in this study that should be acknowledged:

1) Simplified load assumptions: The study applies vehicle loads as point/line loads or area loads along a fixed wheel path of 10 meters. More complex load distributions, such as those caused by variable loading patterns or multi-axle vehicles, have not yet been considered.
2) Fixed wheel path distance: A fixed wheel path of 10 meters is assumed for the sake of computational ease.
3) Limited primary data for advanced material models: While material tests (triaxial, consolidation, hydrometer, and permeability tests) have been performed, the study lacks sufficient primary data for supporting more advanced material models that could provide more accurate representations of pavement behavior under dynamic loading. These advanced models have not yet been considered.
4) Vehicle configurations: The study is based on only two vehicle configurations—the TATA Truck Tipper 1613c and the Ford Ranger. It does not yet include other types of

vehicles, particularly multi-axle, heavily loaded vehicles, or vehicles with different configurations.

5) No two-way traffic considered: The study assumes a unidirectional flow of vehicles and does not yet consider the effects of two-way traffic. This exclusion limits the scope of the findings for roads with bidirectional traffic patterns.
6) Road geometry exclusions: Only straight, flat road sections are considered. The study does not yet consider more complex road geometries such as bends or/and uphill sections, which could influence pavement responses and stress distribution.
7) Impact and collision scenarios not included: The study excludes cases involving vehicle impacts or collisions, which could result in more complex dynamic loading conditions that affect the pavement structure.
8) Temperature effects not considered: The study does not consider temperature variations, which could affect material properties such as asphalt stiffness. The omission of temperature variations may reduce the accuracy of long-term performance predictions, particularly in regions with significant temperature fluctuations.
9) Undulating surface and speed breaker not considered: The study does not yet address scenarios involving undulating road surfaces or the presence of speed breakers. These factors, which have not yet been considered, could significantly alter the dynamic behavior of vehicles and pavement, affecting the results and predictions of the study.

1.6 Organization of Report

The report is structured as follows:

Chapter 1: Introduction introduces the research topic entitled '3D stress-strain analyses of geogrid-reinforced pavements under vehicle load configurations and dynamics' along with background, objectives, significance, scope, and limitations of the study.

Chapter 2: Literature Review discusses previous research related to geogrid-reinforced pavements, including studies on dynamic loading, stress-strain behavior, and various material and vehicle load configurations.

Chapter 3: Methodology outlines the research approach, detailing the computational modeling techniques, vehicle configurations, dynamic load simulation, material testing methods, and data collection procedures.

Chapter 4: Analysis and Design presents the results from the simulations and tests, analyzing the influence of vehicle dynamics, geogrid stiffness, and other factors on

pavement performance. Design recommendations based on these findings are also provided.

Chapter 5: Conclusion and Recommendations summarizes the key findings of the study and offers practical design guidelines, along with suggestions for future research and potential improvements to pavement performance assessment.

CHAPTER 2: LITERATURE REVIEW

2.1 Geosynthetics in Pavement Design

Pavement design has become a critical area of study in civil engineering, especially as the demand for infrastructure increases and traffic volumes rise. Traditional pavement materials and design methods are often insufficient to handle the growing pressures imposed by modern vehicles and challenging environmental conditions. Geosynthetics, a class of synthetic materials used in soil stabilization, reinforcement, filtration, and drainage, have emerged as a solution to improve the performance and longevity of pavements (Koerner, 2013; Khoueiry et al., 2021). The role of geosynthetics in pavement systems is vast, encompassing their use in reinforcing weak subgrades, improving load distribution, and enhancing pavement durability under dynamic loading conditions. Pavement failure, especially in areas with weak soils or high traffic loads, is a significant concern in infrastructure maintenance and development (Huang et al., 2025; Paiva et al., 2024). Studies have shown that geosynthetics such as geogrids, geotextiles, and geocells play a vital role in improving subgrade strength, reducing rutting, enhancing resistance to fatigue cracking, and reducing maintenance costs (Abu-Farsakh et al., 2016; Perkins, 1999).

Various studies have focused on understanding the mechanical behavior of geosynthetic-reinforced pavements under different conditions. Numerical simulations, laboratory tests, and field trials have all been employed to evaluate the effectiveness of these materials in real-world conditions (Al-Qadi et al., 2011; Leonardi & Suraci, 2022). Recent advances have also seen the introduction of smart geosynthetics, which feature integrated sensor systems capable of providing real-time feedback on pavement conditions, allowing for proactive maintenance strategies (Abedi et al., 2023; Wang et al., 2022).

2.2 Main Areas of Focus in Existing Research

Existing research on geosynthetics in pavement design primarily focuses on their structural behavior, particularly how they enhance load distribution, improve subgrade stabilization,

and extend pavement lifespan. Studies have explored the use of geosynthetics like geogrids, geotextiles, and geocells for subgrade reinforcement, preventing excessive deformation, and mitigating rutting and cracking. Another key area of interest is the development of smart geosynthetics, which incorporate sensor systems to monitor pavement conditions in real-time. This innovative approach allows for proactive maintenance and efficient management of pavement performance, promising significant improvements in the durability and longevity of road systems.

2.2.1 Structural Behavior of Geosynthetics in Pavement Design

Research on the structural behavior of pavements reinforced with geosynthetics has highlighted significant improvements in their ability to distribute traffic loads and prevent localized stress concentrations, which can lead to rutting and pavement failure. For example, studies by Khoueiry et al. (2021) demonstrated that geogrids enhance load transfer across the pavement structure, minimizing deformation in the subgrade and preventing the formation of ruts. This is particularly crucial in regions with weak or unstable subgrades, where traditional pavement designs often fail to distribute loads effectively.

Geogrids, especially biaxial and triaxial types, have been extensively studied for their impact on the load-bearing capacity and stability of pavements. Researchers like Paiva et al. (2024) and Leonardi & Suraci (2022) have shown that these geogrids significantly improve the stiffness of the pavement structure, leading to reduced permanent deformation and increased service life. The inclusion of geosynthetics such as geotextiles and geocells has also been found to contribute to enhanced load distribution, resulting in more durable pavements.

Moghaddas-Nejad and Small (1996) also investigated the effect of geogrid reinforcement on flexible pavements over sand. Their study found that geogrids reduce rutting by confining the base material and improving load distribution to the subgrade. They also showed that placing the geogrid at the center of a thin base layer minimized surface deformation, a finding that aligns with similar research emphasizing optimal placement for maximum performance.

In a similar vein, Perkins and Lapeyre (1996) conducted an investigation to examine the reinforcement role of geosynthetics in flexible pavements by constructing a pilot test section. The study aimed to evaluate instrument installation techniques and performance, with a particular focus on understanding base course reinforcement mechanisms and site-specific parameters. Instrumentation measured strain in the geosynthetics, base course, and asphalt concrete, providing insights into the practical effectiveness of geosynthetics in full-scale pavement applications.

2.2.2 Geosynthetics in Subgrade Stabilization

Subgrade stabilization is another critical focus of geosynthetic research. In areas with weak soils, such as clays, silts, and peats, the integration of geosynthetics provides a reliable solution to enhance the strength and stiffness of the subgrade. Geogrids, in particular, are known to improve subgrade bearing capacity by distributing the loads applied by traffic more effectively, reducing the potential for settlement and deformation. Studies such as those by Abu-Farsakh et al. (2016) and Al-Qadi et al. (2011) highlight the benefits of geogrid reinforcement in low-volume pavements, especially over weak or compressible soils.

Geosynthetics also provide benefits in preventing subgrade failure during wet conditions, where saturated soils are prone to shifting or eroding. By providing tensile reinforcement, geosynthetics help maintain soil stability, even in areas with high water tables or unstable conditions (Perkins, 1999). Adlinge and Gupta (2018) discussed the common causes of bituminous pavement failure, including cracking, rutting, and unevenness. The study highlighted that typical maintenance strategies often overlook other forms of distress beyond cracking, rutting, and unevenness. The authors emphasized the importance of considering all forms of distress in the pavement's life cycle to extend its service life through effective preservation measures.

2.2.3 Use of Smart Geosynthetics for Monitoring and Maintenance

With the advent of technology, the integration of sensors into geosynthetics—often referred to as smart geosynthetics—has opened new possibilities for pavement monitoring. These smart materials are equipped with embedded sensors that allow for continuous monitoring of strain, temperature, stress, and other performance indicators within the pavement structure. Research by Abedi et al. (2023) and Wang et al. (2022) has shown that the use of

sensor-enabled geosynthetics provides real-time data, which can be used to track pavement health, detect damage early, and inform maintenance schedules. This technological advancement has the potential to significantly improve the efficiency and cost-effectiveness of pavement maintenance programs.

2.3 Methods Used to Address Pavement Problems

2.3.1 Numerical Modeling and Simulation

Numerical modeling, particularly the use of finite element analysis (FEA), has become an essential tool for understanding the behavior of geosynthetics in pavement systems. FEA allows researchers to simulate how geosynthetics interact with the surrounding soil and how they distribute applied loads across the pavement structure. Studies by Paiva et al. (2024) and Wright et al. (2019) utilized advanced simulation techniques to predict the effects of geosynthetic reinforcement on pavement performance, such as load distribution, stress absorption, and deformation under traffic loads. These models provide valuable insights into the optimal design and placement of geosynthetics within pavement systems.

2.3.2 Laboratory and Field Testing

In addition to numerical modeling, laboratory testing remains a critical method for assessing the performance of geosynthetics in pavements. For instance, Perkins (1999) conducted a series of laboratory tests comparing geosynthetic-reinforced pavements with unreinforced ones. The results indicated that geosynthetics improved the mechanical properties of the pavement, reducing rutting, cracking, and deformation.

Field trials provide invaluable real-world data, confirming the long-term effectiveness of geosynthetics in pavement applications. Researchers like Khoueiry et al. (2021) and Howard and Warren (2005) have conducted large-scale field tests to assess the behavior of geosynthetics under actual traffic loads and environmental conditions. These trials have consistently shown that geosynthetics improve pavement performance and reduce maintenance costs over time.

2.3.3 Development of Smart Geosynthetics

As mentioned, the development of smart geosynthetics has revolutionized pavement design and monitoring. These materials are equipped with sensors that can detect changes in the

pavement structure, such as strain or temperature fluctuations, and send this data to a central monitoring system. This real-time data allows engineers to make more informed decisions regarding maintenance and repairs, ensuring that pavement degradation is detected early and addressed promptly. Abedi et al. (2023) and Wang et al. (2022) have explored the use of sensor-enabled geosynthetics in pavements, highlighting their potential to optimize maintenance schedules and extend the service life of pavements.

2.4 Solutions Found in Research

The existing research highlights several key solutions provided by geosynthetics in pavement systems:

- Improved Load Distribution: Geogrids have been shown to enhance the distribution of traffic loads, leading to reduced rutting and permanent deformation. Khoueiry et al. (2021) demonstrated that geogrid-reinforced pavements experience less settlement and deformation under traffic loads.
- Enhanced Subgrade Strength: Geosynthetics improve subgrade bearing capacity, particularly in weak soil conditions. Abu-Farsakh et al. (2016) showed that the inclusion of geogrids increases the strength of subgrades, allowing for thinner pavements and reducing material costs.
- Reduced Maintenance Costs: Geosynthetics increase the durability and longevity of pavements, reducing the frequency of maintenance. Research by Perkins (1999) and Wright et al. (2019) has shown that pavements reinforced with geosynthetics require less frequent repair and exhibit greater resilience to environmental conditions such as moisture infiltration and freeze-thaw cycles.
- Real-Time Monitoring: The integration of smart geosynthetics allows for continuous monitoring of pavement health, facilitating proactive maintenance. As demonstrated by Abedi et al. (2023) and Wang et al. (2022), these materials can alert engineers to issues such as early cracking or deformation, enabling timely repairs.

2.5 Application of Geogrid in Road Pavement

Geogrid is a geosynthetic material made of interconnected tensile elements forming rectangular or triangular apertures. Typically manufactured from polymers such as polypropylene, polyester, polyethylene, polyamides, polystyrene, and polyvinyl chloride,

geogrids can also incorporate fibers like carbon, glass, or natural fibers (IRC SP 59, 2019). The apertures facilitate interlocking with surrounding materials, enhancing the shear strength of the overlying layers (Nader & Sharbaf, 2016). Geogrids are used in roadway construction to:

- Strengthen subgrades by providing a stable working surface.
- Extend pavement life by reducing strain at the subgrade and bituminous layer.
- Reduce construction costs by allowing thinner pavements.

According to Zornberg (2017), geogrids are essential for stabilizing subgrades, reinforcing road bases, separating layers, and preventing reflective cracking. Their functions are summarized in Table 2.1. The components of Geogrid is shown in Figure 1 (Sakleshpur, 2020).

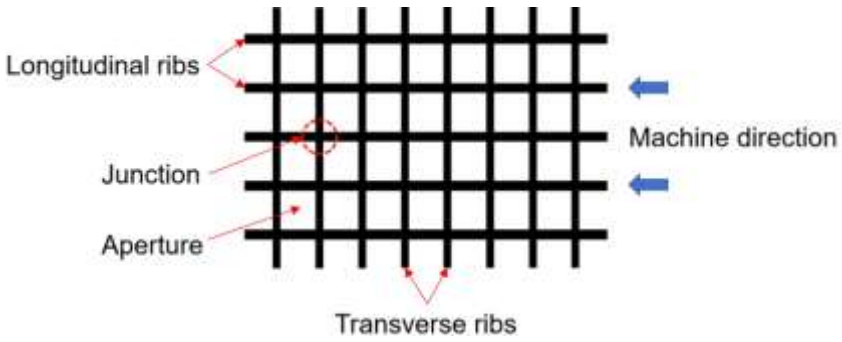

Figure 2.1 Components of Geogrid

Geogrids are categorized based on their directional strength properties into uniaxial, biaxial, and triaxial types, as depicted in Figure 2.2 (Geosolutionsinc, 2021). Uniaxial geogrids are designed to withstand tensile forces in a single direction (machine direction) and are primarily used for applications such as slope stabilization, retaining walls, landfills, and embankments. Biaxial geogrids, on the other hand, are engineered to resist tensile forces in two perpendicular directions, making them ideal for reinforcing subgrades and bases in roadways, airfields, and railways. Triaxial geogrids further enhance the design by incorporating an additional diagonal rib, improving both the in-plane stiffness and the ability to absorb stresses. These geogrids are applied in similar contexts to biaxial ones but offer improved performance due to their added reinforcement.

Geogrids can also be categorized based on their manufacturing process and material composition. According to the manufacturing method, they are classified into extruded,

knitted or woven, and welded types, as shown in Figure 2.2 (Tensar International, 2025). Additionally, based on the material used, geogrids are further classified into fiberglass geogrids, PET (polyethylene terephthalate) geogrids, warp-knitted fiberglass geogrids, and plastic-welded geogrids, as detailed in (Textile Blog, 2025).

Figure 2.2 Geogrid Types by Strength Direction–Uniaxial, Biaxial, Triaxial

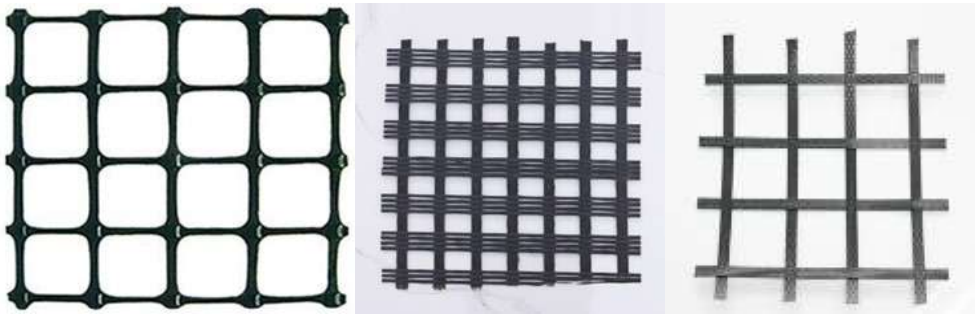

Figure 2.3 Geogrid Types by Manufacturing–Extruded, Knitted/Woven, Welded

Table 2.1 Application of Geogrid in Road Pavement

Application	Mechanism	Function	Implications in Roadway Performance
Mitigation of Reflective Cracking	Reduces stress concentration near existing cracks	Reinforcement	Minimizes degradation in asphalt layers
Separation	Minimizes aggregate loss and fine particle migration	Separation	Preserves base layer thickness and aggregate quality
Stabilization of Road Bases	Reduces lateral displacement of base material	Stiffening	Maintains aggregate confinement and modulus
Stabilization of Soft Road Subgrades	Enhances tension and shear transfer under wheel path	Reinforcement	Reduces vertical stresses and redistributes shear stresses

2.5.1 Geogrid-Soil Interaction

Geogrids are primarily used to reinforce flexible pavement layers by providing lateral confinement to aggregates and minimizing the intermixing of the sub-base and subgrade materials. The effectiveness of this reinforcement comes from the interlocking between the geogrid's apertures and the aggregate particles, as illustrated in Figure 2.4 (Mechanism of reinforced pavement, Qian Yu, 2022). The performance of this interlocking mechanism is influenced by factors such as the grain size distribution of the overlying material and the dimensions of the geogrid's apertures. Optimal efficiency is achieved when the conditions outlined in Equation 2.1 are satisfied (Jie & Anil, 2011; Qian et al., 2013).

$$\frac{s_g}{D_{50}} > 3.0 \qquad (2.1)$$

Where,

s_g: The minimum aperture size of geogrid, and

D_{50}: The particle size at which 50% of the particles are finer

Figure 2.4 Geogrid-Soil Interaction

The effectiveness of geogrid interlocking is governed by its modulus of rigidity and junction stability. According to Nader & Sharbaf (2016), the key mechanisms in geogrid-reinforced pavements are lateral restraint (confinement), increased bearing capacity, and the tension membrane effect, as illustrated in Figures 2.5-2.7. These mechanisms are crucial for understanding the reinforcement provided by geogrids in pavement structures. The three key phenomena according to Nader & Sharbaf (2016) in geogrid-reinforced pavements are:

Lateral Confinement: Geogrids interlock with the aggregates in the base layer, preventing lateral displacement and improving load distribution across the pavement (Figure 2.5). The lateral restraint mechanism enhances:

- Restraint of lateral displacement of granular base materials.

- Increased stiffness of the granular base-subbase layer.
- Reduced shear stress induced by moving loads in the subgrade soil.
- Wider load distribution to the soft subgrade soil.

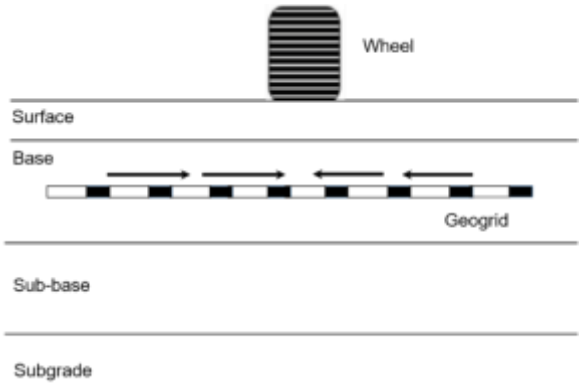

Figure 2.5 Lateral Restraint Mechanism

Increased Bearing Capacity: The presence of the geogrid shifts the failure zone from the subgrade to the base layer, improving the pavement's load-bearing capacity (Figure 2.6).

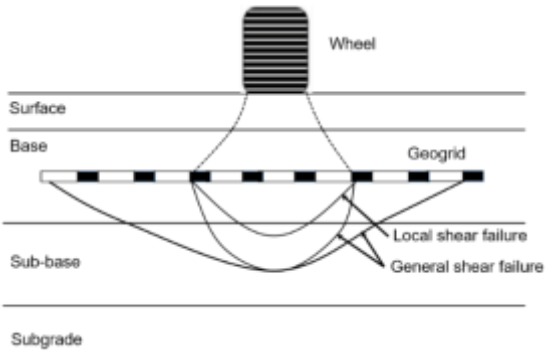

Figure 2.6 Increased Bearing Capacity Mechanism

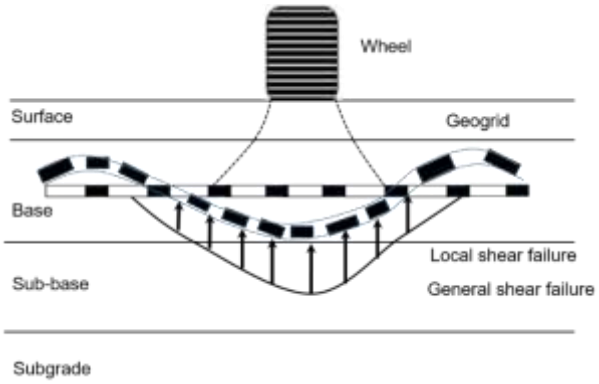

Figure 2.7 Tension Membrane Mechanism

Tension Membrane Effect: The geogrid acts like a membrane under vertical load, reducing vertical stress in the pavement structure by creating an upward force that counteracts the downward pressure from traffic (Figure 2.7).

2.5.2 Design theory

Unreinforced roads: For an axle load P kN applied to a granular layer with thickness $h0$ meters, the vertical stress at the formation surface is P_0. The formation's undrained shear strength, Cu kN/m2, limits the maximum vertical stress that can be applied, given by $(2+\pi)C_u$, representing the undrained bearing capacity. However, horizontal shear stress, which radiates from the wheel load, reduces the vertical stress P_0 that can be applied without causing significant deformation. Figure 2.8 shows the Axle loading on unreinforced roads formation (Cohesive formation, undrained strength Cu kN/m2).

Classical theory indicates the onset of large deformation once

$$P_0 = {}^{1}/_{2}\,(2+\pi)C_u \tag{2.2}$$

However, Giroud and Noiray (1981) have suggested a slightly higher limiting value of

$$P_0 = \pi C_u \tag{2.3}$$

The magnitude of P_0 can be related to the axle load and the contact area of the wheels B*L.

$$P_0 = \frac{P}{2(B+2h_0\tan\alpha_0)(L+2h_0\tan\alpha_0)} \tag{2.4}$$

The dimensions of the contact area can be related directly to tyre pressure P_t.

For highway vehicles

$$L = {}^{B}/_{\sqrt{2}}\ \&\ B = {}^{\sqrt{P}}/_{P_t} \tag{2.5}$$

For off highway vehicles

$$L = {}^{B}/_{2}\ \&\ B = {}^{\sqrt{2P}}/_{P_t} \tag{2.6}$$

For a wide range of applications, $\tan\alpha_0 = 0.6$

Using the axle load P, tyre pressure Pt, and the undrained shear strength of the formation

Cu, the theoretical thickness of the granular fill $h0$ can be determined to prevent overstressing of the formation

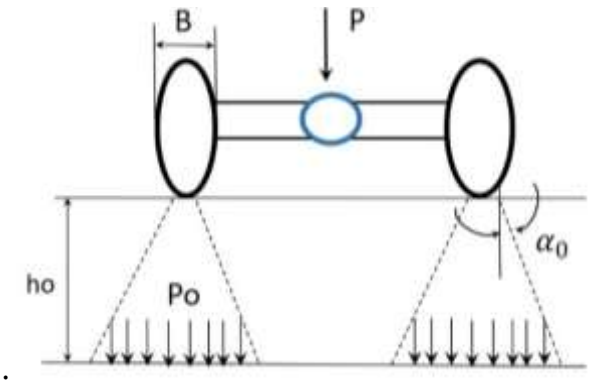

Figure 2.8 Axle Loading on Unreinforced Roads Formation

Reinforced roads: When a geotextile is placed between the formation and fill, three main mechanisms occur:

- Separation: The geotextile prevents intermixing of the fill and formation, maintaining the original fill thickness.
- Shear Stress Absorption: If the geotextile has adequate tensile stiffness, it absorbs horizontal shear stress, restoring the formation's bearing capacity to its classical value ($2+\pi$).
- Membrane Action: Excessive loading causes rutting, generating tensile force T. This force creates inward shear stress, slightly improving bearing capacity, and an upward pressure component $P1$, reducing the vertical pressure on the formation (Figure 2.9).

If the vertical pressure on the formation is limited to its classical bearing capacity, a limiting value of ($P2-P1$) is defined.

$$P_2 - P_1 = (2 + \pi)C_u \tag{2.7}$$

These two pressures P2 and P1 can be evaluated in terms of known parameters:

$$P_1 = \epsilon k \varphi \tag{2.8}$$

Where ϵ is the geotextile modulus, k is the geotextile strain and φ is the function of rut depth and axle geometry?

The pressure P2 can be determined in the same manner as for an unreinforced road:

$$P_2 = \frac{P}{2(B+2h\tan\alpha)(L+2h\tan\alpha)} \quad (2.9)$$

Solving these equations provides the value of h with geotextile reinforcement, resulting in a reduction in the required thickness of the aggregate.

$$\Delta h = h_0 - h \quad (2.10)$$

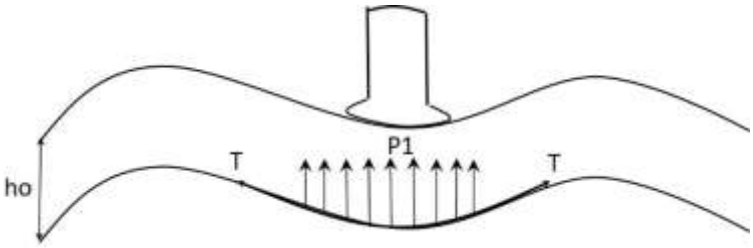

Figure 2.9 Axle Loading on Reinforced Roads Formation

Material Models for FEM modelling: For pavement design, geogrids are commonly modeled as linear elastic materials, as they provide reinforcement and behave elastically under typical loading conditions. The subgrade soil can be modeled using different material models depending on its type: linear elastic for stiff or well-compacted soils, Mohr-Coulomb for granular or cohesive soils under shear stress, Hardening Soil Model for soft soils with nonlinear behavior, and Cam-Clay for clays, particularly in cases of large deformation. These models help accurately predict the pavement's performance and structural integrity under traffic loads.

Table 2.2 Material Models for Modelling the Pavement

Feature	Linear Elastic Model	Mohr-Coulomb Model	Hardening Soil Model	Soft Soil Model	Cam-Clay Model
Stress-Strain Behavior	Linear (Hooke's Law)	Nonlinear, plasticity based on cohesion & friction	Nonlinear, includes hardening/softening	Nonlinear, softening at low pressures	Nonlinear, includes plasticity and volumetric changes
Hardening/ Softening	No hardening or softening	No hardening or softening	Models hardening/softening behavior	Softening, can model both	Models hardening in compression, softening in tension

Yield Criteria	None (Elastic only)	Mohr-Coulomb failure criterion	Modified Drucker-Prager yield function with hardening	Adapted Mohr-Coulomb or Cam-Clay	Cam-Clay yield surface (stress-strain-volumetric)
Applications	Small deformations (metals, concrete)	Soil, rock mechanics under shear loading	Soft soils (clay, silt) under varying loads	Soft soils, embankments, foundations	Clays, deep foundations, large deformations
Complexity	Simple (linear equations)	Moderate (piecewise linear with plasticity)	High (requires numerical methods for hardening)	Moderate to High	High (involves large plastic deformations)
Material Properties	Elastic modulus, Poisson's ratio	Cohesion, friction angle, dilation angle	Elastic modulus, yield stress, hardening parameter	Compression index, softening characteristics	Compression index, yield stress, friction angle

2.6 Summary of Literature Review

Existing literature focuses on the use of geosynthetics to enhance the structural integrity and performance of flexible pavements. These materials address common issues like subgrade failure, rutting, fatigue cracking, and load distribution by improving subgrade strength, reducing pavement thickness, and enhancing resistance to permanent deformation. This study addresses key research gaps in pavement engineering related to geogrid reinforcement. While previous research highlights general performance benefits, limited attention has been given to how geogrid placement improves stress-strain behavior at the subgrade and base layers and its direct connection to structural deficiencies and surface distresses. Additionally, the lack of clarity on which numerical model best aligns with field measurements under dynamic loading conditions remains a challenge. Another gap lies in quantifying the improvement in service life—especially in terms of fatigue and rutting—through a reliable Service Life Ratio (SLR). This research contributes by analyzing field and numerical data to link stress-strain improvements with long-term performance, validating advanced constitutive models against field results, and estimating SLR under varied road geometries, vehicle load configurations, and loading dynamics.

CHAPTER 3: METHODOLOGY

3.1 Research Design

The research framework integrates both numerical and field-based approaches to evaluate geosynthetics in pavement design. As shown in the methodology flow diagram in Figure 3.1, the process begins with the preparation of the numerical model, encompassing both the geometrical and material models. Linear elastic modeling is then carried out in a 3D domain using the Finite Element Method (FEM) in Plaxis, which enables the calculation of stress and strain at critical locations within the pavement structure. These numerical results are compared with field data collected from stress and strain measurements at key locations to validate the model's accuracy under real-world conditions. After model validation, additional numerical analyses are performed to further refine the findings.

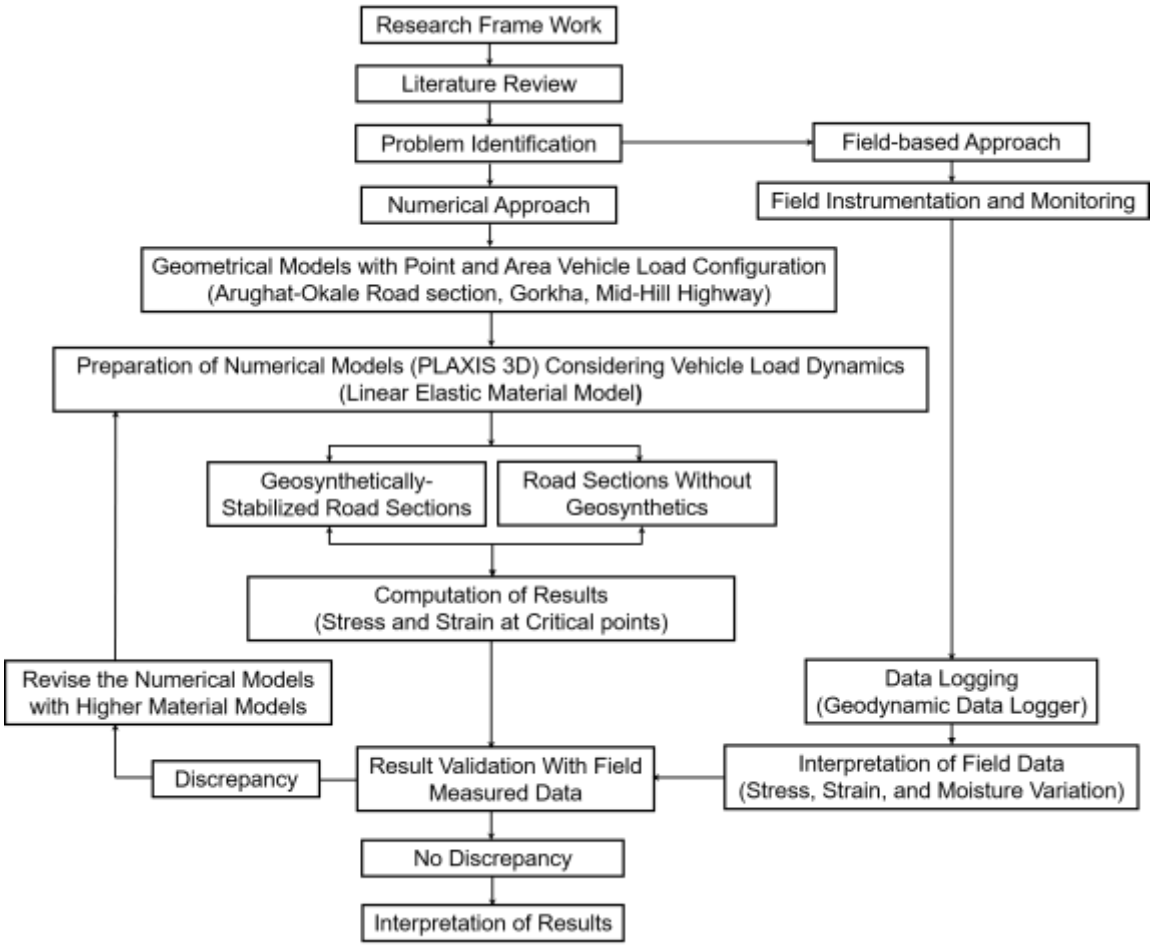

Figure 3.1 Framework of Research

This process also includes considering factors such as vehicle load configurations, load dynamics, advanced material models, drainage, and area load distribution, which are essential for capturing realistic pavement behavior. By validating the numerical models with field data, the study aims to identify the most reliable models for simulating pavement performance under different loading conditions.

3.2 Study Area

The study was conducted along the Arughat-Okhale Road in the Gorkha district of Nepal, as part of the Mid-Hill Road Project. Two straight pavement sections were selected for evaluation: one with geogrid reinforcement and the other without. These sections were chosen to assess and compare pavement performance under dynamic loading conditions caused by moving vehicles. The first site, located at Chainage (CH) 1+700 (28°2'22.51"N, 84°48'29.03"E), had no geogrid reinforcement, while the second site, at CH 1+800 (28°2'20.48"N, 84°48'27.42"E), incorporated geogrid reinforcement into the pavement structure.

The Arughat-Okhale Road runs in an east-west direction, with the Budhigandaki Bridge, located at the Gorkha-Dhading border, marking CH 0+000. Figure 3.2 shows the site location map for Gorkha District, while Figure 3.3 illustrates the location map of the test sites, highlighting CH 1+700 (without geogrid) and CH 1+800 (with geogrid), along with the Budhigandaki Bridge at CH 0+000.

The sites were strategically selected as part of one of Nepal's national pride projects. This selection allows for testing both during the construction phase and immediately after the pavement is opened to traffic. By evaluating the pavement at these different stages of its lifespan, the study provides valuable insights into its long-term durability and effectiveness under real-world conditions.

The study area was chosen not only for its role in the national pride project but also because it offers an opportunity to monitor and assess both the construction and the road use phases. This timeline enables the collection of data early in the project lifecycle, allowing researchers to observe how the pavement performs over time. Additionally, other sections of the Mid-Hill Road have experienced structural deficiencies and surface distresses during

the construction phase at various locations. Therefore, this site was selected to evaluate the potential of geogrid reinforcement in addressing these issues and improving overall pavement performance.

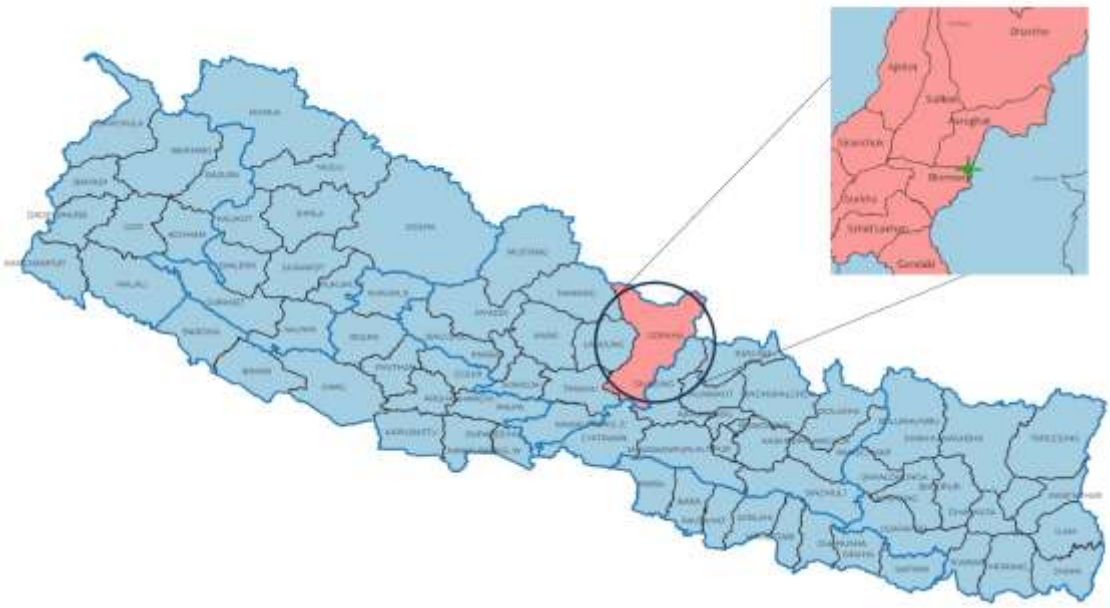

Figure 3.2 Test Site Locations along Arughat-Okhale Road, Gorkha, Nepal

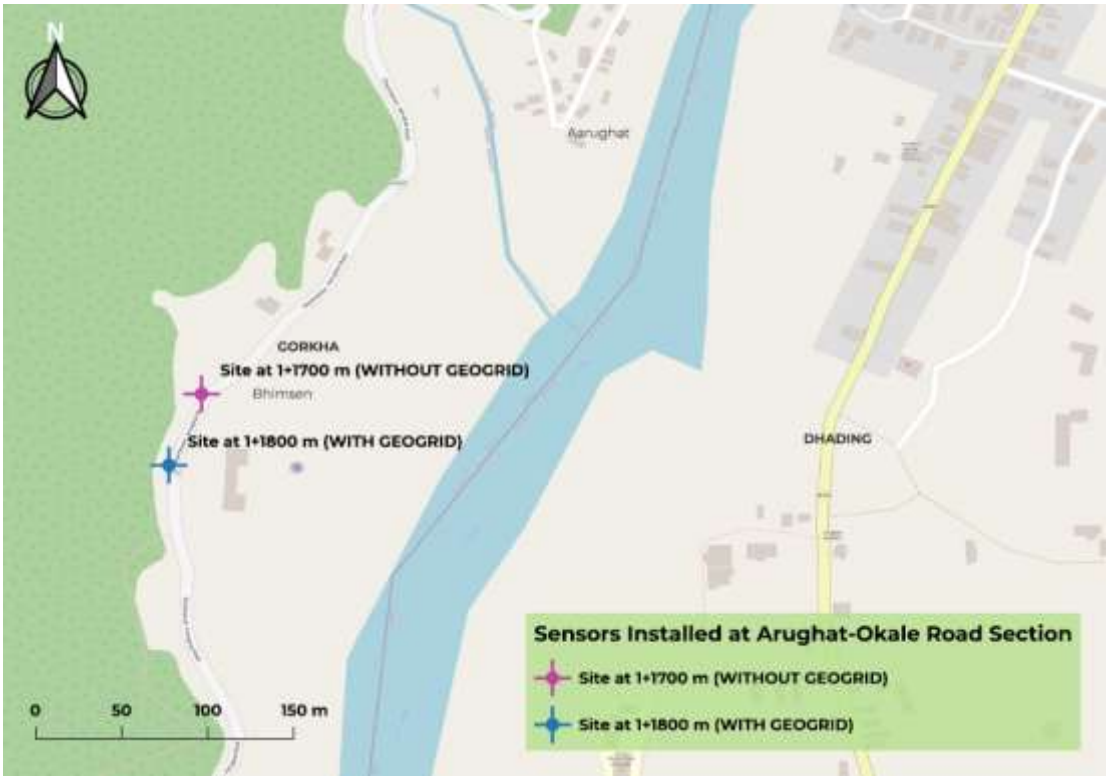

Figure 3.3 Test Sites at CH 1+700 (without Geogrid) and CH 1+800 (G), Gorkha

3.3 Field Setup, Data Acquisition and Monitoring

The field setup involved placing sensors beneath the geogrid at the mid-thickness of the base layer to monitor stress-strain data during vehicle passage. Geodynamic data loggers and sensors were used to capture real-time data, providing insights into the pavement's behavior under dynamic loading conditions. Additionally, Dynamic Cone Penetrometer (DCPT) tests were conducted in each pavement layer (subgrade, subbase, and base) to determine the field CBR values, offering a deeper understanding of the strength and load-bearing capacity of the pavement structure under actual traffic conditions.

3.3.1 Geodynamic High–Speed DAQ-Dynamic Amplifier and Sensors

The GEODYNAMIC Data Logger/Controller, shown in Figure 3.4, is a sophisticated microcontroller-based system designed for high-speed measurements. This advanced equipment includes a dynamic amplifier and is equipped with sensors for capturing and analyzing data with precision and reliability.

Figure 3.4 Geodynamic High–Speed DAQ with Dynamic Amplifier and Sensors

The data logger features earth pressure cells, strain gauges, and moisture sensors, enabling comprehensive monitoring of stress and strain in soil and pavement structures. Detailed specifications of the data logger and sensors are provided in the APPENDIX A. The Earth Pressure Cell is used to measure variations in soil stress, providing valuable insights into stress distribution within soil structures. Dynamic strain gauges are specifically designed to measure axial strain in flexible pavements under high-frequency, dynamic conditions, offering accurate readings for detailed analysis of pavement behavior.

3.3.2. Standard Motorized Dynamic Cone Penetrometer

The Motorized Dynamic Cone Penetrometer (Figure 3.5) is designed to measure soil penetration resistance, providing accurate assessments of soil strength below the surface. The field DCPT test was performed to determine the California Bearing Ratio (CBR) values for the subgrade, subbase, and base layers of the pavement structure. The DCPT uses a portable, wheel-mounted automatic hammer system powered by a generator, ensuring consistent penetration into the soil or pavement layers.

Figure 3.5 Standard Motorized DCPT Dynamic Cone Penetrometer

The test measures the cone's penetration depth under a set number of blows, which is then used to calculate the CBR values for each layer. These values provide crucial information

on the strength and load-bearing capacity of the pavement layers, essential for evaluating pavement performance under traffic loads. Correlations between DCPT results and traditional laboratory CBR values are commonly used, with penetration resistance (mm/blow) correlating to CBR values. Higher resistance typically indicates better strength and stability. Various empirical equations exist for these correlations, with the appropriate choice depending on soil type and local conditions. The detail specification of the equipment is shown in APPENDIX B. DCPT test results are shown in APPENDIX C.

The study primarily focuses on the mid-depth of the base layer, which is the typical location for geogrid reinforcement. This layer plays a crucial role in mitigating surface distresses and addressing structural deficiencies by influencing the distribution of loads within the pavement structure. The performance of the base layer is critical to understanding the overall behavior of the pavement, particularly under real-world traffic loading conditions. As the base layer is directly affected by traffic-induced stresses, its condition and behavior are essential for evaluating the pavement's structural integrity and long-term performance.

Sensor Placement: To ensure the accuracy of data collection while protecting the sensors, they were strategically placed at the mid-depth of the base course layer (Figure 3.6). This depth was chosen because it is considered the most critical zone for capturing stress-strain behavior that influences pavement performance. Placing the sensors at different locations, such as the subbase-base or subgrade-subbase interfaces, would have produced different results. Specifically, the pressure bulb, which is the region affected by higher stress levels, may not extend to these depths, leading to less relevant data for this study. Therefore, placing sensors at the mid-depth of the base course provides a more accurate reflection of the stress distribution within the pavement system.

Layer Characteristics: The pavement section studied consists of a 3 cm thick Double Bituminous Surface Treatment (DBST), which differs from asphalt layers. Due to the need for sensor protection, the sensors were not placed at the surface-base interface (Figure 3.7). In asphalt pavements, placing sensors at the surface-base interface would be ideal for understanding surface-level stress responses. However, given the specific construction of the pavement in this study, alternative sensor placements may provide valuable insights. For instance, heavily loaded lanes may benefit from sensor placement at different depths, such as the base-subbase interface, subgrade-subbase interface, or even within the subgrade

or capping layer. These alternative placements could yield additional data to better understand the pavement's behavior under more intense traffic loading conditions.

Surface Distress and Structural Deficiency: The immediate layer beneath the surface is crucial for both surface distresses and structural deficiencies. This is why the study focused on the base layer at mid-depth, as it is directly influenced by wheel loads. The performance of this layer is critical for preventing issues such as cracking, rutting, and deformation at the surface level, as well as maintaining overall structural integrity. While future studies may consider alternative sensor placements to capture data from other layers, the current setup is well-suited to the objectives of this research, focusing on how stress-strain behavior in the base layer influences pavement performance. By understanding the stresses at this mid-depth location, the study provides valuable insights into how geogrid reinforcement can improve the distribution of these stresses, potentially reducing surface distresses and enhancing the structural performance of the pavement.

This methodology and focus on the mid-depth of the base layer reflect the importance of this region in pavement performance, especially under dynamic loading conditions. The study's approach to sensor placement and analysis is designed to capture the most relevant data for understanding how different factors, such as traffic loads and geogrid reinforcement, impact the overall behavior of the pavement structure.

In this study, the base course was selected for geogrid placement and sensor installation due to its essential role in load distribution and its influence on stress-strain behavior within the pavement structure. Although geogrid reinforcement can be applied in various pavement layers, the base course was prioritized as it directly addresses key zones of stress concentration and deformation. At the top of the subgrade, compressive stresses and strains are significant, which can lead to structural deficiencies if not properly reinforced. At the top of the base, tensile stresses and strains are prominent, making it an ideal location for geogrid reinforcement to prevent failure and surface distress. These two locations—top of the subgrade and top of the base course—are often considered the most critical for mitigating structural deficiencies and surface distresses in flexible pavements.

In this case, sensor placement presented certain challenges. Positioning sensors directly below the DBST layer, which is only 3 cm thick, posed a risk due to the limited protective

cover and potential for damage from repeated wheel loads. As a result, sensors were installed at the mid-depth of the base course, offering a more secure location while still providing critical data to assess the influence of geogrid reinforcement. The geogrid was also placed at the mid-thickness of the base layer for several practical and performance-related reasons: this position aligns well with the stress distribution profile within the base, ensures better interaction between the geogrid and surrounding aggregate, and facilitates sensor integration without compromising structural integrity. In pavement systems that include an asphalt layer, alternative sensor placements—such as at the top of the base or just beneath the surface—might be more suitable for capturing surface-level strains and deformations. The geogrid is placed at the mid-thickness of the base layer for several reasons:

- Optimal Load Distribution: It mitigates tensile and compressive stresses, enhancing load transfer and preventing rutting or deformation.
- Protection and Efficiency: Mid-thickness placement balances geogrid protection from wear while maximizing its reinforcing function.
- Prevention of Deformation: This placement reduces settlement, preventing cracking and enhancing pavement longevity.
- Maximized Interaction: It ensures optimal interaction with the base material, improving shear strength and load-bearing capacity.
- Proven Effectiveness: Previous research shows mid-thickness placement maximizes pavement performance and extends its lifespan.

Field instrumentation, including sensors for stress, strain, and moisture content, was vital for validating simulation results. These measurements provided real-world data on how geogrid reinforcement impacts pavement performance under actual traffic and environmental conditions. The base course, positioned between the subgrade and surface layer, was chosen for both geogrid placement and sensor installation due to its critical role in load distribution and stress-strain behavior. This layer is susceptible to tensile stresses, making it essential for preventing structural failures like cracks and rutting. The mid-depth of the base course was selected for geogrid placement, as it ensures effective force distribution, reduces strain at the subgrade, and enhances the durability of the pavement. Reinforcing this critical location helps mitigate deformation and cracking under dynamic loading, ultimately extending the pavement’s service life.

Figure 3.6 Placement of 40/40Q Biaxial Polypropylene Geogrid (Tensar)

Figure 3.7 Placement of Sensors beneath Geogrid at Mid–Depth of Base Course

A Biaxial 40/40Q Tensar geogrid was employed in this study due to its ability to provide tensile strength in both directions, making it ideal for flexible pavement base courses, where multidirectional stresses are common. This geogrid has a tensile strength of 16 kN/m at 2%

strain, offering strong reinforcement for low to medium-volume traffic pavement structures. Detail Geogrid, Geotextile specifications are shown in APPENDIX D. Figure 3.8 provides a close-up view of the geogrid exposed on the pavement surface, with sensors placed directly beneath it. These sensors were connected to a data logger via cables, allowing for real-time data collection during vehicle passage. This setup was crucial for capturing stress-strain behavior and load distribution at the critical mid-depth of the base layer. This research utilized a Geodynamic data logging system, specifically designed to monitor pavement performance under real-time vehicle loading conditions. This system, referred to as the Instrument GeoDynamic Monitoring Set, consists of various components that collaboratively capture essential data on stress, strain, and moisture within the pavement structure.

Figure 3.8 Data Logging at CH 1+800–Testing Setup (Left) and Geogrid (Right)

3.4 Dynamic Analysis

Dynamic loads were applied in the study. Static loads simulate the effect of stationary vehicles, providing insights into the pavement's behavior under steady loads. Dynamic loads, simulating moving traffic, were included to replicate real-world conditions, where the pavement experiences fluctuating stresses as vehicles pass over it. The dynamic loading conditions are essential for analyzing how the geogrid performs under the repetitive traffic cycles typical of real-world conditions. We have considered both constant and accelerated

motions in dynamic cases. The analysis was conducted to evaluate these dynamic cases, illustrating how the stress-strain values (σ1, σ2, σ3, e1, e2, e3) change under dynamic loading conditions. This demonstrates the variation in stress and strain at critical points within the pavement structure due to vehicle movement and differing loading configurations. It highlights the pavement's response to dynamic forces and emphasizes how the pavement behaves under real-world traffic conditions. The observed variation in stress-strain values underscores the impact of dynamic loading on the pavement's structural performance.

3.4.1 Stresses from Moving Wheel Loads

Stresses induced in the pavement structure by moving wheel loads are analyzed in terms of vertical, horizontal, and shear components. Vertical, horizontal, and shear stresses develop in the bound layers, while compressive and tensile stresses are observed in the unbound layers and subgrade soils. Principal stresses, denoted as σ1 and σ3, exhibit rotational patterns around the wheel load. Compressive stresses are prevalent in the bound layers before and after the wheel load's passage, while tensile stresses concentrate directly beneath the wheel load (Figure 3.9).

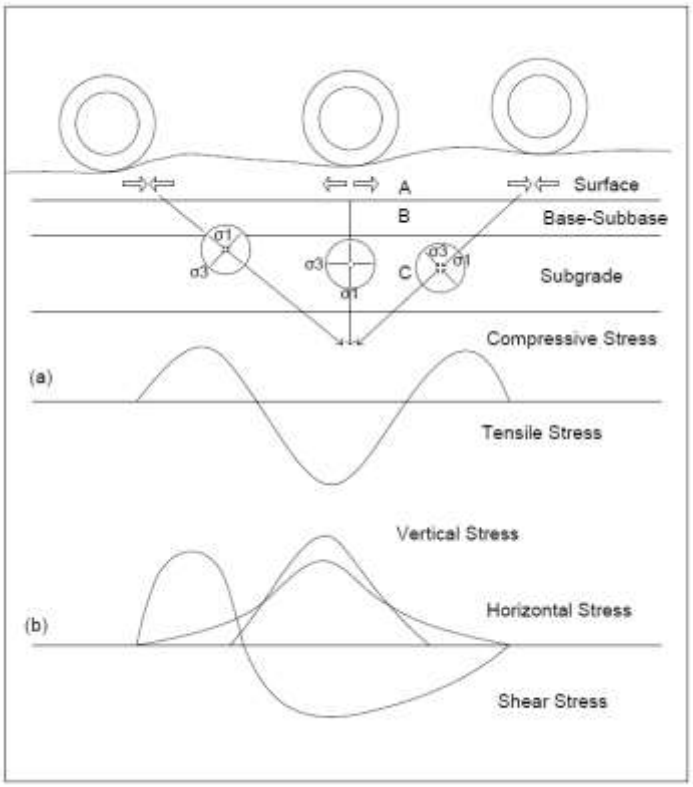

Figure 3.9 Stress-Strain Variations–(a) Compressive/Tensile, (b) Vertical/Shear

The critical points in the Pavement Structure are as follows.

- Horizontal Tensile Strain at the Bottom of the Bound Layers (A): Elevated values in this region indicate a higher risk of pavement fatigue.
- Vertical Compressive Stress and Strain at the Upper Part of the Unbound Layers (B): This area is crucial for rutting development.
- Vertical Compressive Stress and Strain at the Top of the Subgrade (C): High levels in this location are significant for rutting development.

3.5 Geometrical Model

The geometrical model of the pavement structure was developed based on the site-specific conditions of the Arughat-Okhale Road Section. The cross-section was derived from the project specifications and includes the following layers: 20 cm of compacted aggregate material for the base layer, 20 cm of crushed stone material for the subbase layer, and a 3 cm thick DBST layer for the surface course. The model incorporates a 3% slope at the camber and a 5% slope at the shoulder. This cross-section was used for the geometrical modeling, as shown in Figures 3.10 (not to scale) and 3.11 (to scale). In instances where site-specific data was unavailable, dimensions were estimated using relevant codes and the IIT-PAVE software. The point/line load and area load configurations for the TATA TRUCK TIPPER 1613c are shown in Figures 3.12 and 3.13, respectively, while the point/line load and area load configurations for the FORD RANGER are shown in Figures 3.14 and 3.15.

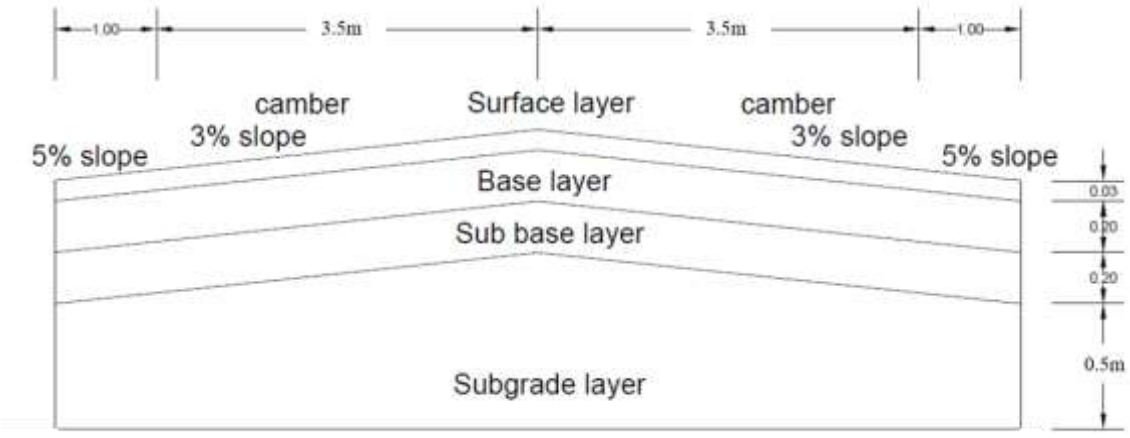

Figure 3.10 Pavement Cross-Section at Arughat-Okhale Road (Not to Scale)

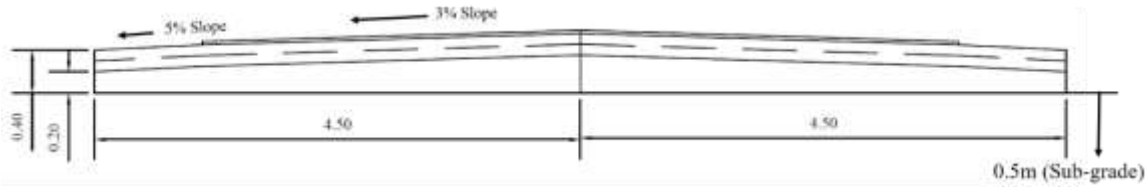

Figure 3.11 Geometrical Model of Arughat-Okhale Section (Scaled, in Meters)

Both point load and area load configurations were used in the study to simulate real-world loading conditions, specifically for a 6-wheel TATA Truck Tipper 1613c and a 4-wheel Ford Ranger 3.2 XLT Pickup. These configurations were chosen to represent both static and dynamic loading cases. By considering both the front and rear axles, a separate single axle load calculation was not necessary, as the full vehicle load was accounted for across the axles.

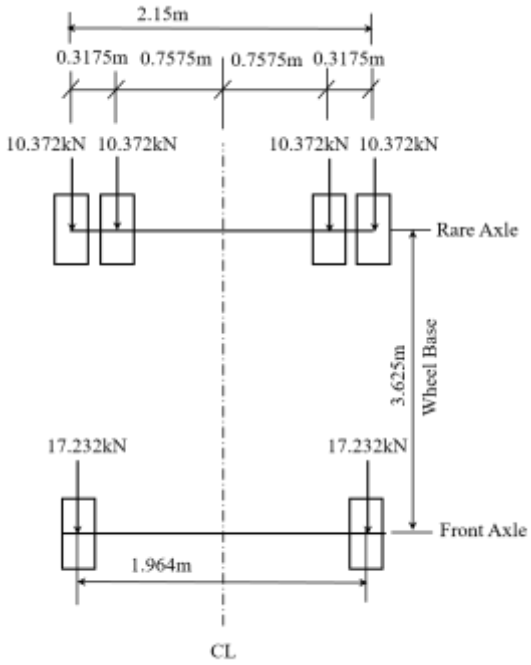

Figure 3.12 Point Load Configuration with Tata Truck 1613c Model Vehicle

For the area load, distribution was applied based on guidelines from the FPDG (2021), ensuring accurate representation of load transfer over the tire–pavement contact area. This method closely mirrors real-world vehicle loading conditions, enhancing the reliability of the simulation. The contact area itself depends on both tire pressure and the pavement surface condition, which directly influence how the load is transmitted. By distributing the load over a defined area rather than a point, stress concentrations are minimized, allowing for a more realistic evaluation of pavement behavior under traffic loads.

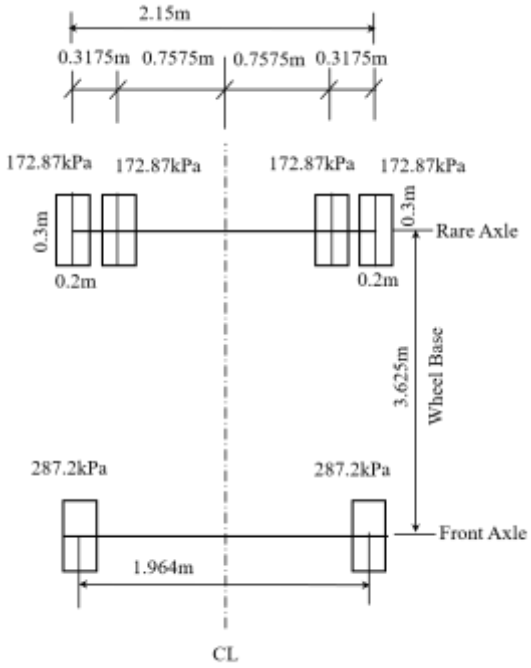

Figure 3.13 Area Load Configuration with Tata Truck 1613c Model Vehicle

For both the Ford Ranger 3.2 XLT Pickup and the Tata Truck 1613c, the front and rear axle weights (Wf and Wr) can be calculated if the distance from the front axle to the vehicle's center of gravity (CGF) is known. The rear axle weight (Wr) is estimated using the formula:

$$Wr = (W \times CGF) / Wb) \quad (3.1)$$

Where W is the total vehicle weight, CGF is the distance from the front axle to the center of gravity, and Wb is the wheelbase of the vehicle.

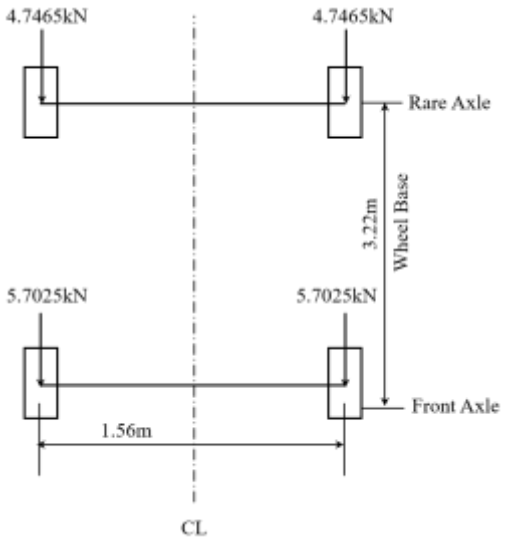

Figure 3.14 Point Load Configuration with Ford Ranger 3.2 XLT Model

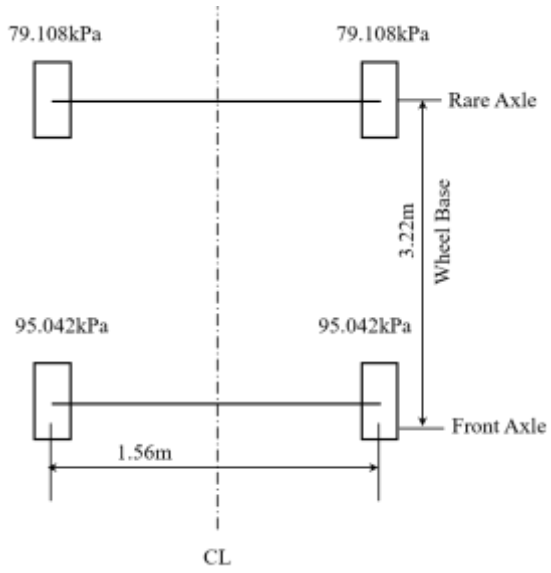

Figure 3.15 Area Load Configuration with Ford Ranger 3.2 XLT Model

The study primarily focused on the area load configuration, as it more accurately represents the tire contact area compared to the point and line load configurations. The 6-wheels Tata Truck Tipper SK 1613 and 4-wheels Ford Ranger Pickup were used, with loads applied at each wheel.

3.6 Material Models

The thickness and properties of the subgrade, sub-base, and base layers were determined through a combination of field and laboratory tests. Laboratory CBR values of subgrade soils were explored and compared with field DCPT, which assessed the subgrade's strength, while Triaxial testing measured the subgrade modulus, crucial for accurately modeling the pavement's behavior under load. Data from the Mid-Hill Road Project were analyzed, revealing that the crushed stone base CBR at 98% maximum dry density was 90.44% at CH 1+200, 90.97% at CH 2+300, 87.58% at CH 8+700, and 81% at CH 12+200. Similarly, the CBR of subbase material at CH 10+000 was 35% (DPR, Midhill project report, 2011). The subgrade modulus, determined from Triaxial testing, was 13099.3 kN/m², with a surface modulus of 35.887 MPa, according to IRC:37 (2018). Field Photographs and Laboratory tests Photographs are respectively shown in APPENDIX E and F. Similarly, Lab Test Results are shown in Appendix G.

The field DCPT test is conducted during the preparation of the subgrade, subbase, and base course, as outlined in Table 3.1. The DCPI, expressed as penetration per blow, is used to calculate the corresponding CBR% based on the correlation provided by the U.S. Army Engineer Waterways Experiment Station (1992).

$$LOG\ (CBR)=2.46-1.12LOG(DPI) \quad (3.2)$$

The results of the Dynamic Cone Penetration Test (DCPT) at various chainages are presented in Table 3.1.

Table 3.1 DCPT at CH 1+700 and CH 1+1800

Pavement Layer	CBR%	CBR% suggested	Reference
Subgrade	4.93	5.0	1+700CH
	5.27		1+750CH
	5.08		1+800CH
Subbase	34.55	35.0	1+700CH
	35.40		1+800CH
Base	85.44	85.0	1+700CH
	85.54		1+800CH

This study employs linear elastic models, requiring only a limited number of soil parameters, such as the unit weights of unsaturated and saturated soil layers and the resilient modulus for each pavement layer. For geogrid reinforcement, a polypropylene biaxial geogrid with a stiffness of 40/40 kN/m at 2% strain was used. The geogrid's stiffness enhances the load distribution capabilities of the pavement, particularly in the base and subbase layers, leading to better pavement performance under heavy traffic conditions. These material models, including the unit weights, resilient modulus, and geogrid stiffness, are summarized in Table 3.2 and 3.3.

Table 3.2 Material Models for Pavement Structure

Item	Description
Identification	Subgrade
Material model	Linear elastic
Drainage type	Undrained/Drained
Unsaturated unit weight, γ_{unsat} (kN/m^3)	18

Saturated unit weight, γ_{sat} (kN/m^3)	20
Resilient modulus, E (MPa)	E = 10.0 * CBR for CBR ≤ 5 % & E = 17.6 * $(CBR)^{0.64}$ for CBR > 5 % (FPDG, 2014) Where, E = Resilient modulus of subgrade soil (MPa). CBR = California bearing ratio of subgrade soil (%)- 5%
Poisson's ratio	0.35
Identification	Granular layer
Material model	Linear elastic
Drainage type	Drained
Unsaturated unit weight, γ_{unsat} (kN/m^3)	19
Saturated unit weight, γ_{sat} (kN/m^3)	21
Resilient modulus, E (MPa)	E = $0.2*(h)^{0.45}$ * $MR_{support}$ (FPDG, 2014) Where, h = Thickness of granular layer (mm) E = resilient modulus of the granular layer (MPa) $MR_{support}$ = (effective) resilient modulus of the supporting layer (MPa)
Poisson's ratio	0.35
Identification	DBST
Material model	Linear elastic
Drainage type	Non porous
Unsaturated unit weight, γ_{unsat} (kN/m^3)	20
Saturated unit weight, γ_{sat} (kN/m^3)	-
Resilient modulus, E (MPa)	2000 (FPDG, 2014)
Poisson's ratio	0.35

Table 3.3 Geogrid strength properties

Item	Description
Identification	Geogrid
Material type	Elastic
Longitudinal stiffness at 2% strain longitudinal, EA1 (kN/m)	800
Transverse stiffness at 2% strain transverse, EA2 (kN/m)	800
Shear stiffness, GA (kN/m)	400

For this study, a biaxial 40/40Q Tensar geogrid was chosen due to its effectiveness in flexible pavement base courses, where multidirectional stresses are common. With a tensile strength of 16 kN/m at 2% strain, this geogrid is well-suited for the expected low to medium traffic volume on the road section, providing essential reinforcement to prevent structural failure under loading. The biaxial configuration is particularly beneficial for reinforcing the base layer, where both horizontal and vertical forces must be efficiently distributed. The selected aperture size of 31 mm x 31 mm allows optimal reinforcement, enabling the base course material to interlock with the geogrid, facilitating effective load transfer, and providing strong support for the pavement structure.

The inclusion of the biaxial 40/40Q Tensar geogrid helps reduce both compressive and tensile stress-strain at the top of the subgrade and base layers. By improving load distribution across the base course, it minimizes surface distresses such as rutting and cracking, significantly enhancing the structural integrity and long-term performance of the pavement. While placing the geogrid at 100% of the base thickness (at the top of the base layer) is generally considered optimal, this configuration is not ideal for DBST layers, as different configurations may yield better results. The thin surface of DBST could interfere with sensor readings, so to ensure accurate data collection and sensor protection, sensors were installed at the mid-depth of the base course. The Tensar 40/40Q geogrid is made of Polypropylene (PP) strands arranged in a regular grid pattern, with each strand having a diameter of 3 mm and an aperture size of 31 mm x 31 mm. It features 32 strands per meter in width, resulting in a total cross-sectional area of 2.26×10^{-4} m². This geogrid is designed to offer robust support for soil reinforcement, with a maximum tensile strength of ≥40 kN/m and an elongation at normal strength of ≤7%. The tensile strength varies at different

elongation levels: 8 kN/m at 1% elongation, 16 kN/m at 2% elongation, and 32 kN/m at 3% elongation. The aperture size of 31 x 31 mm allows effective interlocking with aggregate materials, providing stability and reinforcement in flexible pavements. Additionally, a woven polypropylene geotextile is considered for both separation and reinforcement purposes, with a thickness of 0.5 mm (0.0005 m) and a width of 1 meter, giving a cross-sectional area of 5×10^{-4} m². The geotextile comes with varying tensile strengths of 40 kN/m, 80 kN/m, and 120 kN/m, and its stiffness is calculated based on tensile strength and cross-sectional area. The geogrid used in this study, the monolithic polypropylene 40/40Q Secugrid Q (PP) from Naue GmbH & Co. KG, Germany, has a mass of 240 g/m². Its roll dimensions are 4.75 meters in width and 100 meters in length, providing substantial coverage for large-scale applications. The geogrid's design, with a tensile strength of ≥40 kN/m, is ideal for reinforcing pavement layers, enhancing the pavement's structural integrity and longevity.

For geogrid material, the axial stiffness is the ratio of the axial force F per unit width and the axial strain ($\Delta l/l$ where Δl is the elongation and l is the original length):

$$EA = F/(\Delta l / l) \tag{3.3}$$

For isotropic material Shear stiffness (GA) = EA/2.

3.7 Dynamic Modeling

The analysis considers two dynamic load configurations. In the constant speed case, the vehicle moves at a steady speed within the range of 5-50 km/h, applying both line and area loads to the pavement. In the accelerated speed case, the vehicle accelerates at rates between 0.0-1.0 m/s², with the load applied through line and area loads, reflecting the vehicle's contact area with the pavement. These load configurations were modeled using the Tata Truck Tipper 1613c and Ford Ranger 3.2 XLT. Harmonic motion was employed to capture the dynamic response, accounting for continuous variations in force over time. Dynamic parameters, including frequency, amplitude, phase angle, and time steps, were set based on the vehicle's speed and acceleration to accurately simulate load application. A summary of these dynamic parameters is provided in Table 3.4. In the dynamic modeling of the pavement system, several key parameters are considered to accurately simulate the behavior of the materials and the response to vehicle loads. These parameters include:

- Modulus of Elasticity: This property is crucial for both the geogrid and the pavement layers, as it describes the material's ability to resist deformation under stress.
- Poisson's Ratio: This ratio characterizes the material's response to lateral strain when compressed or stretched, which is particularly important in understanding how the materials behave under dynamic loading.
- Elastic Properties of Geogrid: The geogrid's tensile strength, stiffness, and strain properties must be considered to accurately capture its effect on the pavement structure, particularly in reinforcing the base layer.
- Time for One Complete Cycle of the Wheel: This is the time period for one full rotation of the wheel as it moves across the pavement, which is essential for modeling the cyclic loading and dynamic effects.
- Frequency and Amplitude of Motion: The frequency of the wheel load (how often the load is applied) and its amplitude (the magnitude of the load) are necessary for defining the load characteristics during vehicle movement.
- Dynamic Time Steps for Harmonic Motion: The simulation includes the use of time steps that represent the dynamic interaction of the vehicle with the pavement, capturing the variations in acceleration and deceleration during each loading cycle.
- Angular Velocity: The angular velocity of the vehicle wheels, which refers to the rate at which the wheels rotate, is an important factor in modeling the dynamic load transfer from the wheels to the pavement.
- Phase Angle: The phase angle helps in determining the timing and relative position of the wheel loads as they move across the pavement, which is essential for capturing the dynamic response of the pavement under real-world vehicle motion.

The time period of the wheel cycle, frequency of motion, angular velocity, phase angle, and dynamic time steps can be calculated using Equations (3.4) to (3.8), respectively.

$$\text{Tcycle} = \text{P(perimeter of wheel in m.)/v(velocity in m/sec.)} \quad (3.4)$$

$$\text{Frequency of motion } (\text{f in Hz}) = 1/\text{Tcycle} \quad (3.5)$$

$$\text{Angular velocity } (\Omega, \text{rad/sec,}) = 2\,\pi\,\text{f} \quad (3.6)$$

$$\text{Phase angle } (\phi, \text{degree}) = \text{Wheel base (m)/Radius of curve (m)} \quad (3.7)$$

$$\text{Dynamic time steps } (\Delta\text{t}) = \text{Tcycle (sec)/No. of time steps (No.)} \quad (3.8)$$

The dynamic parameters for harmonic motion of both constant and accelerated motions are shown in Table 3.4.

Table 3.4 Parameters–Harmonic Motion for Constant and Accelerated Motion

Vehicle speed (km/hr)	Speed (m/sec)	Base frequency (Hz)	Base amplitude (m)	Accelerated amplitude at a=0.5m/sec2	Accelerated amplitude at a=1.0m/sec2	Accelerated frequency at a=0.5m/sec2	Accelerated frequency at a=1.0m/sec2	Phase angle (Degrees)	Dynamic Time for time step 100 (Seconds)
Tata Truck 1613c									
5	1.39	0.42	0.525	0.552	0.578	0.44	0.46	0	0.0237
15	4.17	1.25	0.531	0.557	0.584	1.30	1.32	0	0.00794
30	8.33	2.51	0.534	0.560	0.587	2.63	2.73	0	0.00284
50	13.89	4.18	0.538	0.564	0.591	4.39	4.44	0	0.00171
Ford Ranger 3.2 XLT									
5	1.39	0.63	0.494	0.527	0.525	0.65	0.67	0	0.02242
15	4.17	1.90	0.598	0.594	0.591	1.96	2.01	0	0.007535
30	8.33	3.77	0.756	0.752	0.749	3.85	3.90	0	0.00264
50	13.89	6.32	0.913	0.910	0.908	6.43	6.48	0	0.00158

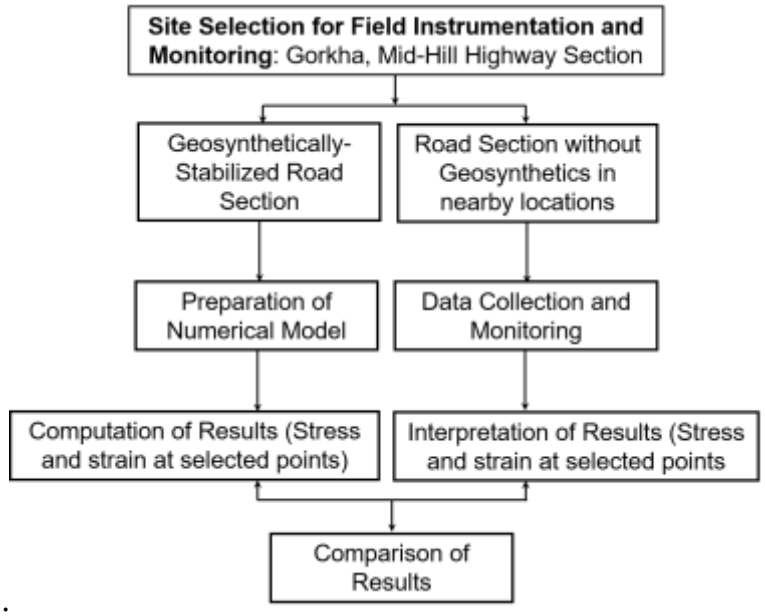

Figure 3.16 Numerical Validation Flowchart for Pavement Reinforcement

The Figure 3.16 outlines the methodology for validating numerical results, comparing geogrid-reinforced and unreinforced pavement sections. The study focuses on stress, strain, and structural integrity to assess the geogrid's impact on load distribution and deformation resistance, aiming to improve pavement stability, longevity, and resilience.

3.7.1 FEM Meshing Scheme

The meshing has been done by assigning the values as illustrated in Table 3.5

Table 3.5 Value Assigned for Meshing FEM Model

Mesh option	Assigned value
Element distribution	Medium
Global scale factor	1.2
Minimum element size factor	0.005
Swept meshing	Yes

Meshing plays a crucial role in finite element analysis, as the quality and size of the mesh directly influence computational accuracy and efficiency. In PLAXIS 3D, the mesh is automatically generated with parameters such as a relative element size of 0.5, element dimension of 0.5, and a global scale factor of 0.2. The software uses ten-node tetrahedral elements, with a minimum element size factor of 0.01 and enhanced refinements enabled. High-quality meshing ensures precise results while minimizing computation time. Ten-noded tetrahedral elements were generated for soil material, whereas six-noded geogrid elements were generated for geogrid, as shown in Figure 3.17. To refine the models, the meshing scheme can be employed according to Table 3.5.

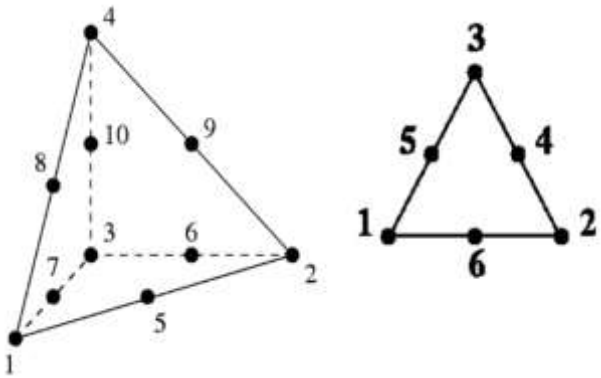

Figure 3.17 Meshing Scheme–Tetrahedral Soil (Left) and Geogrid (Right)

Element's target element dimension and minimum sizes were computed accordingly with Equation 3.9.

$$\boldsymbol{l_e = r_e * 0.05 * \sqrt{(x_{max} - x_{min})^2 + (y_{max} - y_{min})^2 + (z_{max} - z_{min})^2}} \quad (3.9)$$

Where l_e = target element dimension (m);

r_e = relative element size factor;

$x_{max}, y_{max,} z_{max}$ = maximum coordinate of the model in x, y, and z directions, respectively; and

$x_{min}, y_{min,} z_{min}$ = minimum dimension of the model in x, y, and z directions, respectively

*Min size of element = Bounding box diagonal * Minimum element size factor* (3.10)

Where,

Bounding box diagonal = $\sqrt{(x_{max} - x_{min})^2 + (y_{max} - y_{min})^2 + (z_{max} - z_{min})^2}$

To refine the meshing at the central portion where the axle load acts, the local coarseness factor was assigned as illustrated in Table 3.6 during the meshing of the geometric model.

Table 3.6 Meshing Scheme

Meshing Scheme	Local coarseness factor
Point load, Line load	*0.1*
Base and geogrid	*0.1*
Sub-base	*0.3*
Subgrade	*0.4*

To have a smooth, accurate, and numerically stable calculation, the quality of generated mesh was analyzed. FE-model after meshing and the mesh quality in terms of signed inverse condition number (SICN).

Figures 3.18 to 3.21 depict the meshing schemes used for different loading configurations of the TATA Truck Tipper 1613c and the Ford Ranger 3.2 XLT Pickup. Figures 3.18 and 3.19 represent the line load and area load meshing schemes, respectively, for the 6-wheeled TATA Truck Tipper 1613c. Similarly, Figures 3.20 and 3.21 illustrate the line load and area load configurations for the 4-wheeled Ford Ranger 3.2 XLT Pickup.

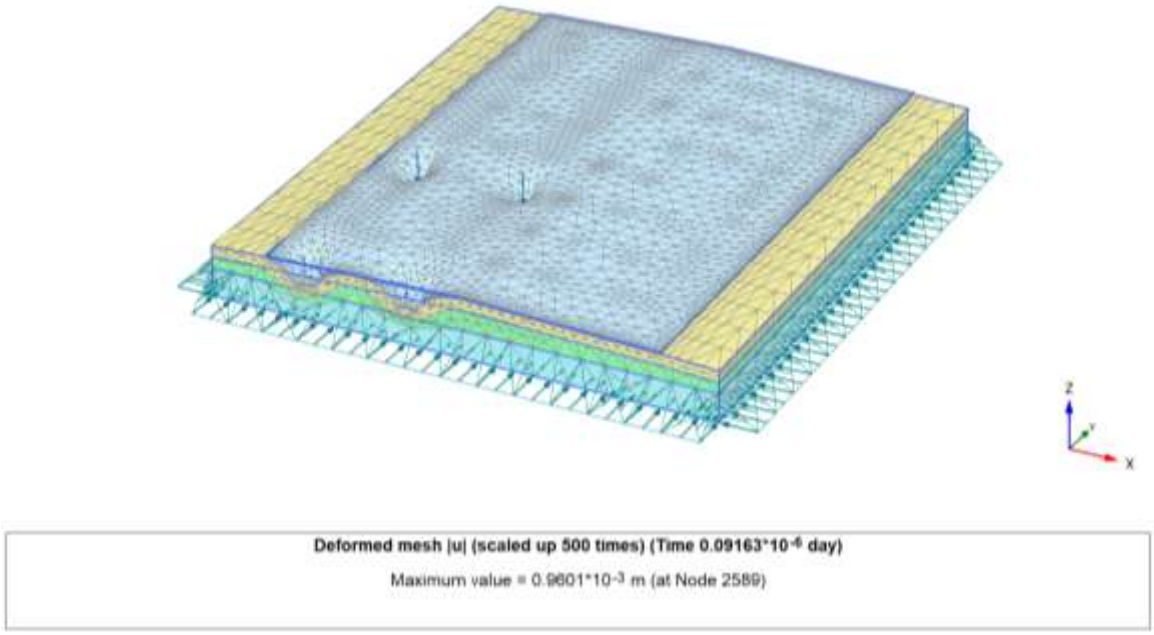

Figure 3.18. Meshing Scheme of 6–Wheel Tata Truck 1613c Line Load

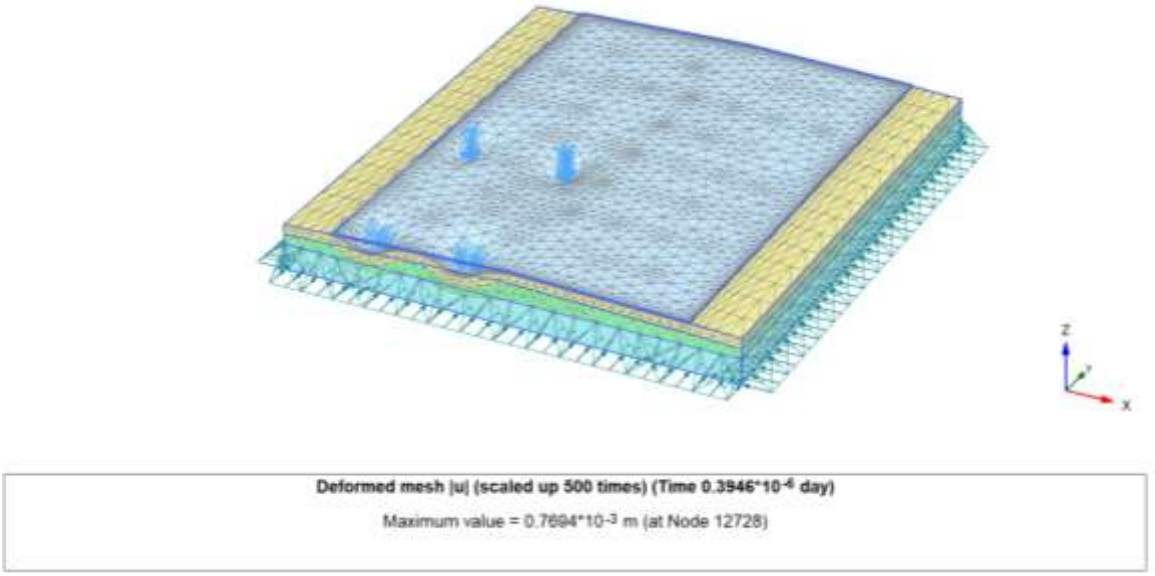

Figure 3.19 Meshing Scheme of 6–Wheel Tata Truck 1613c Area Load

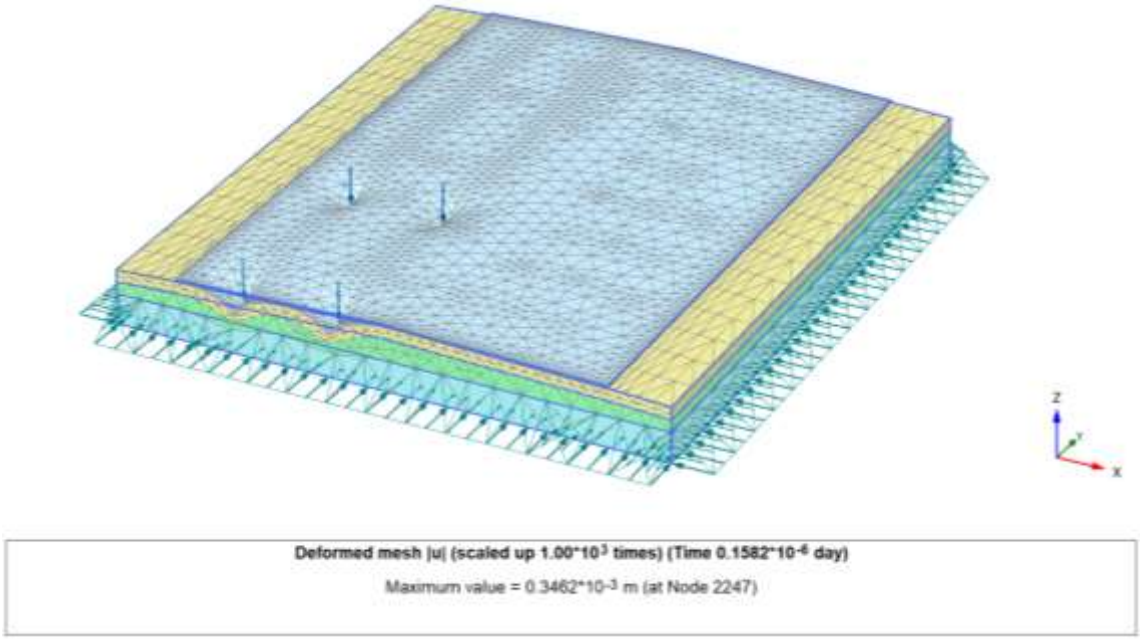

Figure 3.20 Meshing Scheme of 4–Wheel Ford Ranger 3.2 XLT Line Load

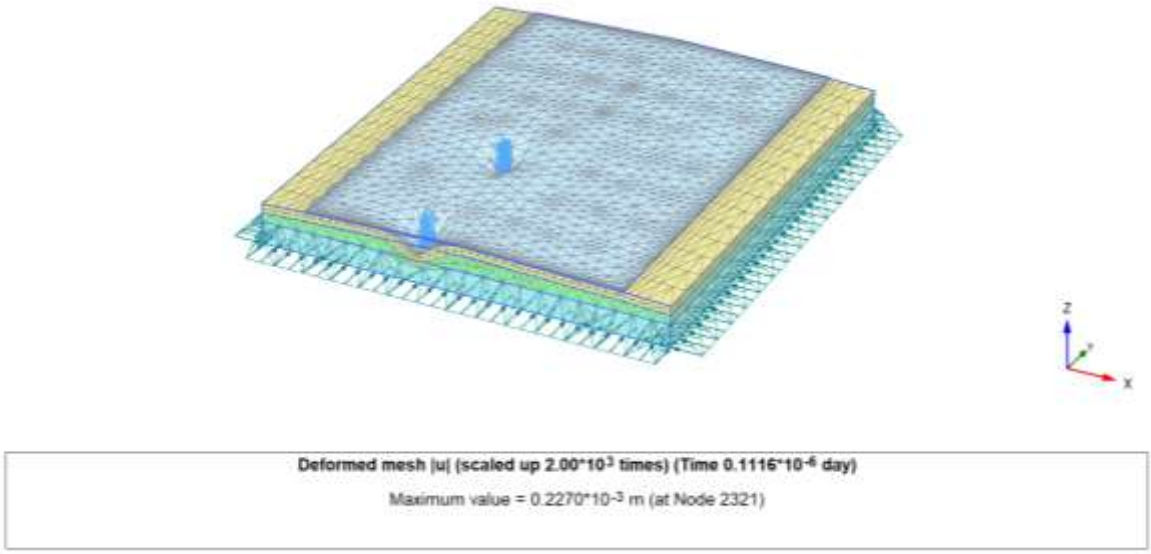

Figure 3.21 Meshing Scheme of 4–Wheel Ford Ranger 3.2 XLT Area Load

3.7.2 FEM Boundary Conditions

In the process of calculating the stresses and strains within the model, the FEM-based software carries out an iterative analysis to converge on a solution that satisfies the imposed boundary conditions. These boundary conditions must be carefully selected to reflect realistic site conditions, ensuring that the displacement or strain near the boundary in all

three directions corresponds to the actual behavior observed on-site. For this study, the displacement or strain perpendicular to the plane of interest at any point several meters from the load application point is assumed to be zero, which serves as a reasonable representation of the actual site conditions. The specific deformation and dynamic boundary conditions used in the pavement model are outlined in Table 3.7.

Table 3.7 Static and Dynamic Boundary Conditions

Type of Boundary Condition	BC @ X_{min}	BC @ Y_{min}	BC @ Z_{min}	BC @ X_{max}	BC @ Y_{max}	BC @ Z_{max}
Deformation	Normally Fixed	Normally Fixed	Fully Fixed	Normally Fixed	Normally Fixed	Free
Dynamic	Viscous	Viscous	None	Viscous	Viscous	None
Note: BC: Boundary Condition; min: minimum; and max: maximum						

For the deformation boundary condition, the term "normally fixed" means that displacement in the direction normal to the considered plane is restricted, while displacement in the other directions is permitted. "Fully fixed" refers to a condition where displacement in all three directions of the considered plane is constrained to zero. On the other hand, the "free" boundary condition allows displacement in all three directions of the considered plane, representing the opposite of the "fully fixed" condition.

Regarding dynamic boundary conditions, the "viscous" boundary condition signifies that outgoing wave energy is absorbed, while "none" implies complete reflection of downward-propagating waves. The "none" boundary condition simulates a soft soil layer over a rigid bedrock, where no energy is allowed to pass through the boundary.

3.7.3 Stage Construction Process

Staged construction in PLAXIS 3D divides the computation into multiple phases, activating soil and structural elements as needed. In dynamic modeling, the calculation type is set to dynamic, and the process is further divided into time steps. Deformation control parameters reset displacements and small strains at load activation, and the mesh is updated depending on whether geogrid is activated. The Picos solver (multicore iterative) is used to ensure efficient computation. These phase parameters, along with dynamic time steps, are crucial

for accurately simulating soil and structural behavior under dynamic loading conditions. The parameters set to the vehicle movement function for dynamic analysis are presented (Validation purpose) in Table 3.8.

Table 3.8 Parameters for Vehicle Movement Function

Parameter	Unit	Assigned value
Direction of axle load movement	axis	Along the Y axis
Starting Y coordinate of axle load	m	-0.500
End Y coordinate of axle load	m	9.500
Distance covered by the axle load	m	9.000
Velocity of the axle load	km/h	15.0
Acceleration of the vehicle	m/s^2	0.0.
No of pass to be covered	nos	1
Dynamic time steps to store	sec	100

Once meshing was completed, the overall computation was divided into multiple project phases within the construction stage tab of PLAXIS 3D. The activation of soil and structures was carried out according to the requirements of each phase. Each calculation phase is automatically subdivided into load steps for plastic analysis and time steps for dynamic analysis by the software. The first calculation phase, referred to as the Initial Phase, is automatically defined and represents the calculation of the initial stress field for the initial geometry using the K0 procedure. The numerical calculation parameters, including those for general settings, deformation, and numerical control, are summarized in Table 3.9.

Table 3.9 Parameters assigned for Initial K0 Procedure

Type of parameter	Parameter	Assigned value
General	Calculation type	K0 procedure
General	ΣM_{stage}	1.00
Deformation control parameter	Ignore suction	False
Numerical control parameter	Use compression for result	False

Following the initial phase, the subsequent calculation phases were manually defined by activating the relevant geometry and structure. Critical locations within the pavement section were selected for node and stress points to visualize displacement and stress-strain parameters both during and after the numerical calculations. The general parameters, deformation control parameters, and numerical control parameters used in the software for both plastic (static) and dynamic (moving load) analysis are outlined in Tables 3.10 and 3.11, respectively.

Table 3.10 Parameters for Static–Phases other than Initial K0 Procedure

Type of parameter	Parameter	Assigned value
General	Calculation type	Plastic
General	Loading type	Staged construction
General	ΣM_{stage}	1.00
General	ΣM_{weight}	1.00
General	Pore pressure calculation type	Phreatic
Deformation control parameter	Reset displacement to zero	True
Deformation control parameter	Reset small strain	True
Deformation control parameter	Updated mesh	True for geogrid activated phase only
Deformation control parameter	Ignore suction	True
Numerical control parameters	Solver type	Picos (multi-iterative)
Numerical control parameters	Max cores to use	256
Numerical control parameters	Max steps to store	1 (last step only)
Numerical control parameters	Use default iteration parameters	True

The static phases except K0 procedure, include material properties such as modulus of elasticity, Poisson's ratio, and strength parameters (e.g., cohesion, friction angle) that govern how the pavement structure responds under static loading. Boundary conditions,

load types, and construction sequences are also defined in these phases. In addition to the static parameters, dynamic phases a harmonic motion is introduced to simulate the vehicle's movement, which is configured based on axle loads, speed, and vehicle dynamics.

Table 3.11 Parameters for Dynamic–Phases other than Initial K0 Procedure

Type of parameter	Parameter	Assigned value
General	Calculation type	Dynamic
General	Loading type	Staged construction
General	Dynamic time interval	Depends on acceleration and velocity
General	Special option	0 (default)
General	Pore pressure calculation type	Phreatic
Deformation control parameter	Reset displacement to zero	True
Deformation control parameter	Reset small strain	True
Deformation control parameter	Updated mesh	True (for geogrid activated phase only)
Deformation control parameter	Ignore suction	True
Numerical control parameters	Solver type	Picos (multi-iterative)
Numerical control parameters	Max cores to use	256
Numerical control parameters	Max steps to store	100 (last step plus 100 intermediate steps)
Numerical control parameters	Use default iteration parameters	True

3.7.4 Parametric Analysis

Further parametric analysis was conducted by varying the normal elastic stiffness of the geogrid, along with considering both constant and accelerated motion scenarios. The analysis was conducted to determine the optimum location and benefits of geogrid reinforcement. The analysis incorporated point/line and area loads, as outlined in Table

3.12. This helped in understanding the influence of geogrid properties and loading conditions on stress-strain distribution and pavement performance.

Table 3.12 Parameters for Parametric Analysis

Parameter	Unit	Assigned value
Position of geogrid (% of base thickness) from top of pavement surface	%	*0, 25, 50, 75, 100*
Normal elastic stiffness of geogrid	(kN/m)	*800, 1100, 1250 (Tensar Product), 1600, 3200, 5000 (Macafeeri Product)*
Uniform acceleration of standard axle load	(m/s^2)	*0.0, 0.5, 0.75, 1.0*
Velocity of the standard axle load	(km/h)	***0***, ***5***, *10*, ***15***, *20, 25* ***30***, *35 40, 45,* ***50***, *55, 60*

3.8 Data Analysis and Validation

The field measurement data were compared with the numerical model results to validate the accuracy of the modeling approach. Upon successful validation, these models can be utilized to analyze the effects of dynamic loading under various conditions, such as heavily loaded lanes, curves, and uphill sections. This research specifically focuses on the straight section of the pavement, integrating both numerical simulations and field-based observations. The comparison between field data and numerical results ensures the reliability and applicability of the models in real-world scenarios.

3.9 Rutting and Fatigue Life of Pavement

According to IRC: 37-2018 (Indian Roads Congress guidelines), the Rutting and Fatigue Life of pavement are two key performance criteria used in the design of flexible pavements:

- Fatigue Life refers to the number of load repetitions a pavement can withstand before cracking due to repeated tensile strain at the bottom of the bituminous layer.
- Rutting Life is based on the pavement's ability to resist permanent deformation (rutting) under compressive strain on the subgrade.

Subgrade Rutting Criteria: Rutting is considered a failure when the average rut depth reaches 20 mm. Rutting life (N_R) is the number of standard 80 kN axle load repetitions the pavement can withstand before reaching this limit. It is calculated using the following formulas.

80% Reliability:

$$N_R = 4.1656 \times 10^{-8}(1/\varepsilon_v)^{4.5337} \quad (3.11)$$

90% Reliability:

$$N_R = 1.4100 \times 10^{-8}(1/\varepsilon_v)^{4.5337} \quad (3.12)$$

Where:

N_R = Rutting life (in standard 80 kN axle loads)

ε_v = Vertical compressive strain at the top of the subgrade, calculated using linear elastic layered theory

Fatigue Cracking Criteria for Bituminous Layer: Fatigue failure is said to occur when 20% or more of the surface area develops interconnected cracks. The fatigue life (N_f) is the number of standard axle load repetitions until this condition is reached. The fatigue life is calculated using the following equations:

80% Reliability:

$$N_f = 1.6064 \times C \times 10^{-4}(1/\varepsilon_t)^{3.89}\,(1/M_{Rm})^{0.854} \quad (3.13)$$

90% Reliability:

$$N_f = 0.5161 \times C \times 10^{-4}(1/\varepsilon_t)^{3.89}\,(1/M_{Rm})^{0.854} \quad (3.14)$$

Where:

N_f= Fatigue life (in standard 80 kN axle loads)

ε_t= Horizontal tensile strain at the bottom of the bituminous layer

M_{Rm} = Resilient modulus (in MPa) of the bituminous mix

$$C = 10^M \quad (3.15)$$

$$M = 4.84\left(\frac{V_{be}}{V_a+V_{be}} - 0.69\right) \quad (3.16)$$

C = Adjustment factor accounting for the volumetric properties of the bituminous mix

V_a – Air Voids: The percentage of air spaces in the compacted bituminous mix.

Recommended Range of Design air voids: 2–2.5%

Maximum in-place air voids: Less than 4%

Low air voids help reduce moisture damage and aging. Proper compaction ensures mix durability and resistance to environmental damage.

V_{be} – Effective Bitumen Content: The percentage of bitumen that effectively coats and binds the aggregates, excluding bitumen absorbed into aggregate pores.

Recommended Range: 4–5%

3.10 Service Life Ratio (SLR) of Pavement

The Service Life Ratio (SLR) is used to evaluate the improvement in pavement durability achieved through reinforcement, while keeping the pavement thickness unchanged. It is calculated as the ratio of vertical compressive strain at the top of the subgrade in the unreinforced condition to the strain after reinforcement. A higher SLR indicates improved durability and extended pavement life. A parametric analysis can be conducted using different subgrade CBR values to identify the most effective range for pavement performance. For this analysis, subgrade CBR values in the range of 5% to 15% are considered.

In IRC:37-2018, the Service Life Ratio (SLR) is a key metric used to assess pavement performance. It is the ratio of the design service life (e.g., 10–20 years) to the predicted life based on rutting and fatigue analysis. A higher SLR indicates a more conservative design, while a lower SLR suggests a design closer to its performance limits. SLR helps ensure the pavement can withstand anticipated traffic and environmental conditions without premature failures, guiding maintenance planning and validating structural adequacy.

CHAPTER 4: ANALYSIS AND DESIGN

4.1 Validation of Numerical Model with Field Measurements

The stress-strain analysis of the Tata Truck 1613c (6-wheels) and Ford Ranger 3.2 XLT (4-wheels) reveals that both vehicles cause higher stress-strain near the wheel path, which is reduced when geogrid reinforcement is employed. For both vehicles, the geogrid limits horizontal displacement and helps evenly distribute the load across the pavement, improving stability and reducing deformation. Stress and strain analyses show that while both vehicles exhibit higher stress near the wheel path, geogrid reinforcement reduces these stresses. The geogrid's effectiveness varies with different material stiffnesses, where a higher stiffness (1250 kN/m) offers slightly better load redistribution, particularly in the subgrade and mid-base layers. However, stress concentrations still occur in the base layer, indicating that additional reinforcement may be needed to address these high-stress points.

The stress–strain behavior of the pavement system was evaluated under both drained and undrained subgrade conditions for 4-wheel and 6-wheel vehicle configurations. While increased vehicle speed typically implies greater kinetic energy, it also results in shorter contact time between the wheel and pavement surface. This reduced contact duration at higher speeds (50 km/h) generally leads to lower stress and strain levels, particularly in the surface and base layers. However, under undrained subgrade conditions, this effect is countered by limited pore pressure dissipation, causing elevated stress concentrations—especially under area loading and rapid loading conditions.

In contrast, drained conditions offer more efficient pore pressure relief, leading to a more uniform stress distribution and reduced stress magnitudes, especially at lower speeds (15 km/h). Geogrid reinforcement helps further by redistributing loads more effectively, minimizing deformation and enhancing structural integrity. Comparing the 4-wheel and 6-wheel load cases, the 6-wheel configuration results in slightly higher displacement, stress, pore pressure, and groundwater head due to the increased load. These differences are consistently observed across both drainage conditions, underscoring the importance of proper drainage in maintaining pavement performance.

i. Computational Results: TATA TRUCK

The computational analysis of stress under a TATA Truck 1613c shows that constant and accelerated motion and higher speeds (50 km/h vs. 15 km/h) lead to increased stress at all road layers, particularly the subgrade and base layers. Stress is notably higher during accelerated motion (1.0 m/s²) compared to constant speed, with geogrid reinforcement reducing stress, especially in the subgrade and base layers.

At lower speeds (15 km/h), geogrid reinforcement effectively reduces peak stresses by enhancing load distribution. In contrast, at higher speeds (50 km/h), the shorter contact duration between the tire and pavement generally results in lower stress and strain levels overall. However, the geogrid's influence under these rapid loading conditions becomes less pronounced. While it still contributes to improved structural performance—especially near the surface and base layers—its relative effectiveness tends to reduce as speed and acceleration increase. The computational analysis of the pavement model under point load conditions was conducted using both Tata Truck 1613c and Ford Ranger 3.2 XLT, with and without geotextile reinforcement, at a constant speed of 15 km/h and an accelerated speed of 1.0 m/s². The results from various figures illustrate the pavement's behavior under both static and dynamic loading conditions.

Figures 4.1-4.12 present the computational results for the Tata Truck 1613c model. These figures show sectional views of the total displacement and principal stress (Sigma 1) along different paths (symmetric half-width and wheel paths), highlighting the effects of geotextile reinforcement on stress distribution and displacement patterns. The results demonstrate significant stress concentrations near the wheel paths, especially in the dynamic case, and the reinforcement helps mitigate these stresses. Figures 4.13-4.26 depict the corresponding results for the Ford Ranger 3.2 XLT. Similar to the Tata Truck model, these figures show stress and displacement distributions along the symmetric half-width and wheel paths. The results indicate comparable behavior, with the geotextile reinforcement again providing notable improvements in reducing displacement and stress concentrations, particularly in the dynamic loading cases.

Figure 4.1 shows the discretized pavement model with a Tata Truck 1613c under a point load, reinforced with geotextile, moving at a constant speed of 15 km/h. Figure 4.2 presents the computational results for the pavement model with a Tata Truck 1613c under a point

load, reinforced with geotextile at 15 km/h. The left figure shows a sectional view of the Principal stress ‘Sigma 1’ along the pavement's symmetric half-width, while the right figure compares the static and dynamic cases, as considered in Phase-7 and Phase-8. The dynamic case shows higher stress values, with a maximum of -6.095 kN/m² and a minimum of -16.24 kN/m². Figure 4.3 displays field measurements confirming these results, with fluctuations observed in the pavement width as mentioned in Figure 4.2. Figure 4.4 shows the computational results for the pavement model with a Tata Truck 1613c under a point load, reinforced with geotextile at 15 km/h. The left figure presents a sectional view-2 of the Principal stress ‘Sigma 1’ along the symmetric half-width of the pavement, while the right figure compares the static and dynamic cases. The maximum stress is -6.28 kN/m², and the minimum is -33.14 kN/m². The right figure confirms these results, showing width-wise fluctuations in Section-2. Figure 4.5 shows that field observation data confirms the numerical evaluation presented in Figure 4.4.

Figure 4.6 shows the computational results for the pavement model with a Tata Truck 1613c under a point load, reinforced with geotextile at 15 km/h. The left figure presents a sectional view-1 of the Principal stress ‘Sigma 1’ along the wheel path of the pavement at the second wheel position, while the right figure compares the static and dynamic cases. The maximum stress value obtained is -6.657 kN/m², and the minimum value is -40.83 kN/m². Figure 4.7 shows the computational results for the pavement model with a Tata Truck 1613c under a point load, reinforced with geotextile at 15 km/h. The left figure presents a sectional view-2 of the Principal stress ‘Sigma 1’ along the wheel path of the pavement at the fourth wheel position, while the right figure compares the static and dynamic cases. The maximum stress value is -4.753 kN/m², and the minimum value is -40 kN/m². Figure 4.8 shows the computational results for the pavement model with a Tata Truck 1613c under a point load, reinforced with geotextile at 15 km/h. The left figure presents a sectional view-1 of the total displacement ‘u’ along the symmetric half-width of the pavement, while the right figure compares the static and dynamic cases. The maximum displacement value obtained is 0.7643×10^{-3}. Figure 4.9 shows the computational results for the pavement model with a Tata Truck 1613c under a point load, reinforced with geotextile at 15 km/h. The left figure presents a sectional view-2 of the total displacement ‘u’ along the symmetric half-width of the pavement, while the right figure compares the static and dynamic cases. The maximum displacement value obtained is 0.9508×10^{-3}.

Figure 4.10 shows the computational results for the pavement model with a Tata Truck 1613c under a point load, reinforced with geotextile at 15 km/h. The left figure presents a sectional view-1 of the total displacement 'u' along the wheel path of the pavement, while the right figure compares the static and dynamic cases. The value obtained from numerical computation is 0.93×10^{-3}. The maximum displacement value obtained is 1.07×10^{-3} numerically and 1.29×10^{-3} by field observation, as shown in Figure 4.11. Figure 4.12 shows the computational results for the pavement model with a Tata Truck 1613c under a point load, reinforced with geotextile at 15 km/h. The left figure presents a sectional view-2 of the total displacement 'u' along the wheel path of the pavement, while the right figure compares the static and dynamic cases. The maximum displacement value obtained is approximately 0.9445×10^{-3}.

Figure 4.13 shows the discretized pavement model with a Ford Ranger 3.2 XLT under a point load, reinforced with geotextile at a constant speed of 15 km/h. The maximum displacement value obtained is 0.3462×10^{-3}. Figure 4.14 shows the computational results for the pavement model with a Ford Ranger 3.2 XLT under a point load, reinforced with geotextile at a speed of 15 km/h. The left figure presents a sectional view-1 of the Principal stress 'Sigma 1' along the symmetric half-width of the pavement, while the right figure compares the static and dynamic cases. The maximum principal stress is -3.594 kN/m², and the minimum is -19.76 kN/m². Figure 4.14 shows the computational results for the pavement model with a Ford Ranger 3.2 XLT under a point load, reinforced with geotextile at a speed of 15 km/h. The left figure presents a sectional view-1 of the Principal stress 'Sigma 1' along the symmetric half-width of the pavement, while the right figure compares the static and dynamic cases. The maximum principal stress is -3.594 kN/m², and the minimum is -19.76 kN/m².

Figure 4.15 indicates that field observation confirms the numerical evaluation obtained in Figure 4.14. The value obtained is 20kN/m2. Figure 4.16 shows the computational results for the pavement model with a Ford Ranger 3.2 XLT under a point load, reinforced with geotextile at a speed of 15 km/h. The left figure presents a sectional view-2 of the Principal stress 'Sigma 1' along the symmetric half-width of the pavement, while the right figure compares the static and dynamic cases. The maximum principal stress is -4.785 kN/m², and the minimum is -16.35 kN/m². Figure 4.17 shows the earth pressure measurement data for

the Tata Truck 1613c with geotextile reinforcement at a speed of 15 km/h, closely matching the numerical analysis presented in Figure 4.16-Right (4.0kN/m2 to 25kN/m2).

Figure 4.18 shows the computational results for the pavement model with a Ford Ranger 3.2 XLT under a point load, reinforced with geotextile at a speed of 15 km/h. The left figure presents a sectional view-1 of the Principal stress 'Sigma 1' along the wheel path of the pavement at the second wheel position, while the right figure compares the static and dynamic cases. The maximum principal stress is -7.008 kN/m², and the minimum is -11.00 kN/m². Figure 4.19 shows the computational results for the pavement model with a Ford Ranger 3.2 XLT under a point load, reinforced with geotextile at a speed of 15 km/h. The left figure presents a sectional view-2 of the Principal stress 'Sigma 1' along the wheel path of the pavement at the fourth wheel position, while the right figure compares the static and dynamic cases. The maximum principal stress is -0.8594 kN/m², and the minimum is -11.06 kN/m². Figure 4.20 shows the computational results for the pavement model with a Ford Ranger 3.2 XLT under a point load, reinforced with geotextile at a speed of 15 km/h. The left figure presents a sectional view-1 of the total displacement 'u' along the symmetric half-width of the pavement, while the right figure compares the static and dynamic cases. The maximum total displacement value obtained is 0.09940×10^{-3} m. Figure 4.21 shows that field observation confirms the numerical evaluation presented in Figure 4.21. Figure 4.22 shows the computational results for the pavement model with a Ford Ranger 3.2 XLT under a point load, reinforced with geotextile at a speed of 15 km/h. The left figure presents a sectional view-2 of the total displacement 'u' along the symmetric half-width of the pavement, while the right figure compares the static and dynamic cases. The maximum total displacement value obtained is 0.2531×10^{-3} m.

Figure 4.23 confirms the field observation as mentioned in the numerical evaluation in Figure 4.22. Figure 4.24 shows the computational results for the pavement model with a Ford Ranger 3.2 XLT under a point load, reinforced with geotextile at a speed of 15 km/h. The left figure presents a sectional view-1 of the total displacement 'u' along the wheel path of the pavement, while the right figure compares the static and dynamic cases. The maximum total displacement value obtained is 0.3391×10^{-3} m. Figure 4.25 shows the strain gauge measurement data for the Tata Truck 1613c with geotextile reinforcement at a speed of 15 km/h, closely matching the numerical analysis presented in Figure 4.24-Right ($+0.18\times10^{-3}$ m to 0.32×10^{-3} m). Figure 4.26 shows the computational results for the

pavement model with a Ford Ranger 3.2 XLT under a point load, reinforced with geotextile at a speed of 15 km/h. The left figure presents a sectional view-2 of the total displacement ‘u’ along the wheel path of the pavement, while the right figure compares the static and dynamic cases. The maximum total displacement value obtained is 0.3251×10^{-3} m. Overall, the presence of geotextile reinforcement reduces the total displacement and helps distribute stresses more evenly across the pavement, especially under dynamic loading conditions. This highlights the potential of geotextiles to improve pavement performance and durability under traffic loads.

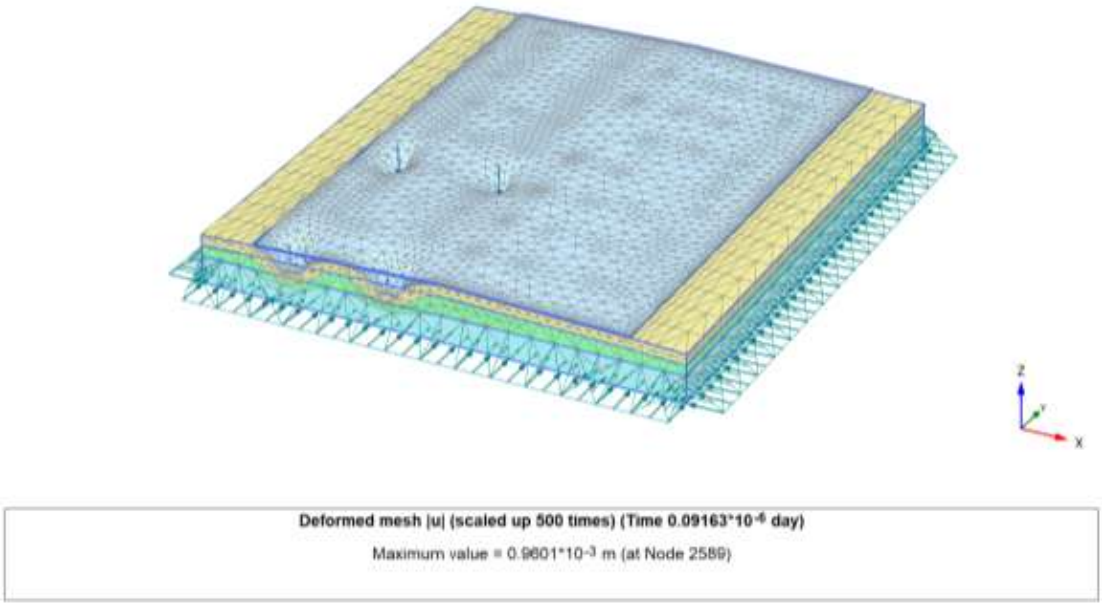

Figure 4.1 Model–Tata Truck 1613c, Point Load, Geogrid, 15 km/h, 1.0 m/s²

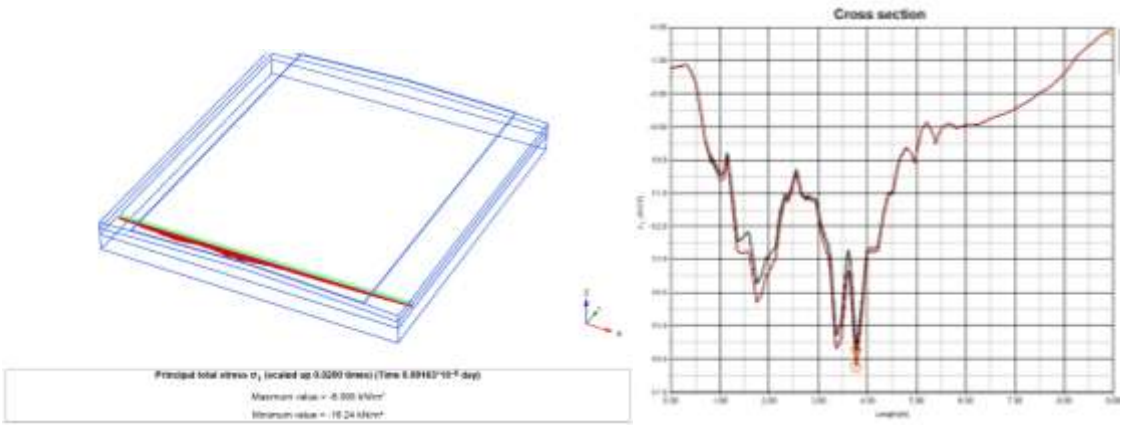

Figure 4.2 Results–Left: σ_1 (Section 1), Right: σ_1

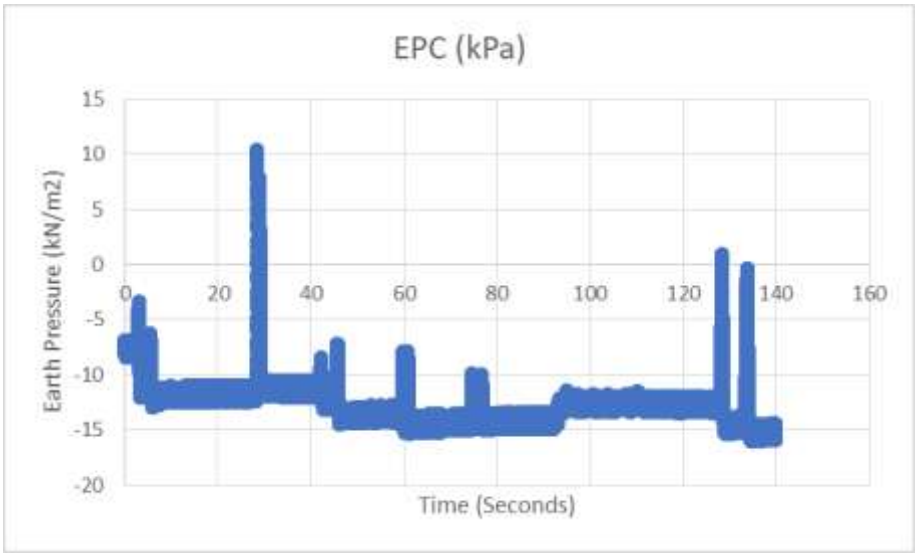

Figure 4.3 Earth Pressure–Tata Truck 1613c at 15 km/h, Matching Figure 4.2

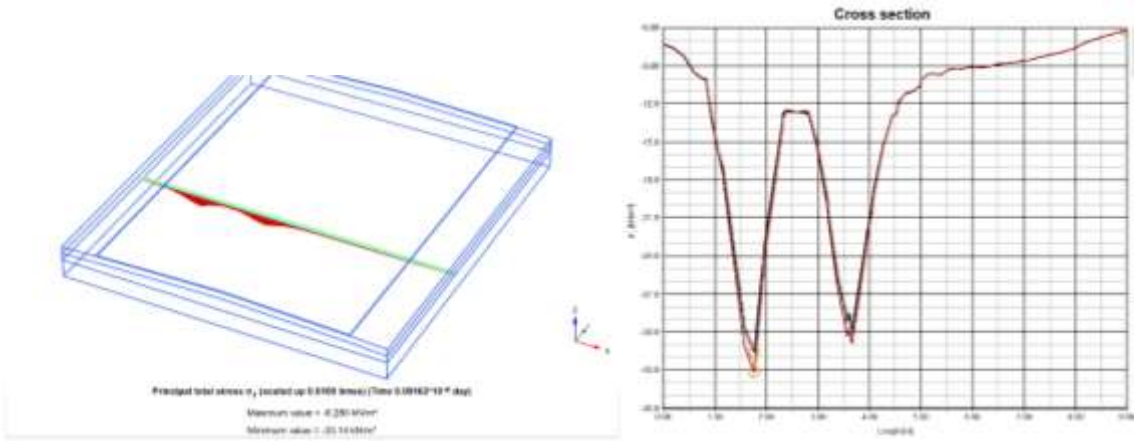

Figure 4.4 Results–Left: σ_1 (Width, 15 km/h, 1.0 m/s²), Right: σ_1

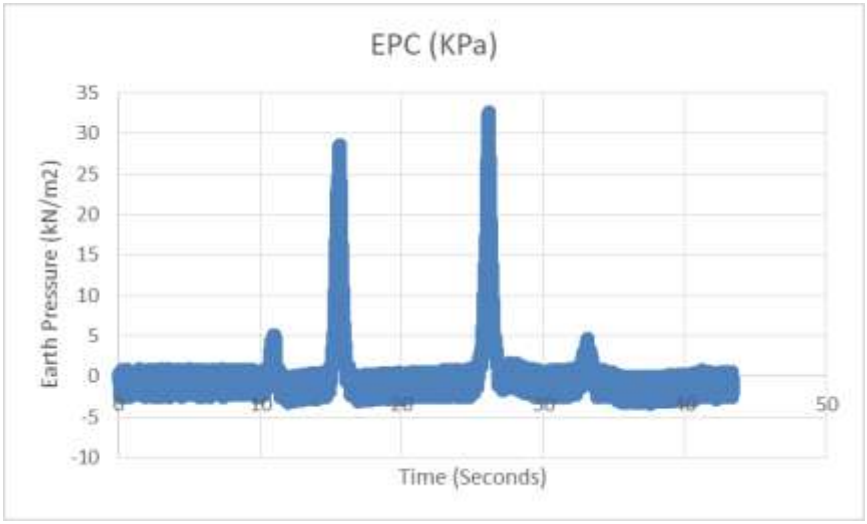

Figure 4.5 Earth Pressure–Tata Truck 1613c at 15 km/h, Matching Figure 4.4

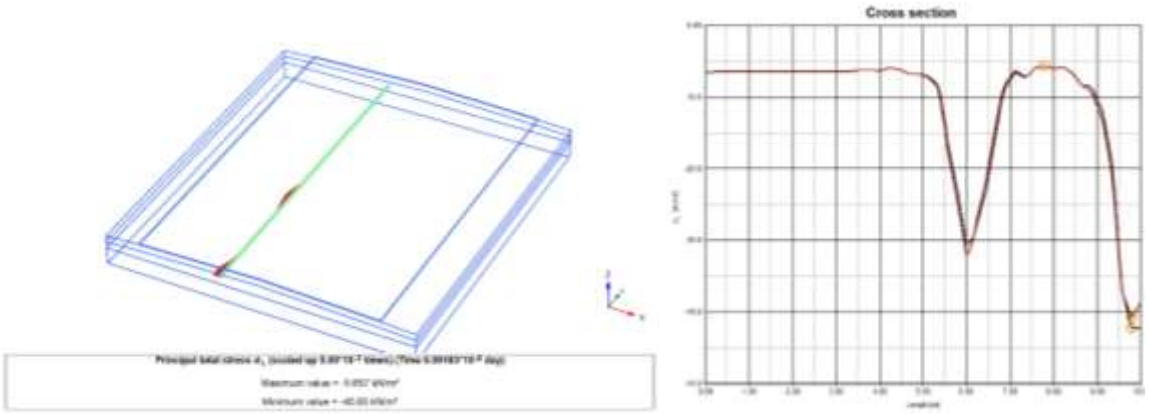

Figure 4.6 Results–Left: σ_1 (Wheel Path, 2nd, 15 km/h, 1.0 m/s²), Right: σ_1

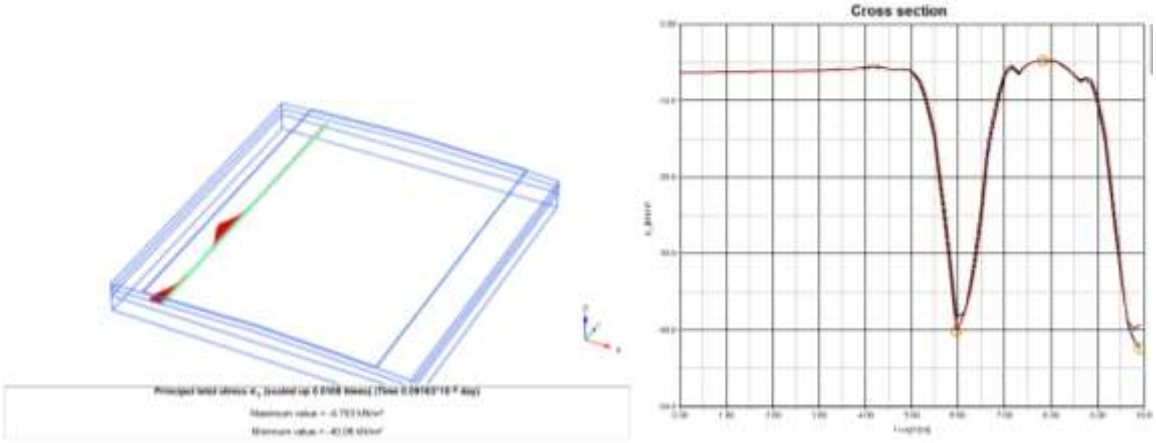

Figure 4.7 Results–Left: σ_1 (Wheel Path, 4th, 15 km/h, 1.0 m/s²), Right: σ_1

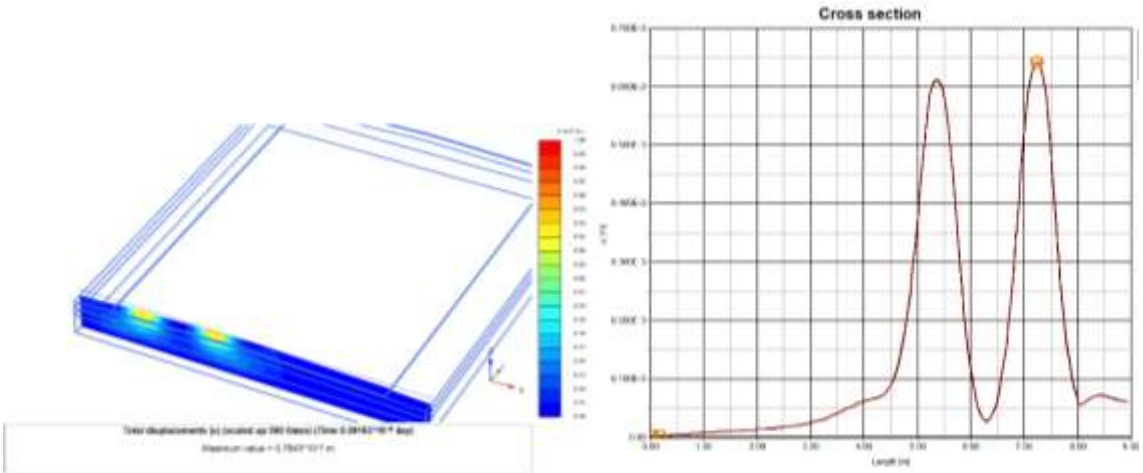

Figure 4.8 Computational Results–Left: u, Right: u

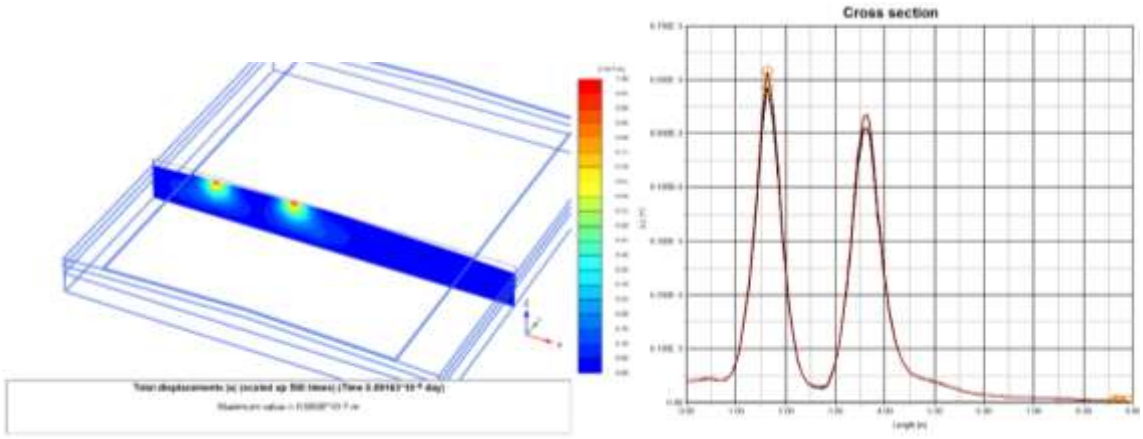

Figure 4.9 Results–Left: u (Width, 15 km/h, 1.0 m/s²), Right: u

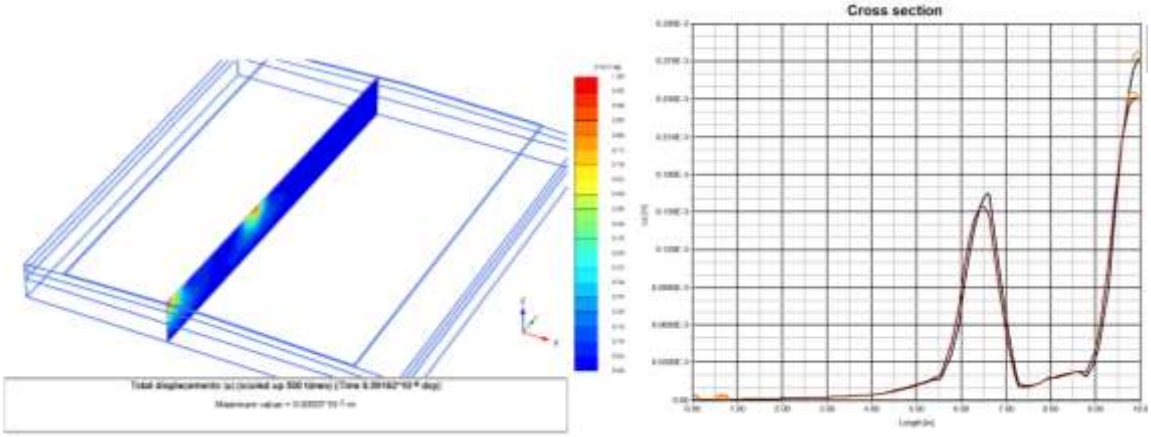

Figure 4.10 Results–Left: u (Wheel Path, 15 km/h, 1.0 m/s²), Right: u

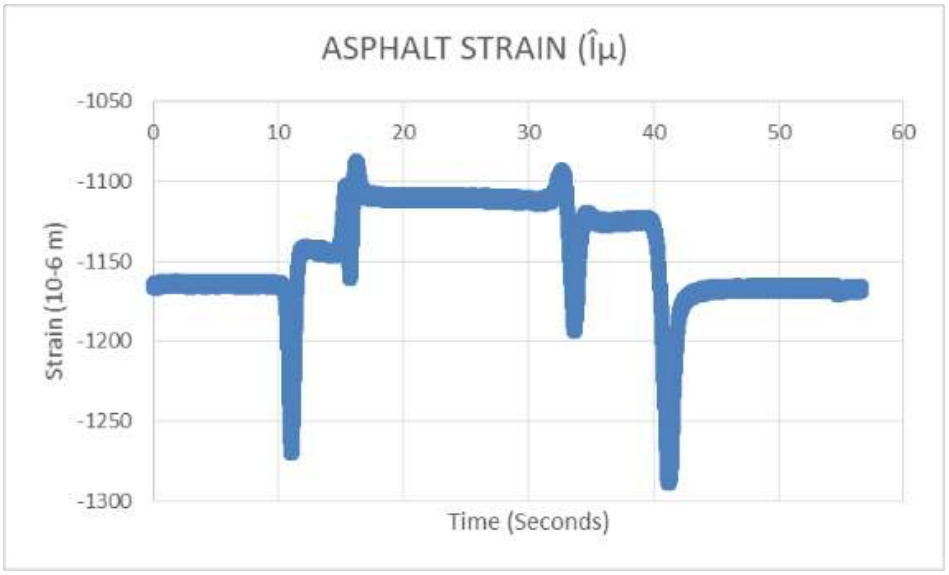

Figure 4.11 Strain Gauge–Tata Truck 1613C at 15 km/h, Matching Figure 4.10

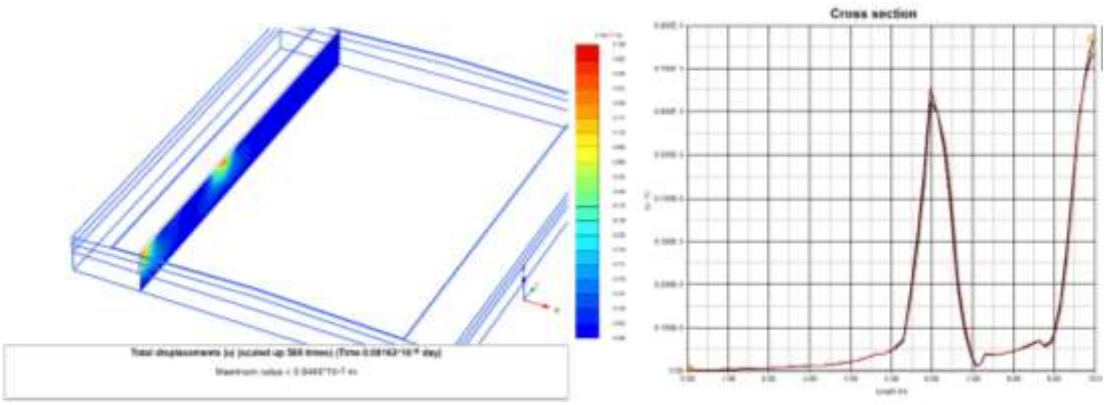

Figure 4.12 Results–Left: u (Wheel Path, 15 km/h, 1.0 m/s²), Right: u

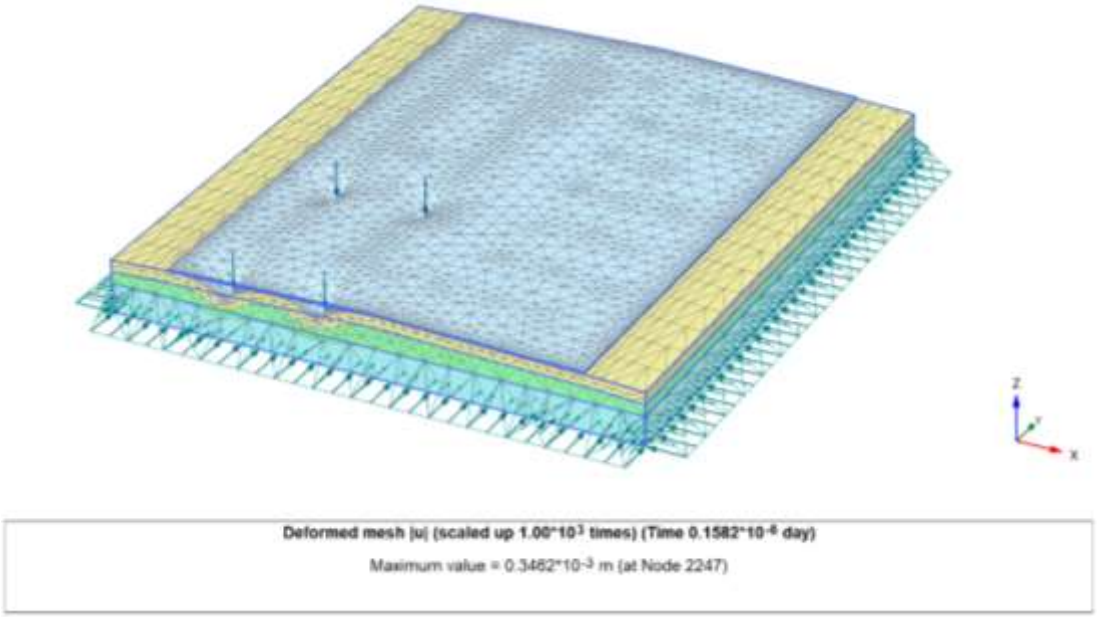

Figure 4.13 Discretized Model with FR 3.2 XLT, Point Load, 15 km/h, 1.0 m/s²

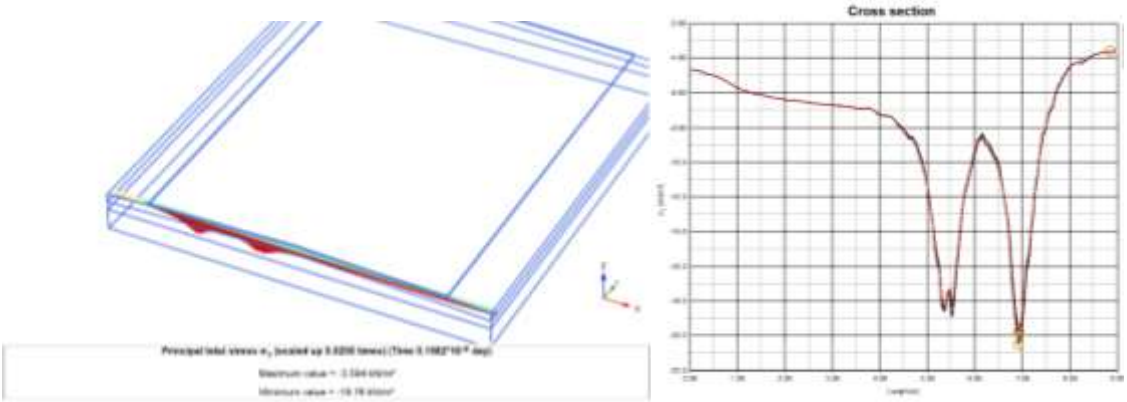

Figure 4.14 Results–Left: σ_1 (Width, 15 km/h, 1.0 m/s²), Right: σ_1

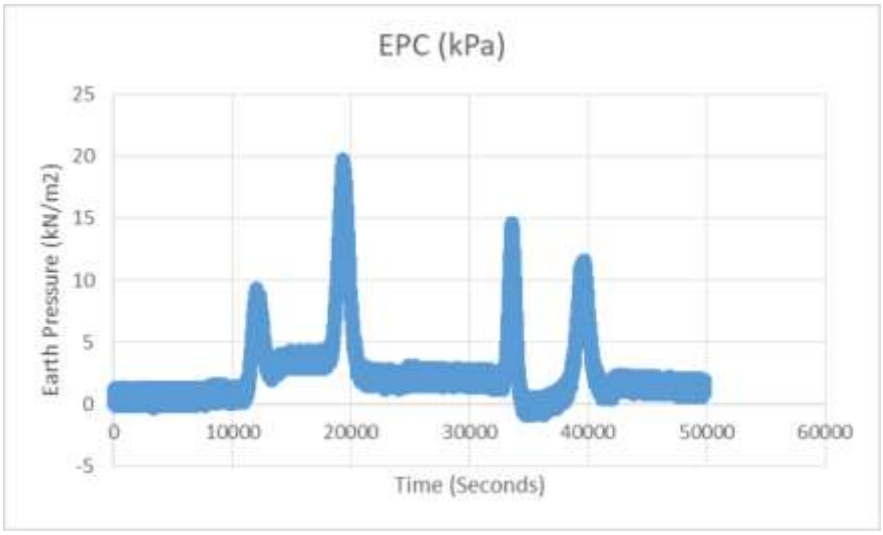

Figure 4.15 Earth Pressure–Tata Truck 1613c at 15 km/h, Matching Figure 4.14

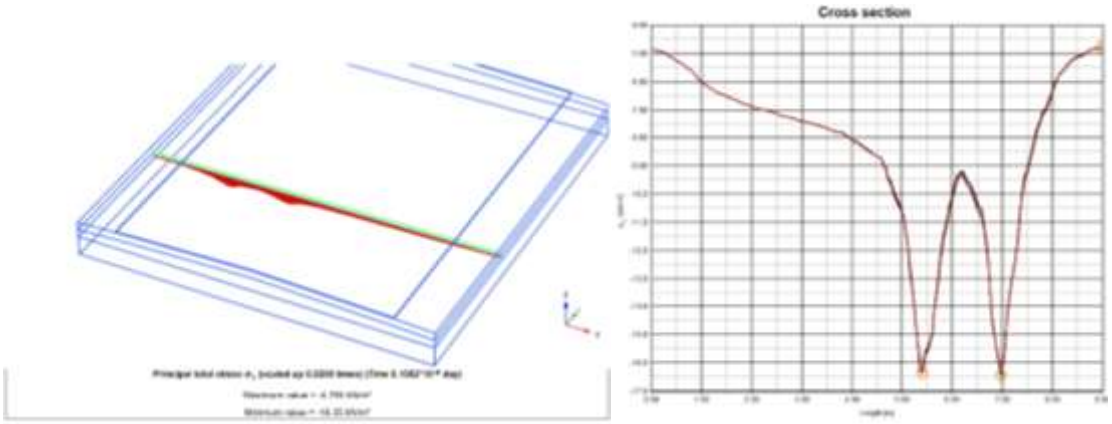

Figure 4.16 Results–Left: σ_1 (Width, 15 km/h, 1.0 m/s²), Right: σ_1

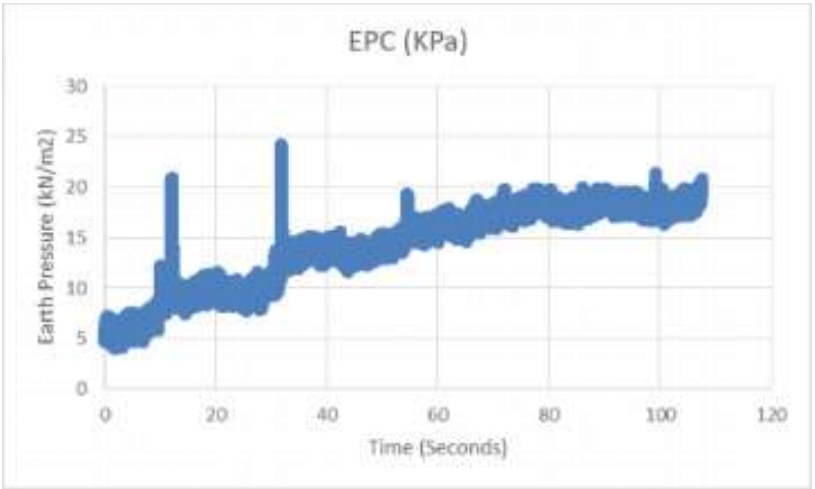

Figure 4.17 Earth Pressure–Tata Truck 1613c at 15 km/h, Matching Figure 4.16

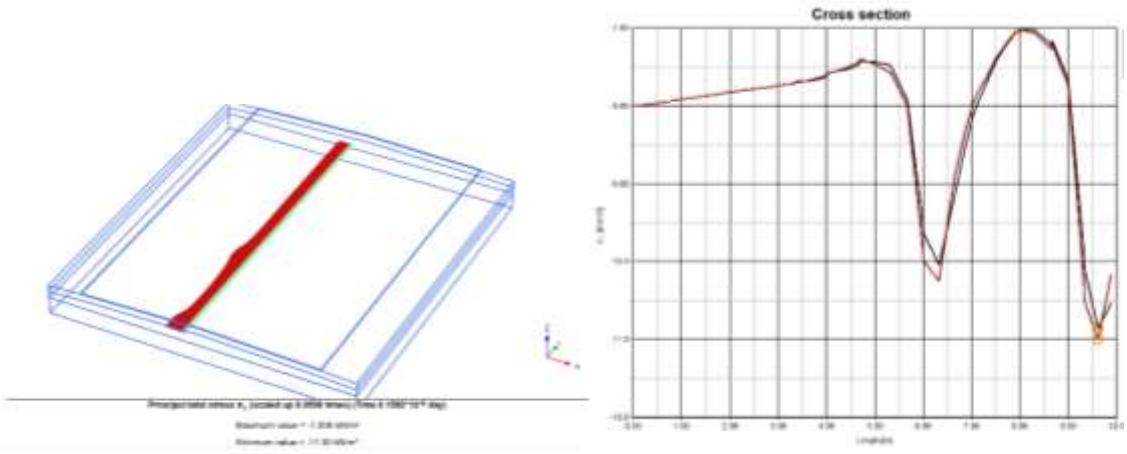

Figure 4.18 Results–Left: σ_1 (Wheel Path, 2nd, 15 km/h, 1.0 m/s²), Right: σ_1

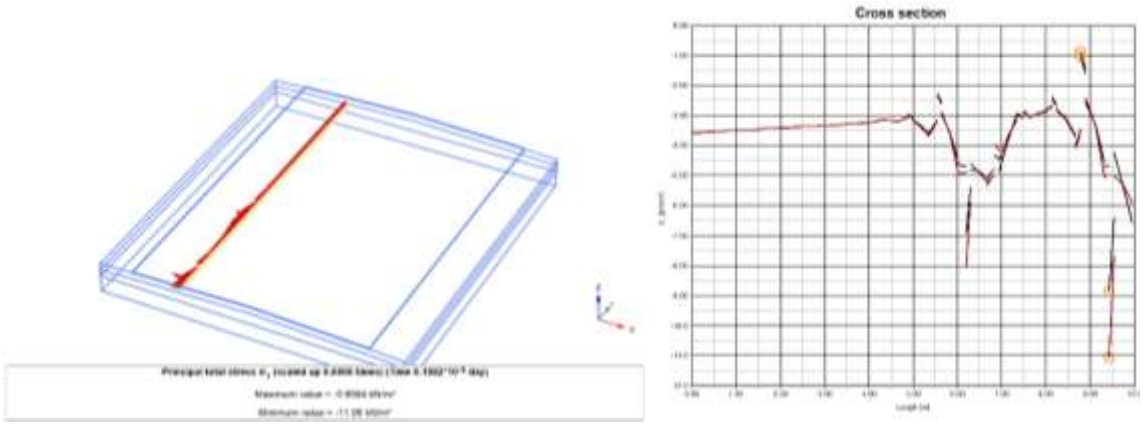

Figure 4.19 Results–Left: σ_1 (Wheel Path, 4th, 15 km/h, 1.0 m/s²), Right: σ_1

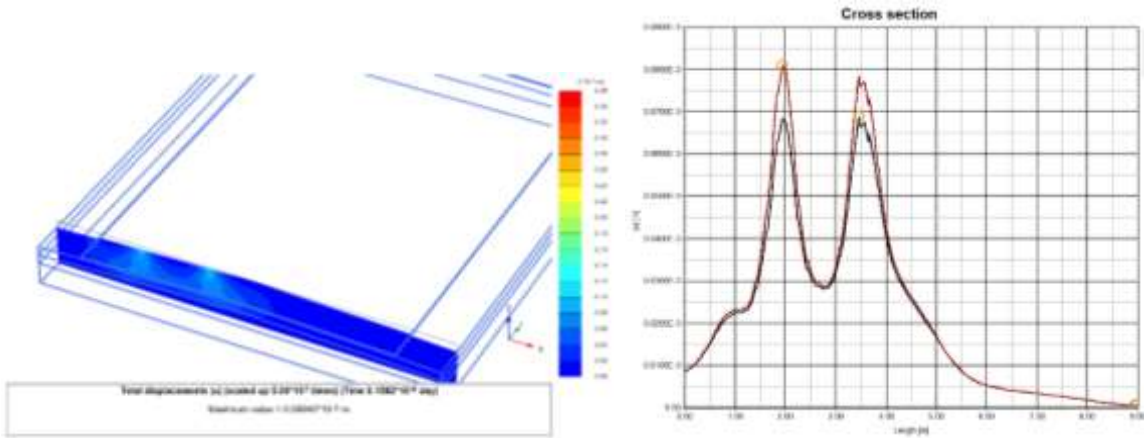

Figure 4.20 Results–Left: u (Width, 15 km/h, 1.0 m/s²), Right: u

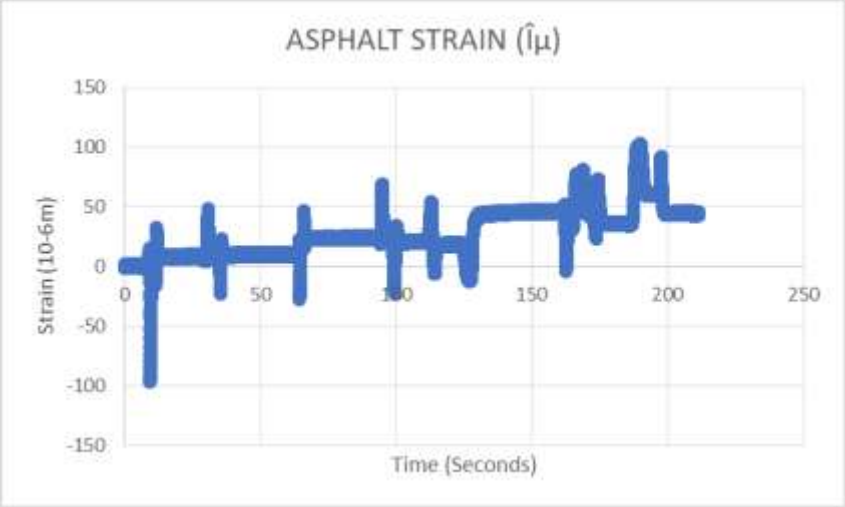

Figure 4.21 Strain Gauge–Tata Truck 1613c at 15 km/h, Matching Figure 4.20

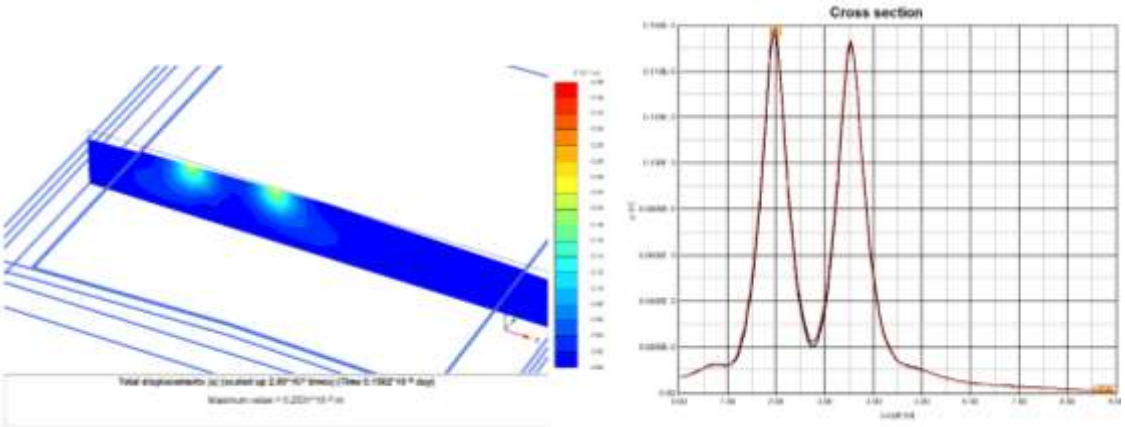

Figure 4.22 Results–Left: u (Width, 15 km/h, 1.0 m/s²), Right: u

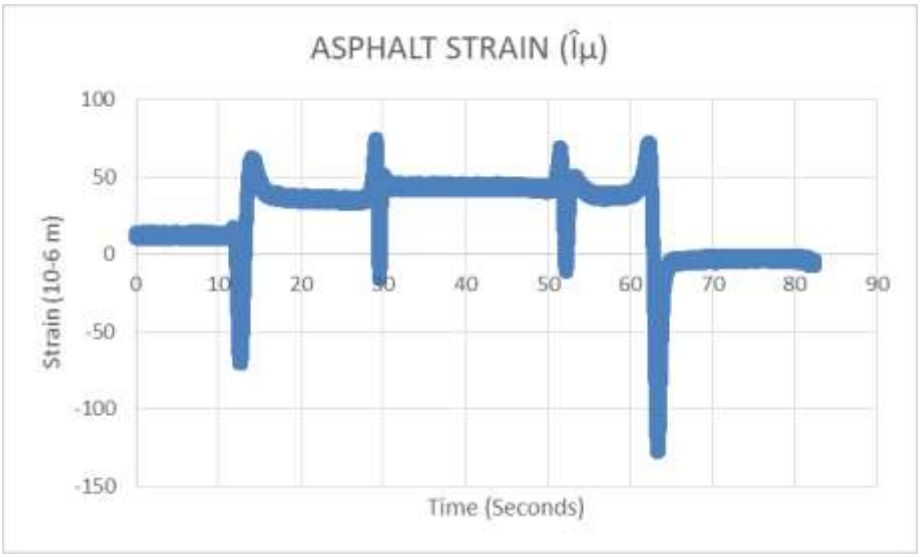

Figure 4.23 Strain Gauge–Tata Truck 1613c at 15 km/h, Matching Figure 4.22

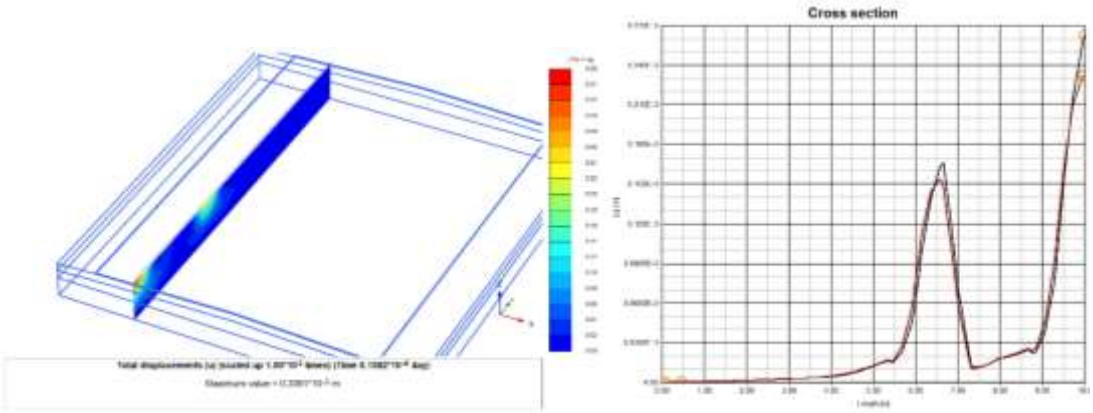

Figure 4.24 Results–Left: u (Wheel Path, 15 km/h, 1.0 m/s²), Right: u

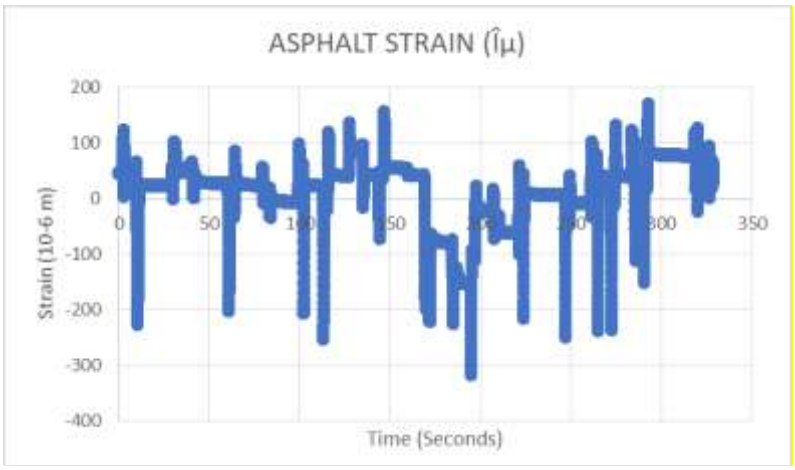

Figure 4.25 Strain Gauge–Tata Truck 1613c at 15 km/h, Matching Figure 4.24

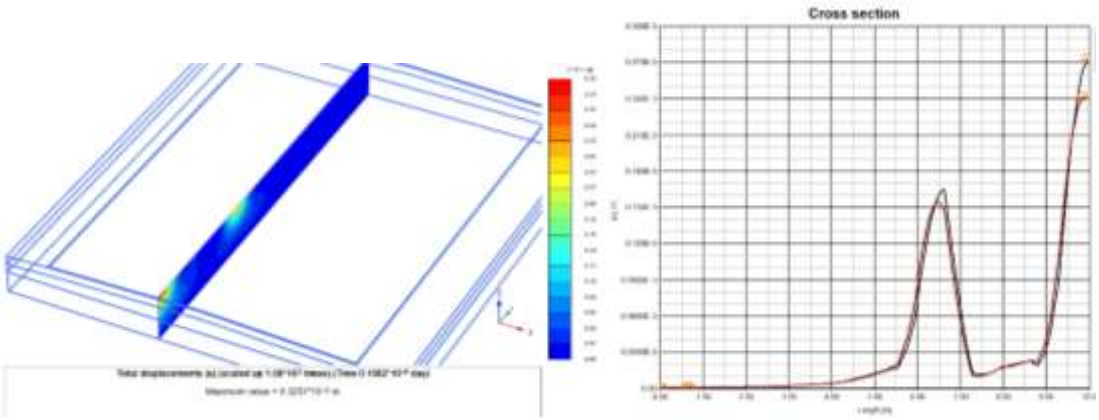

Figure 4.26 Results–Left: u (Wheel Path, 15 km/h, 1.0 m/s²), Right: u

Seasonal variations in soil moisture also affect pavement behavior, with higher moisture levels leading to increased strain and stress, highlighting the importance of considering soil conditions in pavement design. The analysis underscores the value of geogrid in improving

pavement performance, load distribution, and longevity, but stresses the need for further reinforcement to mitigate stress concentrations in deeper layers (Figure 4. 27 to 4.29).

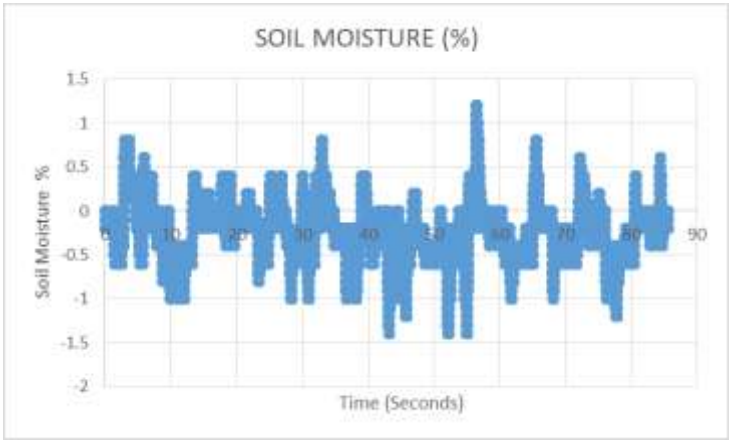

Figure 4.27 Soil Moisture (Mar 26, 2024), without Geogrid, Ford 3.2 XLT at 5 km/h

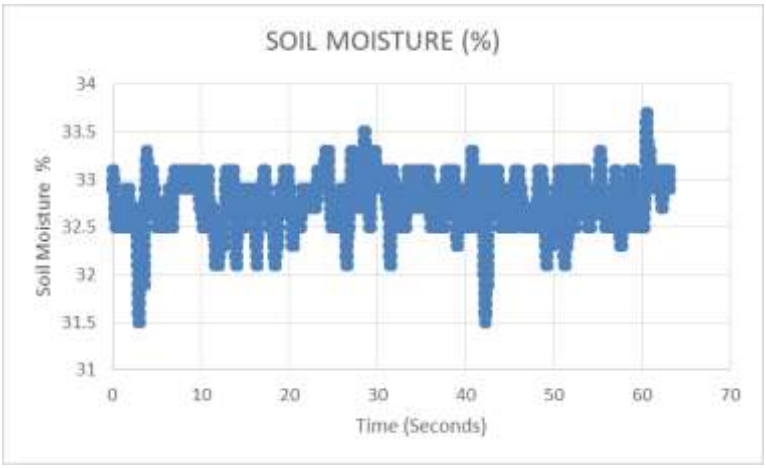

Figure 4.28 Soil Moisture (June 21, 2024), without Geogrid, Ford 3.2 XLT at 5 km/h

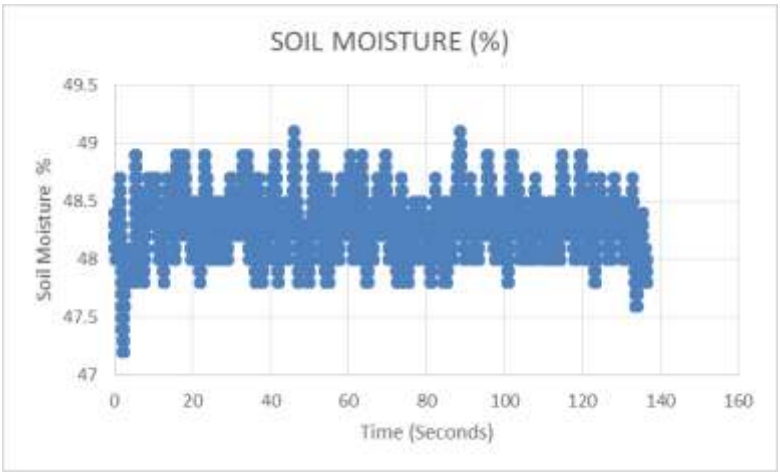

Figure 4.29 Soil Moisture (Aug 21, 2024), without Geogrid, Ford 3.2 XLT at 5 km/h

The significant changes in subgrade and base layer stresses, both in compression and tensile stress-strain, help mitigate structural deficiencies and surface distresses by improving stress distribution and reducing stress concentrations, thereby enhancing overall pavement performance. The enhancement in subgrade stress-strain aids in mitigating structural deficiencies, while improvements in the base layer stress-strain help alleviate surface distresses, leading to better pavement performance (Figure 4.30 to Figure 4.47).

Figure 4.30 illustrates the stress at the subgrade under a point load from a Tata Truck 1613c in the transverse direction of the road, moving at a constant speed of 15 km/h, both with and without geogrid reinforcement. The analysis shows that the percentage change in stress due to the presence of geogrid reinforcement ranges from 3.85% to 8.73%, indicating a noticeable reduction in stress when the reinforcement is applied.

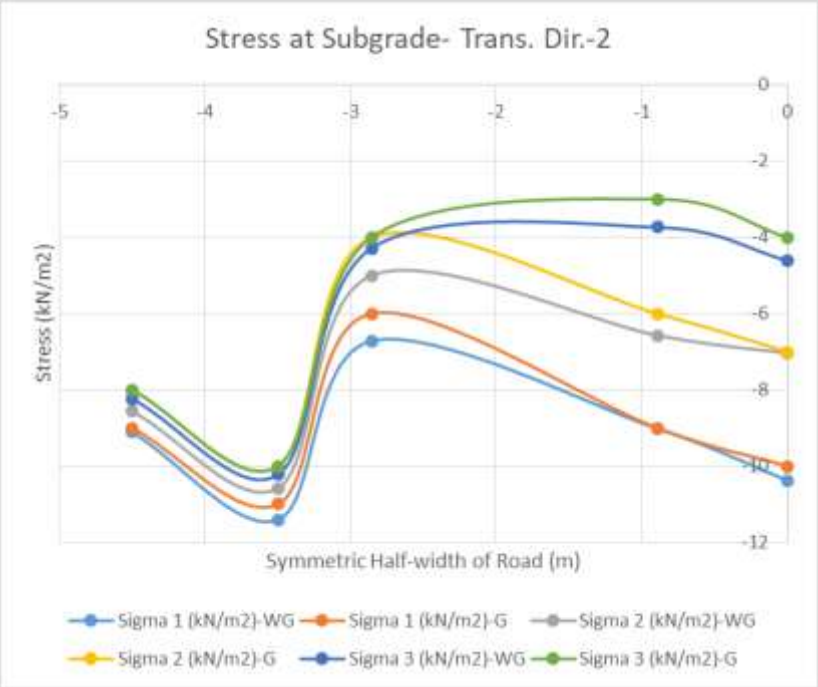

Figure 4.30 Subgrade Stress (Truck 1613c, 15 km/h), T–2, with/without Geogrid

Figure 4.31 illustrates the stress at the mid-base under a point load from a Tata Truck 1613c in the transverse direction of the road, both with and without geogrid reinforcement, at a speed of 15 km/h and an accelerated speed of 1.0 m/s². The percentage reduction in stress due to the geogrid reinforcement ranges from 6.66% to 40.15%, highlighting the effectiveness of the reinforcement in reducing stress levels. Figure 4.32 shows the stress at the pavement layers under a point load from a Tata Truck 1613c in the longitudinal

direction of the road, both with and without geogrid reinforcement, at a speed of 15 km/h and an accelerated speed of 1.0 m/s². The percentage change in stress ranges from 3% to 27%, reflecting the variation in stress levels due to the applied conditions.

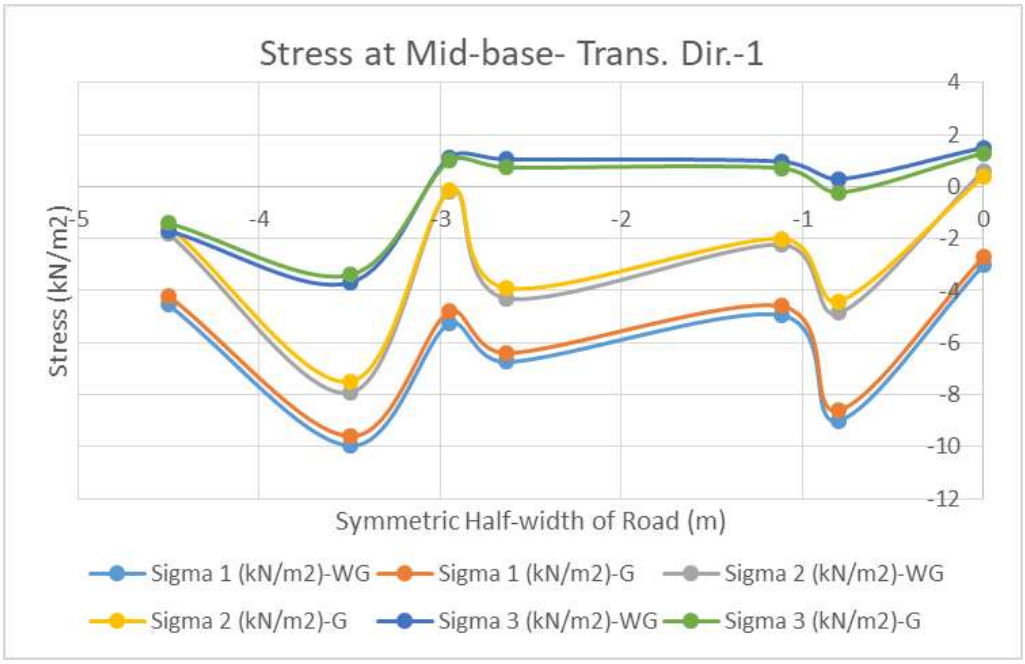

Figure 4.31 Mid–Base Stress (Truck, 15 km/h, 1.0 m/s²), T–1, with/without Geogrid

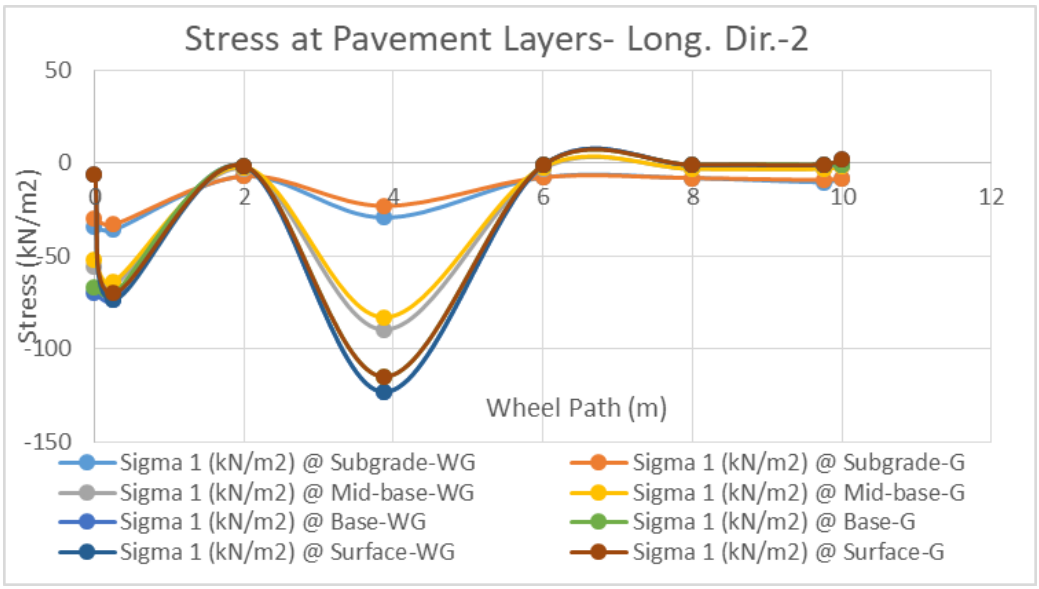

Figure 4.32 Pavement Stress (Truck, 15 km/h, 1.0 m/s²), L–2, with/without Geogrid

Figure 4.33 shows the stress at the base layer under an area load from a Tata Truck 1613c in the transverse direction of the road, both with and without geogrid reinforcement, at a

speed of 15 km/h and an accelerated speed of 1.0 m/s². The percentage reduction in stress ranges from 7.19% to 8.50%, indicating a moderate reduction in stress levels due to the presence of geogrid reinforcement. Figure 4.34 illustrates the stress at the base layer of a road under an area load from a Tata Truck 1613c, considering the longitudinal direction-2 of the road, with speeds of 15 km/h and an acceleration of 1.0 m/s². The analysis shows that the presence of geogrid reinforcement results in a stress reduction ranging from 4.31% to 12.44%, indicating that the geogrid improves the load distribution and helps reduce stress concentrations at the base layer.

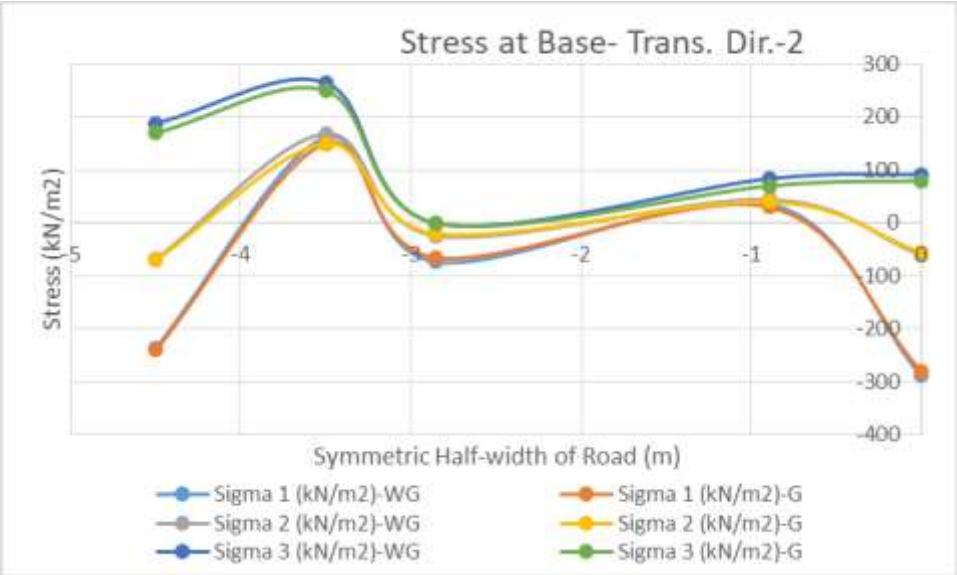

Figure 4.33 Base Stress (Truck, 15 km/h, 1.0 m/s²), T–2, with/without Geogrid

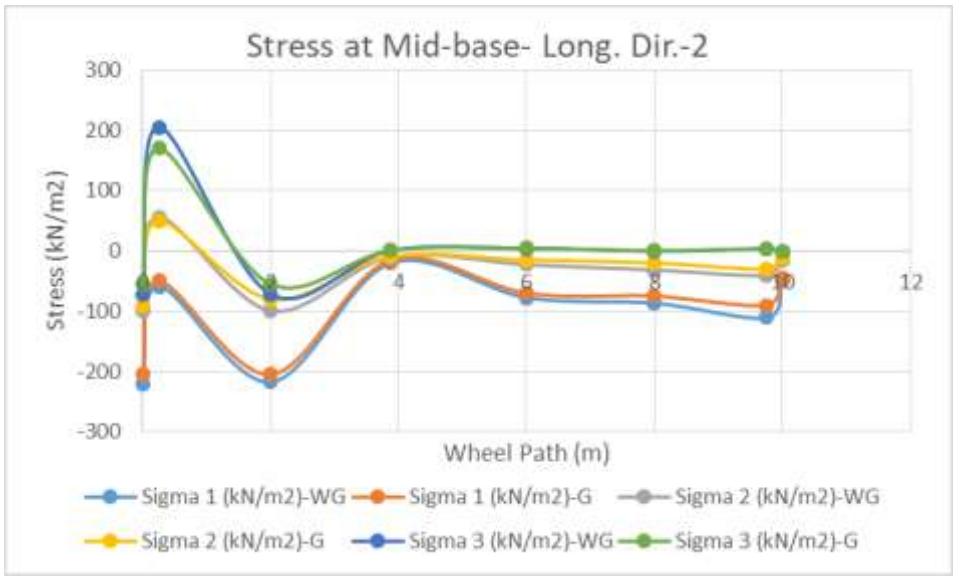

Figure 4.34 Mid–Base Stress (Truck, 50 km/h, 1.0 m/s²), T–1, with/without Geogrid

Figure 4.35 shows the stress at the mid-base layer of a road under a point load from a Tata Truck 1613c, applied in the transverse direction-1 of the road. The analysis is conducted at a speed of 50 km/h with an acceleration of 1.0 m/s². The results indicate that with geogrid reinforcement, the stress is reduced by 6.91% to 21.85%, suggesting that the geogrid effectively distributes the load and decreases stress concentrations at the mid-base layer.

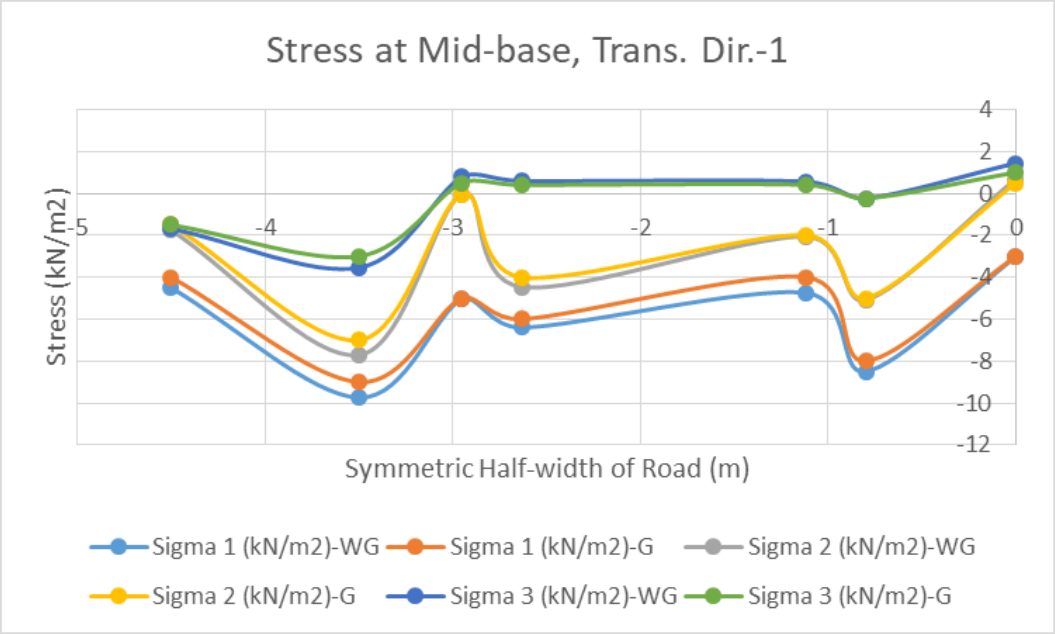

Figure 4.35 Base Stress (Truck, 50 km/h, 1.0 m/s²), L–2, with/without Geogrid

Figure 4.36 shows the stress at the base layer of a road under an area load from a Tata Truck 1613c, applied in the transverse direction-1 of the road. The analysis is performed at a speed of 50 km/h with an acceleration of 1.0 m/s². The results indicate that with geogrid reinforcement, the stress is reduced by 13.21% to 19.49%, demonstrating the geogrid's effectiveness in improving load distribution and significantly reducing stress concentrations at the base layer.

Figure 4.37 shows the stress at the surface layer of a road under an area load from a Tata Truck 1613c, applied in the transverse direction-1 of the road. The analysis is performed at a speed of 50 km/h with an acceleration of 1.0 m/s². The results demonstrate that with geogrid reinforcement, the stress is reduced by 7.42% to 32.67%, indicating that the geogrid significantly enhances load distribution and substantially reduces stress concentrations at the surface layer, improving the road's overall durability.

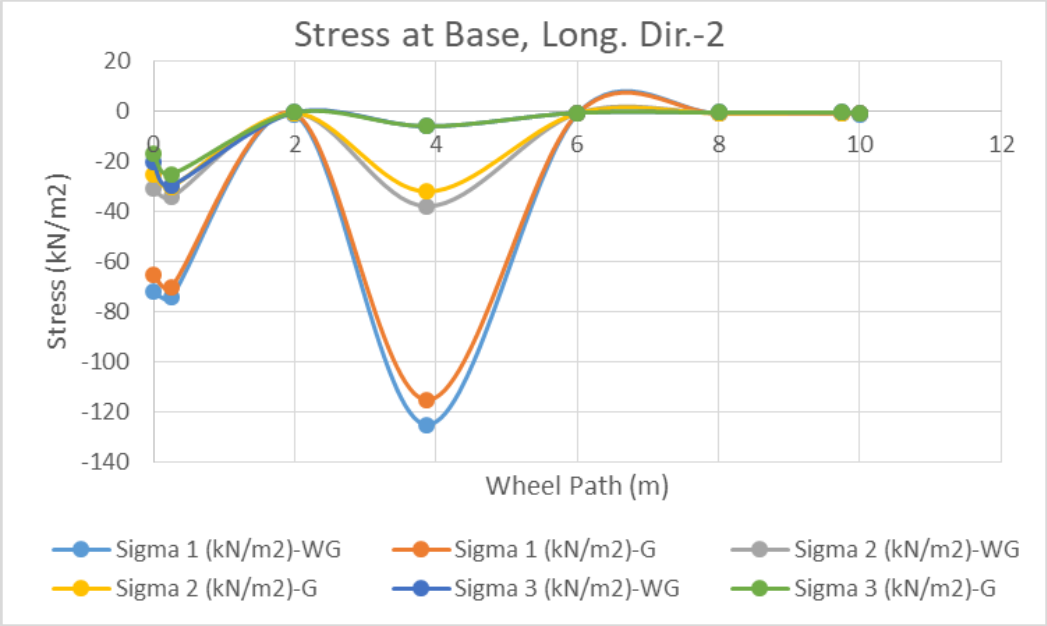

Figure 4.36 Base Stress (Truck, 50 km/h, 1.0 m/s²), T–2, with/without Geogrid

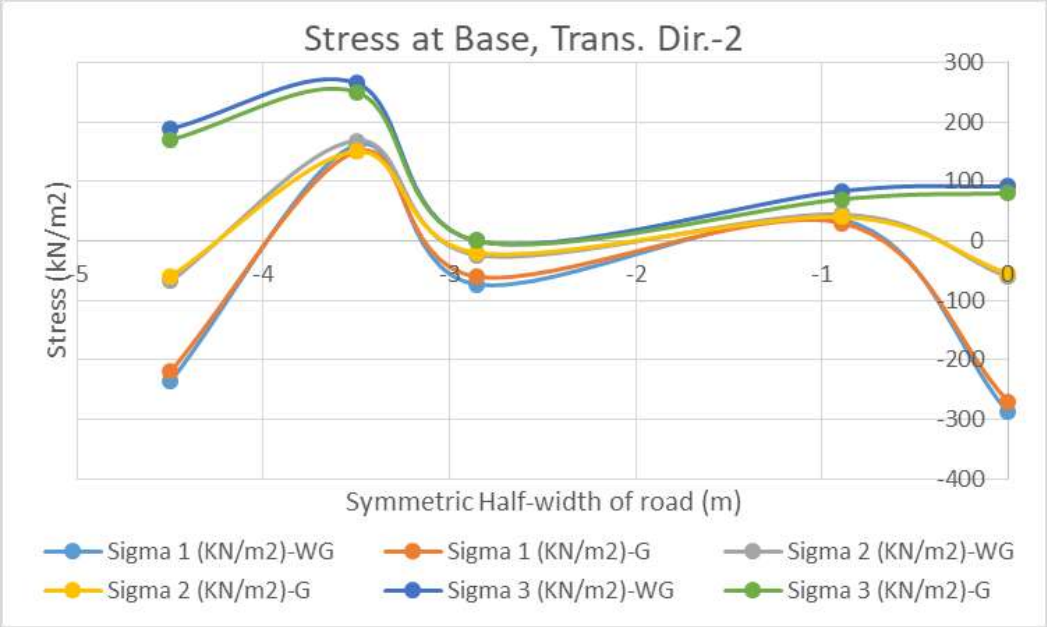

Figure 4.37 Surface Stress (Truck, 50 km/h, 1.0 m/s²), T–2, with/without Geogrid

Figure 4.38 shows the stress at the surface layer of a road under an area load from a Taya Truck 1613c, applied in the longitudinal direction-1 of the road. The analysis is performed at a speed of 50 km/h with an acceleration of 1.0 m/s². The results indicate that with geogrid reinforcement, the stress is reduced by 7.92% to 10.93%, suggesting that the geogrid helps

in improving load distribution and reducing stress concentrations at the surface layer, thereby enhancing the road's performance and longevity.

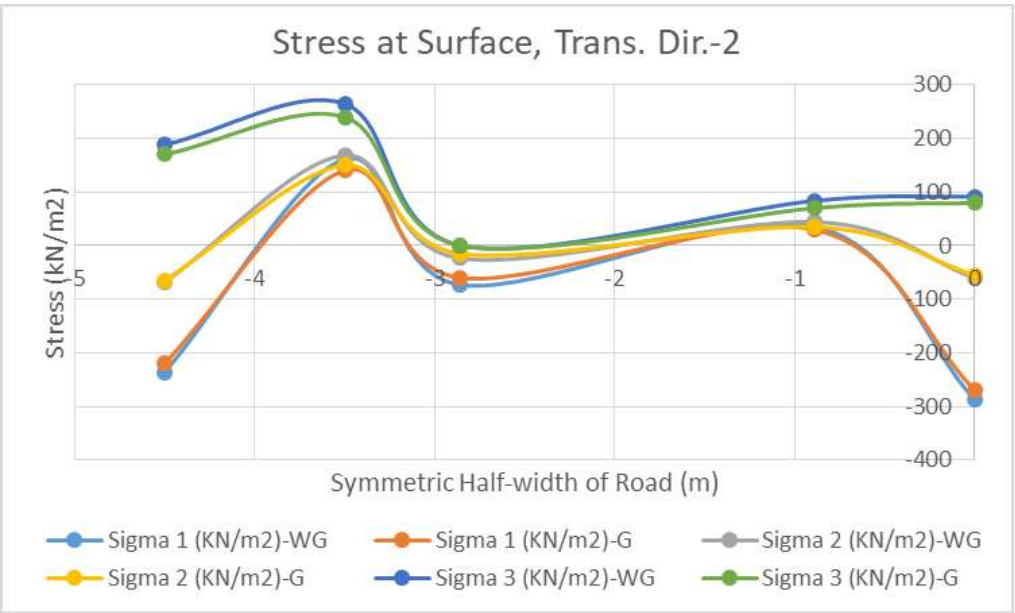

Figure 4.38 Mid–Base Stress (Ford, 15 km/h, 1.0 m/s²), T–2, with/without Geogrid

ii. Computational Results: FORD RANGER 3.2 XLT

The computational analysis of the Ford Ranger 3.2 XLT reveals that accelerated motion (1.0 m/s²) increases stress at the mid-base layer compared to constant speed, with higher stress observed at both 15 km/h and 50 km/h under acceleration. The presence of geogrid reinforcement reduces stress, particularly at lower speeds (15 km/h), but its effectiveness diminishes as speed increases, with notable stress remaining at higher speeds (50 km/h). The results indicate that while geogrid reinforcement helps mitigate stress, its impact is less significant under higher speeds and acceleration. Thus, additional measures may be needed to enhance road durability under such dynamic loading conditions (Figure 4.39 to Figure 4.42).

Figure 4.39 shows the stress at the mid-base of a road under a point load from a Ford Ranger 3.2 XLT, applied in the transverse direction-2 of the road. The analysis is conducted at a speed of 15 km/h with an acceleration of 1.0 m/s². The results indicate that with geogrid reinforcement, the stress is reduced by 5.59% to 12.53%, demonstrating the geogrid's effectiveness in improving load distribution and reducing stress concentrations at the mid-base layer. Figure 4.40 shows the stress at the mid-base of a road under a point load from

a Ford Ranger 3.2 XLT, applied in the longitudinal direction-2 of the road. The analysis is performed at a speed of 15 km/h with an acceleration of 1.0 m/s². The results indicate that with geogrid reinforcement, the stress is reduced by 8.32% to 20.50%, highlighting the geogrid's role in improving load distribution and reducing stress concentrations at the mid-base layer, thus enhancing the structural integrity of the road. Figure 4.41 shows the stress at the mid-base of a road under a point load from a Ford Ranger 3.2 XLT, applied in the transverse direction-2 of the road. The analysis is conducted at a speed of 50 km/h with an acceleration of 1.0 m/s². The results indicate that with geogrid reinforcement, the stress is reduced by 10.45% to 14.54%, demonstrating the geogrid's effectiveness in improving load distribution and reducing stress concentrations at the mid-base layer.

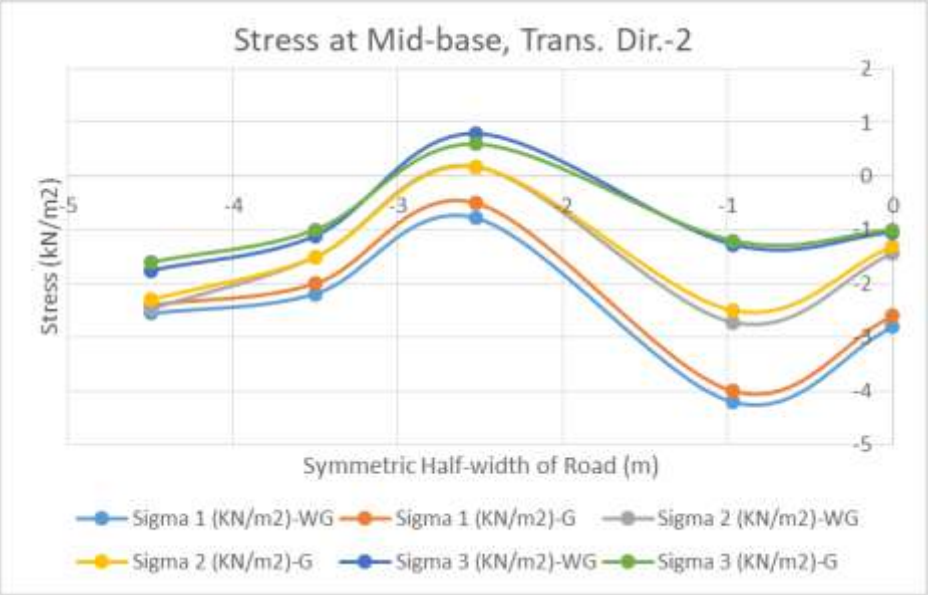

Figure 4.39 Mid–Base Stress (Ford, 15 km/h, 1.0 m/s²), L–2, with/without Geogrid

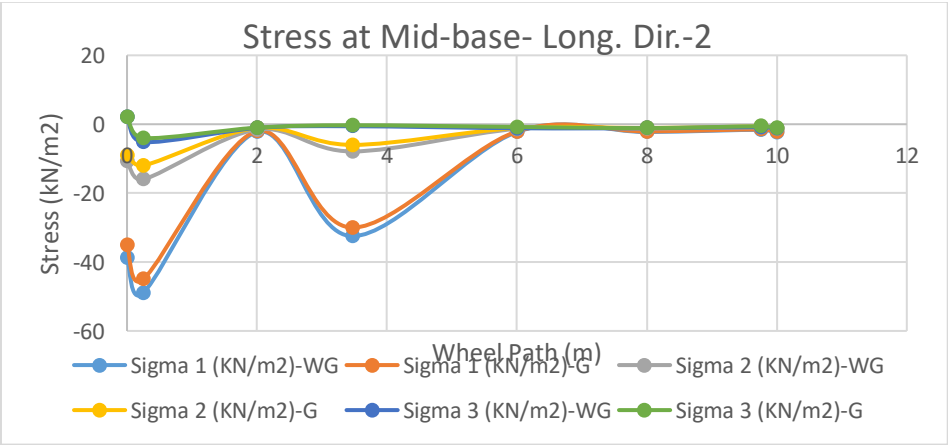

Figure 4.40 Mid–Base Stress (Ford, 50 km/h, 1.0 m/s²), T–2, with/without Geogrid

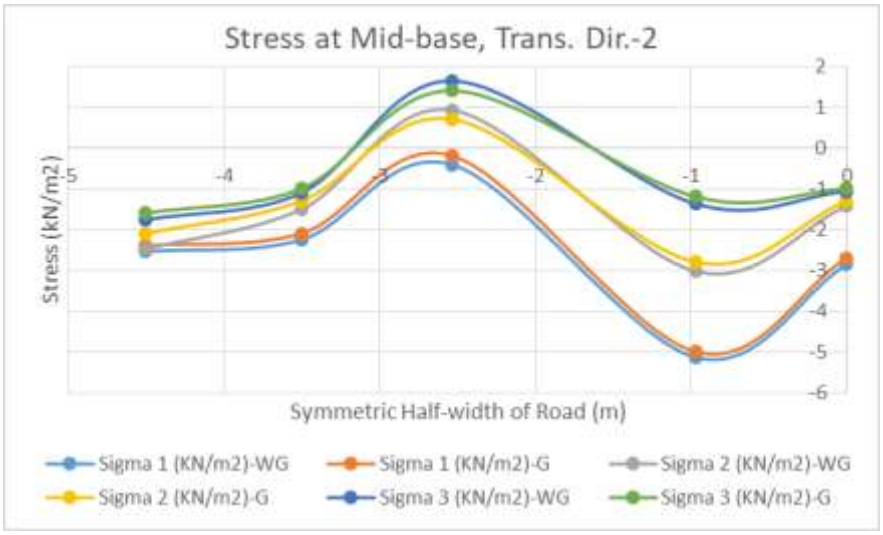

Figure 4.41 Mid–Base Stress (Ford, 50 km/h, 1.0 m/s²), L–2, with/without Geogrid

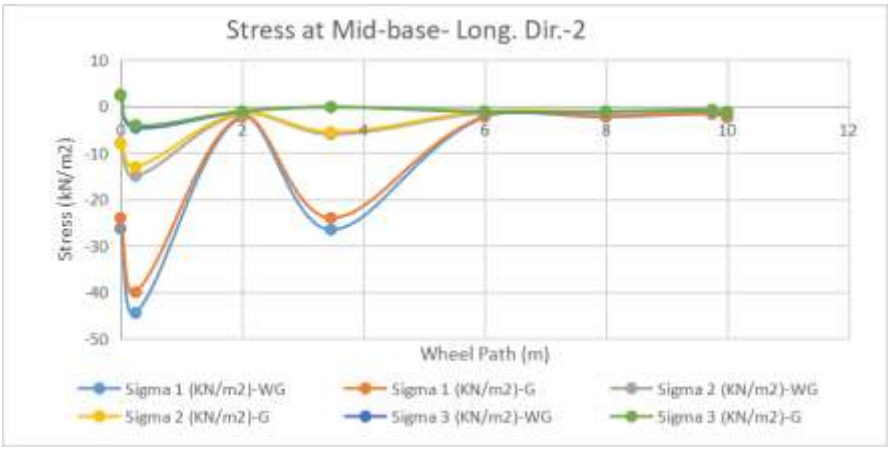

Figure 4.42 σ_1 Stress at Mid–base (Truck, 50 km/h, 1.0 m/s²), T–1, without Geogrid

Figure 4.42 shows the stress at the mid-base of a road under a point load from a Ford Ranger 3.2 XLT, applied in the longitudinal direction-2 of the road. The analysis is conducted at a speed of 50 km/h with an acceleration of 1.0 m/s². The results indicate that with geogrid reinforcement, the stress is reduced by 8.97% to 12.54%, highlighting the geogrid's role in improving load distribution and reducing stress concentrations at the mid-base layer, thereby enhancing the road's structural performance.

4.2 Modeling with Higher Material Models

This modeling is conducted specifically for the subgrade soil layers, while the remaining pavement layers are kept consistent across all cases. Field data were recorded at a speed of

15 km/h for both the TATA Truck 1613c and the Ford Ranger 3.2 XLT, and the analysis further explores potential variations at higher speeds. The table below presents the principal stress (σ_1 in kN/m²) and total displacement (u in meters) obtained from various material models: Linear Elastic, Mohr-Coulomb, Hardening Soil, Soft Soil, and Modified Cam-Clay.

The material models aligned with field measurements were identified using data from the TATA Truck 1613c and the Ford Ranger 3.2 XLT, both moving at a constant speed of 15 km/h. Two criteria were evaluated: stress and deformation. Under the stress criterion, all material models—except the modified Cam-Clay model—produced results closely matching field observations. The percentage differences in stress compared to field data are as follows: Linear Elastic – 10%, Mohr-Coulomb – 6.93%, Hardening Soil – 12.3%, Soft Soil – 0.91%, and Cam-Clay – 18.51%. Among these, the Soft Soil model showed the best agreement with field data, although the Linear Elastic, Mohr-Coulomb, and Hardening Soil models are also reasonably applicable (Table 4.1).

Considering the deformation criterion, the Hardening Soil model shows the closest agreement with field measurements, with a difference of just 1.08%. In comparison, the differences for other models are: Linear Elastic – 27%, Mohr-Coulomb – 43.67%, Soft Soil – 16.27%, and Cam-Clay – 187%. However, all models except the Cam-Clay model are reasonably applicable to field conditions. In summary, the Linear Elastic, Mohr-Coulomb, Hardening Soil, and Soft Soil models can be used with confidence. Among them, the Hardening Soil and Soft Soil models show the best alignment with field data based on both stress and deformation criteria.

Table 4.1 Material Model(s) aligned with Field Measurements

Field Measurement vs Numerical	Field Measurement	Linear Elastic	Mohr-Coulomb	Hardening Soil	Soft Soil	Modified Cam-Clay
Stress (kN/m2), % difference	30.00	33.00 (10%)	32.08 (6.93%)	33.70 (12.3%)	**29.73 (0.9%)**	24.45 (18.5%)
Displacement (m), % difference.	0.00129	0.0009303 (27.88%)	0.0007266 (43.67%)	**0.001276 (1.08%)**	0.00108 (16.27%)	0.003705 (187%)

The stress distribution at the mid-base under point loads from both the Tata Truck 1613c and Ford Ranger 3.2 XLT was analyzed for various road directions (transverse and longitudinal) at a speed of 50 km/h and an acceleration of 1.0 m/s², with and without geogrid reinforcement. Without geogrid reinforcement, significant stress concentrations were observed, particularly in the transverse direction and longitudinal direction-2, with Sigma 1 stresses being the highest. However, when geogrid reinforcement was applied, stress levels were significantly reduced, especially in the transverse direction-1 and transverse direction-2, indicating better load distribution and less concentration of stress. The Ford Ranger 3.2 XLT exhibited similar stress patterns, with Sigma 1 stresses being the highest, but the effect of geogrid reinforcement was slightly less pronounced compared to the Tata Truck 1613c, likely due to the difference in vehicle load and dynamics. Overall, geogrid reinforcement effectively mitigates stress concentrations, enhancing the durability of road structures under heavy load conditions (Figure 4.43 to Figure 4.5).

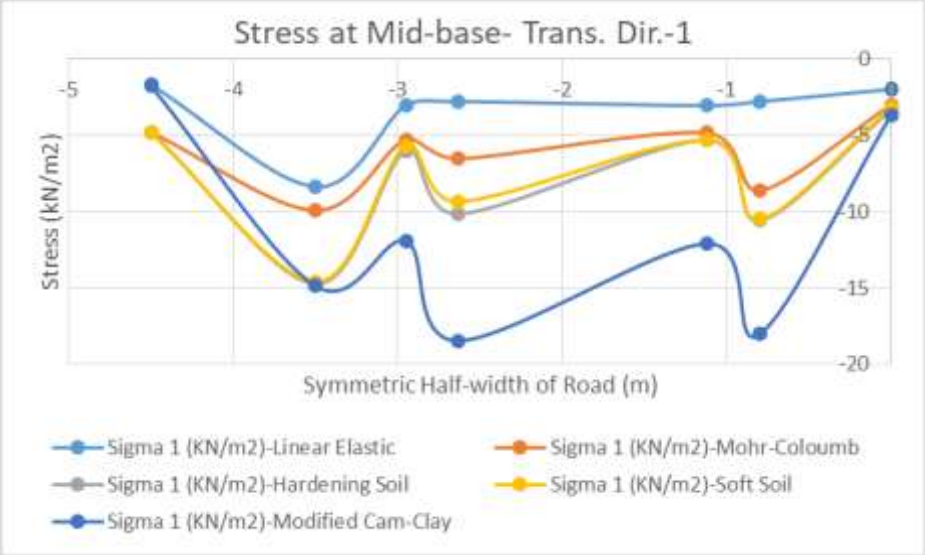

Figure 4.43 σ_1 Stress at Mid–base (Truck, 50 km/h, 1.0 m/s²), L–2, without Geogrid

Figure 4.43 presents the stress (Sigma 1) at the mid-base under a point load from a Tata Truck 1613c in the transverse direction-1 of the road, without geogrid reinforcement, at a speed of 50 km/h and an accelerated speed of 1.0 m/s². The percentage change in stress compared to the Linear Elastic (LE) model is as follows: 105.57% for the Mohr-Coulomb (MC) model, 150.40% for the Hardening Soil (HC) model, 143.46% for the Soft Soil (SS) model, and 268.86% for the Modified Cam-Clay (MCC) model. The results show that the HC and SS models yield similar stress values, indicating compatibility, and are closer to

the MC model, whereas the MCC model shows a much higher increase in stress compared to the LE model. This suggests that the MC, HC, and SS models provide comparable stress distributions, while the MCC model significantly deviates from the LE model. Figure 4.44 shows the stress (Sigma 1) at the mid-base under a point load from a Tata Truck 1613c in the longitudinal direction-2 of the road, without geogrid reinforcement, at a speed of 50 km/h and an accelerated speed of 1.0 m/s². Although there is a significant difference in stress compared to the Linear Elastic (LE) model, the four material models—Mohr-Coulomb (MC), Hardening Soil (HC), Soft Soil (SS), and Modified Cam-Clay (MCC)—are compatible with each other. There is no significant change in the percentage of stress between the models, indicating that the models exhibit similar behavior in terms of stress distribution, even though they differ from the LE model.

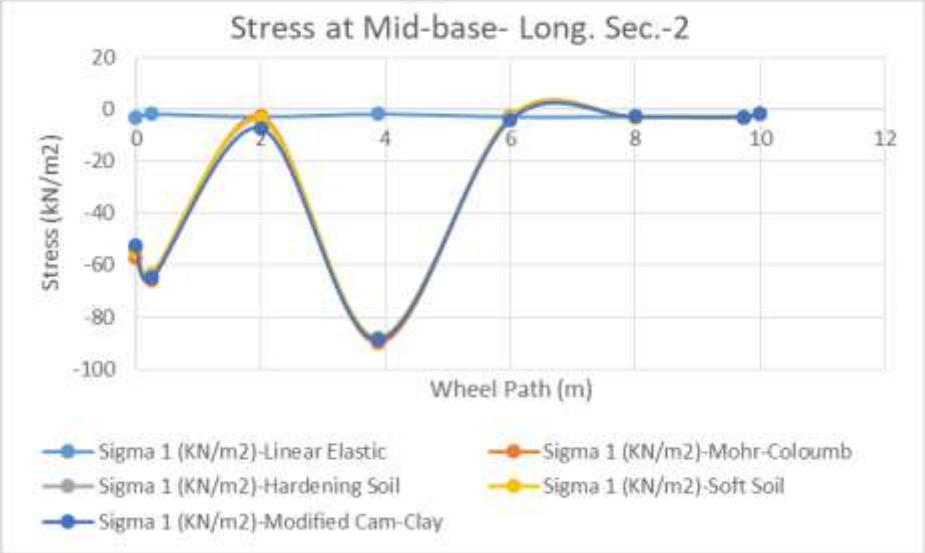

Figure 4.44 σ_1 Stress at Mid–base (Truck, 50 km/h, 1.0 m/s²), T–2, with Geogrid

Figure 4.45 shows the stress (Sigma 1) at the mid-base under the point load from a Tata Truck 1613c in the transverse direction-2 on the road with geogrid reinforcement, at a speed of 50 km/h and an acceleration of 1.0 m/s². The percentage reductions in stress are as follows: Mohr-Columb (MC) 0.64%, Hardening Soil (HS) 4.26%, Soft Soil (SS) 1.86%, and Modified Cam-Clay (MCC) 60.19%. When compared to the Linear Elastic (LE) method, the MC method shows the smallest reduction in stress, while HS, SS, and MCC exhibit larger reductions. The MCC method shows the most significant deviation, indicating a larger difference in stress response under the given loading scenario.

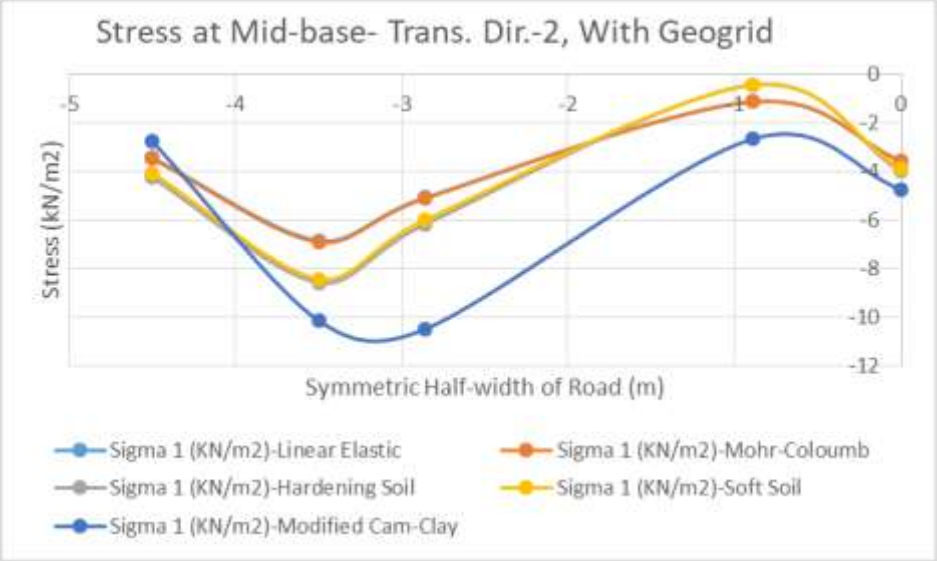

Figure 4.45 σ_2 Stress at Mid–base (Truck, 50 km/h, 1.0 m/s²), L–2, with Geogrid

Figure 4.46 shows the stress (Sigma 2) at the mid-base under the point load from a Tata Truck 1613c in the longitudinal direction-2 on the road with geogrid reinforcement, at a speed of 50 km/h and an acceleration of 1.0 m/s². The percentage changes in stress are as follows: Mohr-Columb (MC) 2.73%, Hardening Soil (HS) 13.75%, Soft Soil (SS) 11.04%, and Modified Cam-Clay (MCC) 18.15%. When compared to the Linear Elastic (LE) method, the MC method shows the closest result. However, HS, SS, and MCC are not much different from each other but are closer to each other than to the MC or LE methods.

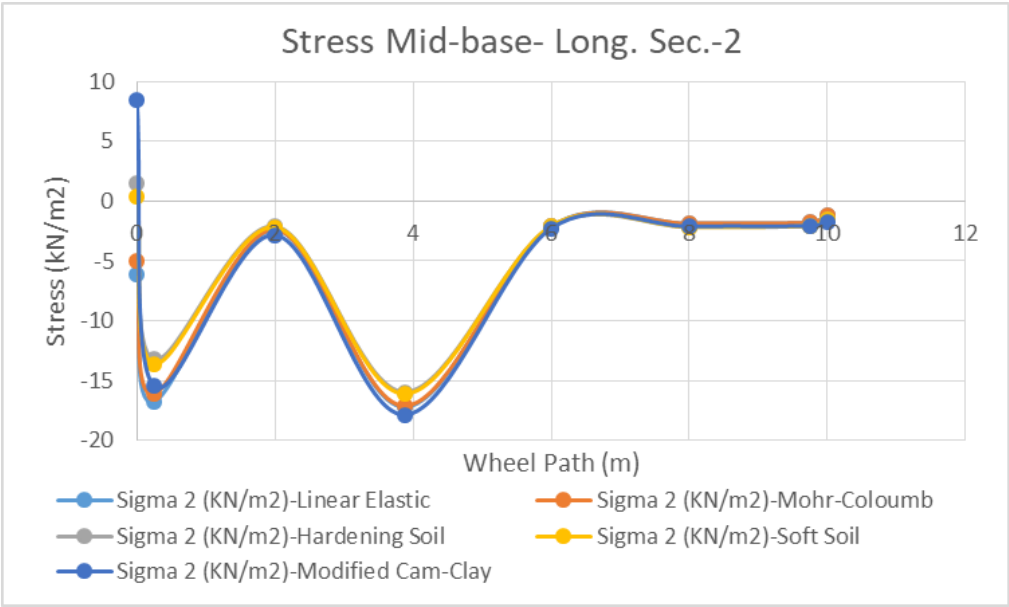

Figure 4.46 σ_1 Stress at Mid–base (Truck, 50 km/h, 1.0 m/s²), T–1, without Geogrid

Figure 4.47 shows the stress (Sigma 1) at the mid-base under the point load from a Ford Ranger 3.2 XLT in the transverse direction-1 on the road without geogrid reinforcement, at a speed of 50 km/h and an acceleration of 1.0 m/s². The percentage changes in stress are as follows: Mohr-Columb (MC) 0.11%, Hardening Soil (HS) 6.54%, Soft Soil (SS) 4.74%, and Modified Cam-Clay (MCC) 26.04%. When compared to the Linear Elastic (LE) method, the MC method shows the smallest reduction in stress. The HS, SS, and MCC methods are not much different from each other, with MCC showing a larger reduction, but they are still closer in comparison.

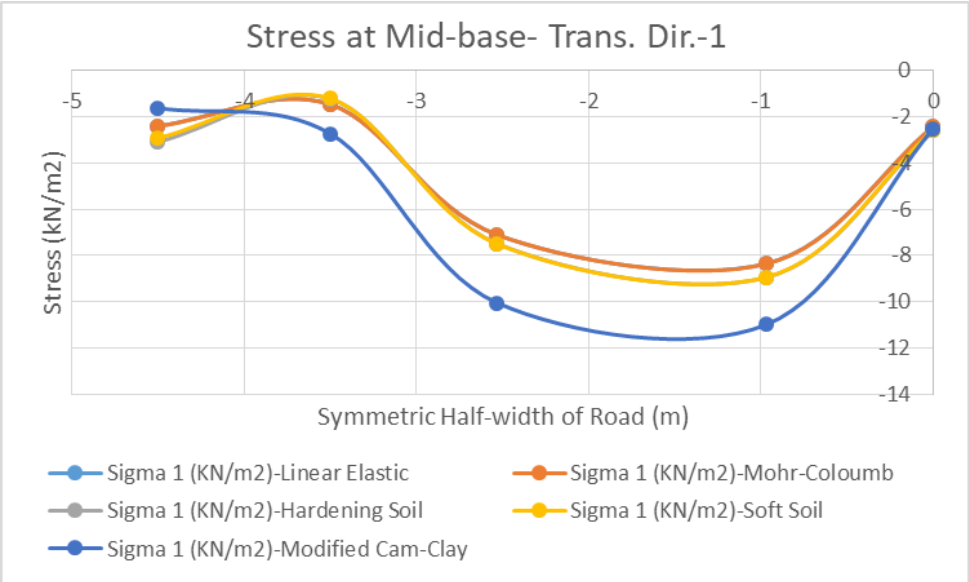

Figure 4.47 σ_3 Stress at Mid–base (Ford, 50 km/h, 1.0 m/s²), T–2, without Geogrid

Figure 4.48 illustrates the stress (Sigma 3) at the mid-base layer under a point load from a Ford Ranger 3.2 XLT traveling in the transverse direction-2, without geogrid reinforcement, at a speed of 50 km/h and an acceleration of 1.0 m/s². The percentage differences in stress, relative to the Linear Elastic (LE) model, are as follows: Mohr-Coulomb (MC) 0.04%, Hardening Soil (HS) 2.98%, Soft Soil (SS) 3.15%, and Modified Cam-Clay (MCC) 17.96%. Among these, the MC model shows the closest agreement with LE, indicating minimal variation. The HS and SS models exhibit similar results with slightly higher stress values, while the MCC model shows a significantly larger deviation, suggesting a considerable difference in its stress prediction compared to the other models.

These results emphasize the relative consistency of MC, HS, and SS models in representing realistic pavement responses under dynamic conditions. The notable deviation of the MCC model indicates its limited suitability for mid-base layer stress evaluation in this context.

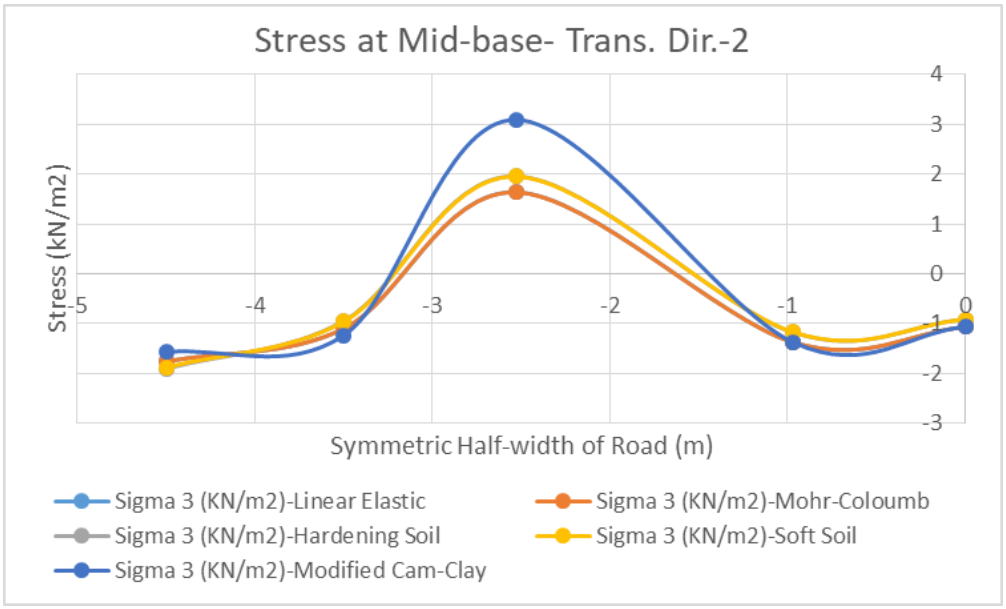

Figure 4.48 σ_1 Stress at Mid–base (Ford, 50 km/h, 1.0 m/s²), L–2, without Geogrid

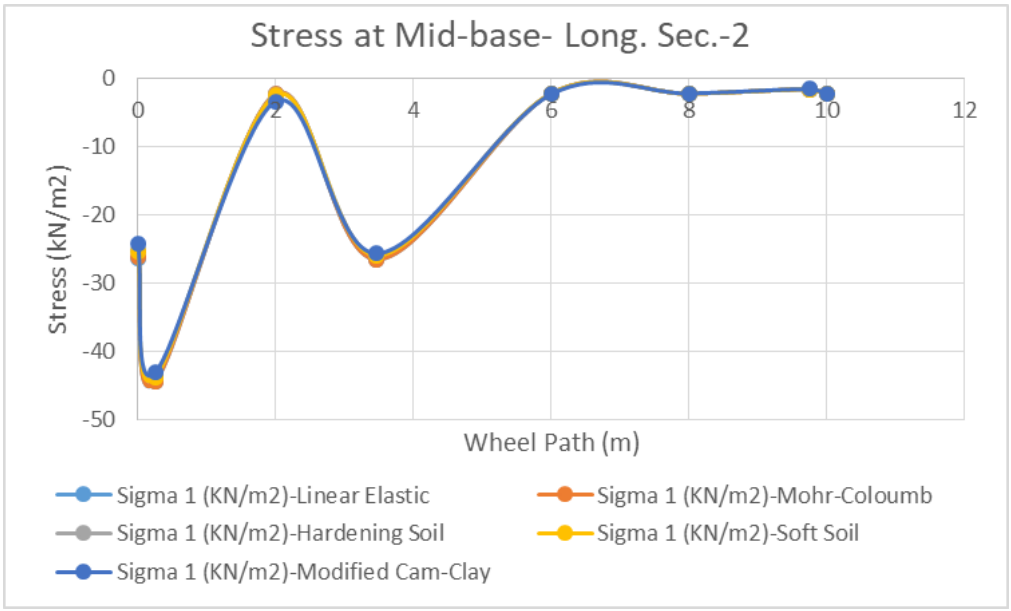

Figure 4.49 σ_1 Stress at Mid–base (Ford, 50 km/h, 1.0 m/s²), T–1, without Geogrid

Figure 4.49 shows the stress (Sigma 1) at the mid-base under the point load from a Ford Ranger 3.2 XLT in the longitudinal direction-2 on the road without geogrid reinforcement, at a speed of 50 km/h and an acceleration of 1.0 m/s². The percentage changes in stress are

as follows: Mohr-Columb (MC) 0.03%, Hardening Soil (HS) 0.09%, Soft Soil (SS) 0.15%, and Modified Cam-Clay (MCC) 4.23%. When compared to the Linear Elastic (LE) method, all methods (MC, HS, SS, and MCC) show relatively close results, with the changes in stress being similar across the different models, though MCC shows a slightly larger deviation.

Figure 4.50 shows the stress (Sigma 1) at the mid-base under the point load from a Ford Ranger 3.2 XLT in the transverse direction-1 on the road without geogrid reinforcement, at a speed of 50 km/h and an acceleration of 1.0 m/s². The percentage changes in stress are as follows: Mohr-Columb (MC) 0.32%, Hardening Soil (HS) 32.67%, Soft Soil (SS) 32.22%, and Modified Cam-Clay (MCC) 63.21%. When compared to the Linear Elastic (LE) method, the MC method shows the smallest change in stress, while the results for HS and SS are quite close to each other. MCC shows the largest deviation, indicating a significantly higher increase in stress compared to the other methods.

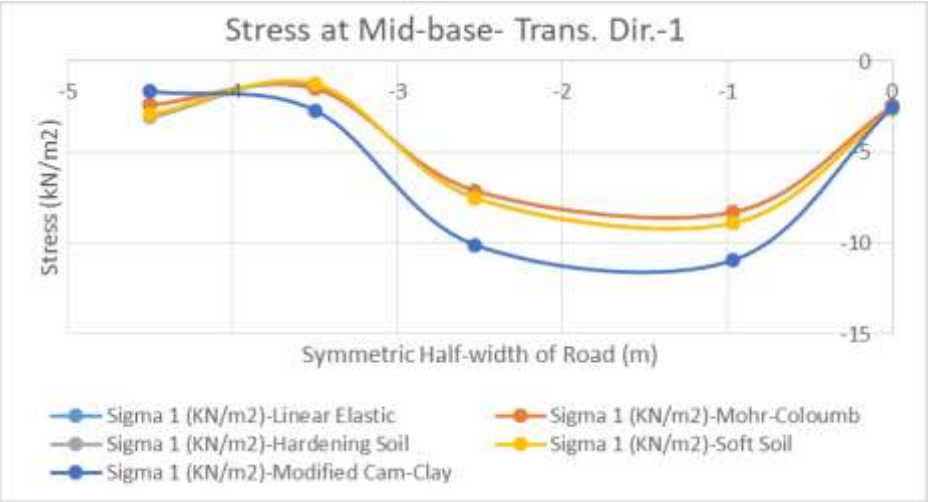

Figure 4.50 σ_1 Stress at Mid–base (Ford, 50 km/h, 1.0 m/s²), L–1, without Geogrid

Figure 4.51 shows the stress (Sigma 1) at the mid-base under the point load from a Ford Ranger 3.2 XLT in the longitudinal direction-1 on the road without geogrid reinforcement, at a speed of 50 km/h and an acceleration of 1.0 m/s². The percentage changes in stress are as follows: Mohr-Columb (MC) 0.03%, Hardening Soil (HS) 0.09%, Soft Soil (SS) 0.15%, and Modified Cam-Clay (MCC) 4.18%. When compared to the Linear Elastic (LE) method, all methods (MC, HS, SS, and MCC) show relatively small changes in stress, with MC and

HS exhibiting very similar results. The differences across all methods are minimal, with MCC showing a slightly larger deviation but still relatively close.

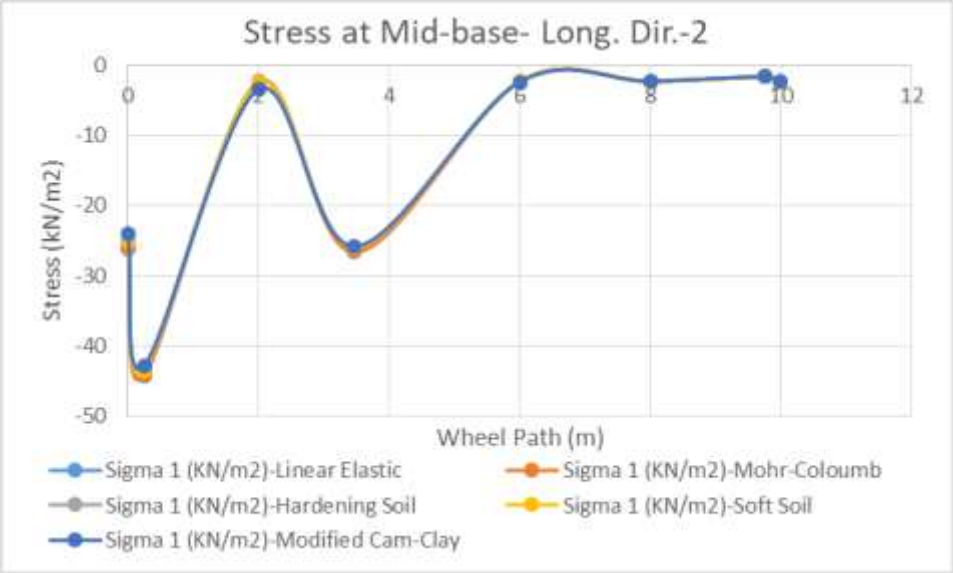

Figure 4.51 Stress at Mid–base (Truck, 50 km/h, 1.0 m/s²), T–1, with Geogrid

4.3 Acceleartion vs Deaccelertaion modelling

In the analysis of acceleration vs. deceleration with geogrid reinforcement, the stress at the mid-base under a point load from a Tata Truck 1613c was evaluated in two directions. Figure 4.81 shows the stress in the transverse direction-1 of the road, while Figure 4.82 focuses on the longitudinal direction-2. Both figures present the results at a speed of 50 km/h with an acceleration of 1.0 m/s².

The results indicate that the geogrid reinforcement plays a crucial role in mitigating stress concentrations under acceleration, as the stresses are notably reduced compared to scenarios without geogrid reinforcement. In both directions, the application of geogrid significantly improves stress distribution, preventing high stress accumulation at the mid-base. This demonstrates that geogrid reinforcement helps to better manage dynamic loading conditions, especially during acceleration, by spreading out the forces more effectively (Figure 4.52 and Figure 4.53).

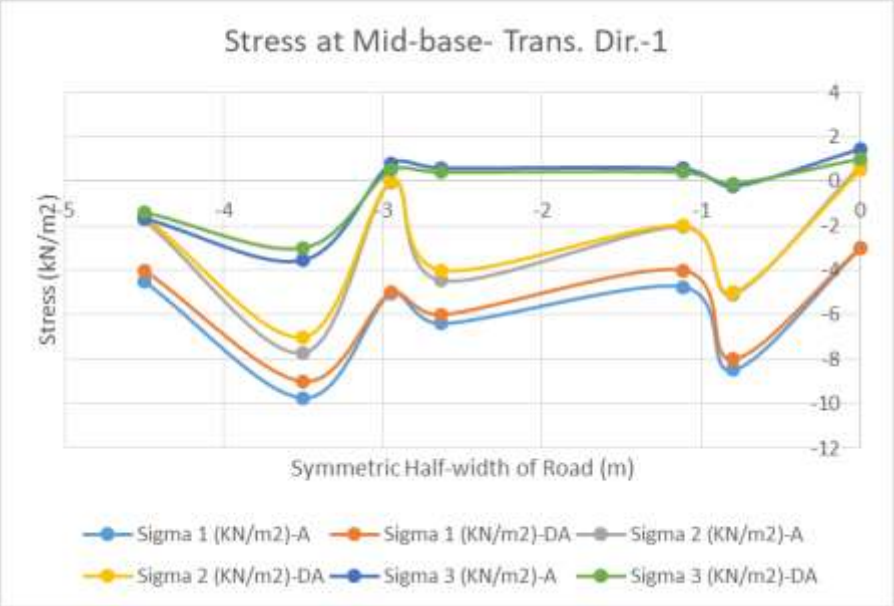

Figure 4.52 Stress at Mid–base (Truck, 50 km/h, 1.0 m/s²), L–2, with Geogrid

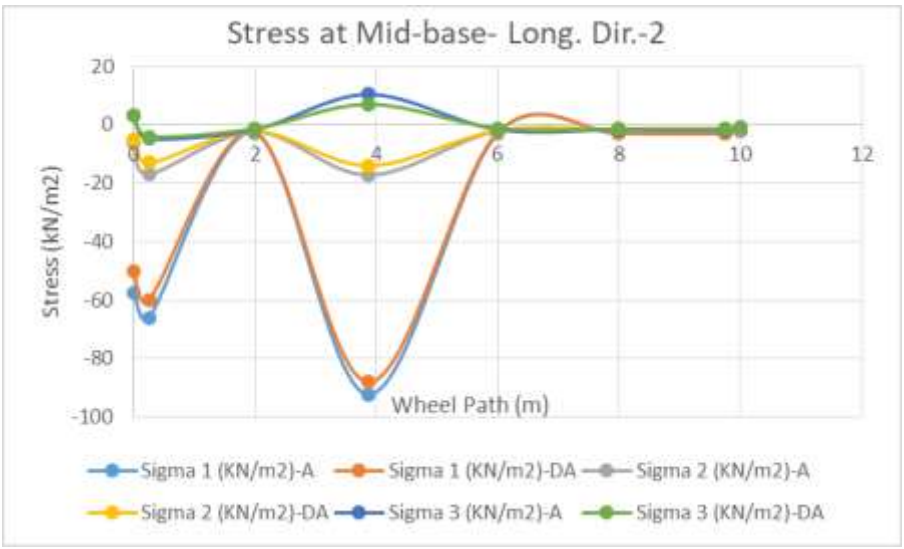

Figure 4.53 SLR vs CBR % at Mid-base (Truck, 50 km/h, 1.0 m/s²), with/without Geogrid

Figure 4.52 shows the stress at the mid-base under the point load from a Tata Truck 1613c in the transverse direction-1 on the road with geogrid reinforcement, at a speed of 50 km/h and an acceleration of 1.0 m/s². The percentage reduction in stress due to acceleration and deceleration for Sigma-1, Sigma-2, and Sigma-3 are respectively: 6.91, 11.82, and 30.94. Figure 4.53 shows the stress at the mid-base under the point load from a Tata Truck 1613c in the longitudinal direction-2 on the road with geogrid reinforcement, at a speed of 50 km/h and an acceleration of 1.0 m/s². The percentage reduction in stress due to acceleration

and deceleration for Sigma-1, Sigma-2, and Sigma-3 are respectively: 7.76, 16.53, and 17.85. The notation A and DA respectively indicates acceleration and de-acceleration.

4.4 Percentage Changes in Stress-strain for Pavement Mitigation

Based on the data from the field measurements and numerical computations, the geogrid significantly reduced both stress and displacement in the mid-base layer, particularly under dynamic loading conditions. In both static and dynamic cases, the geogrid consistently showed a decrease in displacement and stress compared to conditions without geogrid. For example, under static conditions, the Ford Ranger showed a displacement reduction of -1.74% (field) and -1.94% (numerical), and the Tata Truck Tipper showed reductions of -1.73% (field) and -2.70% (numerical). When subjected to dynamic conditions at 50 km/h, the displacement reduction increased to -3.30% (field) and -3.15% (numerical) for the Ford Ranger, and -3.85% (field) and -4.15% (numerical) for the Tata Truck Tipper. These improvements in stress and displacement highlight the geogrid's role in mitigating structural deficiencies and surface distresses by enhancing pavement stability under various loading conditions. The results show that geogrid reinforcement significantly improves pavement performance, with more pronounced effects observed at higher vehicle speeds and under dynamic loading conditions (Table 4.2-4.6). The detailed sheets of stress points and computational results are provided in Appendix H.

Table 4.2 Field Measurement Summary (Mid–base Layer)

Condition	Compressive Stress (%)	Tensile Stress (%)	Compressive Strain (%)	Tensile Strain (%)
Geogrid (vs. No Geogrid)	-9.38%	-10.71%	-10.45%	4.30%
6-wheel Load (vs. 4-wheel)	7%	6.50%	5%	5.70%
Undrained vs Drained	5%	4%	4.50%	5%
Point Load vs Area Load	12.50%	10%	10%	9.50%

Table 4.3 Numerical Computation Summary (Mid–base Layer)

Condition	Compressive Stress (%)	Tensile Stress (%)	Compressive Strain (%)	Tensile Strain (%)
Geogrid (vs. No Geogrid)	-11.43%	-9.09%	-13.23%	5.50%
6-wheel Load (vs. 4-wheel)	8%	7%	6%	6.30%
Undrained vs Drained	6%	-10%	6.50%	5.30%
Point Load vs Area Load	15%	12%	13%	11%

Table 4.4 Comparison of Field and Numerical Stress (Mid–base Layer)

Condition	Compressive Stress (%) (Field - Numerical)	Tensile Stress (%) (Field - Numerical)
Geogrid (vs. No Geogrid)	(-9.38% - (-11.43%)) = 2.05%	(-10.71% - (-9.09%)) = -1.62%
6-wheel Load (vs. 4-wheel)	(7% - 8%) = -1%	(6.50% - 7%) = -0.50%
Undrained vs Drained	(5% - 6%) = -1%	(4% - (-10%)) = 14%
Point Load vs Area Load	(12.50% - 15%) = -2.50%	(10% - 12%) = -2%

Table 4.5 Comparison of Field and Numerical Strain (Mid–base Layer)

Condition	Compressive Strain (%) (Field - Numerical)	Tensile Strain (%) (Field - Numerical)
Geogrid (vs. No Geogrid)	(-10.45% - (-13.23%)) = 2.78%	(4.30% - 4.30%) = 0%
6-wheel Load (vs. 4-wheel)	(5% - 6%) = -1%	(5.70% - 6%) = -0.30%
Undrained vs Drained	(4.50% - 6.50%) = -2%	(5% - 6%) = -1%
Point Load vs Area Load	(10% - 13%) = -3%	(9.50% - 13%) = -3.50%

Table 4.6 Summary of Percentage Change in Stress and Deformation

Vehicle Type	Load Type	Speed (km/h)	Strain Change (%)	Stress Change (%)	Field/ Numerical
Ford Ranger	Point Load	Static	-1.74% (Field), -1.94% (Numerical)	-0.47% (Field), -0.80% (Numerical)	Field / Numerical

Tata Truck Tipper	Point Load	Static	-1.73% (Field), -2.70% (Numerical)	-1.25% (Field), -1.26% (Numerical)	Field / Numerical
Ford Ranger	Point Load	15 km/h	-2.25% (Field), -2.15% (Numerical)	-1.60% (Field), -1.50% (Numerical)	Field / Numerical
Tata Truck Tipper	Point Load	15 km/h	-2.58% (Field), -2.77% (Numerical)	-1.88% (Field), -2.00% (Numerical)	Field / Numerical

Note:

Plus (+) means increase (stress or displacement is higher).

Minus (–) means decrease (stress or displacement is lower).

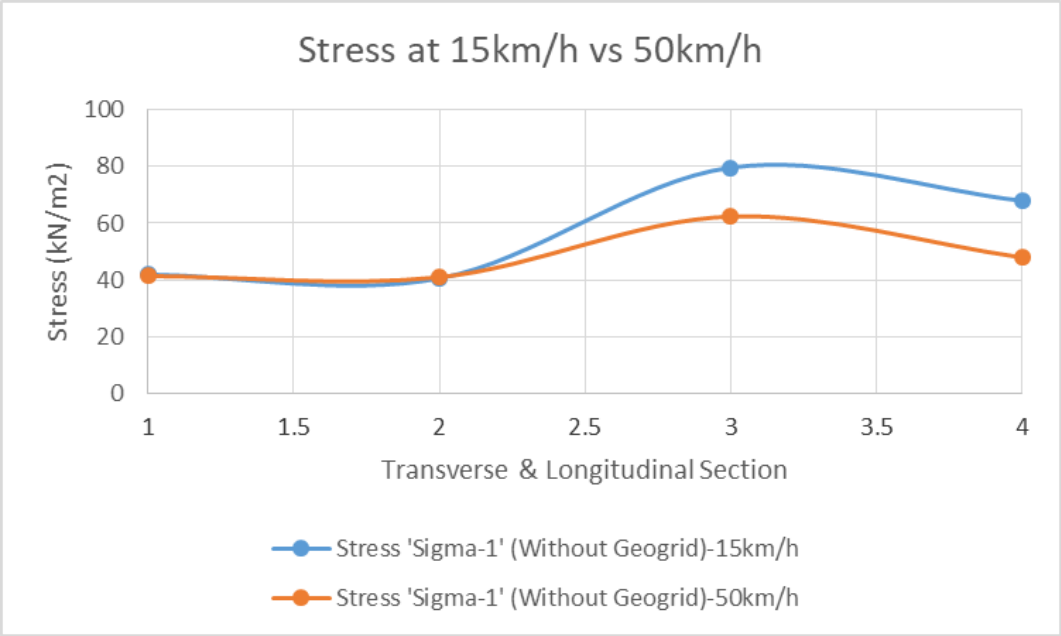

Figure 4.54 σ_1 Variation (Transverse & Longitudinal, with Geogrid)

Figures 4.54 and 4.55 show the variation of principal stress (σ_1) in both transverse and longitudinal directions for cases without and with geogrid reinforcement, respectively. In the absence of geogrid, the stress at higher speeds is observed to be lower. However, in the geogrid-reinforced case, the stress values exhibit both higher and lower extremes. This variation may be attributed to the membrane effect of the geogrid, which influences the stress distribution within the pavement structure.

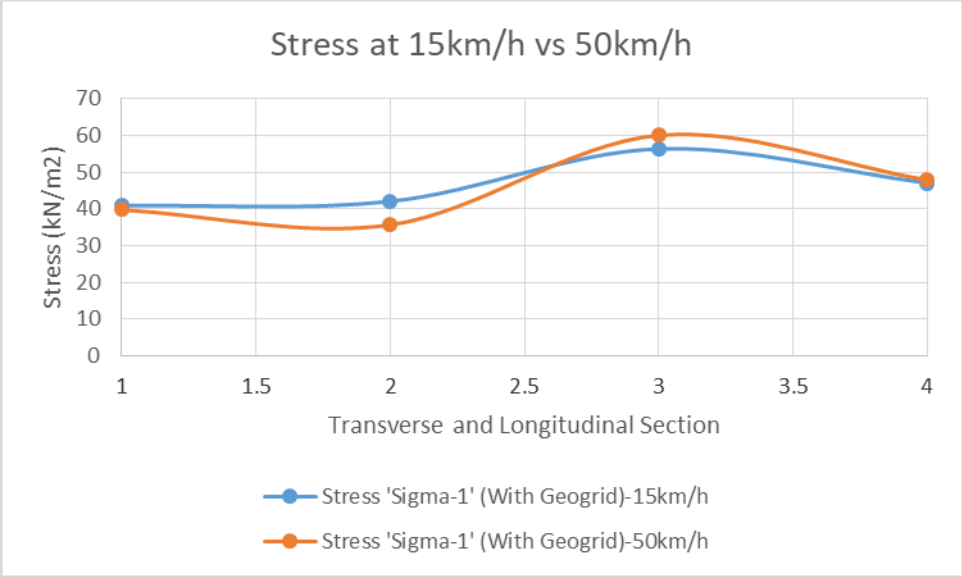

Figure 4.55 σ_1 Variation (Transverse & Longitudinal, without Geogrid)

4.5 Rutting and Fatigue Life of Pavements, and Service Life Ratio

The rutting and fatigue life of pavement has been evaluated by considering various factors and relationships as outlined in IRC: 37-2018. The results indicate a significant improvement in both rutting and fatigue life with the inclusion of geogrid reinforcement. For the analysis, a 20 mm rutting criterion was initially adopted based on linear elastic modeling using IITPAVE software. Similarly, fatigue failure was considered to occur when 20% of the pavement area developed interconnected cracks. Both performance criteria showed noticeable enhancement with the use of geogrids. The Pavement rutting and fatigue analysis is done and correlate this with service life ratio (SLR)

- Rutting Life: Rutting is primarily a serviceability issue caused by plastic deformation in the subgrade, sub-base, or asphalt layer. For pavements designed for 5 MSA and a 10-year design life, rutting is generally expected to remain within acceptable limits (typically ≤20 mm) during the first 4–6 years, depending on asphalt mix design, construction quality, and environmental conditions. According to IRC:37-2018, rutting failure may begin around 40–60% of the pavement life in medium MSA roads, particularly in cases of poor compaction or weak subgrade conditions (i.e., low CBR values). Figure 4.56 illustrates the variation in rutting life with respect to subgrade CBR values ranging from 5–15%, for both unreinforced and reinforced pavements. As shown in Figure 4.58, rutting failure is more critical at lower CBR percentages.

- Fatigue Life: Fatigue cracking occurs due to repetitive tensile strain at the bottom of the asphalt layer. For a 10-year, 5 MSA design, fatigue failure typically becomes critical during years 6–10. It depends on factors such as asphalt layer thickness and annual traffic loading. The AASHTO Pavement Design Guide (1993) and IRC:37-2018 provide fatigue life equations based on tensile strain and cumulative load repetitions. The variation in fatigue life with respect to subgrade CBR values ranging from 5–15% is shown in Figure 4.57. As indicated in Figure 4.59, fatigue failure tends to be more critical at higher CBR percentages.

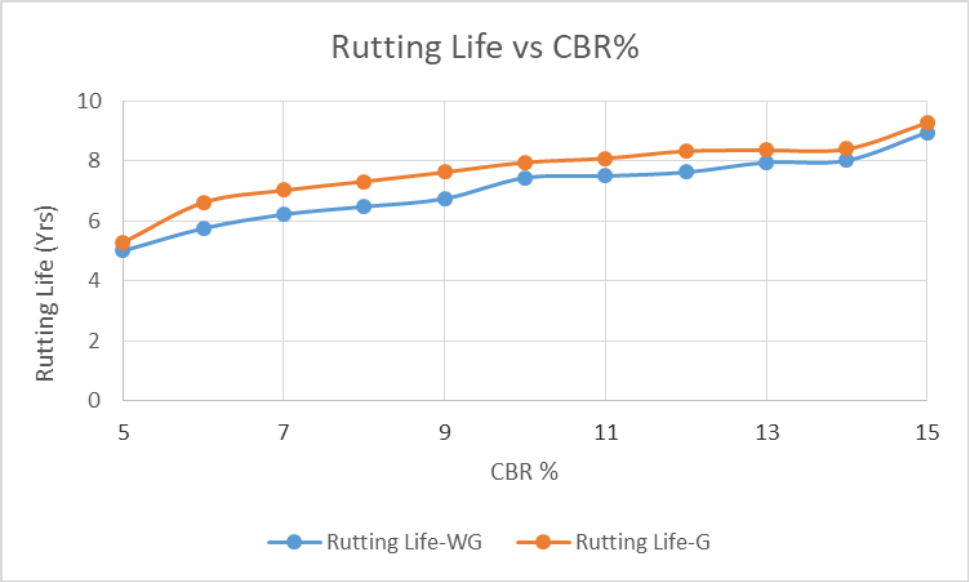

Figure 4.56 Rutting Life vs. Subgrade CBR%

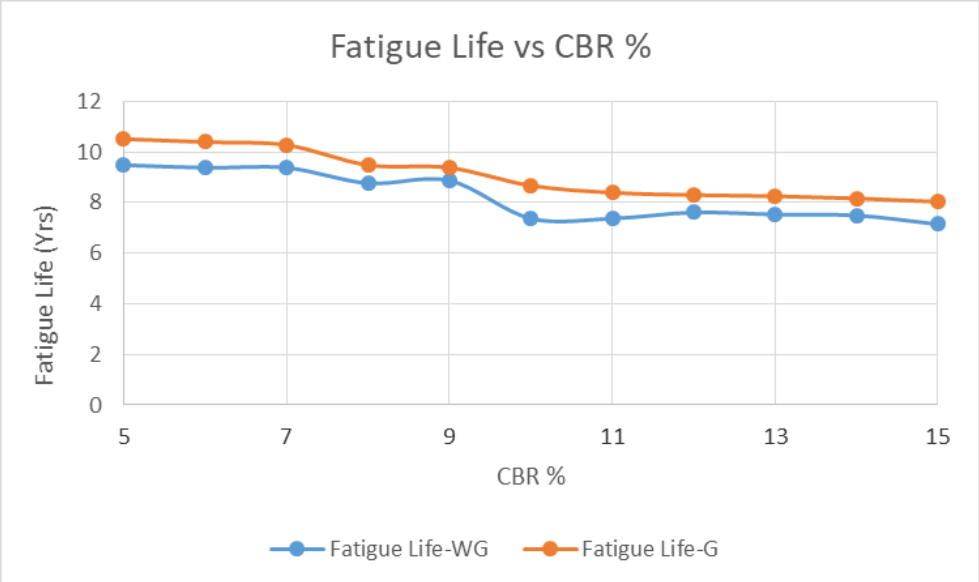

Figure 4.57 Fatigue Life vs. Subgrade CBR%

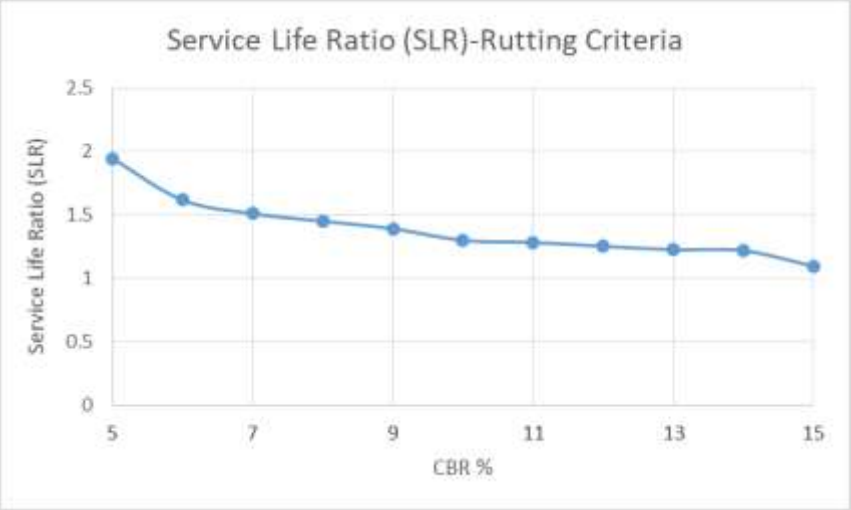

Figure 4.58 SLR vs. Subgrade CBR% (Rutting Criteria)

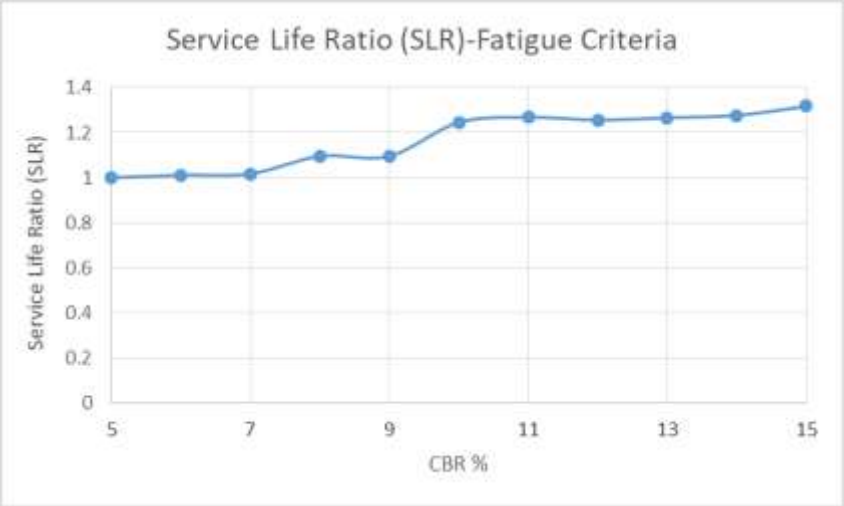

Figure 4.59 SLR vs. Subgrade CBR% (Fatigue Criteria)

The Service Life Ratio (SLR) evaluates the improvement in pavement durability by comparing performance before and after reinforcement, based on empirical relationships for rutting and fatigue failure criteria, while maintaining consistent pavement thickness. It is calculated as the ratio of vertical compressive strain at the top of the subgrade in the unreinforced state to that after reinforcement, indicating the extent of durability enhancement. Key Findings are as follows:

- ***SLR and CBR***: As CBR increases, SLR decreases, showing geogrid reinforcement's effectiveness in pavements with weaker subgrades.
- ***SLR and Traffic Load***: SLR increases with higher traffic loads, highlighting geogrid reinforcement's ability to enhance durability under increased traffic.

CHAPTER 5: CONCLUSION AND RECOMMENDATION

5.1 Conclusion

This study examined the effectiveness of the Biaxial 40/40Q Tensar geogrid (k=800 kN/m) in improving pavement performance, particularly in enhancing stress and deformation distribution across various pavement layers. A comprehensive analysis of both field measurements and numerical computations under different loading conditions (static and dynamic) revealed several important conclusions:

- Geogrid reinforcement significantly enhanced pavement performance by reducing stress concentrations and deformation in both base and subgrade layers under static and dynamic loading. Numerical and field results were closely aligned, with slight over-predictions of stress reductions by 0.5–3.3%. In comparison of field vs numerical results at constant speed (15 km/h), stress was 30.00 kN/m² (field) vs 33.00 kN/m² (numerical), showing a 10% difference. Displacement was 0.00129 m (field) vs 0.0009303 m (numerical), showing a 27.88% difference. Area load cases provided more even stress distribution than point loads. Pavement response varied with speed: at 50 km/h, the contact time was shorter, resulting in lower stress and deformation, though the geogrid's membrane effect altered this load distribution. Seasonal moisture fluctuations increased subgrade stress by up to 15.8% (field) and 14.5% (numerical), but geogrid remained effective in reducing stress even in wet conditions. These findings emphasize the geogrid's role in improving pavement durability across varying load types, speeds, and field scenarios.
- Model validation using both stress and deformation criteria demonstrated strong agreement with field data for subgrade soil. Based on stress prediction, the Soft Soil model performed best (0.91% deviation), while for deformation, the Hardening Soil model was most accurate (1.08% deviation). When considering both criteria together, these two models showed the closest alignment with field results. The Linear Elastic model, though simpler, also provided reasonably close results (10% stress, 27% deformation) and is considered equally applicable for general analysis. The Mohr-Coulomb model showed moderate agreement (6.93% stress, 43.67% deformation), whereas the Cam-Clay model exhibited significant deviations (18.5%

stress, 187% deformation), making it less suitable. Notably, all models effectively captured pavement behavior under both acceleration and deceleration conditions. This evaluation was conducted specifically for the subgrade soil layer

- Geogrid reinforcement substantially improved the fatigue and rutting life of pavements, especially in subgrades with low CBR values (5–9%), where structural support is most critical. In such cases, pavement life extended by 1 to 2 years on average compared to unreinforced sections. Although benefits were also noted in higher CBR subgrades (10–15%), the gains were relatively less due to the stronger inherent support. Service Life Ratio (SLR) analysis showed that rutting failure dominates at low CBR, whereas fatigue failure becomes critical at higher CBR. These findings emphasize that CBR-based pavement design, when combined with geogrid reinforcement, leads to longer-lasting and more resilient road structures.

5.2 Recommendation

Based on the study, the following recommendations for optimizing geogrid use in pavement design are:

- It is important to account for stress distributions from multi-axle and two-way vehicles, particularly in high-traffic areas, to enhance pavement performance.
- The use of geogrids with higher stiffness could help in reducing peak stresses, thereby improving durability under dynamic loading conditions.
- Seasonal moisture changes should be factored in, and incorporating soil-moisture models could help in addressing variations in subgrade stiffness.
- Long-term monitoring of geogrid performance would provide valuable insights, allowing for further refinement of pavement designs under diverse conditions.

REFERENCES

Abedi, M., Fangueiro, R., Correia, A. G., & Shayanfar, J., 2023, "Smart Geosynthetics and Prospects for Civil Infrastructure Monitoring: A Comprehensive and Critical Review", *Sustainability*, vol. 15(12), pp. 9258. https://doi.org/10.3390/su15129258.

Abu-Farsakh, M. Y., & Chen, Q., 2011, "Evaluation of Geogrid Base Reinforcement in Flexible Pavement Using Cyclic Plate Load Testing", *International Journal of Pavement Engineering*, vol. 12(3), pp. 275-288. https://doi.org/10.1080/10298436.2010.549565.

Abu-Farsakh, M., Hanandeh, S., Mohammad, L., & Chen, Q., 2016, "Performance of Geosynthetic Reinforced/Stabilized Paved Roads Built Over Soft Soil under Cyclic Plate Loads", *Geotextiles and Geomembranes*, pp. 1-9. https://doi.org/10.1016/j.geotexmem.2011606.009.

Adlinge, S. S., & Gupta, A. K., 2018, "Pavement Deterioration and its Causes", IOSR *Journal of Mechanical & Civil Engineering (IOSR-JMCE)*, pp. 9–15.

Agbelele, K. J., Agossou, D. Y., Zevounou, C., Otenia, B. J., Soglo, O. M. E., & Koudoro, J. B., 2023, "Geosynthetic Reinforcement: A Strategy for Preventing Deformation of Flexible Pavements on Unstable Ground", *International Journal of Research and Review*, vol. 10(12), pp. 32.

Ahirwara, S. K., & Mandal, J. N., 2017, "Finite Element Analysis of Flexible Pavement with Geogrids", *Procedia Engineering*, vol. 189, pp. 411-416. https://doi.org/10.1016/j.proeng.2017.05.065.

Ahmed, M., Mennatallah, A., Hussain, S., Khedr, S., Breakah, T., Saudy, M., Elkadi, O., & Abou-Zeid, M., 2018, "Geogrid Reinforcement in Flexible Paved Roads", Fredericton, Canada, June 13–16.

Al-Shamaa, M. F. K., Sheikha, A. A., Karkush, M. O., Jabbar, M. S., & Al-Rumaithi, A. A., 2021, "Numerical Modeling of Honeycombed Geocell Reinforced Soil", in M. O. Karkush & D. Choudhury (Eds.), *Modern Applications of Geotechnical Engineering and Construction (Lecture Notes in Civil Engineering 112)*, Springer Nature. https://doi.org/10.1007/978-981-15-9399-4_22.

Al Qurishee, M., 2017, "Application of Geosynthetics in Pavement Design", *International Research Journal of Engineering and Technology (IRJET)*, vol. 4(7), pp. 1-2.

Al-Qadi, I. L., Dessouky, S. H., Kwon, J., & Tutumluer, E., 2012, "Geogrid-Reinforced Low-Volume Flexible Pavements: Pavement Response and Geogrid Optimal Location", *Journal of Transportation Engineering*, vol. 138(9), pp. 1083–1090.

Al-Qadi, I., Brandon, T., et al., 1994, "Laboratory Evaluation of Geosynthetic-Reinforced Pavement Sections", Experts.Illinois.Edu. Retrieved from https://experts.illinois.edu/en/Publications/laboratory-evaluation-of-geosynthetic-einforced.

Akel, N., Stoltz, G., Wautier, A., Nicot, F., & Touze, N., 2025, "Rate-Dependent Tensile Response of Polyvinyl Chloride Geomembranes", *Geotextiles and Geomembranes*, vol. 53, pp. 445–456. https://doi.org/10.1016/j.geotexmem.2024.11.004.

Alimohammadi, H., Schaefer, V.R., Zheng, J., & Li, H., 2021, "Performance Evaluation of Geosynthetic Reinforced Flexible Pavement: A Review of Full-Scale Field Studies", *International Journal of Pavement Research and Technology*, vol. 14, pp. 30–42. https://doi.org/10.1016/j.ijprt.2020.07.003.

Alkawaaz, N. G. A., AL-Badran, Y. M., & Muttashar, Y. H., 2017, "Evaluation of Geogrid-Reinforced Flexible Pavement System Based on Soft Subgrade Soils Under Cyclic Loading", *Civil and Environmental Research*, vol. 9(12).

Al-Qadi, I. L., Dessouky, S., Tutumluer, E., & Kwon, J., 2011, "Geogrid Mechanism in Low-Volume Flexible Pavements: Accelerated Testing of Full-Scale Heavily Instrumented Pavement Sections", *International Journal of Pavement Engineering*, vol. 12(2), pp. 121–135. https://doi.org/10.1080/10298436.2010.535534.

Al Qurishee, M., 2017, "Application of Geosynthetics in Pavement Design", *International Research Journal of Engineering and Technology (IRJET)*, vol. 4(7), pp. 2395-0056.

Appea, A. K., 1997, "In-Situ Behavior of Geosynthetically Stabilized Flexible Pavement", *Master's Thesis*, Virginia Polytechnic Institute and State University.

Attoh-Okine, N. O., Ayenu-Prah, A. Y., & Mensah, S. A., 2005, "Monitoring the Performance of Geosynthetic Materials Within Pavement Systems Using MEMS", in Smart Structures and Materials 2005: *Smart Structures and Integrated Systems* (pp. 527-538), SPIE. https://doi.org/10.1117/12.603578.

Banerjee, S., Srivastava, M. V. K., Manna, B., & Shahu, J. T., 2022, "A Novel Approach to the Design of Geogrid-Reinforced Flexible Pavements", *International Journal of Geosynthetics and Ground Engineering*, vol. 8(29). https://doi.org/10.1007/s40891-022-00373-3.

BharatBenz, 2020, "Body Building Guidelines", BharatBenz, Heavy Truck Manufacturer in India. Retrieved from https://www.bharatbenz.com/trucks/tipper-trucks-1.

Bazine, R., Abdessemed, M., Kenai, S., & Ouadah, N., 2024, “Experimentation and Numerical Analysis of the Influence of Geogrids with Emulsion Insertion on the Behavior of Bituminous Pavements - Case of Ouargla Aerodrome”, *Mater. Construcc.*, vol. 74(353), e339. https://doi.org/10.3989/mc.2024.355723.

Benmebarek, S., Remadna, M. S., & Belounar, L., 2013, “Numerical Modeling of Reinforced Unpaved Roads by Geogrid”, *TOJSAT*: The Online Journal of Science and Technology, vol. 3(2).

Behiry, A. E. A., 2012, “Fatigue and Rutting Lives in Flexible Pavement”, Ain Shams *Engineering Journal*, vol. 3(3), pp. 367–374. https://doi.org/10.1016/j.asej.2012.04.008.

Bazine, R., Abdessemed, M., Kenai, S., & Ouadah, N., 2024, “Experimentation and Numerical Analysis of the Influence of Geogrids with Emulsion Insertion on the Behavior of Bituminous Pavements - Case of Ouargla Aerodrome”, Mater. Construcc., vol. 74(353), e339. https://doi.org/10.3989/mc.2024.355723.

Behiry, A. E. A., 2012, “Fatigue and Rutting Lives in Flexible Pavement”, Ain Shams Engineering Journal, vol. 3(3), pp. 367–374. https://doi.org/10.1016/j.asej.2012.04.008.

Bhutta, S. A., 1998, "Mechanistic-Empirical Pavement Design Procedure for Geosynthetically Stabilized Flexible Pavements" (*Doctoral dissertation*, Virginia Polytechnic Institute and State University). UMI Number: 3065425.

Brandon, T. L., Al-Qadi, I. L., Bhutta, S. A., et al., 1996, "Construction and Instrumentation of Geosynthetically Stabilized Secondary Road Test Sections", *Journal of Transportation Engineering*, vol. 1534(1). https://doi.org/10.1177/0361198196153400108.

Calvarano, L. S., Palamara, R., Leonardi, G., & Moraci, N., 2021, "3D-FEM Analysis on Geogrid Reinforced Flexible Pavement Roads", *IOP Conference Series: Earth and Environmental Science*, vol. 738, 012040. https://doi.org/10.1088/1755-1315/738/1/01204.

Chahan, S. J., Patel, A., Prajapati, B., & Kanojia, N., 2017, "Literature Review on Types of Flexible Pavement Failures", IJSRD - *International Journal for Scientific Research & Development*, vol. 5(2), pp. 145.

Canestrari, F., & Ingrassia, L. P., 2020, "A Review of Top-Down Cracking in Asphalt Pavements: Causes, Models, Experimental Tools and Future Challenges", *Journal of Traffic and Transportation Engineering (English Edition)*, vol. 7(5), pp. 541–572. https://doi.org/10.1016/J.JTTE.2020.08.002.

Chatti, K., Manik, A., Salama, H., El Mohtar, C., & Lee, H. S., 2009, "Effect of Michigan Multi-Axle Trucks on Pavement Distress: Volume II – Flexible Pavements", Final Report, Project RC-1504, *Pavement Research Center of Excellence*, Michigan State University.

Chatti, K., & Yun, K. K., 1995, "Dynamic Analysis of Multi-Layered Pavement Systems under Moving Loads", *SAE Transactions*, vol. 104(2), pp. 568-574.

Chou, Y. T., & Larew, H. G., 1980, "Stresses and Displacements in Viscoelastic Pavement Systems under a Moving Load", *Journal of Engineering Mechanics*, vol. 106(4), pp. 805-820.

Chua, B. T., & Nepal, K. P., 2023, "Numerical Modelling and Predicting Performance of Geogrid-Reinforced Low-Volume Unpaved Roads Over Soft Subgrades", *International Journal of Pavement Research and Technology*. https://doi.org/10.1007/s42947-023-00389-6.

Correia, N. S., & Zornberg, J. G., 2016, "Mechanical Response of Flexible Pavements Enhanced with Geogrid-Reinforced Asphalt Overlays", *Geosynthetics International*, vol. 23(3), pp. 183–193. https://doi.org/10.1680/jgein.15.00041.

Deep, P., Andersen, M. B., Rasmussen, S., Thom, N., Marradi, A., & Presti, D. L., 2020, "Evaluation of Load Transfer in Rigid Pavements by Rolling Wheel Deflectometer and Falling Weight Deflectometer", *Transportation Research Procedia*, vol. 45, pp. 376–383. https://doi.org/10.1016/j.trpro.2020.03.029.

Dhule, S. B., Valunjkar, S. S., Sarkate, S. D., & Korrane, S. S., 2011, "Improvement of Flexible Pavement with Use of Geogrid", *Bund. C, EJGE*, vol. 16, pp. 1-7.

Ekwulo, E. O., & Eme, D. B., 2014, "Fatigue and Rutting Strain Analysis of Flexible Pavements Designed Using CBR Methods", *Advanced Journal of Environmental Science and Technology*, vol. 5(3), pp. 001-010.

Gillespie, T. D., Karamihas, S. M., Cebon, D., Sayers, M. W., Nasim, M. A., Hansen, W., & Ehsan, N., 1992, "Effects of Heavy Vehicle Characteristics on Pavement Response and Performance: Final Report (Project 1-25(1))", National Cooperative Highway Research Program, Transportation Research Board, National Research Council.

Gillespie, T. D., Karamihas, S. M., Sayers, M. W., Nasim, M. A., Hansen, W., Ehsan, N., & Cebon, D., 1993, "Effects of Heavy-Vehicle Characteristics on Pavement Response and Performance", National Cooperative Highway Research Program Report 353, Transportation Research Board, National Research Council.

Government of Nepal, Ministry of Physical Planning and Works, Planning and Design Branch, 2011, "Preparation of Detailed Project Report of Puspalal (Mid-Hill) Highway Project", Final Report, Tech Studio of Engineering, Dillibazar, Kathmandu, Nepal.

Geosolutionsinc, 2025 https://www.geosolutionsinc.com/blog/what-are-geogrids.html (Assessed on, June 1st, 2025)

Giroud, J. P., & Noiray, L., 1981, “Geotextile reinforced unpaved road design”. *Journal of the Geotechnical Engineering Division, ASCE,* 107, 1233-1254.

Gu, F., Luo, X., Luo, R., Lytton, R. L., Hajj, E. Y., Siddharthan, R. V., 2016, "Numerical Modeling of Geogrid-Reinforced Flexible Pavement and Corresponding Validation Using Large-Scale Tank Test", *Construction and Building Materials*, vol. 122, pp. 214–230. https://doi.org/10.1016/j.conbuildmat.2016.06.081.

Gu, F., Luo, X., Luo, R., Hajj, E. Y., & Lytton, R. L., 2017, "A Mechanistic-Empirical Approach to Quantify the Influence of Geogrid on the Performance of Flexible Pavement Structures", *Transportation Geotechnics*, vol. 13, pp. 69–80. https://doi.org/10.1016/J.TRGEO.2017.08.005.

Güler, E., & Atalay, I., 2016, "The Effects of Geosynthetics on Mitigation of Rutting in Flexible Pavements", *E&E Congress 2016*, Prague, Czech Republic. https://dx.doi.org/10.14311/EE.2016.101.

Han, B., 2019, "Investigating the Reinforcement Effect of Geogrids in Flexible Pavements", PhD diss., University of Tennessee. https://trace.tennessee.edu/utk_graddiss/5794.

Han, J., & Bhandari, A., 2011, "The Influence of Geogrid Aperture Size on the Behavior of Reinforced Granular Bases", *in Geomechanics and Geotechnics: From Micro to Macro* (pp. 683–687), Taylor & Francis Group.

Harish, G. R., Ali, J., & Patil, K. D., 2018, "Design of Flexible Pavements Using Geogrid Reinforcement", *Proceedings of National Conference on Application of Geo-synthetics in Ports, Waterways, and Coasts*.

Haas, R., Walls, J., & Carroll, R. G., 1988, "Geogrid Reinforcement of Granular Bases in Flexible Pavements", *Transportation Research Record*, vol. 1188, pp. 84-93.

Howard, I., & Warren, K., 2005, "Improved Data Acquisition for Instrumented Flexible Pavements Reinforced with Geosynthetics", *Computing in Civil Engineering*, vol. 10.1061/40794(179)67. https://doi.org/10.1061/40794 (179)67.

Huang, M., Pokharel, S. K., Liu, M., & Lin, C., 2025, "Freeze-Thaw Impacts on Geocell-Stabilized Bases Considering Effects of Water Supply and Compaction", *Geotextiles and Geomembranes*, vol. 53, pp. 81–95. https://doi.org/10.1016/j.geotexmem.2024.09.002.

Huang, M., Liu, J., Pokharel, S. K., Dagenais, T., Chatterjee, A., & Lin, C., 2025, “Full-scale testing and monitoring of geosynthetics-stabilized flexible pavement in Alberta, Canada,” *Geotextiles and Geomembranes*, vol. 53, pp. 427–444. https://doi.org/10.1016/j.g

eotexmem.2024.11.003.

Hunter, R., 2017, "Disproving bottom-up fatigue cracking in well-constructed asphalt pavements," *Proceedings of the Institution of Civil Engineers - Construction Materials*, vol. 170, pp. 1–8. https://doi.org/10.1680/jcoma.16.00019.

Ibrahim, E. M., El-Badawy, S. M., Ibrahim, M. H., Gabr, A., & Azam, A., 2017, "Effect of geogrid reinforcement on flexible pavements," *Innovative Infrastructure Solutions*, vol. 2, no. 1. https://doi.org/10.1007/S41062-017-0102-7.

Imjai, T., Pilakoutas, K., & Guadagnini, M., 2018, "Performance of geosynthetic-reinforced flexible pavements in full-scale field trials," *Geotextiles and Geomembranes*, vol. 46, no. 6, pp. 1-13. https://doi.org/10.1016/j.geotexmem.2018.12.012.

Indian Roads Congress, 2019, IRC:SP:59-2019 Guidelines for Use of Geosynthetics in Road Pavements and Associated Works (First Revision), Indian Roads Congress, New Delhi.

Indian Roads Congress, 2018, IRC:37-2018 Guidelines for Design of Flexible Pavements (4th Revision), Indian Roads Congress.

Indian Roads Congress, 2019, IRC SP 59. Guidelines for the use of Geosynthetics in Road Pavement and Associated Works (First Revision), Indian Roads Congress.

Jawaharlal Nehru Technological University Anantapur, 2018, Usage of Geogrids in Flexible Pavement Design (Bachelor of Technology Thesis, Department of Civil Engineering), Pulivendula, Andhra Pradesh, India.

Jie, H. & Anil, B, 2011. "The influence of geogrid aperture size on the behavior of reinforced granular bases", *Geomechanics and Geotechnics : From Micro to Macro*, pp 683–687

Juraszek, J., Gwóźdź-Lasoń, M., & Logoń, D., 2021, "FBG strain monitoring of a road structure reinforced with a geosynthetic mattress in cases of subsoil deformation in mining activity areas," *Materials*, vol. 14, no. 7, 1709. https://doi.org/10.3390/ma14071709.

Kaleem, M. A., & Reddy, N., 2023, "Analysis of advanced pavement using geo-synthetic material," *International Research Journal of Modernization in Engineering Technology and Science*, vol. 5, no. 2, pp. 1945.

Kalyan, M. P., & Krishna, S. V. R. B. P., 2022, "Use of geogrids in flexible pavement design," *Journal of Engineering Sciences*, vol. 13, no. 08, ISSN: 0377-9254.

Karim, C., & Kyong, K. Y., 1995, "Dynamic analysis of multi-layered pavement systems under moving loads," *SAE Transactions, Journal of Commercial Vehicles*, vol. 104, pp. 568–574.

Katahira & Engineers International, in association with Full Bright Consultancy (Pvt.) Ltd., 2015, Road Transport Safety and Axle Load Control Study in Nepal: Review and Assessment of Vehicle Overloading Fines and Payment Modalities, Ministry of Physical Infrastructure and Transport, Government of Nepal.

Khadka, A., Rijal, S., Thapa, R., Khanal, S., & Shah, U. K., 2021, "Geogrid for road construction in Nepal," *Journal of Earthquake Science and Soil Dynamics Engineering*, vol. 4, no. 3, pp. 1-7.

Khan, S., Nagabhushana, M. N., Tiwari, D., & Jain, P. K., 2013, "Rutting in flexible pavement: An approach of evaluation with accelerated pavement testing facility," *Procedia - Social and Behavioral Sciences*, vol. 104, pp. 149–157. https://doi.org/10.1016/J.SBSPRO.2013.11.107.

Khoueiry, N., Briançon, L., Riot, M., & Daouadji, A., 2021, "Full-scale laboratory tests of geosynthetic reinforced unpaved roads on a soft subgrade," *Geosynthetics International*, vol. 28, no. 1, pp. 1-14. https://doi.org/10.1680/jgein.21.00001.

Kim, H.-J., Corsino Jr., V. A., Park, T.-W., & Kim, T.-E., 2025, "Analytical model and stress behavior of consolidated load-bearing geotextile tubes," *Geotextiles and Geomembranes*, vol. 53, pp. 55–69. https://doi.org/10.1016/j.geotexmem.2024.09.003.

Leng, J., & Gabr, M. A., 2002, "Characteristics of geogrid-reinforced aggregate under cyclic load," *Transportation Research Record*, vol. 1786, no. 1, pp. 29–35. https://doi.org/10.3141/1786-04.

Lehn, J., Moormann, C., & Aschrafi, J., 2016, "Numerical investigations on the load distribution over the geogrid of a basal reinforced piled embankment under cyclic loading," *Procedia Engineering*, vol. 143, pp. 435–444. Advances in Transportation Geotechnics 3. 3rd International Conference on Transportation Geotechnics (ICTG 2016).

Leonardi, G., & Suraci, F., 2022, "A 3D-FE model for the rutting prediction in geogrid reinforced flexible pavements," *Sustainability*, vol. 14, 3695. https://doi.org/10.3390/su14063695.

Ling, H. I., & Liu, Z., 2001, "Performance of geosynthetic-reinforced asphalt pavements," *Journal of Geotechnical and Geoenvironmental Engineering*, vol. 127, no. 2, pp. 177–184. https://doi.org/10.1061/(ASCE)1090-0241(2001)127:2(177).

Liu, J., Pan, J., Wang, B., Hu, C., & Liu, Q., 2024, "Study on the shear and deformation characteristics of geogrid-reinforced gravelly soils based on large-scale triaxial tests," *Frontiers in Earth Science*, vol. 12, 1287718. https://doi.org/10.3389/feart.2024.1287718.

Mamatha, K. H., & Dinesh, S. V., 2017, "Performance evaluation of geocell-reinforced pavements," *International Journal of Geotechnical Engineering*, vol. 11, no. 4, pp. 361-370. https://doi.org/10.1080/19386362.2017.1343988.

Manzoor, M. A., & Akram, W., 2023, "Design of flexible pavement using geo textiles and geo grid," *European Chemical Bulletin*, vol. 12, Special Issue 5, pp. 5016-5030. https://doi.org/10.48047/ecb/2023.12.si5a.0412.

Markiewicz, A., Koda, E., & Kawalec, J., 2022, "Geosynthetics for filtration and stabilisation: A review," *Polymers*, vol. 14, no. 24, 5492. https://doi.org/10.3390/polym14245492.

Moghaddas-Nejad, F., & Small, J. C., 1996, "Geogrid Reinforcement in Flexible Pavements," *Journal of Transportation Engineering*, vol. 122, no. 6, pp. 468–474.

Moayedi, H., Kazemian, S., Prasad, A., & Huat, B. B. K., 2009, "Effect of geogrid reinforcement location in paved road improvement," *Electronic Journal of Geotechnical Engineering*, vol. 14, Bund. P. EJGE.

Mojtahedi, M., & Marandi, S., 2017, "Prediction of geogrid-reinforced flexible pavement performance using artificial neural network approach," *Journal of Road Materials and Pavement Design*, https://doi.org/10.1080/14680629.2017.1302357.

Mshali, M. R. S., & Steyn, W. JvdM., 2022, "Effect of truck speed on the response of flexible pavement systems to traffic loading," *International Journal of Pavement Engineering*, vol. 23, no. 4, pp. 1213–1225. https://doi.org/10.1080/10298436.2020.1797733.

Nader, G., & Sharbaf, M., 2016, "Use of GEOGRID for Strengthening and Reducing the Roadway Structural Sections," Effectiveness of Geotextiles/Geogrids in Roadway Construction; Determine a Granular Equivalent (GE) Factor: Final Report, prepared by Hossein Alimohammadi, Vernon R. Schaefer, Junxing Zheng, Charles T. Jahren, and Guangfan Zheng, Department of Civil, Construction, and Environmental Engineering and the Institute for Transportation, Iowa State University, Ames, Iowa. Published by Minnesota Department of Transportation.

Nader, G., & Sharbaf, M., 2016, "Use of GEOGRID for Strengthening and Reducing the Roadway Structural Sections," Minnesota Department of Transportation.

Nik Daud, N. N., Jalil, F. N. A., Celik, S., & Albayrak, Z. N. K., 2019, "The important aspects of subgrade stabilization for road construction," IOP Conference Series: *Materials Science and Engineering*, vol. 512, no. 1. https://doi.org/10.1088/1757-899X/512/1/012005.

Ojha, K. N., 2018, "Overloading and Pavement Service Life—A Case Study on Narayanghat-Mugling Road, Nepal," *Journal of Transportation Technologies*, vol. 8, pp. 343-356. https://doi.org/10.4236/jtts.2018.84019.

Paiva, L., Pinho-Lopes, M., Paula, A. M., & Valente, R., 2024, "3D Numerical Modeling of Geosynthetics for Soil Reinforcement: A Bibliometric Analysis and Literature Review," *Geotechnics*, vol. 4, pp. 673–692. https://doi.org/10.3390/geotechnics4020036.

Panta, L. and Tiwari, R.C., 2024, "Study on Geogrid Reinforced Flexible Pavement Sections," Proceedings of the 12th IOE Graduate Conference, Proceedings of the 14th IOE Graduate Conference.

Patel, Gopi, et al., 2019, "Flexible Pavement Design Using Geo-Synthetic Material," *International Research Journal of Engineering and Technology (IRJET)*, vol. 6, no. 4, pp. 3546.

Pawar, Pranoti V., & Sinha, Madhulika, 2021, "Review on Geogrid Application in Flexible Pavement," *International Research Journal of Engineering and Technology* (IRJET), vol. 8, no. 4, pp. 3493.

Perkins, S. W., 2001, "Numerical modelling of geosynthetic reinforced flexible pavements," Montana Department of Transportation, https://rosap.ntl.bts.gov/view/dot/44038.

Perkins, S. W., 1999, "Geosynthetic Reinforcement of Flexible Pavement Laboratory-Based Pavement Test Section (FHWA MT-99-001/8138)," Final Report, Montana Department of Transportation.

Perkins, S. W., 2004, "Numerical modeling of geosynthetic reinforced flexible pavements," Montana Department of Transportation.

Perkins, S. W., 2006, "Mechanical Response of Geosynthetic-Reinforced Flexible Pavements," *Geosynthetics International*, vol. 13, no. 3, pp. 157-171. https://doi.org/10.1680/gein.6.0157.

Perkins, S. W., & Lapeyre, J. A., 1996, "Instrumentation of a Geosynthetic-Reinforced Flexible Pavement System," *Transportation Research Record*, vol. 1596, pp. 41-48. https://doi.org/10.3141/1596-05.

Poudel, A. and Tiwari, R.C., 2023, "Numerical Study on Geogrid-Reinforced Flexible Pavement Sections," *Proceedings of the 12th IOE Graduate Conference*, Peer Reviewed, ISSN 2350-8914 (Online), 2350-8906 (Print)

Powell, W. D., Potter, J. F., Mayhew, H. C., & Nunn, M. E., 1984, The Structural Design of Bituminous Roads (TRRL Laboratory Report 1132), Transport and Road Research Laboratory, Department of Transport, Crowthorne, Berkshire.

Prakash, K. K., & Rathod, D., 2024, "Role of Geogrids and Geofoams as Interlayers in Pavement Foundation System: A Review," *International Journal of Pavement Research and Technology*, https://doi.org/10.1007/s42947-024-00475-3.

Pratapa, M., & Raj, A. S. N., 2021, "Design of flexible pavements by using geo-grids," *International Journal of Research Publication and Reviews*, vol. 2, no. 3, pp. 200-207.

Qamhia, I. I. A., & Tutumluer, E., 2021, "Evaluation of Geosynthetics Use in Pavement Foundation Layers and Their Effects on Design Methods (FHWA-ICT-21-020)," Illinois Center for Transportation, https://doi.org/10.36501/0197-9191/21-025.

Qian, Y., Han, J., Pokharel, S. K., & Parsons, R. L., 2013, "Performance of triangular aperture geogrid-reinforced base courses over weak subgrade under cyclic loading," *Journal of Materials in Civil Engineering*, vol. 25, no. 8, pp. 1013–1021. https://doi.org/10.1061/(ASCE)MT.1943-5533.0000577.

Qian, Y., Tutumluer, E., & Huang, H., 2011, "A validated discrete element modeling approach for studying geogrid-aggregate reinforcement mechanisms," *Geo-Frontiers* 2011, pp. 4653–4662. https://doi.org/10.1061/41165(397)476.

Rababah, S., Aldeeky, H., Qasrawi, H., & Al Hattamleh, O., 2020, "Performance of subgrade soil stabilized with by-product recycled mill scale and cementitious materials," *International Journal of Pavement Engineering*, https://doi.org/10.1080/10298436.2020.1766686.

Research and Training Unit (RTU), 2024, "Research and Development of Geosynthetics Application for Road Pavement," Submitted by the Research and Training Unit (RTU), Department of Civil Engineering, Pulchowk Campus, to the Quality of Research and Development Centre (QRDC), Department of Roads, Ministry of Physical Infrastructure and Transport, Government of Nepal, Chakupat, Lalitpur, April 30, 2024.

Saad, B., Mitri, H., & Poorooshasb, H., 2006, "3D FE analysis of flexible pavement with geosynthetic reinforcement," *Journal of Transportation Engineering*, vol. 132, no. 5, pp. 402-415. https://doi.org/10.1061/(ASCE)0733-947X(2006)132:5(402).

Sharbaf, M. R., 2016, "Laboratory Evaluation of Geogrid-Reinforced Flexible Pavements," Master's thesis, University of Nevada, Las Vegas.

Shields, M. K., Sprague, C. J., Gilbert, R. B., and Allen, S. R., 2004, "Bending Stiffness Index Test for Geogrid Reinforcement of Pavement Base Material", GSP 130 *Advances in Pavement Engineering*.

Siriwardane, H., Gondle, R., and Kutuk, B., 2010, "Analysis of Flexible Pavements Reinforced with Geogrids", *Geotechnical and Geological Engineering*, vol. 28, no. 3, pp. 255-267.

Tensar International Limited, 2019, "Tensar SS Geogrids Product Specifications and Aggregates in Construction of Structures such as Road Pavements, Working Platforms, and Reinforced Foundations", TN/SS spec, issued 26 November 2019 (Accessed on; January 1st, 2025)

Tensar International, 2020, "Installation Guideline for Tensar Biaxial Geogrid at the Subgrade/Subbase Interface (IG/Biaxial_Geogrid)" (Accessed on; January 1st, 2025)

Tensar International, 2021, "Geogrids Solutions", accessed at: https://www.tensarinternational.com/solutions/geogrids (Accessed on; January 1st, 2025)

Textile Blog, 2021, "Geogrid Types, Structures, and Installation", accessed at: https://www.textileblog.com/geogrid-types-structures-installation/ (Accessed on; January 1st, 2025)

U.S. Army Engineer Waterways Experiment Station, 1992, "Correlation between California Bearing Ratio (CBR) and Dynamic Plate Load Index (DPI)", Technical Report, U.S. Army Corps of Engineers, Vicksburg, MS.

Vamos, M. J., and Szendefy, J., 2024, "Determination of Permanent Deformations of Non-Cohesive Soils in Pavement Structures under Repeated Traffic Load", *Engineering*, vol. 5, pp. 1067-1084, https://doi.org/10.3390/eng5020058.

Vakili, A., Salimi, M., and Shamsi, M., 2021, "Application of the Dynamic Cone Penetrometer Test for Determining the Geotechnical Characteristics of Marl Soils Treated by Lime", *Heliyon*, vol. 7, e08062, https://doi.org/10.1016/j.heliyon.2021.e08062.

Wathugala, G. W., Huang, B., and Pal, S., 1996, "Numerical Simulation of Geosynthetic-Reinforced Flexible Pavements", *Transportation Research Record*, vol. 1534, no. 1, pp. 58–65, https://doi.org/10.1177/0361198196153400109.

Wang, D., Wang, S.-L., Tighe, S., Bhat, S., and Yin, S., 2023, "Construction of Geosynthetic–Reinforced Pavements and Evaluation of Their Impacts", *Applied Sciences*, vol. 13, 10327, https://doi.org/10.3390/app131810327.

Wang, W., Zhang, C., Guo, J., Li, N., Li, Y., Zhou, H., and Liu, Y., 2019, "Investigation on the Triaxial Mechanical Characteristics of Cement-Treated Subgrade Soil Admixed with Polypropylene Fiber", *Applied Sciences*, vol. 9, no. 21, 4557, https://doi.org/10.3390/app9214557.

Wang, Y., Cui, X., Liu, K., and Jiang, P., 2022, "Manufacture, Development, and Application of Sensor-Enabled Geosynthetics: State-of-the-Art Review", *Intelligent Transportation Infrastructur*e, vol. 1, pp. 1–28, https://doi.org/10.1093/iti/liac012.

Wang, S., Zhou, H., Chen, X., Gong, M., Hong, J., and Shi, X., 2021, "Fatigue Resistance and Cracking Mechanism of Semi-Flexible Pavement Mixture", *Materials*, vol. 14, no. 18, 5277, https://doi.org/10.3390/ma14185277.

Wang, S.-L., Wang, D., Tighe, S., Bhat, S., and Yin, S., 2023, "Investigation of Rutting Performance in Geogrid-Reinforced Asphalt by Penetration Test", *Materials*, vol. 16, no. 22, 7221, https://doi.org/10.3390/ma16227221.

Warren, K. A., Christopher, B., and Howard, I. L., 2010, "Geosynthetic Strain Gage Installation Procedures and Alternative Strain Measurement Methods for Roadway Applications", *Geosynthetics International*, vol. 17, no. 6, pp. 403-430, https://doi.org/10.1680/gein.2010.17.6.403.

Warren, K. A., and Howard, I. L., 2007, "Sensor Selection, Installation, and Survivability in a Geosynthetic-Reinforced Flexible Pavement", *Geosynthetics International*, vol. 14, no. 5, pp. 298-308, https://doi.org/10.1680/gein.2007.14.5.298.

Wilde, W. J., 2014, "Assessing the Effects of Heavy Vehicles on Local Roadways: Final Report 2014-32", Center for Transportation Research and Implementation, Minnesota State University, Mankato, Minnesota Department of Transportation.

Wright, J., Kim, S. S., Durham, S. A., et al., 2019, "Utilization of Large-Scale Rolling-Wheel Tester to Investigate the Stress Reduction in Pavement Layers Due to the Use of Geosynthetic Materials", *Journal of Materials in Civil Engineering*, vol. 2673, no. 2, 0361198119827909, https://doi.org/10.1177/0361198119827909.

Wu, H., Yao, C., Li, C., Miao, M., Zhong, Y., Lu, Y., and Liu, T., 2020, "Review of Application and Innovation of Geotextiles in Geotechnical Engineering", *Materials*, vol. 13, no. 7, 1774.

Wulandari, P. S., and Tjandra, D., 2006, "Determination of Optimum Tensile Strength of Geogrid Reinforced Embankment", *Proceedings of the International Civil Engineering Conference* "Towards Sustainable Civil Engineering Practice", Surabaya, 25-26 August 2006.

Wu, C., Wang, H., Zhao, J., Jiang, X., Yanjun, Q., and Yusupov, B., 2020, "Prediction of Viscoelastic Pavement Responses under Moving Load and Nonuniform Tire Contact Stresses Using 2.5-D Finite Element Method", *Mathematical Problems in Engineering*, 2020, 1029089, https://doi.org/10.1155/2020/1029089.

Xiao, L., and Xue, J., 2024, "Effects of Subgrade Spatial Variability on Critical Strains and Effectiveness of Geogrid Reinforcement in Flexible Pavement", *Acta Geotechnica*, https://doi.org/10.1007/s11440-024-02326-8.

Yadav, P. M. G., Bharath, S., and Kumar, M. M., 2018, "Usage of Geogrids in Flexible Pavement Design", *International Journal of Engineering Sciences & Research Technology*, vol. 7, no. 3, pp. 120-126.

Yin, Z., Ndiema, K. M., Lekalpure, R. L., and Kiptum, C. K., 2022, "Numerical Study of Geotextile-Reinforced Flexible Pavement Overlying Low-Strength Subgrade", *Applied Sciences*, vol. 12, no. 20, 10325, https://doi.org/10.3390/app122010325.

Zhao, J., and Wang, H., 2020, "Dynamic Pavement Response Analysis under Moving Truck Loads with Random Amplitudes", *Journal of Transportation Engineering*, Part B: Pavements, vol. 146, no. 2, 04020020, https://doi.org/10.1061/JPEODX.0000173.

Zornberg, J. G., 2017, "Functions and Applications of Geosynthetics in Roadways", *Procedia Engineering*, vol. 189, pp. 298–306,

https://doi.www.maccaferri-usa.com (Accessed on; January 1st, 2025)

https://doi.org/10.1016/j.proeng.2017.05.048. (Accessed on; April 2nd, 2025)

https://cvbu.sipradi.com.np/vehicle/sk-1613-1 (Assessed on; April 2nd, 2025)

https://www.carexpert.com.au/ford/ranger/2021-xlt-32-4x4-4937f2f1 (Assessed on, April 2nd, 2025)

APPENDIX A: GeoDynamic Data Logger and Sensors with Working Procedure

Table A1 Details of Dynamic Data Logging system

S.N.	Equipment Name	Specifications
1	High speed Data Acquisition system 16 channels (GEO Dynamic Data-Logger/Controller) including GEODYNAMIC Amplifier for DAQ	No. of Analog Input channel: 16 Analog output: ±10 VDC Voltage from DC output amplifier through BNC connector DAQ type: 32-bit architecture Data sampling rate: 1 to 1000 SPS (Samples per sec.) No. of Digital Input channel: 4 no. No. of Digital Output channel: 4 no. System resolution [bits]: 24-bit On PC Display: On PC Safety features: Audio visual identity Data export facility: Excel / ASCII format Measurement accuracy: ±0.2% ±1-digit Class A Balance: Auto balancing with start command Calibration: Through PC using software Conversion time: <1ms/channel Mode of operation: Peak Hold or Normal Mode (Actual Values) Data Logging Modes: Record continuously at set Logging Interval, or manual through button Power supply: 200 to 250VAC ± 10%, 50 Hz. PC Interface: USB Weight [kg]: ~5 Enclosure: Rust free Metal Operating temperature: -40°C to 60°C. (-40°F to 140°F) Operating humidity: 90% relative humidity (non-condensing)

		Input connection: Removable Connector
2	Earth Pressure Cell (The strain type mini-earth pressure cell/gauge)	Range: Up to 20 MPa Resistance: 350 (Ω) Insulation Resistance: >200 (M Ω) Bridge: Full Resolution: ≤0.1 %F·S Over Load: 120% Size Dia.: 28mm, Height: 11mm Operational Temperature Range: -25 to 60 ºC
3	Strain Gauge Embedment	Input Resistance: 350Ω Nominal Output Resistance: 350Ω Nominal Sensitivity at 1000 με: ~1.3mV/V Nominal Excitation: 2-5 VDC Operating Temperature Range: -34° to 200° C Lead Wire: #22 AWG Truck-Weight Lead Wire
4	Capacitive Soil Moisture Sensor	Output: Analog Operating Voltage: 3.3 ~ 5.5 VDC Output Voltage: 0 ~ 3.0VDC Operating Current: 5mA

WORKING PROCUDURE

Field Instrumentation and Monitoring Procedure Using GeoDynamic Data Logger and sensors

Preparation and Setup:

Ensure all sensors (Earth Pressure, Strain Gauge, and Moisture Sensors) are calibrated.

Identify the critical position within the pavement structure for sensor placement, ensuring it captures relevant data from both geosynthetic-reinforced and non-reinforced sections.

Installation of Sensors:

Earth Pressure Cell: Install at the selected position beneath the pavement surface, typically in the subgrade layer, to measure vertical stresses due to vehicle load.

Strain Gauge: Embed the strain gauge within the base or subgrade layer at the same location to measure tensile strain resulting from traffic.

Moisture Sensor: Place in the subgrade layer to monitor any changes in moisture content.

GeoDynamic Data Logger Setup:

Connect all sensors to the GeoDynamic Data Logger using armored cables.

Set up the logger to capture real-time data during vehicle movement over the sensor position, with a sampling rate adjusted to project needs (typically between 1 and 1000 samples per second). It depends on the type of data logger.

Monitoring Procedure:

Record short-term data during vehicle movement to capture immediate changes in pressure, strain, and moisture at the selected position.

For long-term monitoring, configure the system to log data periodically (e.g., hourly or daily) to assess changes in pavement behavior over time.

Data Logging:

The GeoDynamic system logs earth pressure, strain, and moisture data from the sensor positions. The focus is on capturing the dynamic responses under vehicle loads.

Data Export and Analysis:

Export the logged data in Excel or ASCII format for analysis.

Compare the data from the geosynthetic-reinforced section with that from the non-reinforced section to evaluate performance.

APPENDIX B: Dynamic Cone Penetration Test (DCPT) Specifications and Working Procedure

Table B1 Details of Subgrade penetrometer (DCPT)

S.N.	Equipment Name	Specifications
1	Dynamic Cone Penetration Test (DCPT) for Subgrade Assessment Standard motor DCP DYNAMIC CONE PENETROMETER	Customized support: OEM, ODM, OBM Power: Electronic Hammer weight: 9kg Free fall height: 600±5/510±5mm adjustable Standard: AS1289.6.3.2 Product name: Standard motor DCP DYNAMIC CONE PENETROMETER Penetration rod: dia.16mm Single package size: 100X100X180 cm Single gross weight: 150.000 kg Package Type: packages suitable for export (Penetration rod: 10 Pcs DCP cone: 1 Pcs Perth penetrometer tip: 1 pcs Spare flexible shaft: 1 pcs Spanner: 2 pcs Manual rod extractor: 1 set)

WORKING PROCUDURE

Equipment Setup:

The DCPT apparatus consists of a steel cone, penetration rod, and hammer.

The steel cone should have a standard 60-degree tip angle with a base diameter of 20 mm.

The hammer weighs 9 kg (as per AS1289.6.3.2 standard), with a free-fall height adjustable between 600±5 mm and 510±5 mm.

The penetration rod has a diameter of 16 mm.

Ensure all equipment, including the rod extractor and spare parts, is properly assembled.

Test Location:

Choose an appropriate test location on the subgrade, ensuring it represents the overall condition of the area.

Clear the test area of any loose material or debris to provide a clean surface for the cone to penetrate.

Initial Preparation:

Place the penetration rod vertically, and insert the cone into the subgrade surface until the cone's base is flush with the ground.

Ensure that the setup is stable to begin accurate data collection from the start.

Penetration Process:

Drop the hammer from the fixed height (600 mm, adjustable within the specified limits) repeatedly to drive the cone into the subgrade.

Record the number of hammer blows required to achieve each 100 mm penetration increment.

Continue the test until you reach the desired depth, typically 800 mm, or until refusal (when penetration slows or halts).

Data Recording:

Record the number of blows required for each 100 mm of penetration.

For instance, log the blow counts for penetration depths of 100 mm, 200 mm, 300 mm, etc., until the target depth or refusal is reached.

Data Analysis:

Calculate the penetration rate (mm per blow) for every 100 mm increment.

Correlate the penetration resistance (number of blows) to the California Bearing Ratio (CBR) using established empirical relationships.

Result Interpretation:

The higher the number of blows per 100 mm of penetration, the stronger the subgrade, which correlates to a higher CBR value.

CBR values can be plotted against depth to analyze the variation of subgrade strength across the test depth.

The results are averaged or interpolated to determine the representative CBR value for the subgrade.

Reporting and Usage:

Report the CBR values obtained at various depths.

Use these values to inform pavement design decisions, ensuring appropriate pavement layer thickness based on the subgrade's strength.

APPENDIX C: Dynamic Cone Penetration Test (DCPT) Results

Table C1 DCPT results at Subgrade Layer for CH 1+700

No of Blow	Cumulative No of Blow	Divisions above ground	Cumulative Division penetration	Cumulative Penetration (mm)	Penetration (mm)	DCPI (No.)=Penetration	CBR (%)	Remarks
0	*0*	*30*	*0*	*0*	*0*	*0*	*0*	
5	*5*	*26.2*	*3.8*	*190*	*190*	*38*	*5*	Average CBR=4.93%
5	*10*	*22.1*	*7.9*	*395*	*205*	*41*	*4.5*	
5	*15*	*18.3*	*11.7*	*585*	*190*	*38*	*5*	
5	*20*	*15.2*	*14.8*	*740*	*155*	*31*	*6.2*	
5	*25*	*11.3*	*18.7*	*935*	*195*	*39*	*4.8*	
5	*30*	*7.4*	*22.6*	*1130*	*195*	*39*	*4.8*	
5	*35*	*3*	*27*	*1350*	*220*	*44*	*4.2*	
5	*40*	*3*	*27*	*1350*	*0*	*0*	*0*	

Table C2 DCPT results at Subgrade layer for 1+750CH

No of Blow	Cumulative No of Blow	Divisions above ground	Cumulative Division penetration	Cumulative Penetration (mm)	Penetration (mm)	DCPI (No.)=Penetration	CBR (%)	Remarks
0	*0*	*30*	*0*	*0*	*0*	*0*	*0*	
5	*5*	*27.5*	*2.5*	*125*	*125*	*25*	*7.9*	Average CBR=5.27%
5	*10*	*23.5*	*6.5*	*325*	*200*	*40*	*4.6*	
5	*15*	*19.2*	*10.8*	*540*	*215*	*43*	*4.3*	
5	*20*	*13.5*	*16.5*	*825*	*285*	*57*	*3.2*	
5	*25*	*9.1*	*20.9*	*1045*	*220*	*44*	*4.2*	
5	*30*	*6.3*	*23.7*	*1185*	*140*	*28*	*6.9*	
5	*35*	*3*	*27*	*1350*	*165*	*33*	*5.8*	
5	*40*	*3*	*27*	*1350*	*0*	*0*	*0*	

Table C3 DCPT results at Subgrade layer for 1+800CH

No of Blow	Cumulative No of Blow	Divisions above ground	Cumulative Division penetration	Cumulative Penetration (mm)	Penetration (mm)	DCPI (No.)=Penetration mm/blow	CBR (%)	Remarks
0	*0*	*30*	*0*	*0*	*0*	*0*	*0*	
5	*5*	*27.1*	*2.9*	*145*	*145*	*29*	*6.62*	Average CBR=5.08%
5	*10*	*24.2*	*5.8*	*290*	*145*	*29*	*6.62*	
5	*15*	*19.4*	*10.6*	*530*	*240*	*48*	*3.78*	
5	*20*	*13.6*	*16.4*	*820*	*290*	*58*	*3.06*	
5	*25*	*9.5*	*20.5*	*1025*	*205*	*41*	*4.54*	
5	*30*	*6.2*	*23.8*	*1190*	*165*	*33*	*5.77*	
5	*35*	*3.1*	*26.9*	*1345*	*0*	*0*	*0*	

Table C4 DCPT results at Subbase layer for 1+750CH (Mid-point of Sensors installation)

No of Blow	Cumulative No of Blow	Divisions above ground	Cumulative Division penetration	Cumulative Penetration (mm)	Penetration (mm)	DCPI (No.)=Penetration mm/blow	CBR (%)	Remarks
0	*0*	*20*	*0*	*0*	*0*	*0*	*0*	
5	*5*	*18.2*	*1.8*	*90*	*90*	*18*	*10.07*	Average CBR=34.55%
5	*10*	*16.2*	*3.8*	*190*	*100*	*20*	*17.02*	
10	*20*	*13.7*	*6.3*	*315*	*125*	*12.5*	*26.38*	
10	*30*	*12*	*8*	*400*	*85*	*8.5*	*21.95*	
10	*40*	*10*	*10*	*500*	*100*	*10*	*21.95*	
10	*50*	*8*	*12*	*600*	*100*	*10*	*47.54*	
10	*60*	*7*	*13*	*650*	*50*	*5*	*47.54*	
10	*70*	*6*	*14*	*700*	*50*	*5*	*47.54*	
10	*80*	*5*	*15*	*750*	*50*	*5*	*47.54*	
10	*90*	*4*	*16*	*800*	*50*	*5*	*84.48*	
10	*100*	*3.4*	*16.6*	*830*	*30*	*3*	*10.07*	
10	*110*	*3.4*	*16.6*	*830*	*0*	*0*	*0*	

Table C5 DCPT results at Base layer for 1+7500CH (Mid-point of Sensors installation)

No of Blow	Cumulative No of Blow	Divisions above ground	Cumulative Division penetration	Cumulative Penetration (mm)	Penetration (mm)	DCPI (No.)=Penetration mm/blow	CBR (%)	Remarks
0	*0*	*20*	*0*	*0*	*0*	*0*	*0*	
10	*10*	*18.8*	*1.2*	*60*	*60*	*6*	*38.66*	Average CBR=85.44%
10	*20*	*17.9*	*2.1*	*105*	*45*	*5*	*53.52*	
10	*30*	*17*	*3*	*150*	*45*	*4.5*	*53.52*	
10	*40*	*16.3*	*3.7*	*185*	*35*	*5*	*70.84*	
10	*50*	*15.6*	*4.4*	*220*	*35*	*4*	*70.84*	
10	*60*	*14.9*	*5.1*	*255*	*35*	*2.5*	*70.84*	
10	*70*	*14.3*	*5.7*	*285*	*30*	*2.5*	*84.52*	
10	*80*	*13.8*	*6.2*	*310*	*25*	*3.5*	*103.27*	
10	*90*	*13.3*	*6.7*	*335*	*25*	*2.5*	*103.27*	
10	*100*	*12.8*	*7.2*	*360*	*25*	*3*	*103.27*	
10	*110*	*12.4*	*7.6*	*380*	*20*	*1.5*	*133.51*	
10	*120*	*12.5*	*7.5*	*375*	*0*	*0*	*0*	

APPENDIX D: Geogrid & Geotextile Specifications

Woven Geotextile

This is a woven polypropylene geotextile containing heavy woven flat tape yarns and will meet the following Minimum Average Roll Values (MARV) when tested in accordance with the methods listed below. The geotextile is resistant to ultraviolet degradation and to biological and chemical environments normally found in soils.

It conforms to the property values listed below1 and is subject to internal 'Manufacturing Quality Control' (MQC) tests that meets the requirements set forth by AASHTO M288 (Geotextile Specification For Highway Application).

Table D1 Woven (Stabilization) Geotextile (Maccaferri, 2025)

PROPERTY4	TEST PROCEDURE	UNITS	MINIMUM AVERAGE ROLL VALUES (MARV)2
Mechanical			
Grab Tensile	ASTM D 4632	lb (kN)	315 (1.400)
Grab Elongation	ASTM D 4632	%	15
Trapezoidal Tear	ASTM D 4533	lb (kN)	115 (0.512)
Puncture (CBR)	ASTM D 6241	lb (kN)	900 (4.005)
Endurance			
UV Resistance	ASTM D 4355	% Retained @ 500 hrs.	70
Hydraulic			
Permittivity	ASTM D 4491	sec–1	0.05

Flow Rate	ASTM D 4491	gpm/ft2 (lpm/m2)	4 (163)
Apparent Opening Size (AOS)3	ASTM D 4751	US Sieve (mm)	40 (0.425)
Packaging (Typical)			
Roll Width	Measured	ft (m)	12.5 (3.81) / 15 (4.57) / 17.5 (5.33)
Roll Length	Measured	ft (m)	360 (109.73) / 432 (131.67) / 300 (91.5) / 360 (109.73) / 258 (78.6) / 309 (94.18)
Roll Area	Measured	yd2 (m2)	500 (418) / 600 (501)
Roll Weight	Calculated	lb (kg)	245 (111) / 270 (123)

Notes:

1. Values shown are in weaker principal direction. 'Minimum Average Roll Values' (MARV) are calculated as the typical minus two (2) standard deviations. Statistically, it yields a 97.7% degree of confidence that any sample taken from quality assurance testing will exceed the value reported.

2. AOS (ASTM D 4751) is a 'Maximum Opening Diameter Value'

3. Mullen Burst ASTM D 3786 and Puncture ASTM D 4833 have been removed. Neither test method is recognized by AASHTO M288. CBR Puncture ASTM D 6241 has replaced D4833, under AASHTO M288. Mullen Burst is not recognized by ASTMD35 committee on Geosynthetics.

Non-woven Geotextile

Geotextiles are mechanically bonded nonwovens from 100% ultra violet stabilized Polypropylene. They are characterized by a high resistance to installation damage, high

water permeability, resistance to ultraviolet degradation and to biological and chemical environments normally found in soils.

Table D2 Non-woven (Stabilization) Geotextile (Maccaferri, 2025)

Property	Test Std	Unit	MXC 10	MXC 20	MXC 30	MXC 40	MXC 50	MXC 60	MXC 70	MXC 80	MXC 90	MXC 100	MXC 110
Tensile Strength	ISO	kN/m	7.3	9.5	11	14	15	17	22	24	33	39	41
Tensile Elongation	ISO 10319	%	40	40	40	40	50	50	50	50	50	50	50
CBR Puncture	ISO	N	1150	1500	1700	2200	2350	2800	3500	4000	5350	6150	7150
Vertical water flow 50mm	ISO 11058	mm/s	125	110	105	80	75	70	58	48	40	35	30
Nominal mass	ISO	g/m2	110	130	150	190	210	240	300	350	500	600	700
Strength 2kPa	ISO 9863	mm	1.0	1.2	1.4	1.7	1.9	2.1	2.6	2.9	3.9	4.3	5.2
Grab strength	ASTM D	N	460	550	650	810	900	1000	1250	1430	2150	2800	3100
AOS	ASTM D	mm	0.31	0.27	0.26	0.23	0.21	0.20	0.19	0.18	<0.075	<0.075	<0.075

Permittivity	ASTM D	s-1	3.5	2.9	2.6	2.1	2.0	1.9	1.7	1.7	0.95	0.85	0.70
Form of supply													
Width		m	4	4	4	4	4	4	4	4	4	4	4
Length		m	250	250	225	200	175	125	125	100	65	55	45
Area		m2	1000	1000	900	800	700	500	500	400	260	200	180

Table D3 Geogrid specification (PP-type)

Geogrid

Secugrid® Q (PP)

NAUE GmbH & Co. KG
Gewerbestrasse 2
32339 Espelkamp-Fiestel
Germany
Phone:+49 5743 41-0 Fax: +49 5743 41-240
E-Mail: info@naue.com Internet: www.naue.com

Product description:
Laid geogrid made of stretched, monolithic polypropylene (PP) flat bars with welded junctions used for the reinforcement in many fields of civil engineering including landfill engineering, road construction and hydraulic engineering

Property	Test method*	Unit	20/20 Q1	30/30 Q1	40/40 Q1	60/60 Q1	80/80 Q1
Raw material	-	-	polypropylene (PP), white				
Mass per unit area	EN ISO 9864	g/m²	155	200	240	360	440
Max. tensile strength, md / cmd**	EN ISO 10319	kN/m	≥ 20 / ≥ 20	≥ 30 / ≥ 30	≥ 40 / ≥ 40	≥ 60 / ≥ 60	≥ 80 / ≥ 80
Elongation at nominal strength, md / cmd**	EN ISO 10319	%	≤ 7 / ≤ 7				
Tensile strength at 1% elongation, md / cmd**	EN ISO 10319	kN/m	4 / 4	6 / 6	8 / 8	12 / 12	16 / 16
Tensile strength at 2% elongation, md / cmd**	EN ISO 10319	kN/m	8 / 8	12 / 12	16 / 16	22 / 22	25 / 25
Tensile strength at 5% elongation, md / cmd**	EN ISO 10319	kN/m	16 / 16	24 / 24	32 / 32	48 / 48	50 / 50
Aperture size, md x cmd**	-	mm x mm	approx. 33 x 33	approx. 32 x 32	approx. 31 x 31	approx. 31 x 31	approx. 31 x 30
UV-resistance (remaining tensile strength)	EN 12224	%	95.0				
Weather resistance	FGSV	class	high				
Production specific elongation	-	%	0				
Roll dimensions, width x length	-	m x m	4.75 x 100				

APPENDIX E: Field Photographs

Figure E1 DCPT: At 1+700CH; At 1+800CH

Figure E2 Field data logging setup: At 1+700CH; At 1+800CH

APPENDIX F: Lab Photographs

Figure F1 CBR Sample Test Setup for Soil Samples Collected from 1+700CH and 1+800CH

Figure F2 CBR Sample Preparation: Sample Preparation in CBR Mound (Left Figure); Placement of Sample for 72 Hours of Saturation Prior to Testing (Right Figure)

Figure F3 Triaxial Test of Soil Samples Taken from 1+700CH and 1+800CH: Overall Setup (Left Figure); Placement of Soil Sample from 1+700CH (Right Figure)

Figure F4 Consolidation Test of Soil Samples Taken from 1+700CH and 1+800CH: Overall Setup (Left Figure); Placement of Soil Samples from 1+700CH and 1+800CH (Right Figure)

Figure F5 Unconfined Compression Test of Remolded Soil Samples Taken from 1+700CH and 1+800CH: Sample Extraction (Left Figure); Test Setup (Right Figure); Remolded Soil Samples (Bottom Middle Figure)

Figure F6 Direct Shear Tests of Soil Samples Taken from 1+700CH and 1+800CH: Overall Test Setup (Left Figure); Sample Preparation (Right Figure)

Figure F7 Hydrometer Test: Measurement taken (Left Figure); Sample Preparation (Right Figure)

Figure F8 Sieve Analysis: Mechanical shaking (Left Figure); Sample Preparation (Right Figure)

Figure F9 Specific Gravity Test: Sample Preparation (Left Figure); Dry in Sand Bath (Right Figure)

Figure F10 Casagrande Tests for LL and PL Tests: LL test (Left Figure); Soil sample preparation (Right Figure)

Figure F11 Constant Head Permeability Test: Taking test results Left Figure); Overall Test Setup (Right Figure)

APPENDIX G: Typical Lab Test Results

Consolidation Test Results (Sample 1)

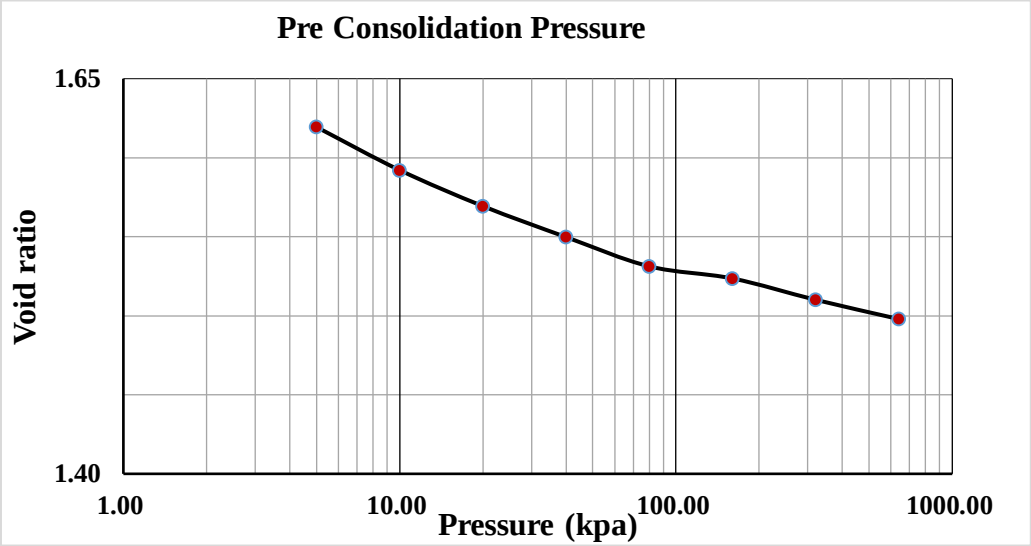

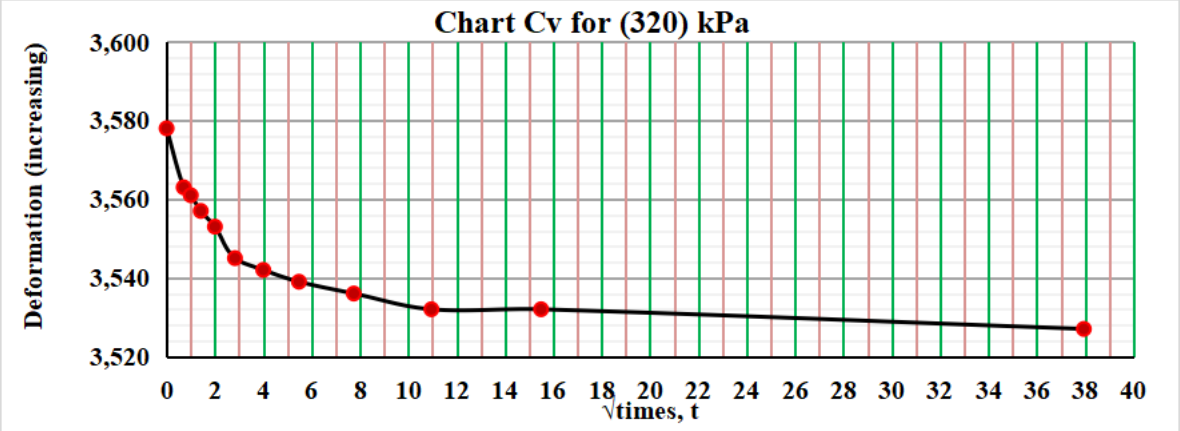

Cv for 320 kPa		
T90	0.848	
t90	9	
Hdr	0.9909	
Cv	0.09251518	cm2/min

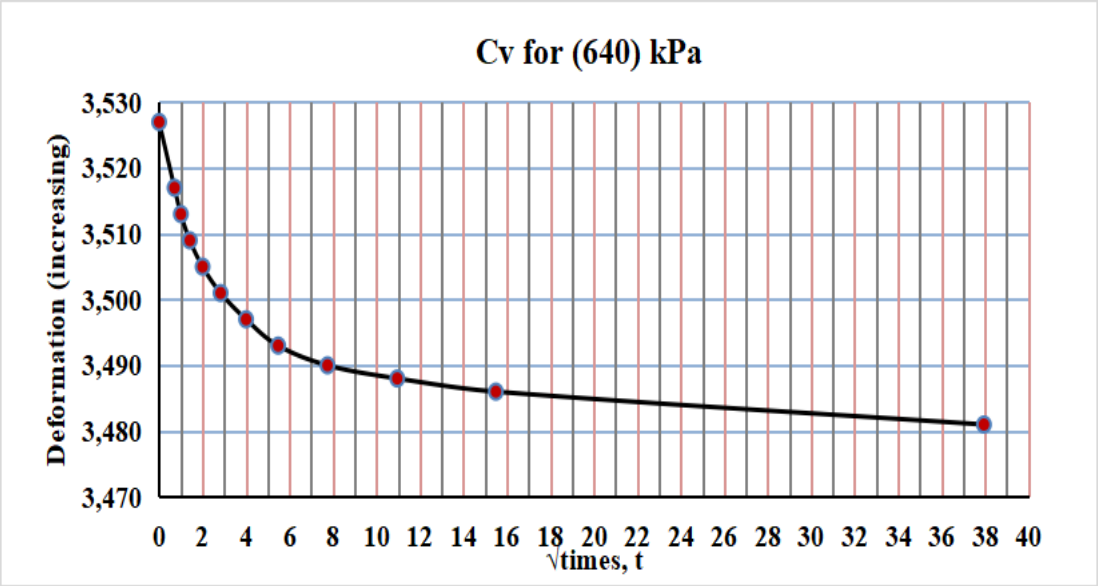

Cv for 640 kPa		
T90	0.848	
t90	4.84	
Hdr	0.9909	
Cv	0.17203236	cm2/min

Complete grain size distribution curve of Sample 1 of 1+700CH (Sieve analysis and Hydrometer Test)

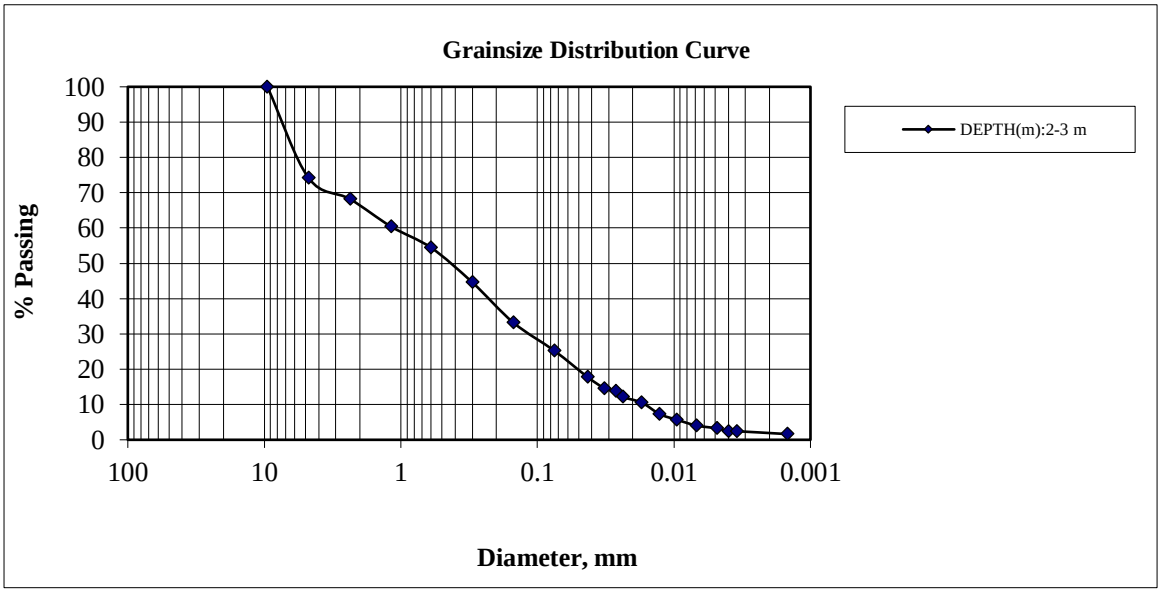

Direct Shear Test-1 (1+700CH)

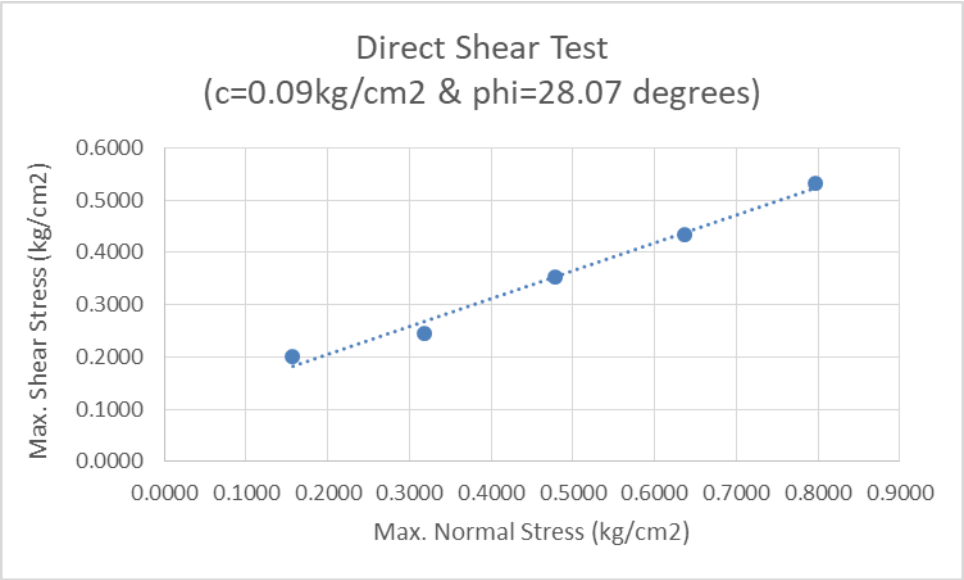

Soil Type: Sandy clay, silty sand

Direct Shear Test-1 (1+800CH)

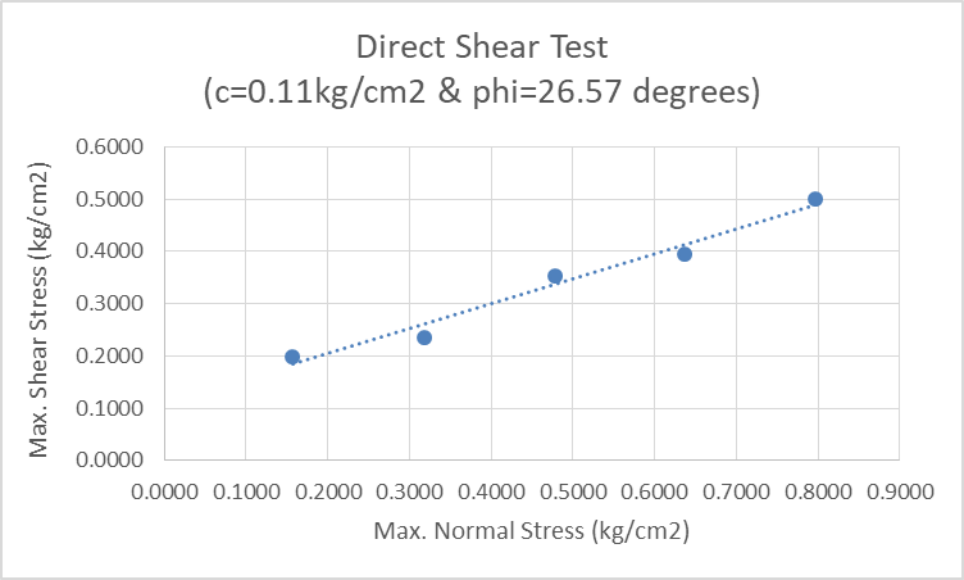

Soil Type: Sandy clay, silty sand

APPENDIX H: Typical Stress Point Data Sets

(Different than Nodal Points)

SP DATA SET 1: 1st-wheel position of 6-wheels considering Area load at v=15 speed and a=1.0m/sec2 (UNDRAINED AND DRAINED) at Subgrade

1) **Deformed Mesh**

   UNDRAINED CASE

   Max Value = 0.1065 m (At Node 25503)

   DRAINED CASE

   Max Value= 0.1080 m (At Node 25503)

2) **Total Displacement (u)**

   UNDRAINED CASE

   Max Value = 0.1065m (Element 23774 at Node 25503)

   DRAINED CASE

   Max Value= 0.1080 m (Element 23774 at Node 25503)

3) **Quality SICN**

   UNDRAINED CASE

   Max Value = 0.9975 (Element 31905)

   Min Value = 0.1629 (Element 16959)

   DRAINED CASE

   Max Value = 0.9975 (Element 31905)

   Min Value = 0.1629 (Element 16959)

4) **Cartesian Effective Stress sigma xx**

   UNDRAINED CASE

   Max Value = 1095 kN/m2 (Element 39615 at Node 1037)

   Min Value = -1154 kN/m2 (Element 40037 at Node 119)

   DRAINED CASE

   Max Value = 1096 kN/m2 (Element 39615 at Node 1037)

   Min Value = -1155 kN/m2 (Element 40037 at Node 119)

5) **Cartesian Effective Stress sigma yy**

   UNDRAINED CASE

   Max Value = 383.3 kN/m2 (Element 39615 at Node 1037)

Min Value = -507.5 kN/m2 (Element 40037 at Node 119)

DRAINED CASE

Max Value = 383.7 kN/m2 (Element 39615 at Node 1037)

Min Value = -507.9 kN/m2 (Element 40037 at Node 119)

6) Cartesian Effective Stress sigma zz

UNDRAINED CASE

Max Value = 169.1 kN/m2 (Element 22253 at Node 6462)

Min Value = - 355.0 kN/m2 (Element 35822 at Node 435)

DRAINED CASE

Max Value = 170.4 kN/m2 (Element 22253 at Node 6462)

Min Value = - 356.0 kN/m2 (Element 35822 at Node 435)

7) Active Pore Pressure

UNDRAINED CASE

Max Value = 0.000 kN/m2 (Element 21135 at Node 7418)

Min Value = -41.95 kN/m2 (Element 51408 at Node 2045)

DRAINED CASE

Max Value = 0.000 kN/m2 (Element 21135 at Node 7418)

Min Value = - 30.00 kN/m2 (Element 51408 at Node 2045)

8) Excess Pore Pressure

UNDRAINED CASE

Max Value = 0.000 kN/m2 (Element 21135 at Node 7418)

Min Value = - 39.05 kN/m2 (Element 57244 at Node 241)

DRAINED CASE

Uniform Value of 0.000kN/m2

9) Ground Water Head

UNDRAINED CASE

Max Value = 3.905 m (Element 57244 at Node 241)

Min Value = 0.000 m (Element 44730 at Node 164)

DRAINED CASE

Max Value= 0.5550 m (Element 22553 at Node 1509)

Min Value = -0.07818 *10-6 m (Element 51450 at Node 2028)

10) Pore-pressure Ratio Ru

UNDRAINED CASE

Max Value = 46.08 m (Element 55608 at Node 149)

Min Value = 0.000 (Element 1 at Node 39716)

DRAINED CASE

Uniform Value of 0.000kN/m2

11) Pore Water Pressure P water

UNDRAINED CASE

Max Value = 0.000 kN/m2 (Element 21135 at Node 7418)

Max Value = -41.95 kN/m2 (Element 51408 at Node 2045)

DRAINED CASE

Max Value = 0.000 kN/m2 (Element 21135 at Node 7418)

Max Value = -30.00 kN/m2 (Element 51408 at Node 2045)

12) Total Cartesian Strain Vxy

UNDRAINED CASE

Max Value = 0.6985 *10-3 (Element 36818 at Node 8330)

Min Value = -1.165*10-3 (Element 34286 at Node 62664)

DRAINED CASE

Max Value = 0.7016*10-3 (Element 19002 at Node 88003)

Min Value = -1.153*10-3 (Element 34286 at Node 62664)

13) Total Cartesian Strain Vyz

UNDRAINED CASE

Max Value = 0.8790 *10-3 (Element 34544 at Node 8310)

Min Value = -0.8217*10-3 (Element 40881 at Node 16115)

DRAINED CASE

Max Value = 0.8701*10-3 (Element 34544 at Node 8310)

Min Value = -0.8264*10-3 (Element 40881 at Node 16115)

14) Total Cartesian Strain Vzx

UNDRAINED CASE

Max Value = 0.01006 (Element 46786 at Node 349)

Min Value = -5.989 *10-3 (Element 21722 at Node 50830)

DRAINED CASE

Max Value = 9.922*10-3 (Element 46786 at Node 349)

Min Value = -6.053*10-3 (Element 21722 at Node 50830)

SP DATA SET 2: 6 wheel surface load 50 speed (UNDRAINED AND DRAINED) Subgrade

1) **Deformed Mesh**

   UNDRAINED CASE

   Max Value = 0.1065 m (at Node 25503)

   DRAINED CASE

   Max Value= 0.06247 m (at Node 9149)

2) **Total Displacement (u)**

   UNDRAINED CASE

   Max Value = 0.1065m (Element 23774 at Node 25503)

   DRAINED CASE

   Max Value= 0.06247 m (Element 24304 at Node 9149)

3) **Quality SICN**

   UNDRAINED CASE

   Max Value = 0.9975 (Element 31905)

   Min Value = 0.1629 (Element 16959)

   DRAINED CASE

   Max Value = 0.9975 (Element 31905)

   Min Value = 0.1629 (Element 16959)

4) **Cartesian Effective Stress sigma xx**

   UNDRAINED CASE

   Max Value = 1095 kN/m2 (Element 39615 at Node 1037)

   Min Value = -1154 kN/m2 (Element 40037 at Node 119)

   DRAINED CASE

   Max Value = 3541 kN/m2 (Element 12028 at Node 33222)

   Min Value = -4188 kN/m2 (Element 3208 at Node 45193)

5) **Cartesian Effective Stress sigma yy**

   UNDRAINED CASE

   Max Value = 383.3 kN/m2 (Element 39615 at Node 1037)

   Min Value = -507.5 kN/m2 (Element 40037 at Node 119)

   DRAINED CASE

   Max Value = 942.2 kN/m2 (Element 10496 at Node 33970)

   Min Value = -2981 kN/m2 (Element 4777 at Node 45195)

6) **Cartesian Effective Stress sigma zz**

UNDRAINED CASE

Max Value = 169.1 kN/m2 (Element 22253 at Node 6462)

Min Value = - 355.0 kN/m2 (Element 35822 at Node 435)

DRAINED CASE

Max Value = 502.4 kN/m2 (Element 40463 at Node 25131)

Min Value = - 1070 kN/m2 (Element 6926 at Node 45185)

7) **Active Pore Pressure**

UNDRAINED CASE

Max Value = 0.000 kN/m2 (Element 21135 at Node 7418)

Min Value = -41.95 kN/m2 (Element 51408 at Node 2045)

DRAINED CASE

Max Value = 0.000 kN/m2 (Element 21135 at Node 7418)

Min Value = - 30.00 kN/m2 (Element 51408 at Node 2045)

8) **Excess Pore Pressure**

UNDRAINED CASE

Max Value = 0.000 kN/m2 (Element 21135 at Node 7418)

Min Value = - 39.05 kN/m2 (Element 57244 at Node 241)

DRAINED CASE

Uniform Value of 0.000kN/m2

9) **Ground Water Head**

UNDRAINED CASE

Max Value = 3.905 m (Element 57244 at Node 241)

Min Value = 0.000 m (Element 44730 at Node 164)

DRAINED CASE

Max Value= 0.5550 m (Element 25002 at Node 1641)

Min Value = -3.153 *10-3 m (Element 54726 at Node 182)

10) **Pore Pressure Ratio Ru**

UNDRAINED CASE

Max Value = 46.08 m (Element 55608 at Node 149)

Min Value = 0.000 (Element 1 at Node 39716)

DRAINED CASE

Uniform Value of 0.000KN/m2

11) **Pore -water Pressure**

UNDRAINED CASE

Max Value = 0.000 kN/m2 (Element 21135 at Node 7418)

Max Value = -41.95 kN/m2 (Element 51408 at Node 2045)

DRAINED CASE

Max Value = 0.000 kN/m2 (Element 21135 at Node 7418)

Max Value = -30.00 kN/m2 (Element 51408 at Node 2045)

12) Total Cartesian Strain Vxy

UNDRAINED CASE

Max Value = 0.6985 *10-3 (Element 36818 at Node 8330)

Min Value = -1.165*10-3 (Element 34286 at Node 62664)

DRAINED CASE

Max Value = 3.927*10-3 (Element 35238 at Node 7602)

Min Value = -5.896 *10-3 (Element 21248 at Node 7529)

13) Total Cartesian Strain Vyz

UNDRAINED CASE

Max Value = 0.8790 *10-3 (Element 34544 at Node 8310)

Min Value = -0.8217*10-3 (Element 40881 at Node 16115)

DRAINED CASE

Max Value = 5.597 *10-3 (Element 24205 at Node 17454)

Min Value = -3.945*10-3 (Element 38292 at Node 24932)

14) Total Cartesian Strain Vzx

UNDRAINED CASE

Max Value = 0.01006 (Element 46786 at Node 349)

Min Value = -5.989 *10-3 (Element 21722 at Node 50830)

DRAINED CASE

Max Value = 0.01406 (Element 46747 at Node 6287)

Min Value = -7.230*10-3 (Element 23731 at Node 1661)

SP DATA SET 3: 4 wheel surface load 15 speed (UNDRAINED AND DRAINED) Subgrade

1) Deformed Mesh

UNDRAINED CASE

Max Value = 2.520*10-3m (At Node 45451)

DRAINED CASE

Max Value= 2.520*10-3m (At Node 45451)

2) Total Displacement (u)

UNDRAINED CASE

Max Value = 2.520*10-3m (Element 1186 at Node 45451)

DRAINED CASE

Max Value= 2.520*10-3m (Element 1186 at Node 45451)

3) 6) Quality SICN

UNDRAINED CASE

Max Value = 0.9953 (Element 29363)

Min Value = 0.1539 (Element 40444)

DRAINED CASE

Max Value = 0.9953 (Element 29363)

Min Value = 0.1539 (Element 40444)

4) Cartesian Effective Stress sigma xx

UNDRAINED CASE

Max Value = 1104 kN/m2 (Element 28970 at Node 988)

Min Value = -1345 kN/m2 (Element 14695 at Node 45463)

DRAINED CASE

Max Value = 1106 kN/m2 (Element 28970 at Node 988)

Min Value = -1346 kN/m2 (Element 14695 at Node 45463)

5) Cartesian Effective Stress sigma yy

UNDRAINED CASE

Max Value = 402.4 kN/m2 (Element 28970 at Node 988)

Min Value = -1077 kN/m2 (Element 1186 at Node 45451)

DRAINED CASE

Max Value = 402.8 kN/m2 (Element 28970 at Node 988)

Min Value = - 1077 kN/m2 (Element 1186 at Node 45451)

6) Cartesian Effective Stress sigma zz

UNDRAINED CASE

Max Value = 296.5 kN/m2 (Element 35606 at Node 25357)

Min Value = - 504.4 kN/m2 (Element 1186 at Node 45451)

DRAINED CASE

Max Value = 297.2 kN/m2 (Element 35606 at Node 25357)

Min Value = - 504.4 kN/m2 (Element 1186 at Node 45451)

7) Active Pore Pressure

UNDRAINED CASE

Max Value = 0.000 kN/m2 (Element 21233 at Node 7423)

Min Value = - 42.49 kN/m2 (Element 51732 at Node 30037)

DRAINED CASE

Max Value = 0.000 kN/m2 (Element 21233 at Node 7423)

Min Value = - 30.00 kN/m2 (Element 51722 at Node 2027)

8) Excess Pore Pressure

UNDRAINED CASE

Max Value = 0.000 kN/m2 (Element 21233 at Node 7423)

Min Value = - 42.49 kN/m2 (Element 51732 at Node 30037)

DRAINED CASE

Uniform Value of 0.000kN/m2

9) Ground Water Head

UNDRAINED CASE

Max Value = 3.902 m (Element 57558 at Node 233)

Min Value = -0.2142*10-3 m (Element 45855 at Node 3849)

DRAINED CASE

Max Value= 0.5550 m (Element 27202 at Node 1530)

Min Value = -0.2380 *10-3 m (Element 55053 at Node 3849)

10) Pore Pressure Ratio Ru

UNDRAINED CASE

Max Value = 62.99 m (Element 55082At Node 159)

Min Value = 0.000 (Element 1 at Node 39188)

DRAINED CASE

Uniform Value of 0.000kN/m2

11) Pore-water Pressure P water

UNDRAINED CASE

Max Value = 0.000 kN/m2 (Element 21233 at Node 7423)

Max Value = -42.49 kN/m2 (Element 51732 at Node 30037)

DRAINED CASE

Max Value = 0.000 kN/m2 (Element 21233 at Node 7423)

Max Value = -30.00 kN/m2 (Element 51722 at Node 2027)

12) Total Cartesian Strain Vxy

UNDRAINED CASE

Max Value = 0.6828*10-3 (Element 36278 at Node 8209)

Min Value = -0.7118*10-3 (Element 24682 at Node 24799)

DRAINED CASE

Max Value = 0.6831*10-3 (Element 36278 at Node 8209)

Min Value = -0.7120*10-3 (Element 24682 at Node 24799)

13) Total Cartesian Strain Vyz

UNDRAINED CASE

Max Value = 2.204 *10-3 (Element 28592 at Node 17420)

Min Value = -2.411*10-3 (Element 25760 at Node 18054)

DRAINED CASE

Max Value = 2.192*10-3 (Element 28592 at Node 17420)

Min Value = -2.411*10-3 (Element 25760 at Node 18054)

14) Total Cartesian Strain Vzx

UNDRAINED CASE

Max Value = 2.678*10-3 (Element 26790 at Node 16830)

Min Value = -2.381*10-3 (Element 23540 at Node 22188)

DRAINED CASE

Max Value = 2.678*10-3 (Element 26790 at Node 16830)

Min Value = -2.381*10-3 (Element 23540 at Node 22188)

SP DATA SET 4: 4 wheel surface load 50 speed (UNDRAINED AND DRAINED) Subgrade

1) Deformed Mesh

UNDRAINED CASE

Max Value = 2.520*10-3m (at Node 45451)

DRAINED CASE

Max Value= 2.520*10-3m (at Node 45451)

2) Total Displacement (u)

UNDRAINED CASE

Max Value = 2.520*10-3m (Element 1186 at Node 45451)

DRAINED CASE

Max Value= 2.520*10-3m (Element 1186 at Node 45451)

3) Quality SICN

UNDRAINED CASE

Max Value = 0.9953 (Element 29363)

Min Value = 0.1539 (Element 40444)

DRAINED CASE

Max Value = 0.9953 (Element 29363)

Min Value = 0.1539 (Element 40444)

4) Cartesian Effective Stress sigma xx

UNDRAINED CASE

Max Value = 1104 kN/m2 (Element 28970 at Node 988)

Min Value = -1345 kN/m2 (Element 14695 at Node 45463)

DRAINED CASE

Max Value = 1106 kN/m2 (Element 28970 at Node 988)

Min Value = -1346 kN/m2 (Element 14695 at Node 45463)

5) Cartesian Effective Stress sigma yy

UNDRAINED CASE

Max Value = 402.4 kN/m2 (Element 28970 at Node 988)

Min Value = -1077 kN/m2 (Element 1186 at Node 45451)

DRAINED CASE

Max Value = 402.8 kN/m2 (Element 28970 at Node 988)

Min Value = - 1077 kN/m2 (Element 1186 at Node 45451)

6) Cartesian Effective Stress sigma zz

UNDRAINED CASE

Max Value = 296.5 kN/m2 (Element 35606 at Node 25357)

Min Value = - 504.4 kN/m2 (Element 1186 at Node 45451)

DRAINED CASE

Max Value = 297.2 kN/m2 (Element 35606 at Node 25357)

Min Value = - 504.4 kN/m2 (Element 1186 at Node 45451)

7) Active Pore Pressure

UNDRAINED CASE

Max Value = 0.000 kN/m2 (Element 21233 at Node 7423)

Min Value = - 42.49 kN/m2 (Element 51732 at Node 30037)

DRAINED CASE

Max Value = 0.000 kN/m2 (Element 21233 at Node 7423)

Min Value = - 30.00 kN/m2 (Element 51722 at Node 2027)

8) Excess Pore Pressure

UNDRAINED CASE

Max Value = 0.000 kN/m2 (Element 21233 at Node 7423)

Min Value = - 39.02 kN/m2 (Element 57558 at Node 233)

DRAINED CASE

Uniform Value of 0.000kN/m2

9) Ground Water Head

UNDRAINED CASE

Max Value = 3.902 m (Element 57558 at Node 233)

Min Value = -0.2142*10-3 m (Element 45855 at Node 3849)

DRAINED CASE

Max Value= 0.5550 m (Element 27202 at Node 1530)

Min Value = -0.2380 *10-3 m (Element 55053 at Node 3849)

10) Pore Pressure Ratio Ru

UNDRAINED CASE

Max Value = 62.99 m (Element 55082At Node 159)

Min Value = 0.000 (Element 1 at Node 39188)

DRAINED CASE

Uniform Value of 0.000KN/m2

11) Pore-water Pressure P water

UNDRAINED CASE

Max Value = 0.000 kN/m2 (Element 21233 at Node 7423)

Max Value = -42.49 kN/m2 (Element 51732 at Node 30037)

DRAINED CASE

Max Value = 0.000 kN/m2 (Element 21233 at Node 7423)

Max Value = -30.00 kN/m2 (Element 51722 at Node 2027)

12) Total Cartesian Strain Vxy

UNDRAINED CASE

Max Value = 0.6828*10-3 (Element 36278 at Node 8209)

Min Value = -0.7118*10-3 (Element 24682 at Node 24799)

DRAINED CASE

Max Value = 0.6831*10-3 (Element 36278 at Node 8209)

Min Value = -0.7120*10-3 (Element 24682 at Node 24799)

13) Total Cartesian Strain Vyz

UNDRAINED CASE

Max Value = 2.204 *10-3 (Element 28592 at Node 17420)

Min Value = -2.411*10-3 (Element 25760 at Node 18054)

DRAINED CASE

Max Value = 2.192*10-3 (Element 28592 at Node 17420)

Min Value = -2.411*10-3 (Element 25760 at Node 18054)

14) Total Cartesian Strain Vzx

UNDRAINED CASE

Max Value = 2.678*10-3 (Element 26790 at Node 16830)

Min Value = -2.381*10-3 (Element 23540 at Node 22188)

DRAINED CASE

Max Value = 2.678*10-3 (Element 26790 at Node 16830)

Min Value = -2.381*10-3 (Element 23540 at Node 22188)

APPENDIX I: Measurement of TATA TRUCK TIPPER 1613c

Figure I1. Weighing TATA TRUCK 1613c (Empty Weight: 7745KG)

Figure I2. Weighing Ticket of TATA TRUCK 1613c (Empty Weight: 7745KG)

Figure I3. Measurement of TATA TRUCK 1613c

TATA TRUCK TIPPER 1613c 2018 Model

Wheel base=3.625m

Front=1.964m & Rare Axle=2.15m

Wheel Diameter=1.05m (Measured & Calculated from Tire size)

Contact Area=0.3 (wheel path)*0.2(Tire width), etc.)

Front and Rear Tire Size 10.00 x 20 -16 PR Diagonal Ply

Max. Speed=93km/h

Verified the data with Sipradi Traders Company web site

FORD RANGER 3.2 XLT (4*4) 2021 Model

Wheel base=3.220m

Empty Weight=2230KG

Front & Rare Axle: 1.570m

Wheel Diameter=0.763m (Calculated from Tire Size)

Front and Rare Tire size: 265/65 R17

Max. Speed=175km/h

Taken the data from FORD RANGER Company web site

APPENDIX J: Higher Material Models

Table J1 Material models for Mohr-Coulomb (MC)

Item	Description
Identification	Subgrade
Material model	Mohr-Coulomb (MC)
Drainage type	Undrained-A/Drained
Unsaturated unit weight, γ_{unsat} (kN/m^3)	18
Saturated unit weight, γ_{sat} (kN/m^3)	20
Initial void Ratio, e_{init}	1.635
Modulus of Elasticity, E (MPa)	E = 10.0 * CBR for CBR ≤ 5 % & E = 17.6 * $(CBR)^{0.64}$ for CBR > 5 % (FPDG, 2014) Where, E= Resilient modulus of subgrade soil (MPa). CBR = California bearing ratio of subgrade soil (%)- 5%
Poisson's ratio, υ	0.35
Cohesion (kPa)	9
Friction (Degrees)	28.07
Dilation Angle (Degrees), Ψ	0
Soil Type	Clay
<2µm% 2µm-50µm% 50µm-2mm%	10 13 17
Flow Parameter	

Horizontal Permeability X-dir. Kx m/day	1.4655
Horizontal Permeability Y-dir Ky m/day	1.4655
Vertical Permeability Kz m/day	0.00977

Table J2 Material models for Hardening Soil (HS)

Item	Description
Identification	Subgrade
Material model	Hardening Soil (HS)
Drainage type	Undrained-A/Drained
Unsaturated unit weight, γ_{unsat} (kN/m^3)	18
Saturated unit weight, γ_{sat} (kN/m^3)	20
Initial void Ratio, e_{init}	1.635
Poisson's ratio, υ	0.35
Cohesion (kPa)	9
Friction (Degrees), ϕ	28.07
Dilation Angle (Degrees), Ψ	0
Secant Stiffness in Standard Drained Triaxial test $E50_{ref}$ (kPa)	18.94*e3
Tangent Stiffness for primary Odometer loading $E_{oed\ ref}$ (kPa)	15.15*e3
Loading/reloading Stiffness E_{ref} (kPa)	$1.05*10^5$
Compression Index, Cc	0.04

Swelling Index, Cs	0.004
OCR	1.0
POP (kN/m2)	0.0
Soil Type <2µm% 2µm-50µm% 50µm-2mm%	Clay 10 13 77
Horizontal Permeability X-dir. Kx m/day Horizontal Permeability Y-dir Ky m/day Vertical Permeability Kz m/day	1.4655 1.4655 0.00977

Table J3 Material models for Soft Soil (SS)

Item	Description
Identification	Subgrade
Material model	Soft Soil (SS)
Drainage type	Undrained-A/Drained
Unsaturated unit weight, γ_{unsat} (kN/m^3)	18
Saturated unit weight, γ_{sat} (kN/m^3)	20
Poisson's ratio	0.35
Cohesion (kPa)	9
Friction (Degrees)	28.07
Dilation Angle (Degrees)	0
Initial void Ratio, e_{init}	1.635
Soil Type	Clay

<2µm% 2µm-50µm% 50µm-2mm%	10 13 77
Horizontal Permeability X-dir. Kx m/day Horizontal Permeability Y-dir Ky m/day Vertical Permeability Kz m/day	1.4655 1.4655 0 .00977
Consolidation Results Cs Cc	 0.04 0.004
Tangent of the critical state, m Compression index, λ for NC Unloading stiffness Swelling index, k for NC	1.3 0.3 0.0 0.05
OCR	1.0
POP (kN/m2)	0.0

Table J4 Material models for Modified Cam-Clay soil

Item	Description
Identification	Subgrade
Material model	Modified Cam-Clay (MCC)
Drainage type	Undrained-A/Drained
Unsaturated unit weight, γ_{unsat} (kN/m^3)	18
Saturated unit weight, γ_{sat} (kN/m^3)	20
Initial void ratio, e_0	1.635
Poisson's ratio	0.35

Cohesion (kPa)	9
Friction (Degrees)	28.07
Dilation Angle (Degrees)	0
Soil Type <2µm% 2µm-50µm% 50µm-2mm%	Clay 10 13 77
Horizontal Permeability X-dir. Kx m/day Horizontal Permeability Y-dir Ky m/day Vertical Permeability Kz m/day	1.4655 1.4655 0 .00977
Tangent of the critical state, m Compression index, λ for NC Unloading stiffness Swelling index, k for NC	1.3 0.3 0.0 0.05
OCR	1.0
POP (kN/m2)	0.0

APPENDIX K: Numerical Evaluation (Sample Results-Area & Point Load Case)

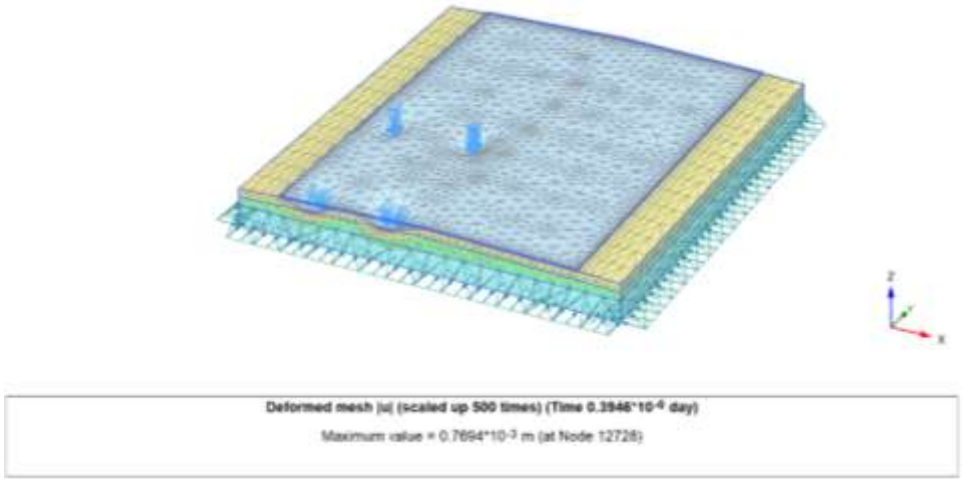

Figure K1. Deformed mesh of Tata Truck 1613c model without geogrid under area load at 15 km/h.

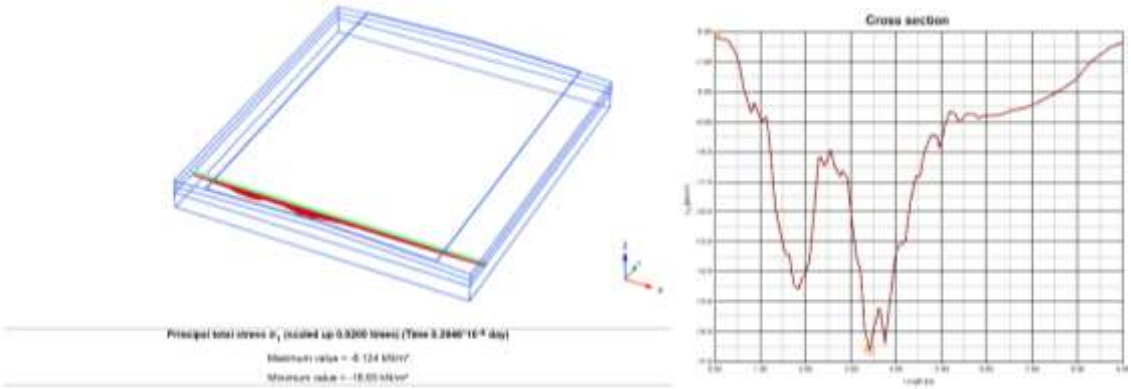

Figure K2. Sigma-1 distribution for Tata Truck 1613c without geogrid under area load at 15 km/h: Left – principal stress plot; Right – cross-sectional view.

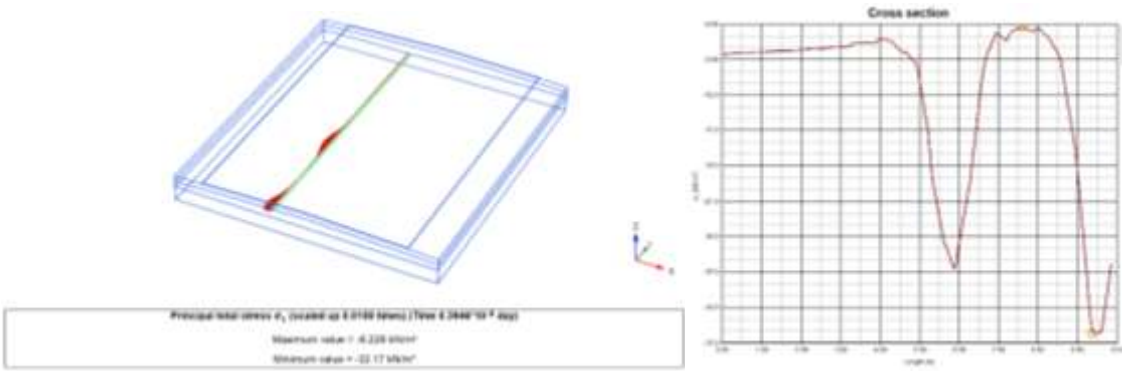

Figure K3. Sigma-1 stress along the longitudinal wheel path at 2nd wheel position for Tata Truck 1613c without geogrid under area load at 15 km/h: Left – principal stress plot; Right – cross-sectional view.

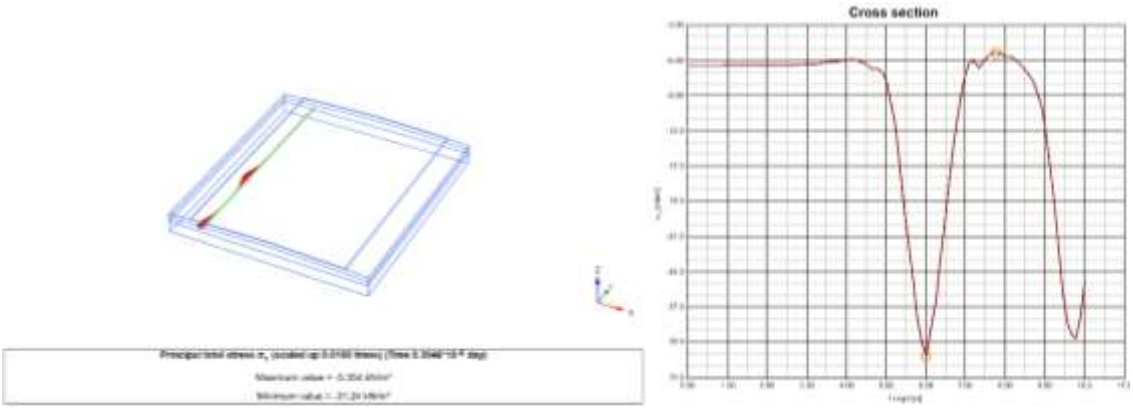

Figure K4. Sigma-1 stress along the longitudinal wheel path at 4th wheel position for Tata Truck 1613c without geogrid under area load at 15 km/h: Left–principal stress plot; Right–cross-sectional view.

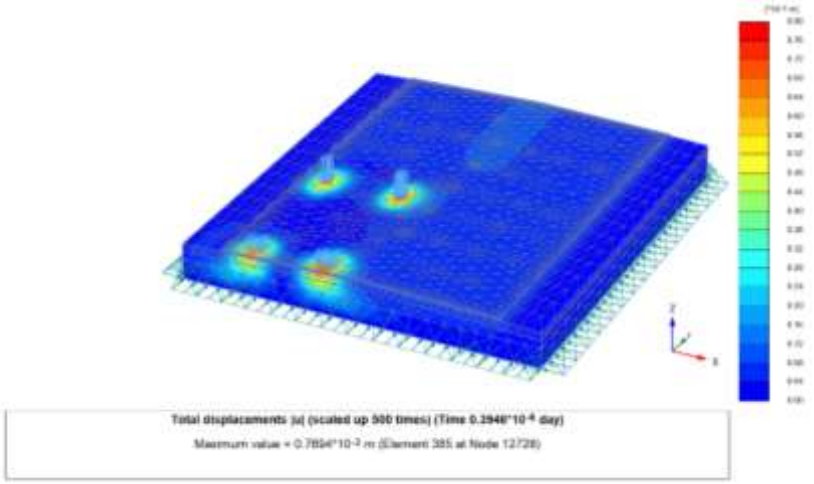

Figure K5. Total displacement (u) in the Tata Truck Tipper 1613c model without geogrid reinforcement under area load at a constant speed of 15 km/h.

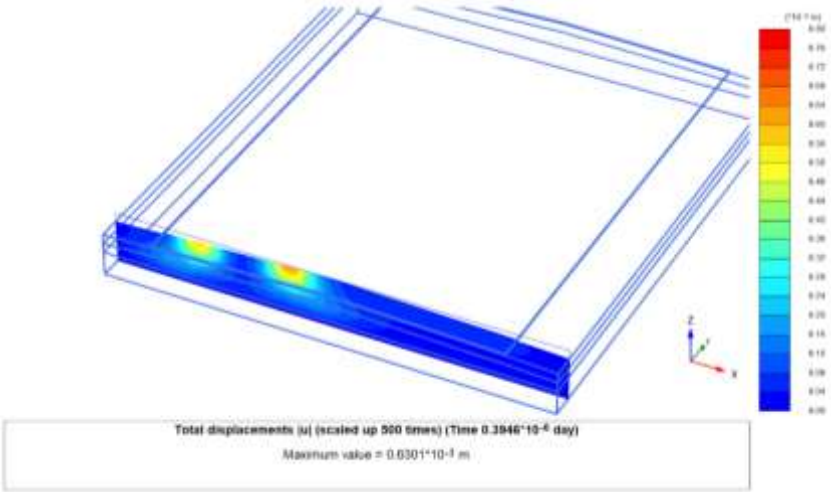

Figure K6. Displacement (u) along the first section of the symmetric road width for the Tata Truck 1613c model without geogrid, under area load at 15 km/h.

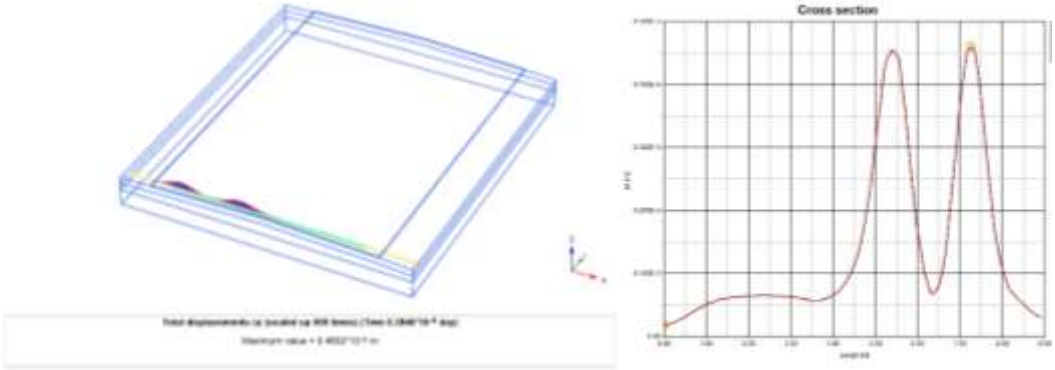

Figure K7. Displacement (u) along the first transverse section of the road for the Tata Truck 1613c model without geogrid, under area load at 15 km/h. Left: Stress plot; Right: Cross-sectional view.

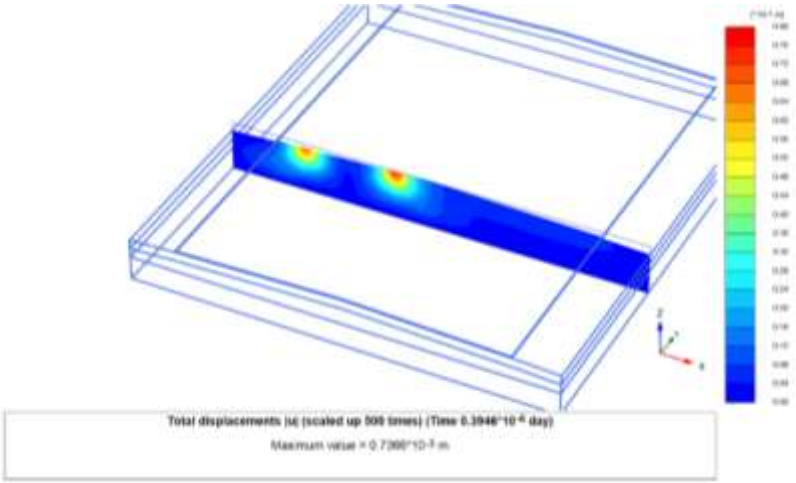

Figure K8. Total displacements (u) along the second section of the symmetric road width for the Tata Truck Tipper 1613c model without geogrid reinforcement at 15 km/h.

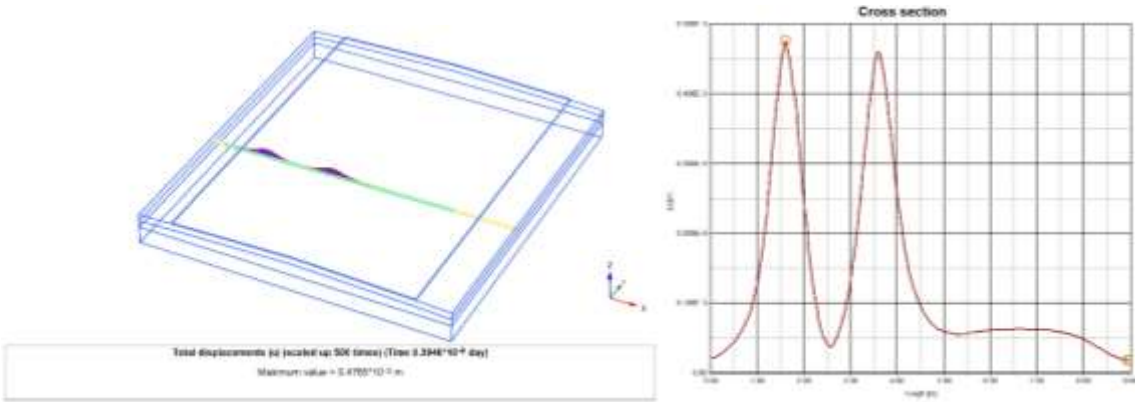

Figure K9. Total displacement (u) along the first transverse section of the road for the Tata Truck Tipper 1613c model at 15 km/h, without geogrid reinforcement. Left: Stress plot; Right: Cross-sectional view.

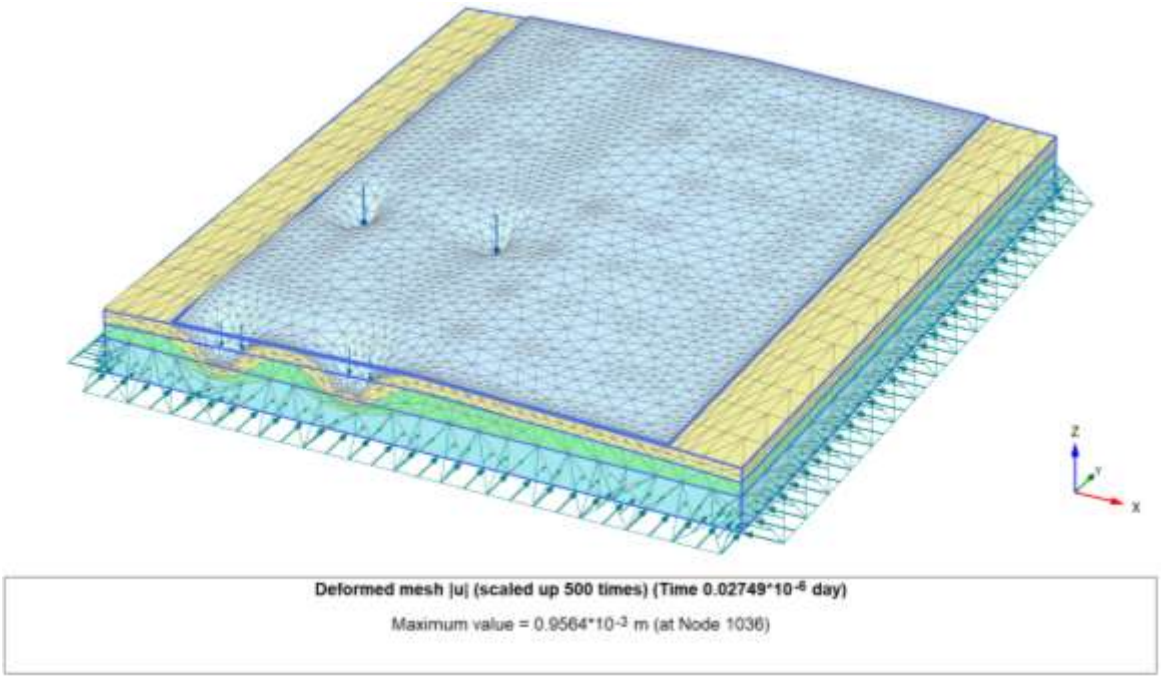

Figure K10 Deformed mesh of the Tata Truck Tipper 1613c model without geogrid reinforcement, subjected to a point load at a constant speed of 50 km/h with acceleration a=1.0m/sec2

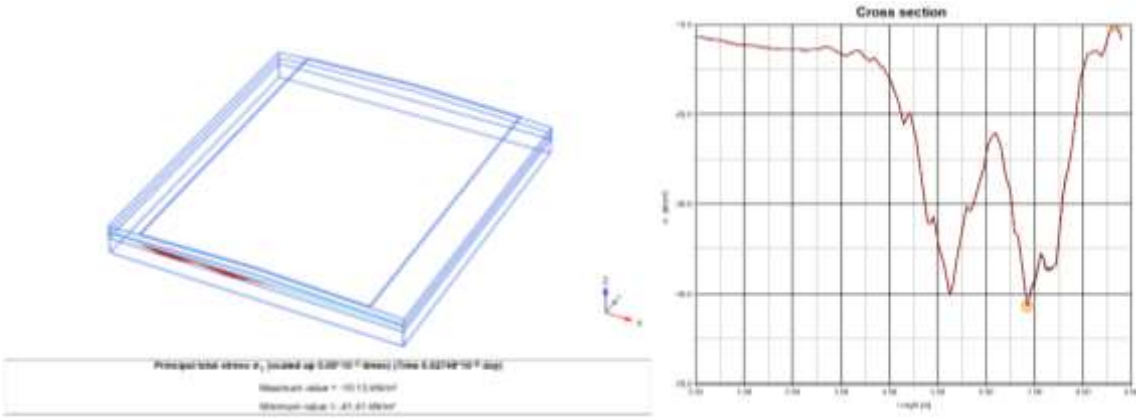

Figure K11: Principal Stress (σ_1) along the symmetric half of the road. Left: σ_1 distribution along Section-1. Right: Cross-sectional view of total σ_1 under a Tata Truck Tipper 1613c (without geogrid), subjected to a point load at 50 km/h with 1.0 m/s^2 acceleration

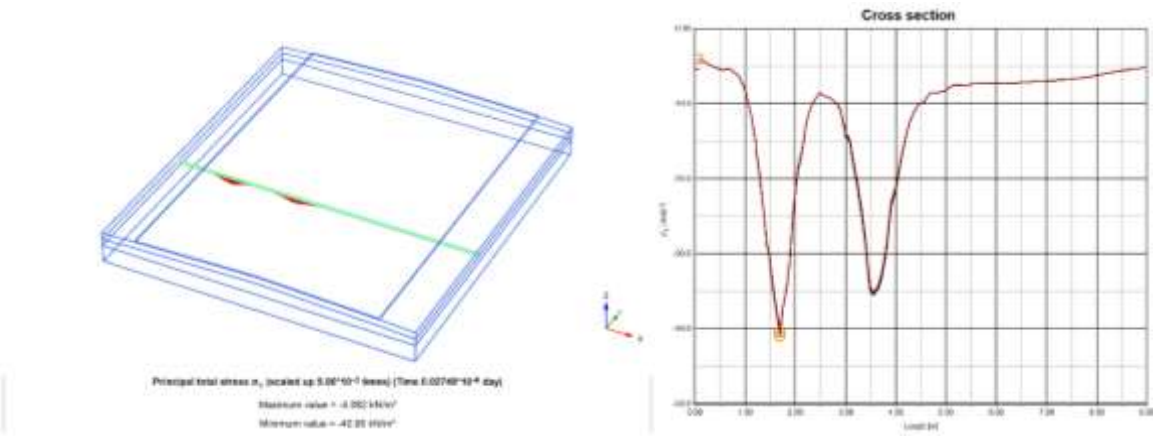

Figure K12: Principal Stress (σ_1) along the symmetric half of the road. Left: σ_1 distribution along Section-2. Right: Cross-sectional view of total σ_1 under a Tata Truck Tipper 1613c (without geogrid), with a point load at 50 km/h and 1.0 m/s^2 acceleration

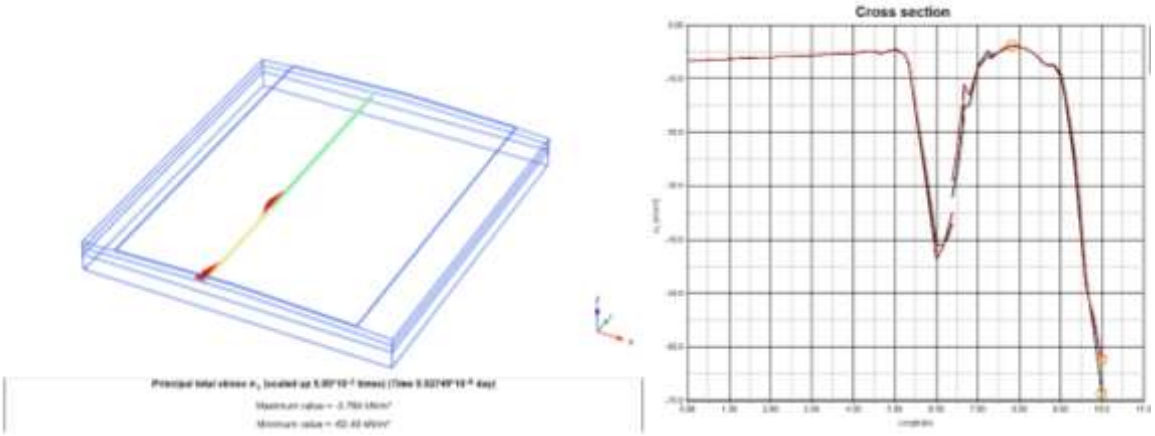

Figure K13: Principal Stress (σ_1) along the wheel path (longitudinal direction) of the road. Left: σ_1 distribution along Section-1. Right: Cross-sectional view of total σ_1 under a Tata Truck Tipper 1613c (without geogrid), with a point load at 50 km/h and 1.0 m/s^2 acceleration

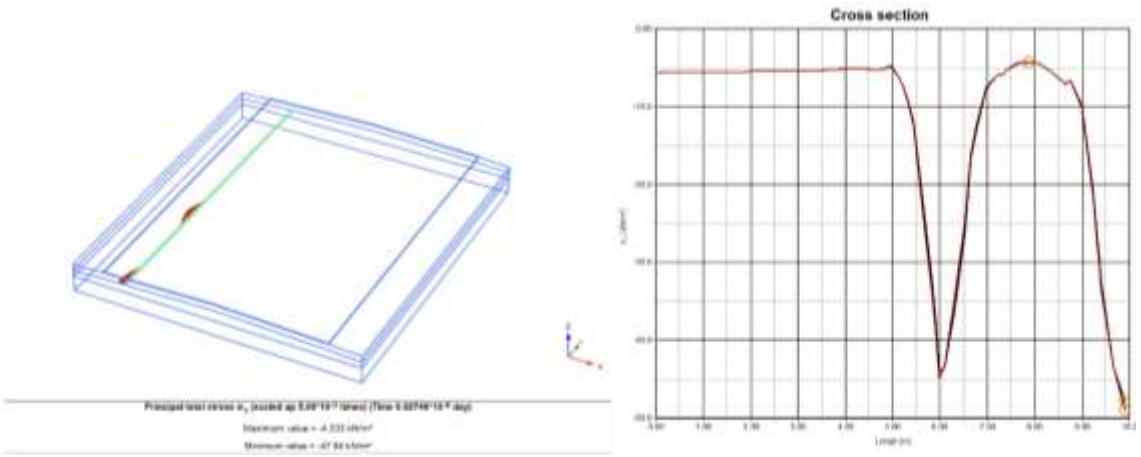

Figure K14: Principal Stress (σ_1) along the wheel path (longitudinal direction) of the road. Left: σ_1 distribution along Section-2. Right: Cross-sectional view of total σ_1 under a Tata Truck Tipper 1613c (without geogrid), with a point load at 50 km/h and 1.0 m/s² acceleration

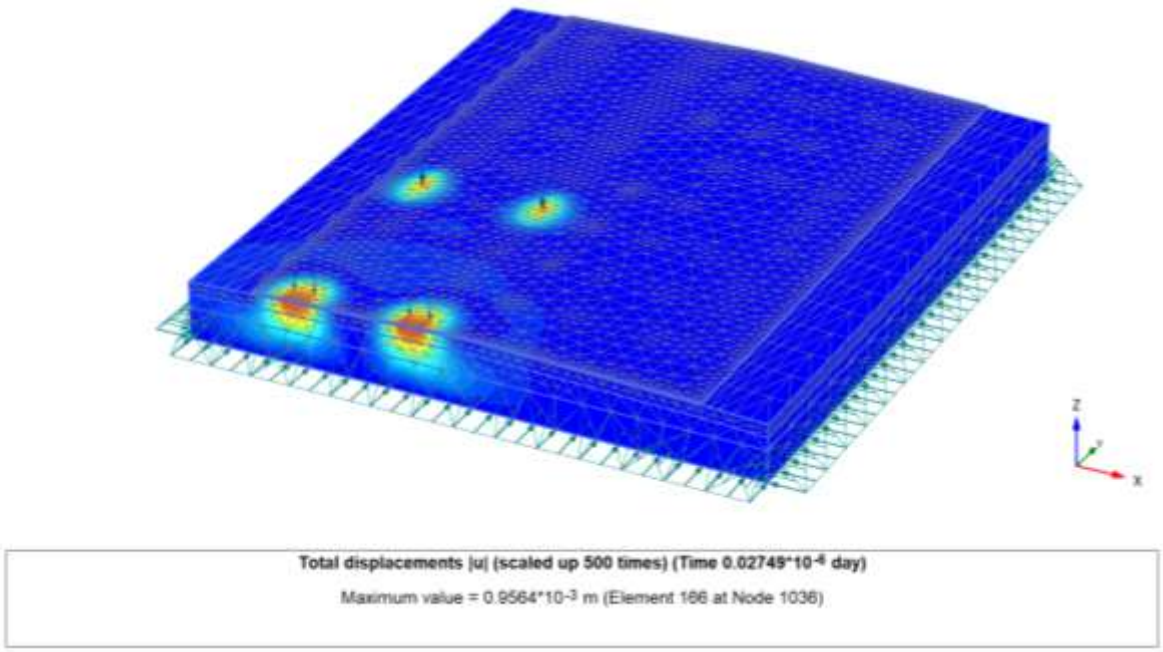

Figure K15: Total displacement (u) in the Tata Truck Tipper 1613c model without geogrid reinforcement, under a point load at 50 km/h and 1.0 m/s² acceleration

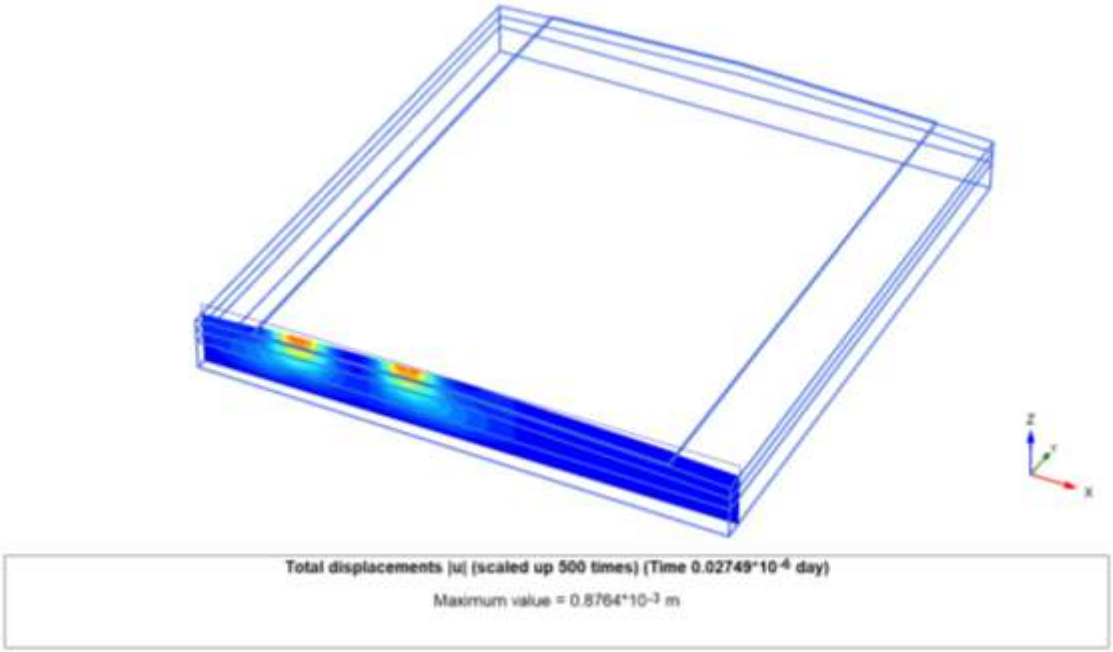

Figure K16: Total displacement (u) along Section-1 of the symmetric half-width of the road in the Tata Truck Tipper 1613c model without geogrid reinforcement, under a point load at 50 km/h and 1.0 m/s² acceleration

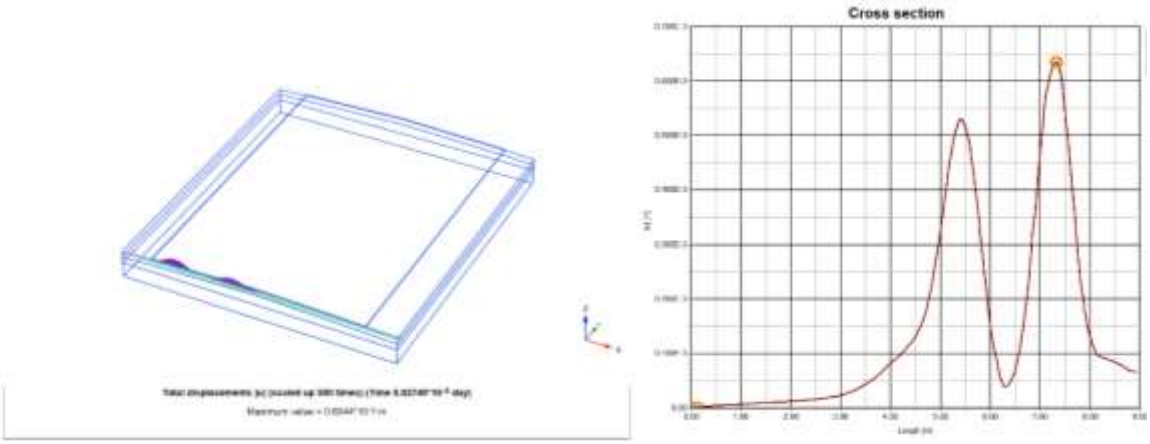

Figure K17: Principal Stress (σ_1) along the symmetric half of the road (transverse direction). Left: σ_1 distribution along Section-1. Right: Cross-sectional view of total σ_1 for the Tata Truck Tipper 1613c model without geogrid reinforcement, under a point load at 50 km/h and 1.0 m/s² acceleration

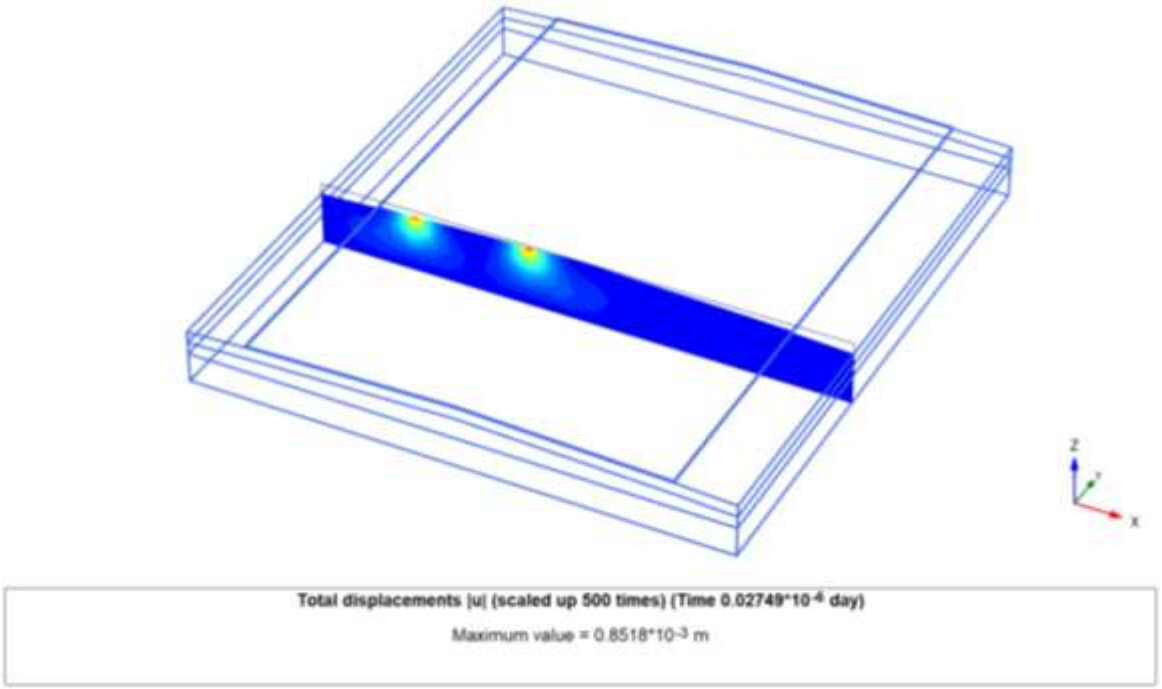

Figure K18: Total displacement (u) along Section-2 of the symmetric half-width of the road (transverse direction) in the Tata Truck Tipper 1613c model without geogrid reinforcement, under a point load at 50 km/h and 1.0 m/s² acceleration

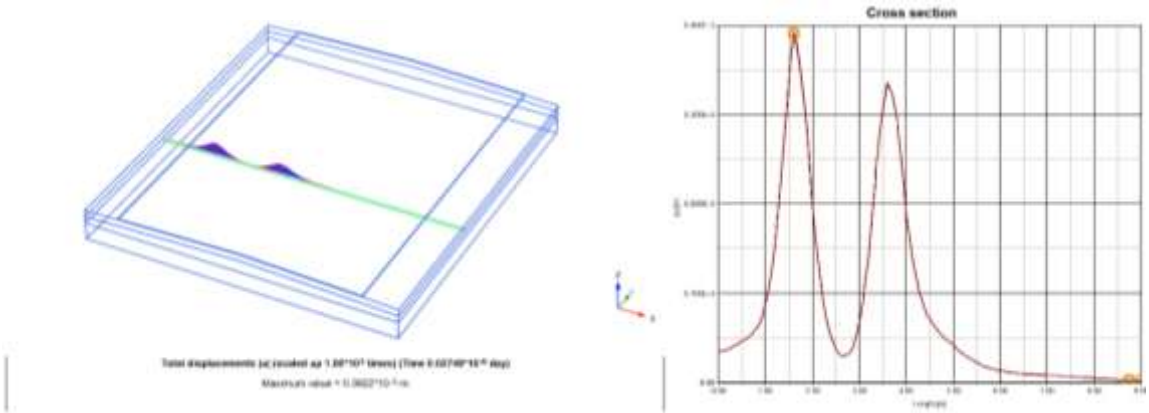

Figure K19: Principal Stress (σ_1) along the symmetric half of the road (transverse direction). Left: σ_1 distribution along Section-2. Right: Cross-sectional view of total σ_1 for the Tata Truck Tipper 1613c model without geogrid reinforcement, under a point load at 50 km/h and 1.0 m/s² acceleration

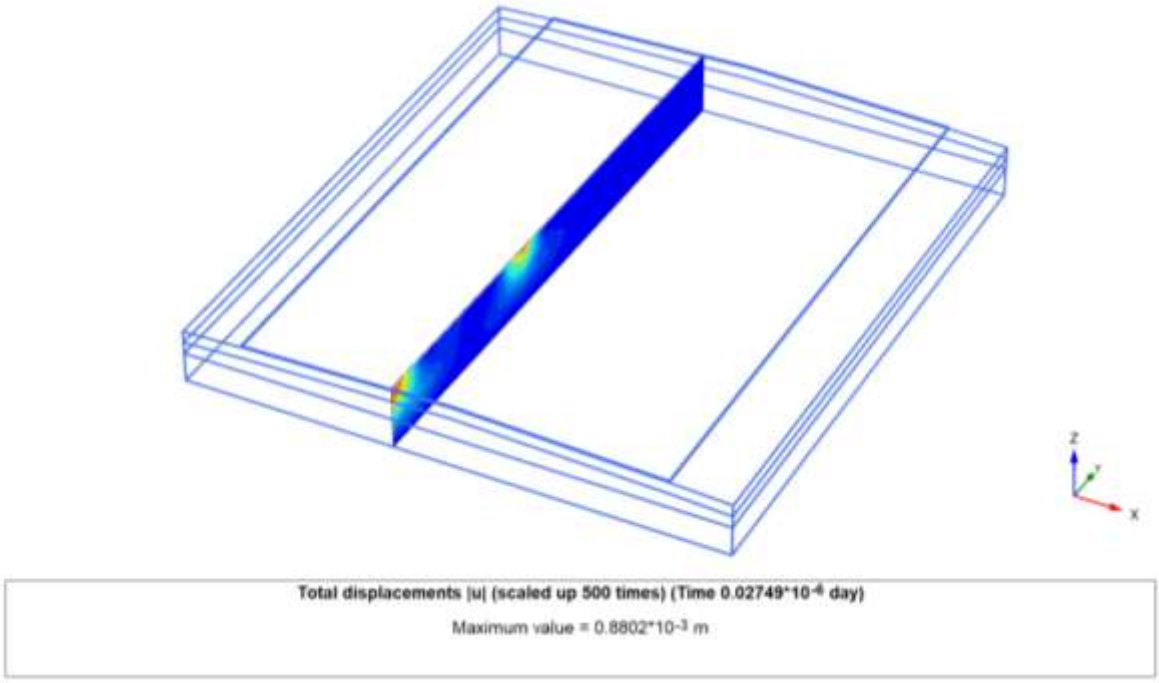

Figure K20: Principal Stress (σ_1) along the wheel path (longitudinal direction-1) of the road, based on the Tata Truck Tipper 1613c model without geogrid reinforcement, under a point load at 50 km/h with 1.0 m/s² acceleration

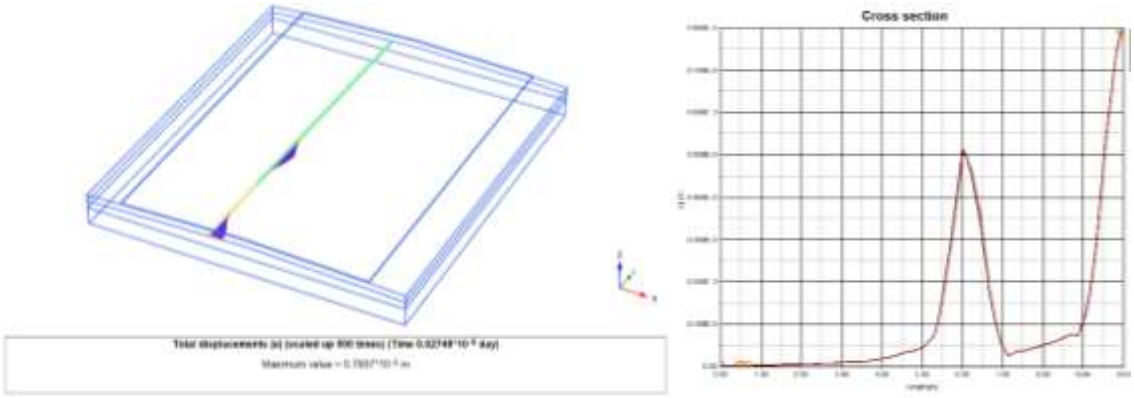

Figure K21: Principal Stress (σ_1) along the wheel path (longitudinal direction-1) of the road. Left: σ_1 distribution along Section-1. Right: Cross-sectional view of total σ_1 for the Tata Truck Tipper 1613c model without geogrid reinforcement, under a point load at 50 km/h and 1.0 m/s² acceleration

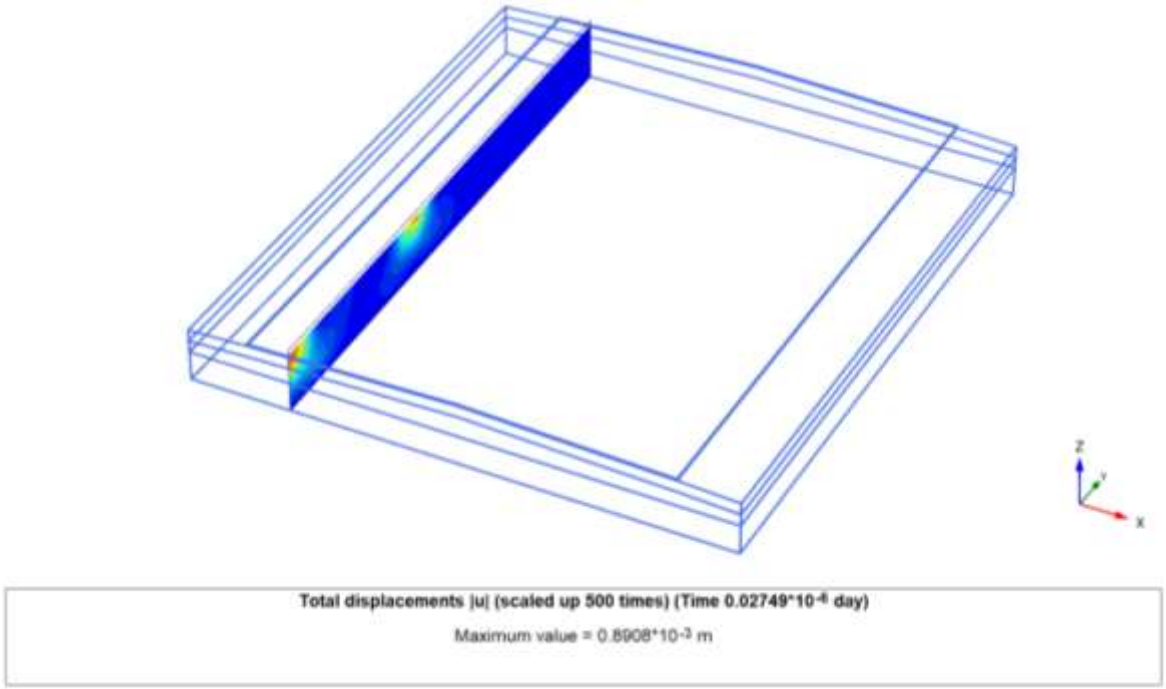

Figure K22: Principal Stress (σ_1) along the wheel path (longitudinal section, Section-2) of the road, based on the Tata Truck Tipper 1613c model without geogrid reinforcement, under a point load at 50 km/h and 1.0 m/s² acceleration

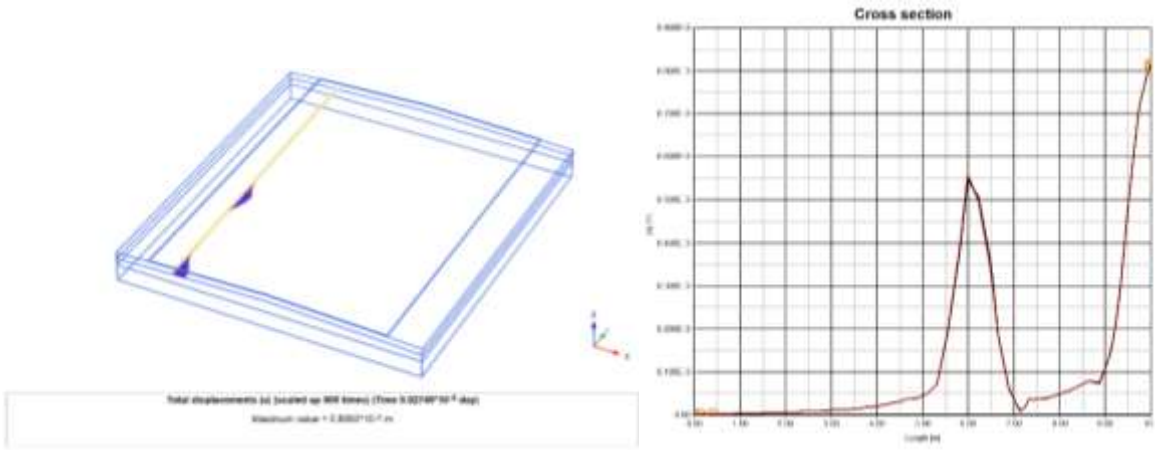

Figure K23: Principal Stress (σ_1) along the wheel path (longitudinal section) of the road. Left: σ_1 distribution along Section-2. Right: Cross-sectional view of total σ_1 for the Tata Truck Tipper 1613c model without geogrid reinforcement, under a point load at 50 km/h and 1.0 m/s² acceleration

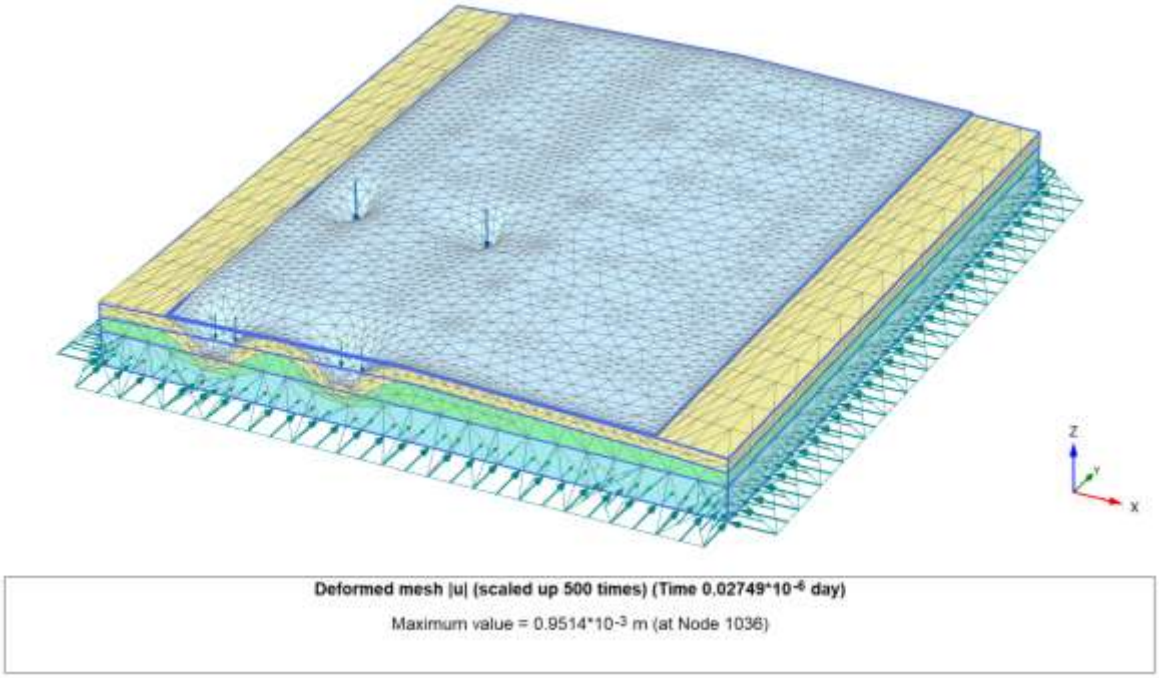

Figure K24: Total displacement (u) in the Tata Truck Tipper 1613c model with geogrid reinforcement, under a point load at 50 km/h and 1.0 m/s² acceleration

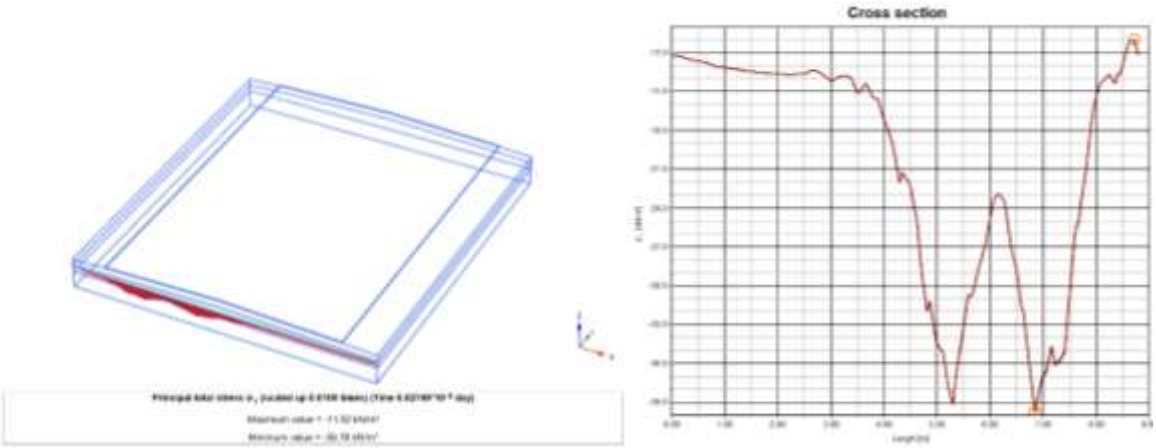

Figure K25: Principal Stress (σ_1) along the symmetric half of the road (transverse direction). Left: σ_1 distribution along Section-1. Right: Cross-sectional view of total σ_1 for the Tata Truck Tipper 1613c model with geogrid reinforcement, under a point load at 50 km/h and 1.0 m/s² acceleration

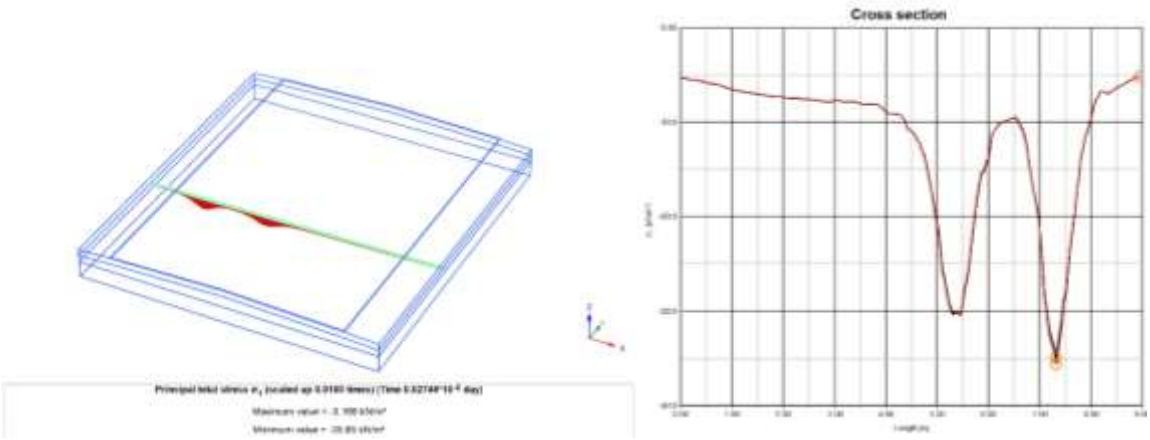

Figure K26: Principal Stress (σ_1) along the symmetric half of the road (transverse direction). Left: σ_1 distribution along Section-2. Right: Cross-sectional view of total σ_1 for the Tata Truck Tipper 1613c model with geogrid reinforcement, under a point load at 50 km/h and 1.0 m/s^2 acceleration

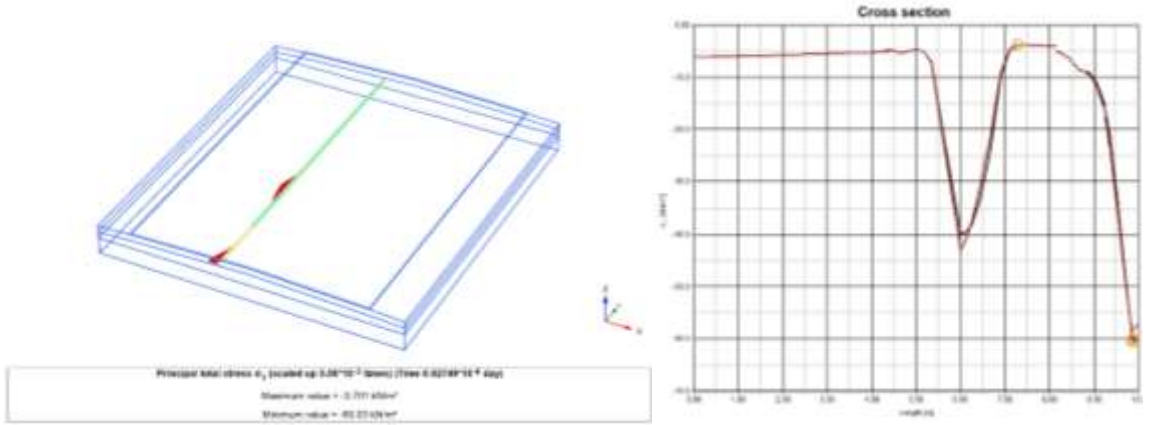

Figure K27: Principal Stress (σ_1) along the wheel path (longitudinal direction) of the road. Left: σ_1 distribution along Section-1. Right: Cross-sectional view of total σ_1 for the Tata Truck Tipper 1613c model without geogrid reinforcement, under a point load at 50 km/h and 1.0 m/s^2 acceleration

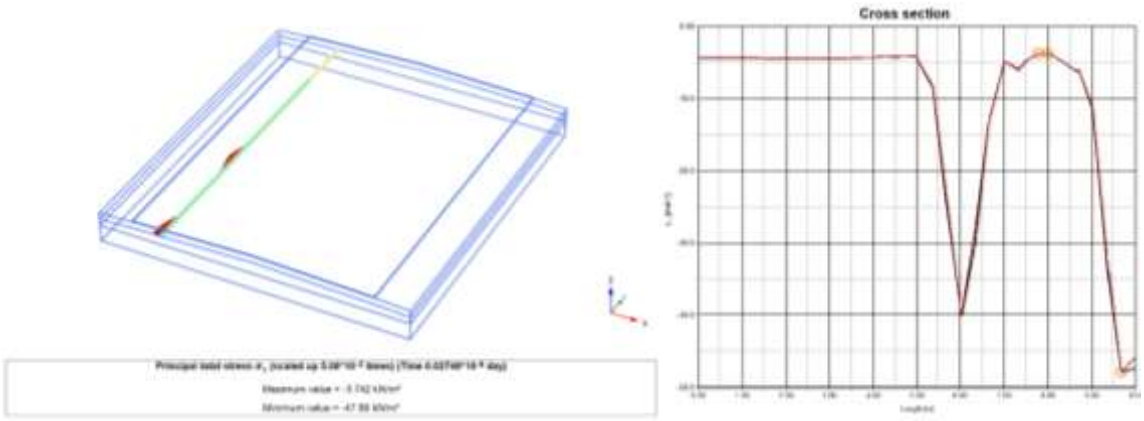

Figure K28: Principal Stress (σ_1) along the wheel path (longitudinal direction) of the road. Left: σ_1 distribution along Section-2. Right: Cross-sectional view of total σ_1 for the Tata Truck Tipper 1613c model without geogrid reinforcement, under a point load at 50 km/h and 1.0 m/s^2 acceleration

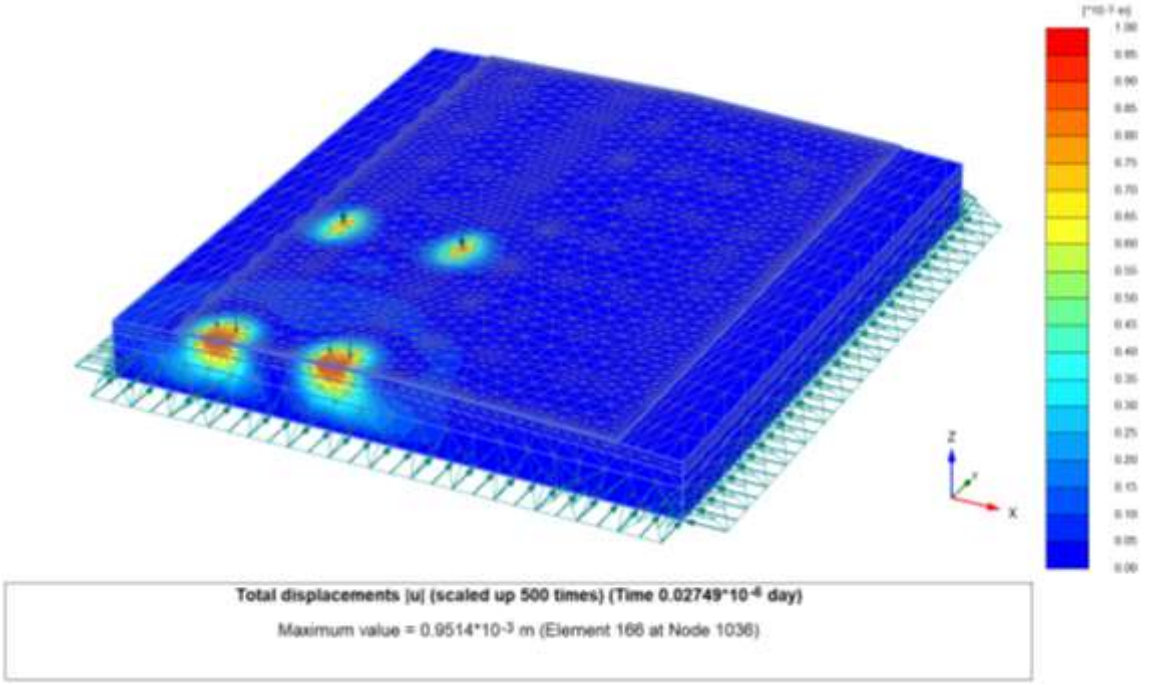

Figure K29: Total displacement (u) for the Tata Truck Tipper 1613c model with geogrid reinforcement, under a point load at 50 km/h and 1.0 m/s^2 acceleration

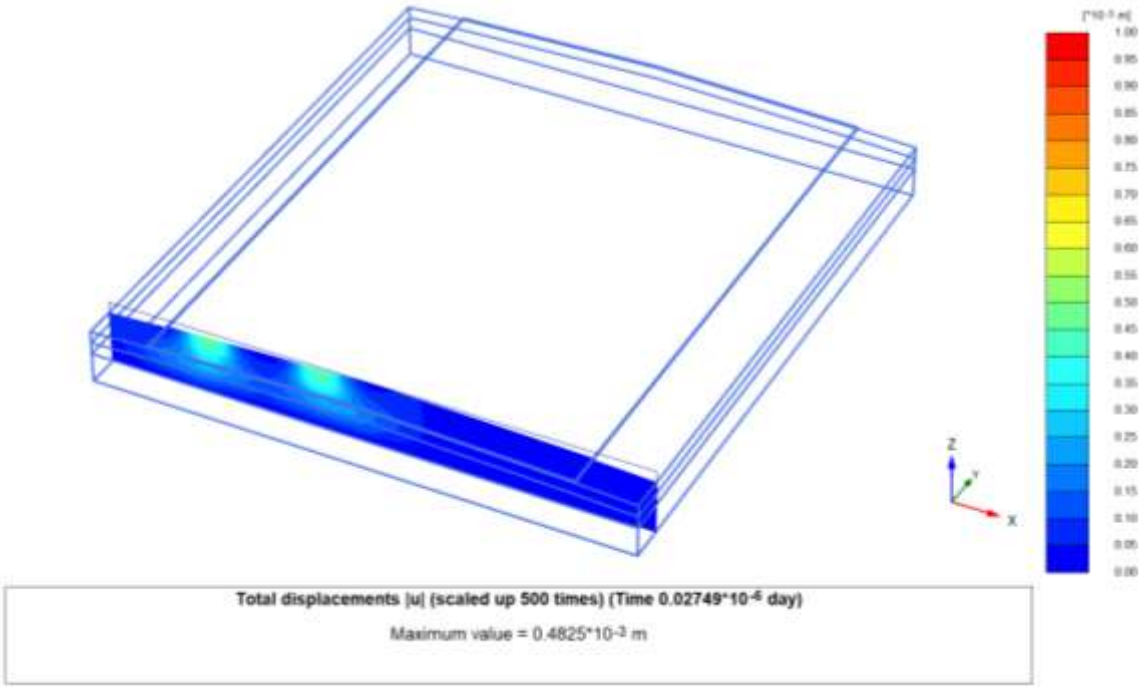

Figure K30: Total displacement (u) along the symmetric half-width of the road (Section-1) in the Tata Truck Tipper 1613c model with geogrid reinforcement, under a point load at 50 km/h and 1.0 m/s² acceleration

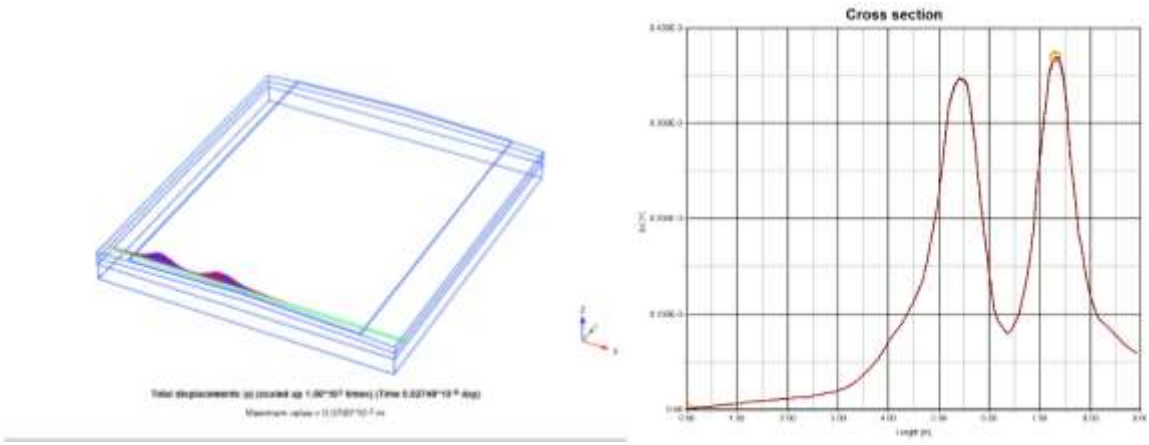

Figure K31: Total displacement (u) along the symmetric half of the road (transverse direction). Left: Total displacement plot along Section-1. Right: Cross-sectional view of total displacement for the Tata Truck Tipper 1613c model with geogrid reinforcement, under a point load at 50 km/h and 1.0 m/s² acceleration

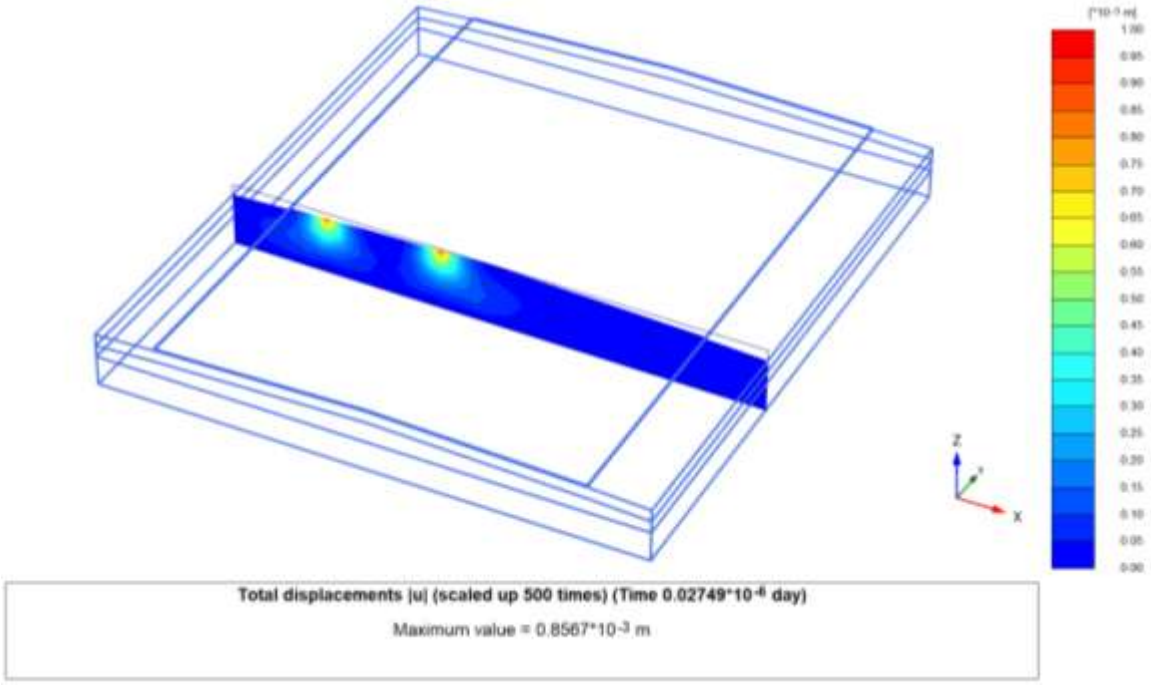

Figure K32: Total displacement (u) along the symmetric half-width of the road (transverse direction, Section-2) in the Tata Truck Tipper 1613c model with geogrid reinforcement, under a point load at 50 km/h and 1.0 m/s² acceleration

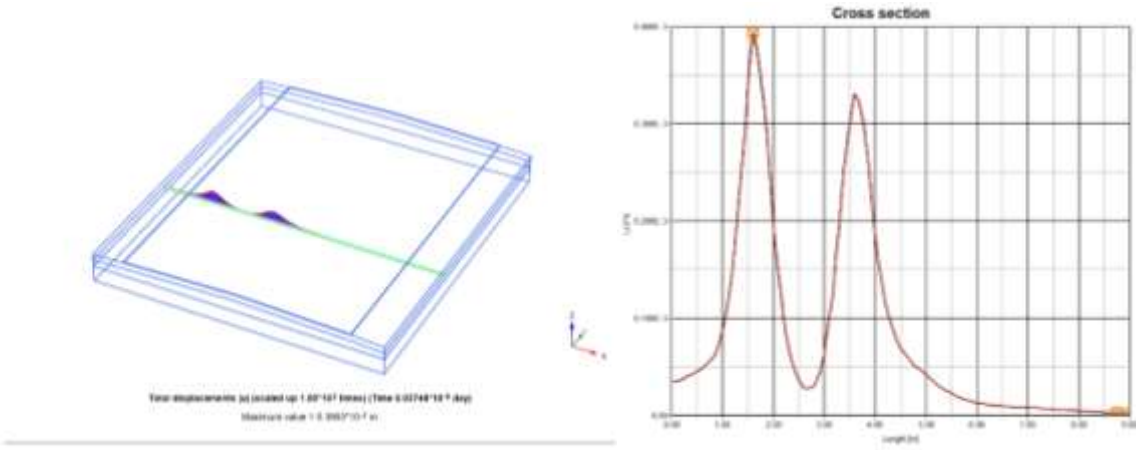

Figure K33: Total displacement (u) along the symmetric half of the road (transverse direction). Left: Total displacement plot along Section-2. Right: Cross-sectional view of total displacement for the Tata Truck Tipper 1613c model with geogrid reinforcement, under a point load at 50 km/h and 1.0 m/s² acceleration

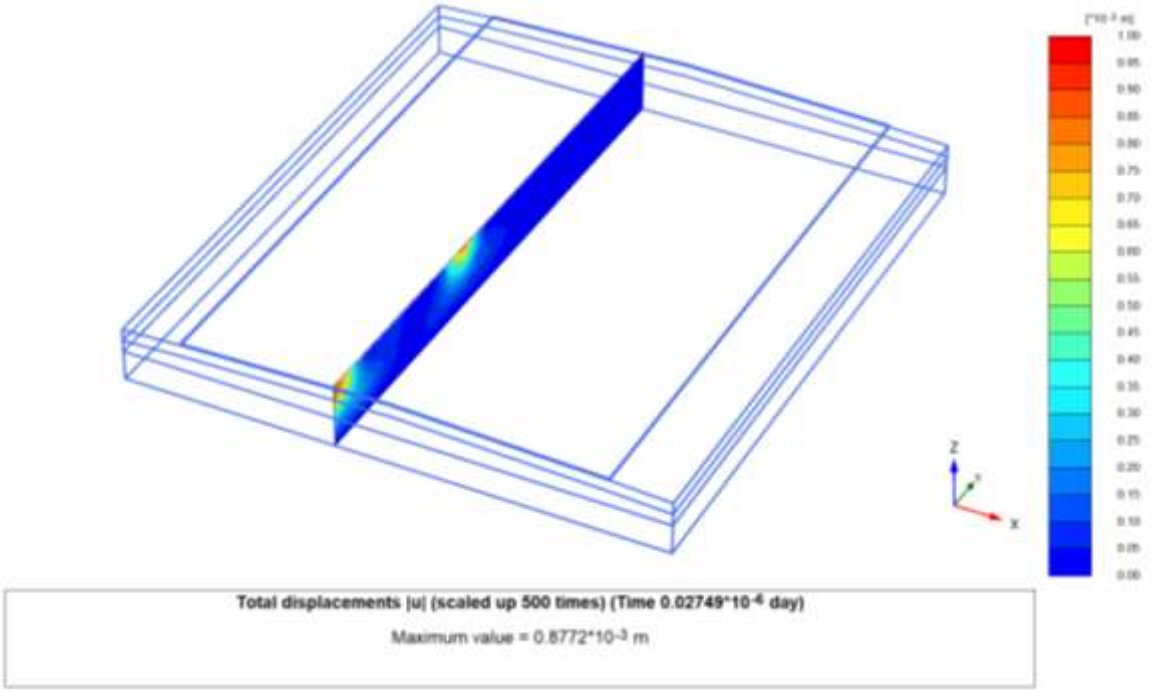

Figure K34: Total displacement (u) along the first section of the wheel path (longitudinal direction, Section-1) of the road in the Tata Truck Tipper 1613c model with geogrid reinforcement, under a point load at 50 km/h and 1.0 m/s² acceleration

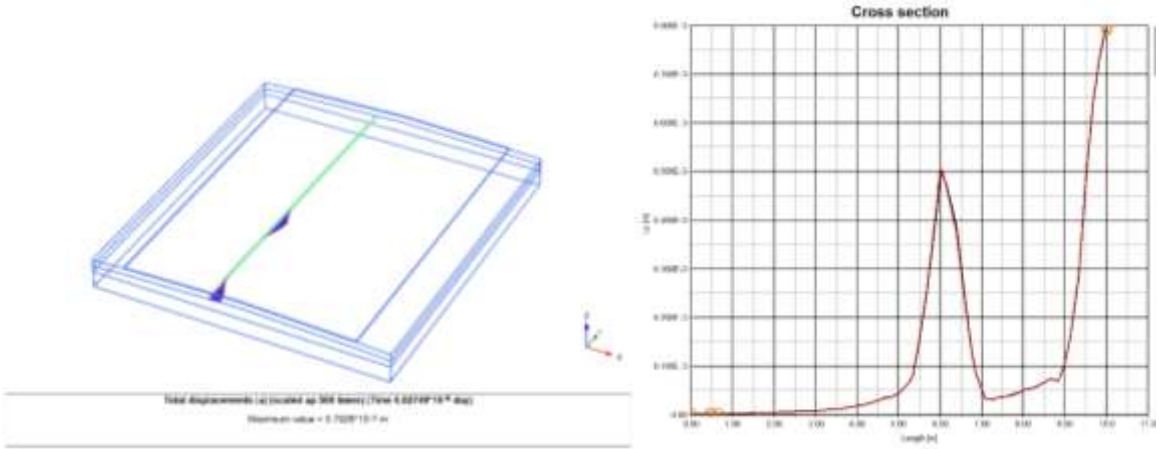

Figure K35: Total displacement (u) along the wheel path (longitudinal direction) of the road. Left: Total displacement plot along Section-1. Right: Cross-sectional view of total displacement for the Tata Truck Tipper 1613c model with geogrid reinforcement, under a point load at 50 km/h and 1.0 m/s² acceleration

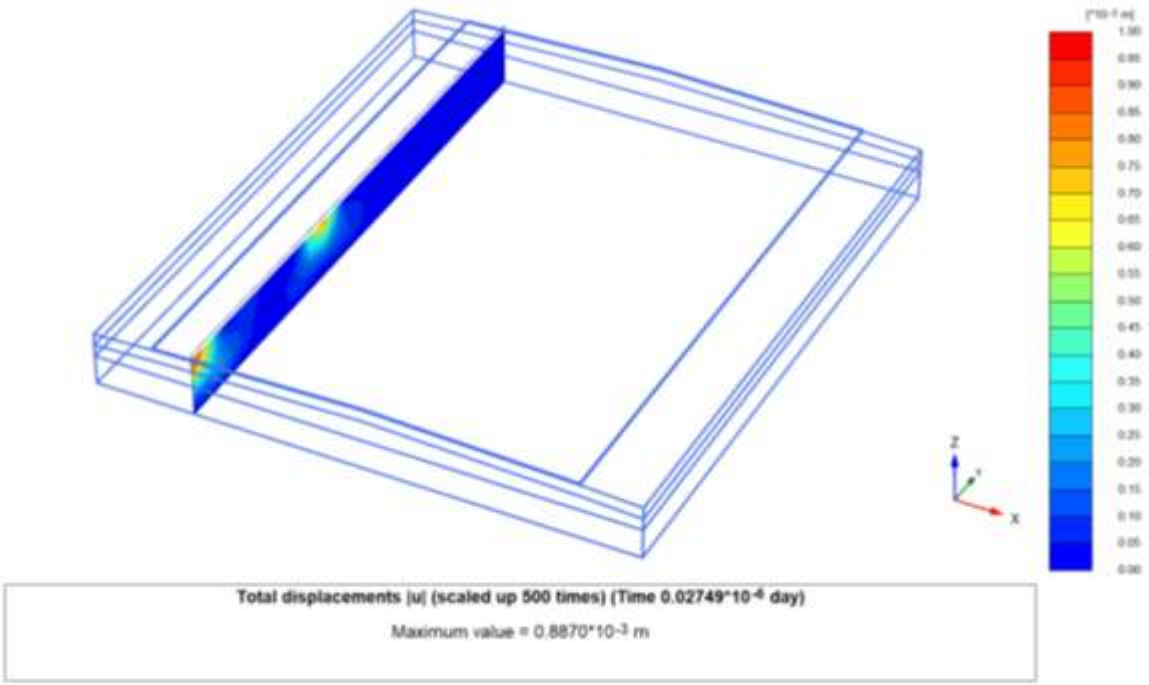

Figure K36: Total displacement (u) along the first section of the wheel path (longitudinal direction, Section-2) of the road in the Tata Truck Tipper 1613c model with geogrid reinforcement, under a point load at 50 km/h and 1.0 m/s² acceleration

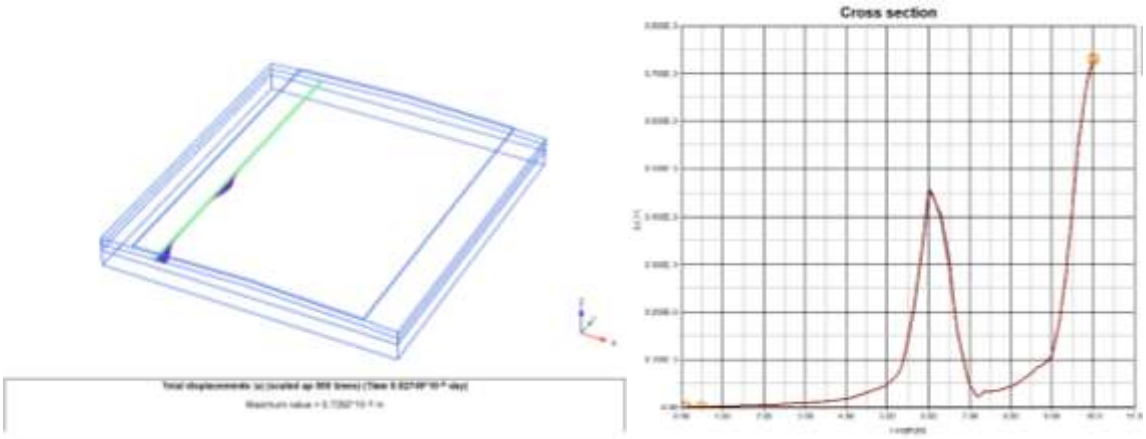

Figure K37: Total displacement (u) along the wheel path (longitudinal direction) of the road. Left: Total displacement plot along Section-2. Right: Cross-sectional view of total displacement for the Tata Truck Tipper 1613c model with geogrid reinforcement, under a point load at 50 km/h and 1.0 m/s² acceleration